Technische Universität München
TUM School of Natural Sciences

Molecular Design of Chemically Fueled Complex Coacervates

Fabian Späth

Vollständiger Abdruck der von der TUM School of Natural Sciences der Technischen

Universität München zur Erlangung eines

Doktors der Naturwissenschaften (Dr. rer. nat.)

genehmigten Dissertation.

Vorsitz: Prof. Dr. Matthias Feige

Prüfende der Dissertation:

1. Prof. Dr. Job Boekhoven
2. Priv.-Doz. Dr. Alexander Pöthig
3. Assoc. Prof. Dr. Jean-Hubert Olivier

Die Dissertation wurde am 17.05.2024 bei der Technischen Universität München eingereicht

und durch die TUM School of Natural Sciences am 28.06.2024 angenommen.

I.Abstract

The process of liquid-liquid phase separation is ubiquitous in nature. It is the basis for the formation of various dynamic structures in cells, like membraneless organelles. These are characterized by non-equilibrium states determining their formation and properties, which are driven by processes that constantly consume energy. As theoretical models show, such active droplets could exhibit life-like behaviors like self-division and controlled growth. These processes result from material flows driven by the constant turnover of precursors and activated species.

We have developed a reaction cycle that mimics these non-equilibrium states. An activation reaction causes the neutralization of negative charges in the precursors, increasing the binding capacity of the activated species with polyanions and thereby initiating phase separation. Due to the constant hydrolysis of the activated species, these chemically driven complex coacervates have a limited lifetime.

These chemically complex emulsions react to the structural features of their building blocks and stimuli, which can be controlled. For this purpose, the influences of the peptide precursor structures and the polymer components had to be tested. I, therefore, investigated how the net charge of the cationic peptide building blocks dominates the life cycle of chemically regulated complex coacervates. The polymer components also influenced droplet formation: long polymer chains led to delayed dissolution of the droplets, block copolymers formed micelles with different morphologies that transformed into each other, and the type of electrolyte group determined the binding strength with the peptides. Special attention was also paid to oligonucleotides as biologically relevant polyanions. These were identified as weak polyelectrolytes whose binding to the peptides is influenced by the nucleobases. Furthermore, the hybridization state of DNA could be used to control the properties of the chemically controlled coacervates, *e.g.* their size, droplet number, or fluidity.

In addition, the carbodiimide-driven reaction cycle was extended by an additional reaction pathway, leading to the formation of ester bonds. Through targeted peptide design with arginine units, aromatic amino acids and tyrosines, condensation of the peptides with themselves, *i.e.,* simple coacervation, could be realized in addition to complex coacervation with polyanions. The active droplets exhibited lifetimes of several hours, making them a promising platform for future applications.

This work contributes to a deeper understanding of molecular designs for synthetic, chemically active coacervates. During the systematic investigations, the established reaction cycles were advanced significantly. This expanded the scope for models for membraneless organelles. The broad design possibilities within this chemically driven coacervate platform provide an ideal basis for developing dynamic and biomimetic materials.

II. Zusammenfassung

Der Vorgang der flüssig-flüssig-Phasentrennung ist allgegenwärtig in der Natur. Er ist auch die Grundlage der Bildung verschiedenster, dynamischer Strukturen in Zellen, wie z.B. von membranlosen Organellen. Diese zeichnen sich dadurch aus, dass ihre Bildung und Eigenschaften von Nichtgleichgewichtszuständen bestimmt werden, die wiederum durch Prozesse gebildet werden, die ständig Energie verbrauchen. Wie theoretische Modelle zeigen, können solche chemisch aktiven Tropfen lebensähnliches Verhalten wie Selbstteilung und kontrolliertes Wachstum zeigen. Diese Prozesse sind die Konsequenz von Materialflüssen, die durch den ständigen Umsatz der Präkursoren und der aktivierten Spezies angetrieben werden. Wir haben einen Reaktionszyklus entwickelt, der diese Nichtgleichgewichtszustände nachempfinden kann. Eine Aktivierungsreaktion führt zur Neutralisation von negativen Ladungen in den Präkursoren, wodurch die Bindefähigkeit der aktivierten Spezies mit Polyanionen erhöht wird und die Phasentrennung bzw. Koazervatbildung initiiert wird. Aufgrund der ständigen Hydrolyse der aktivierten Spezies weisen die chemisch angetriebenen komplexen Koazervate eine begrenzte Lebensdauer auf.

Diese chemisch komplexen Systeme reagieren auf verschiedene Strukturmerkmale ihrer Bausteine und Stimuli, die kontrolliert werden können. Hierfür mussten die Einflüsse der Peptidstrukturen und der Polymerkomponenten untersucht werden. Deshalb habe ich untersucht, wie bereits die Netto-Ladung der kationischen Peptidbausteine die Entwicklung der chemisch regulierten komplexen Koazervate dominieren kann. Auch die Polymerkomponenten zeigten Einflüsse auf die Tropfenbildung: lange Polymerketten führten zu verzögerter Auflösung der Tropfen, Blockcopolymere bildeten Mizellen mit verschiedenen Morphologien die sich ineinander umwandelten und die Elektrolytgruppen bestimmten über die Bindungsstärken mit den Peptiden. Ein besonderes Augenmerk wurde auch auf Oligonukleotide als biologisch relevante Polyanionen gerichtet. Diese wurden als schwache Polyelektrolyte identifiziert, deren Bindung mit den Peptiden von ihren Nukleobasen beeinflusst wird. Darüber hinaus konnte der Hybridisierungszustand von DNA dazu genutzt werden, um Eigenschaften der chemisch gesteuerten Koazervate, nämlichen deren Größe, Zahl oder Fluidität, zu steuern.

Außerdem konnte der Carbodiimid-gesteuerte Reaktionszyklus um einen weiteren Reaktionspfad erweitert werden, nämlich um die Bildung von Esterbindungen. Durch gezieltes Peptiddesign mit Arginineinheiten und aromatischen Aminosäuren konnte so neben der komplexen Koazervation mit Polyanionen auch die Phasentrennung der Peptide mit sich selbst realisiert werden, die sog. einfache Koazervation. Die aktiven Tropfen wiesen eine Lebensdauer von mehreren Stunden auf, weshalb sich diese Emulsion besonders gut als Plattform für biomimetische Systeme und praktische Anwendungen eignen könnte.

Zusammenfassend lässt sich feststellen, dass diese Arbeit zu einem tieferen Verständnis von molekularen Designs für chemisch aktive Koazervate beiträgt. Im Zuge der systematischen Untersuchungen konnte der etablierte Reakionszyklus auf der Basis von Peptiden und Carbodiimiden weiterentwickelt werden. Hierdurch wurde auch der chemische Spielraum für Modelle für membranlose Organelle signifikant erweitert. Die breiten Gestaltungsmöglichkeiten der Plattform stellen eine ideale Grundlage für die Entwicklung von dynamischen und biomimetischen Materialien dar.

III.   Abbreviations

ADP   adenosine diphosphate

ATP   adenosine triphosphate

DIC   *N,N'*-Diisopropylcarbodiimide

DNA   deoxyribonucleic acid

DSA   dissipative self-assembly

e.g.   *exempli gratia,* for example

EDC   1-Ethyl-3-(3-dimethylaminopropyl)carbodiimide

et al.   *et alii, and others*

HPLC   high-performance liquid chromatography

i.e.   *id est,* that is

ITC   isothermal titration calorimetry

MES   2-morpholinoethanesulfonic acid

MLO   membraneless organelle

PEG   polyethylene glycol

polyU   poly(uridylic acid)

PSS   poly(4-styrene sulfonic acid)

PVPA   poly(vinylphosphonic acid)

PVS   poly(vinylsulfonic acid)

RNA   ribonucleic acid

UV   ultraviolet

Vis   visible

IV. Table of contents

1.   Introduction

Abstract

Liquid-liquid phase separation into coacervate droplets is a ubiquitous process in biology and can be applied to generate diverse sets of materials. In this chapter, I introduce the underlying principles of this phase separation process and show examples of coacervate-derived materials. Then, I will describe the difference between complex coacervation as a passive or active process. For this purpose, dynamic coacervate structures in biology are introduced, as well as theoretical models that describe active coacervates' versatile properties and special behavior, such as size control or self-division. Then, artificial dynamic coacervation platforms will be presented that aim at mimicking the complex examples in nature. A special emphasis is put on the unique behaviors of chemically fueled coacervates based on a carbodiimide-driven reaction cycle. These results serve as a starting point for new building block designs and reaction cycles that form droplets with life-like properties. As such, they could also serve as artificial cells or protocell models.

1.1.   Liquid-liquid Phase Separation

1.1.1. Complex Coacervation

Complex coacervation describes an associative phase separation of macromolecules. This liquid-liquid phase separation occurs when oppositely charged polymers are combined in an aqueous solution below a critical salt concentration. In the process, they form a dense, concentrated coacervate phase and a supernatant phase dilute in polyion species.[1] The resulting complex coacervate phase often behaves like a liquid droplet phase, but the complexes can range from solids to liquid droplets and soluble complexes that can be interconverted into each other, *e.g.*, by the addition of salt.[2-3]

The association process is driven by the electrostatic interactions of the charged species and a gain in entropy by the release of counter ions [4-5]. It is considered to proceed through two stages. In the first step, polyion pairs are formed, condensing in the second step to form the coacervate phase (Scheme 1).[6-7]
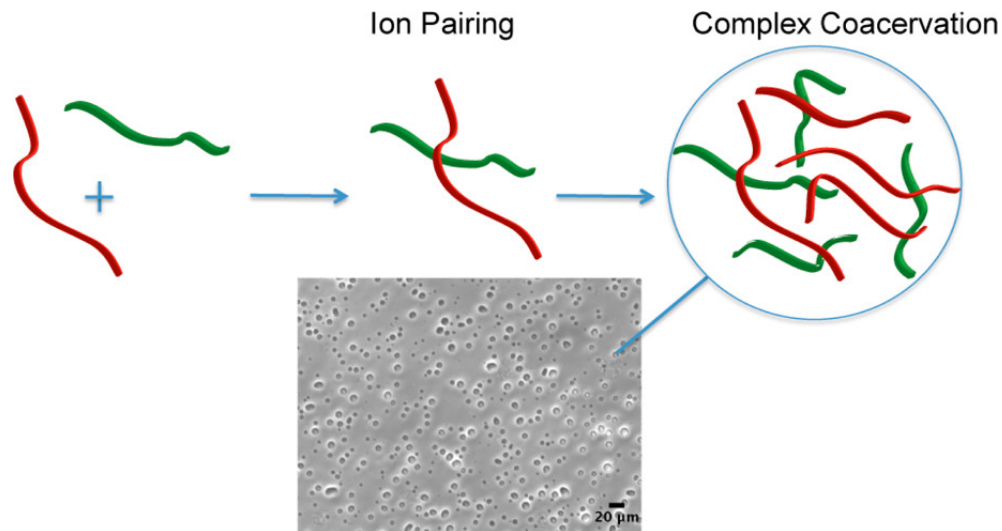
Scheme 1. The two-step process behind complex coacervation of oppositely charged polyions (shown in red and green). Reprinted with permission from reference [6]. Copyright © 2012, American Chemical Society.

In many examples, additional intermolecular interactions, such as hydrogen bonding, aromatic and hydrophobic interactions, contribute as driving forces in the phase separation.[1, 8] Complex coacervation can be controlled by adjusting temperature, the mixing ratio of the components, ionic strength, and pH, making coacervates intrinsically stimuli-responsive and highly dynamic materials.[9] On a molecular level, structural features of the charged macromolecules, such as polymer length, charge density, or their monomer sequence, determine their phase separation behavior.[10-11]

Droplets are not the only possible morphology to be formed through complex coacervation. When block copolymers made of a neutral and an ionic block are combined with another ionic-neutral copolymer or oppositely charged homopolymer, polymeric nanoparticles or micelles, so-called coacervate core micelles, can be generated. [12-13] They have a coacervate core and a neutral corona built from nonionic blocks like polyethylene glycol (PEG) and appear as spherical micelles, worm-like structures, or even polymersomes (Fig. 1).[14-15]
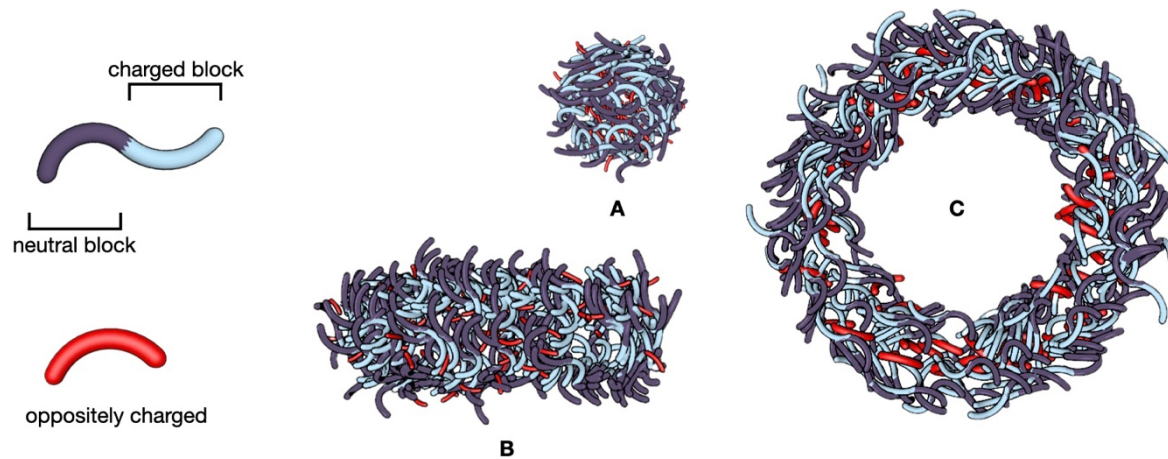
Figure 1. These different coacervate core micelles (C3Ms) morphologies can be formed in the phase-separation of block copolymers with a neutral and an ionic block. Depending on factors such as the interaction strength of the oppositely charged polyelectrolytes and their length, coacervate core micelles can occur in the form of spherical micelles (**A**), wormlike micelles (**B**), or polymersomes (**C**).[12]

Complex coacervation is a process of great biological relevance. Biomacromolecules like proteins and oligonucleotides have the structural features for intermolecular interactions leading to liquid-liquid phase separation. Nature uses so-called membraneless organelles as subcompartments in cells. They usually contain proteins in combination with RNA or DNA and are classified as coacervate-based structures serving as biochemical reaction hubs, participating in processes involved in cellular stress responses and signaling and organizing the internal cellular space.[16]

1.1.2. Simple Coacervation

In contrast to complex coacervation introduced in the previous chapter, another type of liquid-liquid phase separation can occur when only one species condenses into a coacervate phase. This process is called simple coacervation. It can require additives like salts or alcohols to promote condensation by self-charge neutralization.[17-18] Examples in nature, like in the case of intrinsically disordered scaffold proteins of the FUS family, show that one main driving force for the self-association is intramolecular interactions between cationic residues, primarily arginine units, and aromatic residues, mainly with tyrosine side chains. In-depth screenings of corresponding mutants showed that the strong cation-π interactions between these residues were particularly potent in inducing self-assembly compared to arginine-phenylalanine or lysine-tyrosine interactions.[19] Other examples showed that self-association can also result

from mainly electrostatic interactions. In Ddx4 proteins, blocks with alternating net charges were identified as highly conserved features that drive coacervation. However, these motifs occur together with sequences enriched in aromatic amino acids in the positively charged blocks, further stabilizing the droplets.[20]

The self-association of molecules with multiple π-systems was also implemented in synthetic examples. Comblike polymers with pending guanidinium units were synthesized and underwent phase-separation at low temperatures due to stacking of their guanidinium units. Their UCST-type behavior was controlled by polymer and salt concentrations.[21] Further investigations on polyether polymers with pending guanidinium units revealed that salts were needed for phase separation with a strong dependence on the anion type, facilitating guanidinium stacking. Large halide anions were more effective in screening the electrostatic repulsion between the charged guanidinium groups, leading to a higher critical transition temperature for the UCST behavior (Fig. 2).[22]
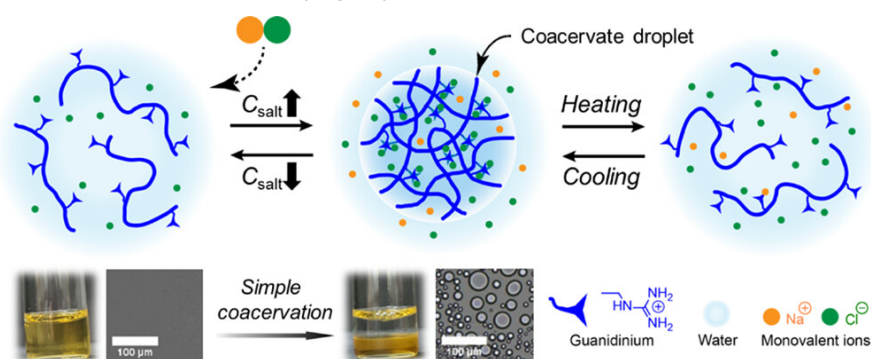

Figure 2. Polyether polymers with pending guanidinium groups can form simple coacervates below a critical transition temperature in the presence of salts. The UCST behavior can be tuned by choosing different anions. Reprinted with permission from reference [22]. Copyright © 2023, American Chemical Society.

1.1.3. Applications of Coacervates

The physical principles of complex coacervation and the interactions involved make the process applicable to many substrates, including synthetic polymers, polynucleotides, and even nanoparticles. The resulting materials are responsive to different stimuli and conditions, such as pH, temperature, and salt concentrations, making them particularly versatile.[23]

Coacervate technologies have gained particularly large attention in biomedicine and as delivery platforms for therapeutic biomolecules.[24-26] For example, polyanionic RNA can be combined with cationic polyamines and other additives to induce complex formation. The RNA cargo is protected from degradation inside the droplets and released at a sustained rate due

to the controlled diffusion stemming from the coacervates' high network density. They can be modified further, enabling targeted delivery to specific cells or tissues.[27] Complex coacervates are also used for microencapsulation in the food, textile, and agriculture industries.[9]

The applications of coacervates are not limited to encapsulating active molecules. They form functional materials in combination with additives like nanoparticles, colloids, or conjugated polymers that can be used for electrochemical applications, *e.g.*, in energy or sensor materials.[28-29]
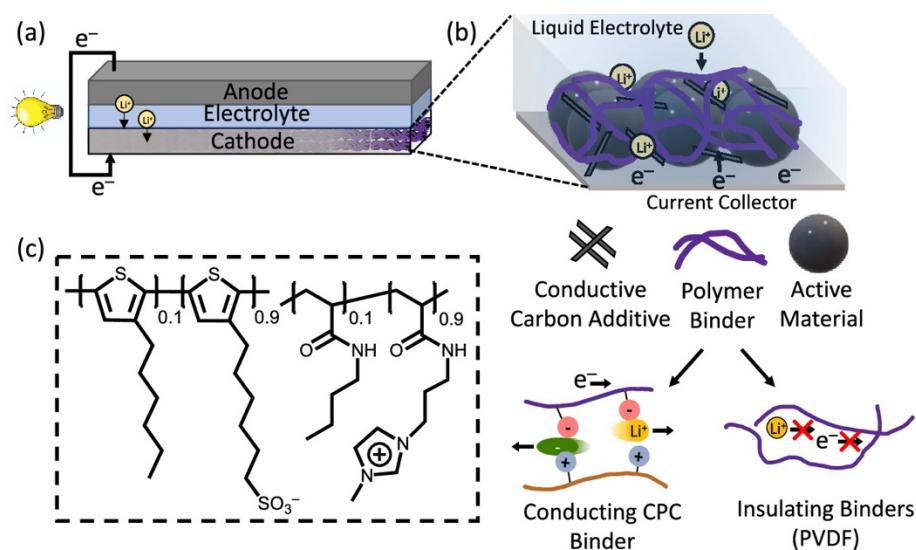

Figure 3. (a) The cathode of a lithium-ion battery as a composite material of (b) active material that is combined with conductive additives and held together by a polymer binder. (c) A conductive polymer with an anionic side chain complexed with a cationic polymeric ionic liquid forms a coacervate-based binder. In contrast to conventional binders, this coacervate-derived material enables both electron and ion conduction. Reprinted with permission from reference [29]. Copyright © 2023, American Chemical Society.

For example, $LiFePO_4$ as an active material and carbon black were added to a coacervate phase of a conducting polymer with anionic side groups that was complexed with a cationic, polymeric ionic liquid as the binder for cathode materials (Fig. 3). The composite material performed superior to standard materials due to an increased charge transport within the electrode.[29]

1.1.4. Conclusion

The principles and mechanisms behind the liquid-liquid phase separation of charged macromolecules into coacervates are universal. Since they work for various substrates and can be combined with other material classes, numerous practical applications of coacervate-based materials were realized. In the next chapter, I will describe how nature uses this material class. Coacervates become even more versatile as they are formed as dynamic structures to fulfill their biological functions. I will also introduce theoretical models describing the dynamic properties of these active droplets. Finally, examples of artificial, dynamic coacervate designs are described. They showed unprecedented dynamic behavior, bringing them closer to living organisms.

1.2. Coacervation Coupled to Chemical Reactions

1.2.1. Dynamic Coacervation in Biology

Biochemical reactions in cells need to be organized and compartmentalized. To do so, cells contain different compartments separated from their surroundings while keeping their contents freely available for chemical reactions. In general, many compartments carry membranes, *e.g.,* mitochondria, but there are also many without.[30]

Such compartments without membranes exist as membraneless organelles (MLOs) and they are ubiquitous in cells (Fig. 4).[31-32] These biomolecular condensates are microns in size and serve many functions, including the regulation of biochemical reaction rates, subcellular organization, modulation of macromolecular folding, and gene regulation.[32-34] They are built from nucleic acids and proteins, often carrying intrinsically disordered regions (IDRs). These sequences do not adopt a preferred three-dimensional structure and promote aggregation via their intramolecular interactions, *e.g.* electrostatics, cation-π, π-π and dipole-dipole interactions.[31, 35]
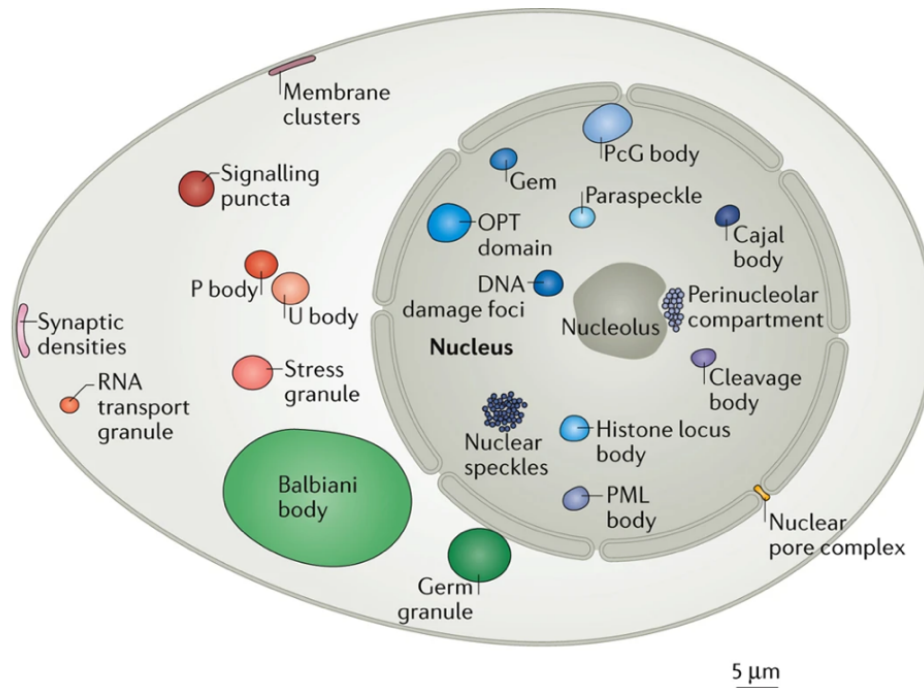
Figure 4. The different types of membraneless organelles in eukaryotic cells. For completeness, the image also shows membraneless organelles that are only present in specific cell types. Adapted with permission from reference [32]. Copyright © 2017, Springer Nature Limited.

Their fluidity, mobility, and ability to exchange with their surroundings must be regulated to maintain their biological functions over time because aging or maturation can lead to arrested states and gelation as they reach equilibrium.[36-38] Some phase transitions of this kind are even associated with the pathogenesis of neurodegenerative diseases like Parkinson's or Alzheimer's disease.[39-40] The non-equilibrium states of membraneless organelles can be maintained enzymatically by consuming high-energy molecules.[38, 41]

The assembly and disassembly of biomolecular condensates can be regulated via posttranslational modifications of their material.[42] One example is stress granules that form in eukaryotic cells upon environmental stress, like glucose deprivation, to increase the cell's survival rate. The critical role of lysine acetylation states of the Pab1 protein – controlled by lysine acetyltransferases and lysine deacetylases – was identified for granule formation in *Saccharomyces cerevisiae*. The acetylation of lysine sites reduces their charge and changes their structure, thus reducing their interactions with other proteins and nucleotides.[43] Arginine methylation in Ddx[N1] proteins was found to suppress Nuage body formation by changing the shape, charge distribution and hydrophobicity of these residues, impacting their ability to participate in cation-π interactions.[44]

In a different way, phosphorylation and dephosphorylation were identified as the relevant posttranslational modifications in forming and dissolving P granules in *C. elegans* embryos.

Phosphorylation of serine-rich MEG (maternal-effect germline defective) proteins leads to the dissolution of P granules, while dephosphorylation promotes their formation.[45] The diverse examples of biochemically regulated membraneless organelles suggest that they can be viewed as active droplets, *i.e.,* droplets that are driven away from thermodynamic equilibrium by chemical reactions. Such droplets can show vastly different behavior than passive droplets, which aligns with recent theoretical works.[46-48]

1.2.2. The Physics of Externally Maintained Chemically Fueled Droplets

When phase separation is coupled to chemical reactions that maintain the droplet material away from equilibrium, emulsions are formed that differ drastically from passive ones, *e.g.*, the in-equilibrium phase separation of two immiscible liquids. For example, passive droplets coarsen over time to form one large separated phase due to fusion and Ostwald ripening.[47, 49] In contrast, the process of Ostwald ripening can be suppressed in active emulsions driven by chemical reaction networks.[47] One example of chemically active droplets is externally maintained droplets. In these droplets, the activation of droplet material happens in the supernatant, while the droplet material is deactivated in the droplet interior (Fig. 5**A**).[50] The activation and deactivation reactions are happening simultaneously, creating droplet material fluxes responsible for their unique properties.

The material fluxes of active emulsion depend on the kinetics of the activation and the deactivation reactions. As soon as the starting material is activated, activated building blocks must diffuse to a coacervate surface to enter it. Hence, this influx of droplet material is scaling with the surface area of the droplet. The droplet deactivation scales linearly with the available peptide anhydride and, therefore, scales with the droplet volume. Since droplet material diffuses out of the droplets as soon as it is deactivated, the deactivation-related efflux also scales with the droplet volume.[49]
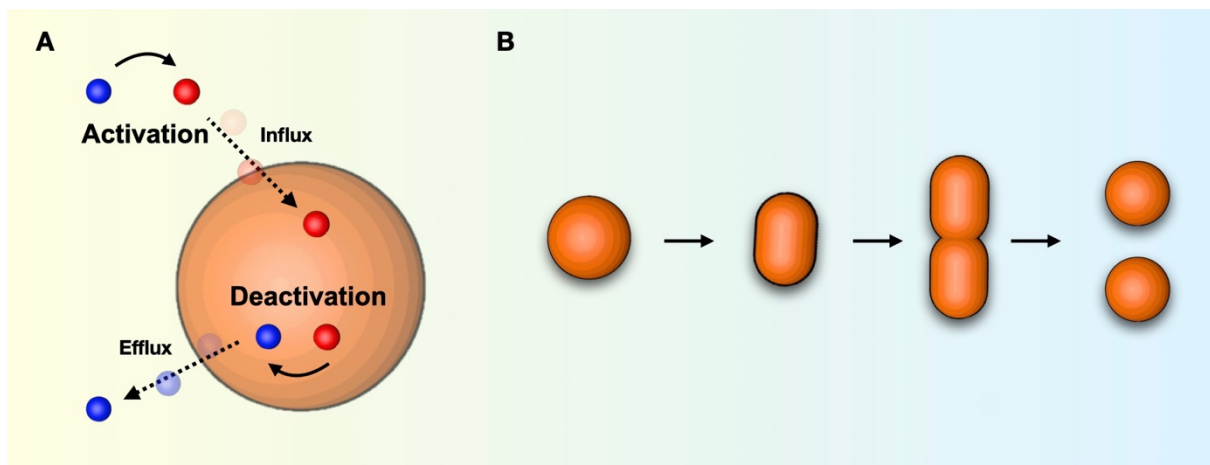
Figure 5. A. For externally maintained droplets, their droplet material is activated in the supernatant phase and diffuses into droplets after their nucleation. The deactivation reaction mainly happens on the inside. The deactivated building blocks diffuse out of the droplet phase into the supernatant. The resulting influx and efflux control the properties and behavior of these droplets. **B.** Elongation and self-division of chemically fueled, externally maintained droplets. Figure inspired by references [46] and [49].

Under these sustained fluxes in steady states, *i.e.*, states with sustained droplet material concentrations under constant fuel supply, droplet growth by supersaturation of the supernatant phase is limited by product degradation inside the droplets.[51] Thus, multiple droplets can coexist and evolve to one stable size.[48] Droplets larger than this stable size will shrink while smaller droplets grow until they reach it. In contrast, passive droplets would grow constantly into a few large droplets due to Ostwald ripening. They exchange droplet material from smaller to larger droplets because of surface tension effects and different Laplace pressures.[49-50]

Another theoretical study shows that externally maintained droplets can also deform, elongate, and self-divide (Fig. 5**B**).[46, 52] In droplets with shape instabilities, elongation of regions with higher curvature is favored due to higher building block influx. In comparison, the efflux of deactivated building blocks in their middle parts with lower mean curvature is dominant, leading to fission into daughter droplets.[50] After their regrowth, these new droplets can repeat this process, making it resemble cell division.[46]

1.3. Artificial Platforms for Chemically Fueled Coacervation

Emulating dynamic coacervates from nature necessitates applying principles from dissipative self-assembly, particularly chemically fueled self-assembly. This type of assembly allows us to mimic the complex structures in nature that are maintained in dynamic equilibria through continuous energy input and dissipation.[53-54] For example, microtubules are polymeric structures assembled from building blocks that are activated and stabilized by guanosine triphosphate, a high-energy molecule.[55]
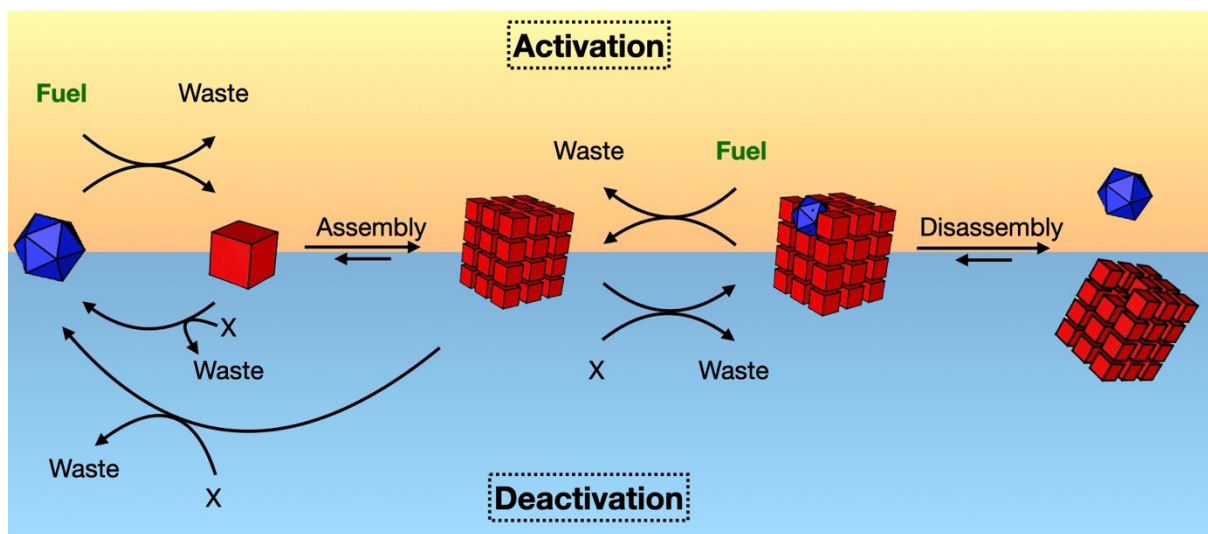
Figure 6. A reaction scheme for chemically fueled self-assembly. A fuel is applied that reacts with the precursor (blue). Only in its activated state (red) the building blocks assemble into a supramolecular structure. A deactivation reaction brings the activated building blocks back to their initial state.[56-58]

Energy input and dissipation can be implemented in chemically fueled supramolecular materials. They are formed via dissipative self-assembly (DSA), where non-assembling precursors reside in an energy minimum. In chemically fueled self-assembly, an activation reaction brings the building blocks into a high-energy state at the expense of a molecule with high chemical potential*, i.e.,* a "fuel". Ideally, the fuel's chemical potential is not released easily without the action of the building blocks. Therefore, the building blocks can also be described as catalysts that accelerate fuel conversion into waste. The waste products are low in energy, and the energy difference between the waste and the fuel is effectively used to assemble the activated building blocks. They only assemble into larger structures or materials in this activated state. Simultaneous deactivation pathways dissipate the energy stored in the activated material, returning it to its initial state, *e.g.* by hydrolysis or reactions with other abundant species. The assembled structure will decompose as soon as the system runs out of energy, *i.e.*, when it is fully depleted of fuel (Fig. 6).[59-60]

In some cases, disassembly of the building blocks does not occur immediately after their deactivation. This trapping occurs when there is an energy barrier between a deactivated building block in its assembled versus in its disassembled state that thermal energy cannot overcome. Such a state corresponds to a kinetically trapped state (Fig. 7).[58]
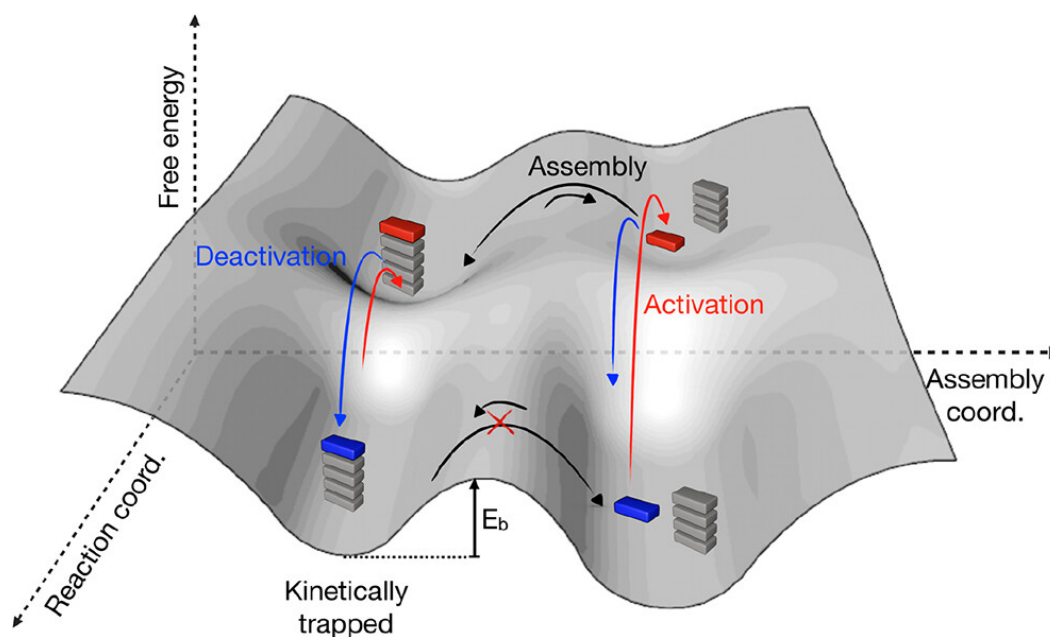
Figure 7. A representative free energy landscape behind the processes of chemically fueled assembly. The reaction coordinate is shown for the building block, not for the fuel or the waste products. Reproduced with permission from Chen *et al.* [58]. Copyright © 2023, The Authors. CC BY-NC-ND 4.0 DEED, https://creativecommons.org/licenses/by-nc-nd/4.0/.

Coacervates are stimuli-responsive and inherently dynamic structures that readily exchange building blocks with their surroundings. Therefore, the concepts of chemically fueled self-assembly and coacervation can be well combined to emulate coacervate structures in nature. Various chemistries were applied for chemically regulated coacervation by charge-switching, a strategy that is common in DSA.[61-63] In these designs, the activation and deactivation pathways would need to be spatially separated between the assembly and the supernatant in order to be classified as externally maintained. Only then would the assemblies be subjected to material fluxes required for life-like behavior.[49]

Researchers took various approaches to examining examples of dynamic and reversible coacervation in nature. They mimicked biological examples in model droplets by reducing the intracellular complexity to the most relevant structural motifs to gain deeper insights into the underlying principles.[64-65]

1.3.1. Reversible Coacervation via Redox Chemistry

Redox chemistry was applied to switch between the charge states of complex coacervate building blocks. Therefore, oxidation and reduction reactions were used on an anionic building block, enabling a redox switch for complex coacervation.[66] Under the right salt concentrations, only $Fe(CN)_6^{4-}$ formed coacervates with poly(lysine), but not its oxidized counterpart

$Fe(CN)_6^{3-}$. $Fe(CN)_6^{4-}$ can easily be oxidized to $Fe(CN)_6^{3-}$, for example, by the action of $S_2O_8^{2-}$. Consequently, this oxidation reaction could dissolve the coacervate droplets. Complex coacervation was then initiated again by reduction, *e.g.*, by glutathione or NADH as reducing agents. The state was switched multiple times by alternating additions of the oxidizing and reducing agents (Fig. 8).[66]
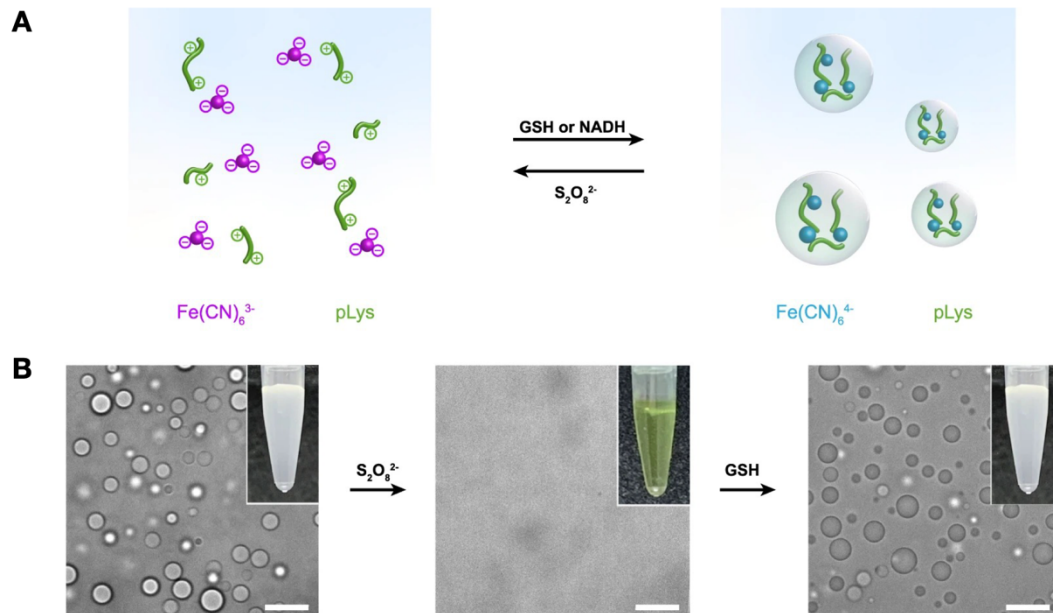

Figure 8. A. Redox-driven complex coacervation of ferrocyanide $Fe(CN)_6^{4-}$ with poly(lysine) that is driven by the reduction of ferricyanide ($Fe(CN)_6^{3-}$) via reducing agents like glutathione (GSH) or NADH. The complex coacervates can be dissolved by adding an oxidizing agent like $S_2O_8^{2-}$. **B.** Micrographs and images of the redox-driven transitions between coacervation and clear solutions. Adapted with permission from Wang *et al.* [66]. Copyright © 2023, The Authors. CC BY 4.0 DEED, https://creativecommons.org/licenses/by/4.0/.

Redox stimuli were also applied to the simple coacervation of short dipeptide sequences based on aromatic or aliphatic amino acids like phenylalanine, tryptophan, or leucine connected via a cysteamine linker. The disulfide bonds in the linker could be reduced by agents like tris(2-carboxyethyl) phosphine (TCEP) or dithiothreitol (DTT), liberating the monomers. Since only the dimers could self-associate, simple coacervates of these dimers could be dissolved by reduction. Coacervation was triggered again by adding an oxidizing agent, *e.g.* $K_3Fe(CN)_6$ or H_2O_2, reforming the dimers. These simple coacervates were used as temporary microreactors that take up small guest molecules and oligonucleotides.[67]

The alternating formation and dissolution of coacervate droplets via redox stimuli can be used as a platform for reversible coacervation. Still, it does not yet fulfill the requirement of simultaneous activation and deactivation reactions in externally maintained droplets.

1.3.2. Enzymatically driven Complex Coacervation in vitro

The biochemical reaction networks regulating membraneless organelles in nature involve numerous components, which makes them complex and complicated to resolve quantitatively. Therefore, models that use enzymes were created to better understand membraneless organelles *in vivo* by reducing them to essential building blocks. For example, a phosphorylation-mediated complex coacervation platform based on RNA as a polyanion and a cationic peptide was introduced. The amino acid sequence RRASL was chosen as a repeat unit because of its positive charges from arginine side chains, responsible for the main driving force inducing complexation with the negatively charged oligonucleotides polyuridylic acid (polyU) or tRNA. With the peptide RRASLRRASL, Keating *et al.* could show that complex coacervates could either be dissolved by enzymatic phosphorylation of serine residues via a kinase or formed via their dephosphorylation by a phosphatase. RRASLRRASL readily forms complex coacervates with polyU. In its phosphorylated state, the positive charges of the guanidinium groups are compensated, and the driving force for coacervation by electrostatic interactions is lost. Dephosphorylation of RRApSLRRApSL liberates the positive net charges which reinduces complex coacervation. The emergence and decay of droplets were controlled in mixtures where both kinases and phosphatases were present with additives modulating their enzymatic activities.[65] Similar to the redox-driven coacervates described earlier, these enzymatic reactions do not work simultaneously and rely on alternating additions of reagents.

Another enzymatic reaction network realized dynamic coacervation of ATP with poly(lysine). A pyruvate kinase was used to generate ATP from ADP by consuming phosphoenolpyruvate (PEP) as a substrate. Due to its higher charge, only ATP forms complex coacervates with poly(lysine). ATP could be hydrolyzed back to ADP by hexokinase activity consuming glucose, leading to the dissolution of the ATP-poly(lysine) coacervate droplets (Fig. 9). Since both enzymes work under similar conditions, switching between droplet formation and dissolution was possible by adding the enzyme substrates subsequently. The solution could be refueled up to 6 times because charged waste products accumulated, hindering coacervation and inhibiting the pyruvate kinase. However, in contrast to the previous examples, the two enzymatic reactions form a true reaction cycle. This is why the time onset for droplet formation or the onset of droplet dissolution could be controlled by changing the fractions of enzymes and their substrates relative to each other.[68]
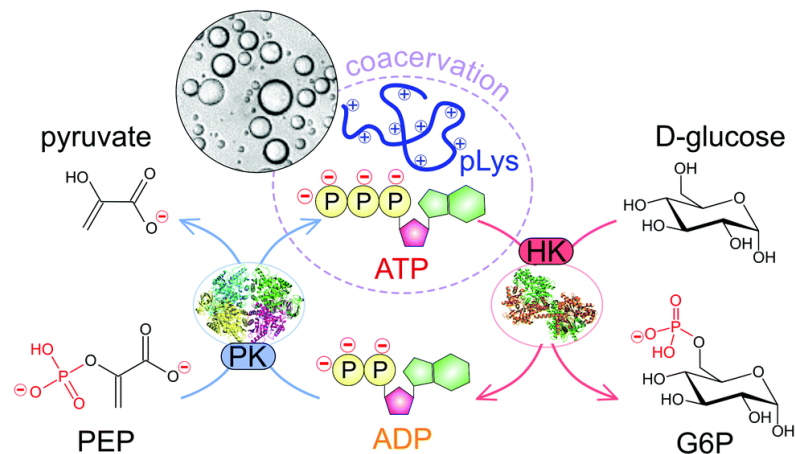
Figure 9. Pyruvate kinase (PK) was used to generate ATP from phosphoenolpyruvate and ADP. ATP was able to undergo complex coacervation with cationic poly(lysine), resulting in turbid droplet solutions. ATP could then be hydrolyzed by hexokinase (HK)-driven hydrolysis, forming back ADP. This hydrolysis leads to coacervate dissolution due to the lower charge of ADP. Reprinted from "Reversible generation of coacervate droplets in an enzymatic network" from Nakashima *et al.* [68], Copyright © 2018, The Authors. CC BY-NC 3.0 DEED, https://creativecommons.org/licenses/by-nc/3.0/.

This phosphorylation/dephosphorylation approach did not lead to any instabilities in coacervate shapes, as theoretical models for externally maintained droplets would predict. Although the enzymatic reactions can work in parallel, one reason for this could be that the activation and deactivation reactions are not spatially separated since both enzymes partition into coacervates [68] or because the enzyme kinetics would require further optimization relative to each other.

1.3.3. Carbodiimide Fueled Complex Coacervation

To further simplify the models for active complex coacervate droplets, we designed a purely chemical, *i.e.*, nonenzymatic, reaction cycle for complex coacervation by exploiting the intramolecular anhydride formation of C-terminal aspartic acids in peptides.[69] This reactivity has already been explored before for other peptides or protected amino acids [54, 70] and alkenyl succinic acids.[71] It uses a water-soluble carbodiimide to initiate a reaction cycle leading to the anhydride's temporal self-assembly.

This anhydride formation was recognized as a tool for creating a charge switch because it compensates for the negative charges of two free carboxylates on a peptide precursor. It was combined with three arginine-glycine repeat units, creating a positively charged peptide backbone in Ac-FRGRGRGD-OH. In its precursor state, the two negative charges from the

dicarboxylate and the three positive charges from the arginine residues result in a net peptide charge of +1. In this state, the overall charge is insufficient to induce complex coacervation with the polyanion polyU. The peptide anhydride with a net charge of +3 is formed upon fueling with N-(3-dimethylaminopropyl)-N'-ethylcarbodiimide (EDC). This net charge is sufficient to induce the phase separation with RNA. Due to the anhydride's hydrolytic instability, it is consumed constantly, and the precursor is recovered (Fig. 10 **A**). A reaction cycle occurs as long as carbodiimide fuel is available. It leads to an initial increase of the cationic peptide anhydride concentration, followed by its decay. Thus, the resulting coacervate droplets have a lifetime of several minutes and dissolve when the peptide anhydride concentration falls below a threshold concentration. The chemical reaction cycle creates dynamic coacervate emulsions (Fig. 10 **B**).
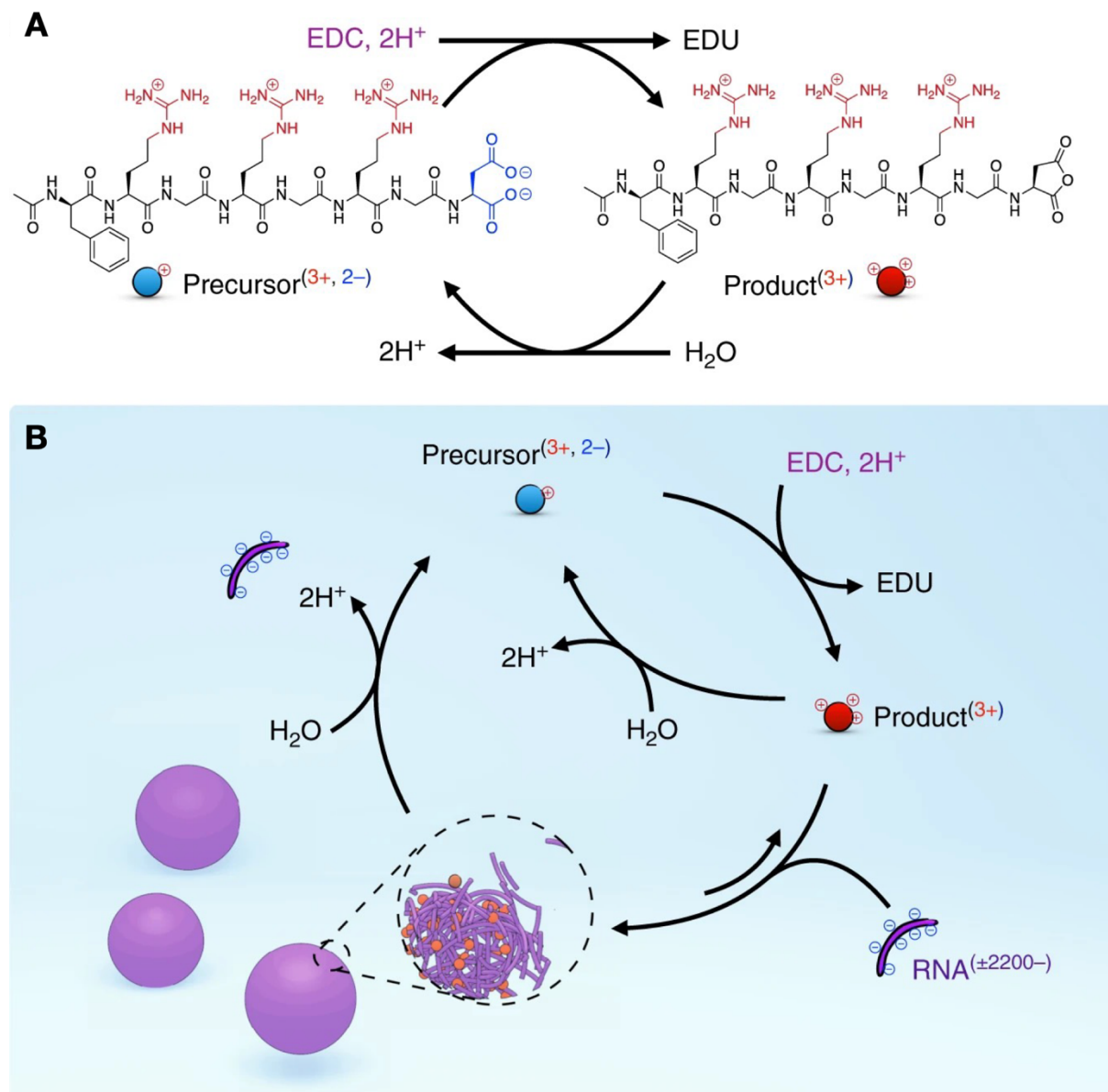
Figure 10. A. In a chemical reaction cycle, the peptide AcF(RG)$_3$D-OH is transformed into the peptide anhydride by an intramolecular condensation reaction using the water-soluble carbodiimide EDC as a fuel. The anhydride is hydrolytically unstable and constantly reverts to the peptide precursor. The reaction pathways create a reaction cycle in aqueous media. **B.** The peptide anhydride has a higher positive net charge and binding affinity towards the polyanionic RNA. Thus, it induces complex coacervation. Inside the coacervate droplets, the hydrolysis reaction takes place, forming the peptide precursor back. This hydrolysis is responsible for the decay of the coacervate droplets as soon as they run low on EDC, leading to a limited lifetime of the resulting coacervates. Adapted with permission from Donau *et al.* [69]. Copyright © 2020, The Authors. CC BY 4.0 DEED, https://creativecommons.org/licenses/by/4.0/.

Analysis of the supernatant revealed that the carbodiimide fuel is not partitioning into the coacervates, and thereby, activation happens predominantly in the supernatant phase. Most of the peptide anhydride product goes into the coacervate phase, localizing the deactivation reaction in the highly hydrated coacervate interior.

A dynamic life cycle was observed for these active droplets that could be refueled multiple times. After their nucleation upon fuel addition, smaller droplets fused in the first minutes. Over time, they started to form vacuoles and fragmented before they dissolved completely. This behavior clearly distinguished them from passive complex coacervates, and it was controlled by varying the peptide, polyanion and fuel concentrations.[69] The spatial separation of activation and deactivation fulfills the requirements for externally maintained droplets. In particular, the activation and deactivation reactions occur truly simultaneously. Next to fragmentation and vacuolization, their chemical activity led to more non-equilibrium phenomena as soon as their composition was changed or a constant fuel supply was realized.

1.3.4. Non-equilibrium Behavior of Chemically Fueled Coacervates

Besides their transient nature, further out-of-equilibrium processes could be observed for these transient droplets by analyzing the coacervates in micro containers built with the help of a microfluidics setup. This technique was implemented to analyze the whole droplet life cycle in great detail.[72]

When the chemically fueled coacervate emulsion was expanded by adding a second type of polyanion, poly(styrene sulfonate) (PSS), active multiphase coacervates were formed.[73] To minimize the total interfacial energy of the coacervate emulsion, one coacervate can be engulfed by another one if the interfacial energy of the resulting multiphase coacervate is lower than the combined interfacial energies of the individual droplets. Coacervates from polyion combinations with high interaction strengths usually have higher densities and interfacial

tensions than coacervates with lower interaction strengths. Hence, the less dense coacervates usually take up the denser coacervates, forming multiphase droplets.[74] Chemically fueled coacervates built from a mixture of the polyanions PSS and polyU form multiphase coacervates that differ from those close to or in equilibrium (Fig. 11). Firstly, the amount of fuel dictated when multiphase coacervate droplets were able to form since a minimal concentration of the peptide anhydride was necessary to induce multiphase coacervation.
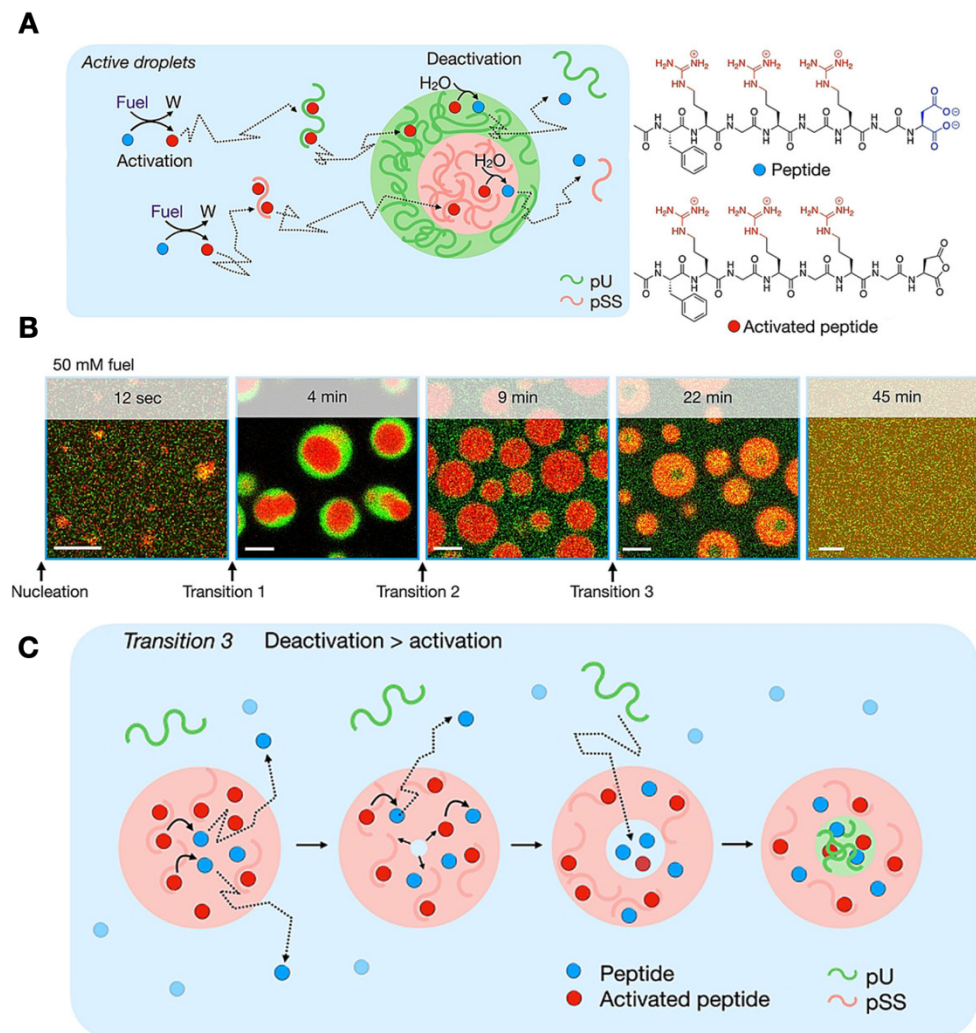

Figure 11. A. The chemical reaction cycle using the activation of AcF(RG)$_3$D-OH with EDC forms multiphase coacervates with polyU and PSS. **B**. Laser confocal micrographs of the evolution of multiphase complex coacervates. Solutions contained 15 mM peptide, 5 mM polyU, and 5 mM PSS, all in 200 mM MES buffer at pH 5.3 and with 0.15 µM Cy3-A15-polyU (green) and 0.15 µM Cy5-PSS (red) as fluorescently labeled components. The samples were fueled with 50 mM EDC. **C.** The mechanism behind transition 3 in chemically fueled multiphase coacervates. The inner polyU phase forms after vacuolization and concentration of peptide and polyU in the core. Adapted with permission from Donau *et. al* [73]. Copyright © 2022, The Authors. CC BY 4.0 DEED, https://creativecommons.org/licenses/by/4.0/.

The multiphase-coacervate structures formed under fueling conditions had a different order of layers compared to in-equilibrium coacervates (Fig. 11 **B** and **C**). Under sufficient fuel supply, an inner PSS core formed first wrapped with a polyU coacervate phase. Due to the decrease in peptide anhydride concentration, the polyU shell dissolved several minutes after the reaction cycle started. Later in the cycle, the remaining PSS core did not just dissolve, but an inner polyU coacervate core was formed. This polyU phase would not be stable in a monophase coacervate state under these peptide anhydride concentrations but was proven to be linked to the vacuolization of the PSS coacervates. The vacuolization of these coacervates is a generally observed behavior due to their chemically active nature. Peptide anhydride and polyU get concentrated in these vacuoles, inducing the formation of an inner polyU phase before the coacervates dissolve completely.[73]

Microfluidic techniques were also applied to generate steady states in the chemical reaction cycle with a constant supply of carbodiimide fuel. Under steady states of droplet material concentrations, the material fluxes in and out of chemically fueled coacervates are sustained. According to the theoretical framework I discussed above, these conditions are required to induce behavior like size control and self-division.[46, 50] To achieve a constant fuel supply, the hydrophobic N,N′-Diisopropylcarbodiimide (DIC) was dissolved in a fluorinated oil phase and all other droplet ingredients (peptide, buffer, polyanion) were dissolved in water. Together, the different phases formed microreactors upon emulsification. DIC has been proven to induce complex coacervation by peptide anhydride formation, like water-soluble EDC. However, in contrast to EDC, it creates a steady-state concentration of fuel in the microreactors by constantly diffusing into the aqueous phase while the urea waste product preferentially diffuses into the oil phase and crystallizes there. Through this mechanism, the continuously fueled system did not suffer from any influences from accumulated waste products because they were constantly removed. This fuel reservoir could induce complex coacervates in a steady state, as indicated by a constant total droplet volume. All droplets in a reactor fused over time, forming a large coacervate droplet in the center by partially wetting the microreactor bottom.

After some time, this homogenous droplet became unstable. It formed a sustained spherical shell morphology (Fig. 12). Calculations showed that above a critical size, the droplet core was depleted of the peptide anhydride. This happens because the initial droplet is externally maintained, and the fuel does not partition into it. Since the peptide anhydride must diffuse into the droplet to sustain it and the deactivation reaction is going on inside, the core destabilizes while the outer parts are still preserved by peptide anhydride from the surrounding solution. This leads to the transition to a shell structure. The extent of depletion was quantified, and theoretical models verified this transition.[75]
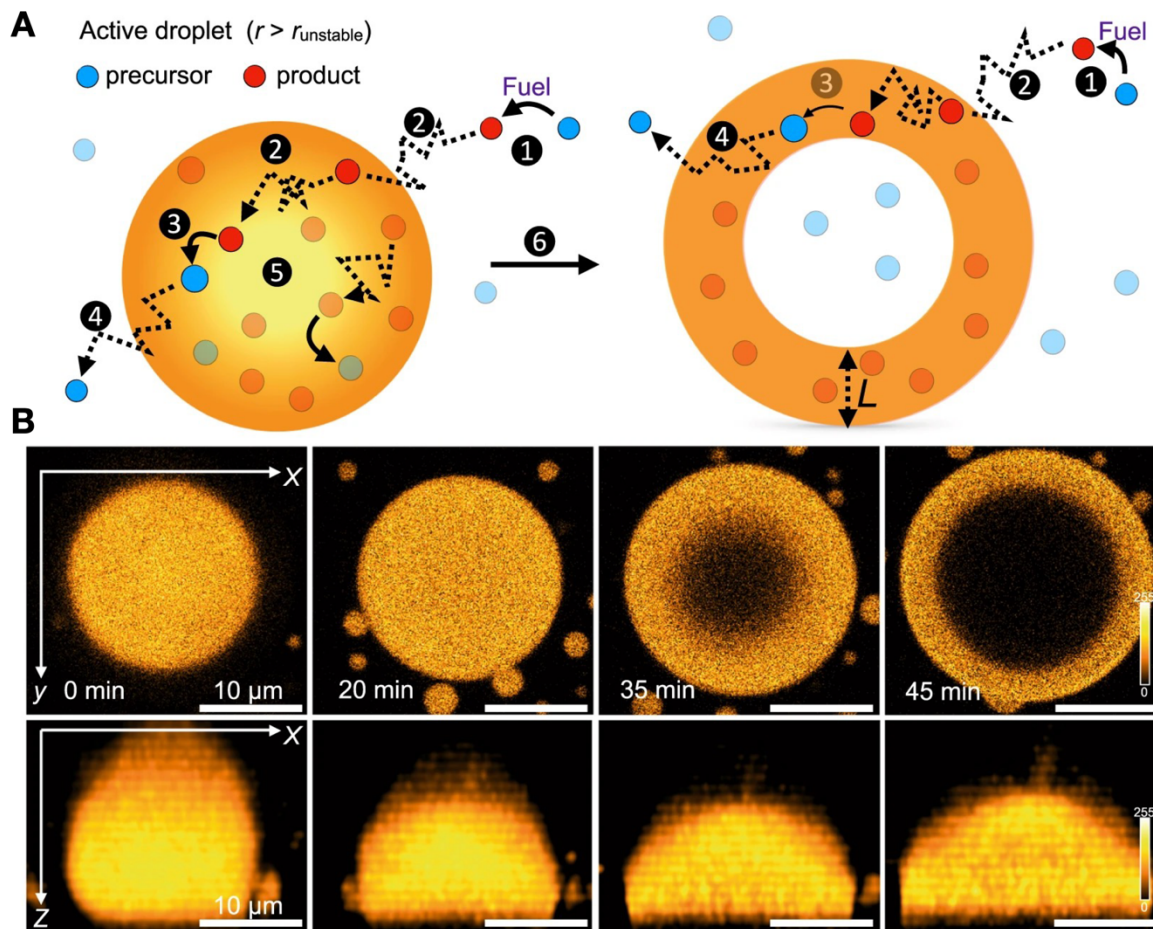
Figure 12. A. Active droplets form spherical shells as a new steady-state morphology. After activation in the supernatant (1), the activated peptide building blocks diffuse into the droplet (2). Deactivation by hydrolysis happens inside of the droplet (3). The deactivated peptide precursor diffuses out of the droplet (4) leading to the depletion of the droplet core from its building blocks (5). Over time, this transforms the droplet into a spherical shell morphology (6) that is maintained through the reaction cycle under constant fuel supply. **B.** Top and side view of active droplets that transform into spherical shells over time. Upper row: Micrographs in one plane as the top view. Lower row: Side view of the droplet that is partially wetting the microreactor. Adapted with permission from Bergmann *et al.* [75]. Copyright © 2023, The Authors. CC BY 4.0 DEED, 2023, https://creativecommons.org/licenses/by/4.0/.

These examples of out-of-equilibrium properties and dynamic behavior of chemically fueled complex coacervates show their versatility and potential. Still, many predicted processes, such as self-division and droplet size control, are yet to be observed. Nevertheless, theoretical frameworks for chemically fueled droplets predict that these externally maintained droplets could meet all the requirements for these phenomena to occur, *e.g.,* low surface tension and a droplet size of several micrometers.[46] Changes to the abovementioned active emulsion

regarding the underlying building block structures or optimization of the reaction cycle conditions are still needed.

1.3.5. Active droplets as synthetic cells and protocell models

Living cells are complex and frangible. As more robust and controllable mimics, artificial cells promise to improve our fundamental understanding of biology, and they are the focus of research aiming at developing new therapeutic approaches for medicine or advancing the field of tissue engineering. They are supposed to mimic the logic of living cells and show either a minimal set of the characteristics of cells, *e.g.,* evolution, self-reproduction, and metabolism, or one specific feature of living cells that is studied in detail.[76] Different bottom-up approaches were attempted to combine macro- and biomolecules to create containers or droplets with cell-like properties from complex coacervates, enabling researchers to study them in a controlled environment.[77-78]

Many examples use membrane-enclosed compartments to copy the hierarchical organization of biological structures. The membranes are created by interfacial assembly of block copolymers, fatty acids or lipids around a separated phase. There, they are used to achieve properties like customizable membrane permeability or to enable controlled signaling between different compartments.[78-83] The roles of coacervate phases in these approaches vary from models for the cytosol - when they fill out the whole core of the membrane-enclosed compartment - to artificial organelles dispersed in larger, membrane-enclosed containers, *e.g.*, vesicles.[31] Many different polyelectrolytes were combined to create the coacervate structures, namely allyl polymers, polypeptides, polyesters, polysaccharides, and poly(meth)acrylates.[77, 80, 83-87]

However, the latest findings on membraneless organelles and their compositions also put pure coacervates in the focus as artificial cells. Their physical and chemical properties enable them to sequester solutes, influence the stability and aggregation of biomolecules, control biochemical reactivity, or undergo dynamic phase separation. All of that makes them great models for cellular behavior.[31] Droplet-in-droplet systems, *i.e.*, droplets with hierarchical compartmentalization, can also be realized via complex coacervation alone in the form of multiphase coacervates.[74, 88]

Coacervates are also investigated as protocells, *i.e.*, primitive compartments that can exist under conditions that are plausible for the origin of life. The all-encompassing goal in this field of research is to decipher the minimal requirements for simple life forms capable of Darwinian evolution.[89] Protocell models based on coacervates can be built from simple building blocks, like inorganic salts and small organic molecules, which could have been present in the early

stages of life, while other approaches rely on the self-assembly of simple variants of biomolecules like polypeptides and oligonucleotides.[82] Most importantly, they can function without a finely tuned biochemical machinery and enable reactions analogous to complex biochemical transformations, like forming amide bonds, RNA-polymerization, or ribozyme catalysis.[66, 90] In the absence of nanoscale machinery that is typical for contemporary cells, most protocell's functions would need to emerge from basic physicochemical interactions.[91] Chemically active droplets, in particular, could show behavior closely resembling cell growth and division.[46, 92] Since even simple chemical reactions could drive coacervates out-of-equilibrium and create the required fluxes of their building blocks, such behavior could have emerged at the earliest stages of life.[93] In advanced systems that can store hereditary information of any kind, like nature does in DNA sequences, the growth and division processes could lead to evolution. For this to occur, the information in the daughter compartments would need to be replicated after the division of the parent containers. Such replications were already achieved in autocatalytic systems without the need for enzymes.[94-95] Particular offspring could develop a survival benefit when specific characteristics or properties emerge via genotype-phenotype coupling that represent an advantage under selection pressure, *e.g.,* higher salt tolerance. Thereby, Darwinian evolution could be realized over several generations in self-replicating droplets.[96-98]

Put differently, chemical reaction networks leading to growth, replication and division offer great potential to mimic the natural cell cycle in all its facets, even with the potential for evolution in such artificial platforms (Fig. 13).[63]
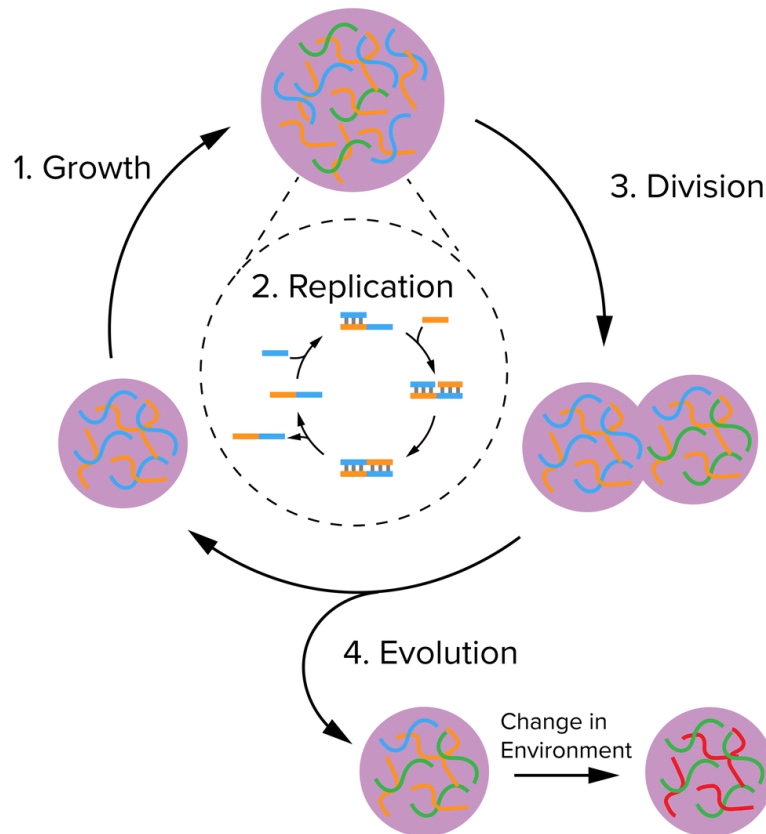
Figure 13. A minimal protocell cycle leading to evolution. The essential steps include droplet growth, the replication of their information contents, their division, and finally, the evolution of their daughter droplets due to changes in their environment. Reprinted from "Growth, replication and division enable evolution of coacervate protocells" from Slootbeek *et al.* [63], Copyright © 2022, The Authors. CC BY-NC 3.0 DEED, https://creativecommons.org/licenses/by-nc/3.0/.

1.4 Conclusion and Outlook

Polyelectrolyte complexes are versatile materials with great potential for applications in different areas and fields. In nature, these dynamic structures are found in a multitude of examples where complex biochemical networks control them. Their dynamic formation adds an additional layer of complexity to this material class. They are difficult to recreate artificially, even though great progress has already been made in the field of artificial dynamic coacervates and polyelectrolyte complexes. The theoretical frameworks describing the physics behind their behavior do not provide straightforward design rules to demonstrate the predicted properties and behaviors in experiments. Based on previous advancements in chemically fueled active droplets, the chemical toolbox for this class of transient structures needs to be expanded to access their full potential, either as transient materials or as protocell models that grow, divide, and evolve.

2. Aim of the Thesis and Research Questions

Chemically active droplets, *i.e.*, droplets whose activation and deactivation occur simultaneously but spatially separated, are versatile candidates for dynamic materials. They can serve as models for membraneless organelles or as a platform for protocell research: They emerge and compete for fuel and decay in its absence. A promising approach is based on a cationic peptide whose charge can be changed with a chemical reaction cycle involving a carbodiimide fuel. In its activated state, the peptide binds to the polyanions polyU and PSS and condenses in response to the evolution of the peptide anhydride concentration. In their dynamic life cycle, the active coacervate droplets did not only grow and shrink, but also showed exciting behavior such as fragmentation, vacuolization, and multiphase formation.

However, the system still suffered from a limited scope of building blocks and regimes of metastability in their phase diagrams, already hinting at influences beyond the evolution of building block concentrations. But how does the precursor peptide structure influence the chemically fueled coacervation behavior or lifetimes, and which role do the polyanions play? Can they be tailored in a way so that other material morphologies besides droplets are accessible with the same reaction cycle? Can the reaction cycle be expanded to enable chemically fueled simple coacervation, and how are complex building block mixtures or libraries behaving as platforms for chemically fueled complex coacervation? This thesis addresses these questions by systematically implementing and testing different molecular designs of building blocks with the goal of creating life-like coacervate materials.

3. Overview of this Thesis

In Chapter 4 I investigate the influence of the peptide precursor charge of the $AcF(RG)_nD$-OH peptide family. I build on the first results from Donau *et al.*[69, 73] and show that the precursor net charge dictates whether dynamic coacervates can form with polyanions after fueling with a carbodiimide. In addition, I investigate how the charge determines whether the resulting complex coacervates follow the reaction cycle. Different polyanion lengths are also tested for their influence on the chemically fueled coacervation without participating in the reaction cycle. Block copolymers are introduced as polymer building blocks to explore new morphologies of active coacervate materials.

The role of the polymer scaffolds in chemically fueled complex coacervation is further explored in Chapter 5, with polyanions carrying different functional groups. Their interactions with the peptide precursor and an anhydride model are compared and the underlying mechanisms for their influence on the outcome of chemically fueled complex coacervation are derived from their binding affinities.

In Chapter 6, a special emphasis is put on oligonucleotides as polyanions in chemically fueled complex coacervates. As information containing biopolymers, their important role in biological contexts and potential for protocells were taken up in a detailed study on how their structural features, *i.e.*, their phosphate backbone and nucleobases, influence chemically fueled complex coacervation. Since these are polyanions potentially forming secondary structures, influences of their hybridization state were also tested.

The last part of this thesis, Chapter 7, expands the EDC-driven reaction cycle by an esterification pathway. The transient ester products formed dynamic combinatorial libraries since intermolecular products also formed, enabling longer droplet lifetimes. Next to chemically fueled complex coacervation, chemically fueled simple coacervation became possible with peptide designs involving aromatic and cationic amino acids. This ultimately completes the toolbox of carbodiimide-fueled liquid-liquid phase separation.

4. Molecular Design of Chemically Fueled Peptide-Polyelectrolyte Coacervate-Based Assemblies

Abstract

In this work, I broadened the scope of the carbodiimide-fueled reaction cycle that was introduced in Chapter 1.3.3. Therefore, I investigated the influence of the building block design on the chemically fueled complex coacervation of the $AcF(RG)_nD\text{-}OH$ peptide family. The limitations of the charge-switching by aspartic anhydride formation were tested for different precursor charges in the range from -1 to +2. The peptides either did not form coacervates at all upon fueling with EDC (precursor with n=1), formed dynamic coacervates (precursors with n=2 or n=3) or coacervates that were no longer influenced by the ongoing reaction cycle (precursor with n=4). The polyanion structure was identified as another factor that influences the emergence and decay of chemically fueled complex coacervates. Due to multivalent binding, samples made from $AcF(RG)_2D\text{-}OH$ and long poly(styrene sulfonate) showed a delay in coacervate dissolution compared to the decay of the peptide anhydride concentration. Block copolymers with a poly(styrene sulfonate) and a neutral poly(ethylene glycol) block were introduced as polymer building blocks. This enabled the formation of chemically fueled complex coacervate core micelles, *i.e.,* nanosized and dynamic micellar assemblies. Excitingly, assemblies of diblock copolymers did not only emerge and decay in response to the fuel but even showed morphological transitions from polymersomes to wormlike micelles and small spherical micelles. All these results elucidate requirements for the building block design to create dynamic coacervate-based assemblies and expand the toolbox for chemically fueled complex coacervation significantly.

This work has been published:

The following section states the individual contributions of each author. F. Späth, J. Boekhoven, C. V. Synatschke and B. Rieger designed the experiments. F. Späth carried out the experiments. C. Donau helped with laser-confocal microscopy. A. M. Bergmann carried out the cryo-TEM analysis. F. Späth and M. Kränzlein performed SEC analyses and polymer syntheses. F. Späth performed peptide synthesis. F. Späth and J. Boekhoven wrote the manuscript. All authors have given approval to the final version of the manuscript.

Article

Molecular Design of Chemically Fueled Peptide−Polyelectrolyte Coacervate-Based Assemblies

Fabian Späth, Carsten Donau, Alexander M. Bergmann, Moritz Kränzlein, Christopher V. Synatschke, Bernhard Rieger, and Job Boekhoven*

Cite This: *J. Am. Chem. Soc.* 2021, 143, 4782−4789

Read Online

ACCESS | Metrics & More | Article Recommendations | Supporting Information

ABSTRACT: Complex coacervated-based assemblies form when two oppositely charged polyelectrolytes combine to phase separate into a supramolecular architecture. These architectures range from complex coacervate droplets, spherical and worm-like micelles, to vesicles. These assemblies are widely applied, for example, in the food industry, and as underwater or medical adhesives, but they can also serve as a great model for biological assemblies. Indeed, biology relies on complex coacervation to form so-called membraneless organelles, dynamic and transient droplets formed by the coacervation of nucleic acids and proteins. To regulate their function, membraneless organelles are dynamically maintained by chemical reaction cycles, including phosphorylation and dephosphorylation, but exact mechanisms remain elusive. Recently, some model systems also regulated by chemical reaction cycles have been introduced, but how to design such systems and how molecular design affects their properties is unclear. In this work, we test a series of cationic peptides for their chemically fueled coacervation, and we test how their design can affect the dynamics of assembly and disassembly of the emerging structures. We combine them with both homo- and block copolymers and study the morphologies of the assemblies, including morphological transitions that are driven by the chemical reaction cycle. We deduce heuristic design rules that can be applied to other chemically regulated systems. These rules will help develop membraneless organelle model systems and lead to exciting new applications of complex coacervate-based examples like temporary adhesives.
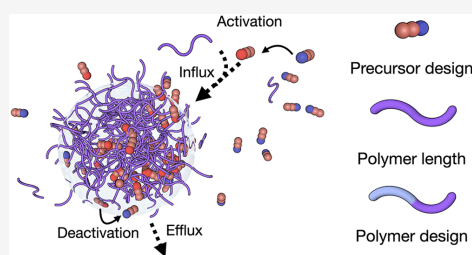
■ INTRODUCTION

Complex coacervate-based assemblies comprise two oppositely charged polyelectrolytes that phase separate to form a polyelectrolyte-rich phase in a polyelectrolyte-dilute solution.[1] The assemblies formed by complex coacervation range from droplets, complex coacervate core micelles that can be spherical or worm-like micelles, to polymersomes,[2−4] and find application in the food, pharmaceutical, and personal care industries.[5−9] Nature also uses emerging properties when two polyelectrolytes are brought together, such as underwater adhesives used by marine organisms like the sandcastle worm.[10,11] In these adhesive sites, coacervate-based assemblies are formed by two oppositely charged proteins and represent a dynamic and transient phase that facilitates adhesion, but the exact details are often unclear.[12] Another prominent natural assembly formed by the complexation of polyelectrolytes is the class of membraneless organelles. These droplet-like organelles, which are ubiquitous in eukaryotic cells, e.g., nucleoli, Cajal bodies, P-bodies, or stress granules, rely on the phase separation of RNA and proteins to form liquid compartments.[13] Interestingly, most of these droplets are highly dynamic and transient, i.e., they only temporarily exist and

perform their function before redissolving.[14−16] It was recently discovered that their transient nature and their dynamic properties are regulated by nonequilibrium reactions that consume ATP as they progress.[17] Thus, membraneless organelles can be active droplets, i.e., droplets whose properties are regulated by energy-driven chemical reactions, and their transient and dynamic nature can also be regulated by chemical reactions.[18,19] However, many of the underlying biological mechanisms that regulate these droplet-based organelles remain elusive.

Experimental model systems for biological complex coacervate-based assemblies can answer open questions related to complex coacervation in biology. Initial studies focused on complex coacervate-based droplets that exist close to equilibrium,[1,4,20] and later work studied droplets that are
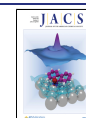
regulated by nonequilibrium chemical reactions. For example, it was shown that the phase-separation of RNA could be chemically regulated by enzymatic phosphorylation or dephosphorylation of a cationic peptide.[21]

Our group recently introduced a synthetic complex coacervate system that is regulated by an energy-consuming chemical reaction cycle.[22] A zwitterionic peptide is converted into a cationic one in a carbodiimide-consuming activation reaction. In essence, the activation reaction converts an aspartate-based C-terminus into its corresponding acid anhydride (Scheme 1A). This activation increases the affinity

Scheme 1. Schematic Representation of the Design of Active Coacervate-Based Droplets[a]
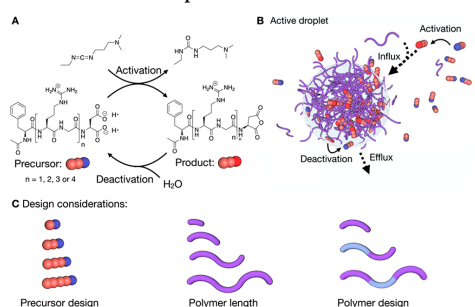
[a](A) Chemical reaction cycle that transiently activates peptides for coacervation. (B) Schematic representation of an active coacervate-based droplet. Upon activation of the precursor (blue), the product can bind an anionic polymer (purple strands). Strands with activated peptides are held together through complex coacervation to form a droplet. Simultaneously, the activated product is reverted to precursor through deactivation, which leads to the expulsion of the peptide from the droplet.

to anionic polymers, and when a sufficient amount of peptide is activated, the increased affinity can lead to coacervate-based droplet formation. Simultaneously, hydrolysis of the anhydride reverts the activation, which undoes its affinity for RNA. The result is a dynamic interplay between droplet material flowing into the droplets by activation and droplet material leaving the droplet through deactivation (Scheme 1B). As such, this system is an excellent model for biological counterparts of coacervate-based active assemblies like membraneless organelles and marine adhesive, particularly when the role of chemical reactions and how these regulate droplet properties are studied. However, we currently lack clear design rules for coacervate-based active assemblies. Moreover, we also do not know which parameters affect the dynamics of assembly and disassembly of these assemblies. Tailoring the building blocks of our dissipative complex coacervates is necessary to further elucidate their dynamic properties in response to our proposed reaction cycle. Therefore, in this work, we introduce rules on how the dynamics of our active droplets can be regulated through molecular design. We test the effect of the peptide design on the dynamics of the emerging droplets, as well as the effect of the polymer length. Finally, we introduce a polymer design that changes the morphology of our complex coacervation-based assemblies (Scheme 1C).

RESULTS AND DISCUSSION

Role of Peptide Design. In the first part of this study, we focus on how the peptide design affects droplets' emergence and dynamics. We varied the number of RG-repeats in our peptide design to tune the electrostatic interactions between our peptides and the anionic polymers (Figure 1A). At the lowest extreme (peptide **1**), our peptide consisted of one RG-repeat. At the other extreme (peptide **4**), our peptide comprised four RG-repeats. Given that C-terminal aspartic acid has a −2 charge, the overall charge of the precursor state of the peptides is −1, 0, +1, +2, respectively (Figure 1B). These peptides were synthesized using solid-phase peptide synthesis (see Supporting Information). We tested for the formation of droplets for each of our four peptides in response to chemical fuel. We used a plate reader to measure the absorbance at 600 nm as a measure for turbidity, and we used confocal microscopy with sulforhodamine as a fluorescent dye to examine the nature of the turbidity. For all experiments, we used a concentration of 16 mM peptide in 200 mM MES buffer at pH 5.3. As an anionic polymer, we used polystyrenesulfonate (PSS) of 17 kg/mol. The concentration of the PSS was 25 mM, expressed as styrenesulfonate monomer units. We tested for the emergence of turbidity by the addition of 50 mM of EDC as fuel.

For peptide **1**, no increased turbidity was observed, and confocal microscopy confirmed the absence of assemblies (Figure 1C,D). Peptide **1** does also not form droplets with longer PSS strands up to 1000 kg/mol after up to 200 mM of EDC were added (Figure S12 A). In contrast, the addition of fuel to peptide **2** resulted in the formation of droplets evidenced by confocal microscopy (Figure 1C). The emergence and decay of droplets was completed within 15 min. We found that the solution's turbidity rapidly evolved, i.e., it rapidly increased, peaked at around 2 min, after which it decayed rapidly to its original level (Figure 1D). The fast rates and high dynamics reflect the fast kinetics of our reaction cycle on which we will comment in the next paragraph. Lower amounts of EDC shorten the lifetime, whereas higher amounts of EDC lead to prolonged turbidity (e.g., 21 min for 100 mM of EDC, Figure S6). Different peptide-to-EDC ratios also lead to different lifetimes since the amount of EDC that is available per precursor is changed, too (Figure S7). For the next peptide, peptide **3**, a similar response was observed. However, the decay in the turbidity was delayed compared to peptide **2**. Specifically, it took almost 20 min for the original transparent solution to recover. In contrast, peptide **4** formed coacervate droplets before the addition of fuel (see Figure 1C). The addition of fuel did not alter the turbidity or the nature of the droplets (Figure 1D, Figure S13). The turbidity of this sample did decrease over the course of the experiments. However, even after 1 h, it was still present, and the droplets started sedimenting. Peptide **4** also did not form dynamic coacervates with other PSS lengths (Figure S12 B). All samples were also refueled with 50 mM of EDC, which led to a reproducible transient increase of turbidity in solutions containing peptides **2** and **3** indicating that the system can be recycled (Figure S14). Finally, we introduce peptide **3-NH₂** (Ac-F(RG)₃N-NH₂, Figure 1A), which is similar to **3**, except for that we substituted the C-terminal aspartic acid for the amidated asparagine C-terminus. This mutation makes **3-NH₂** permanently cationic 3+. Indeed, **3-NH₂** formed droplets at a
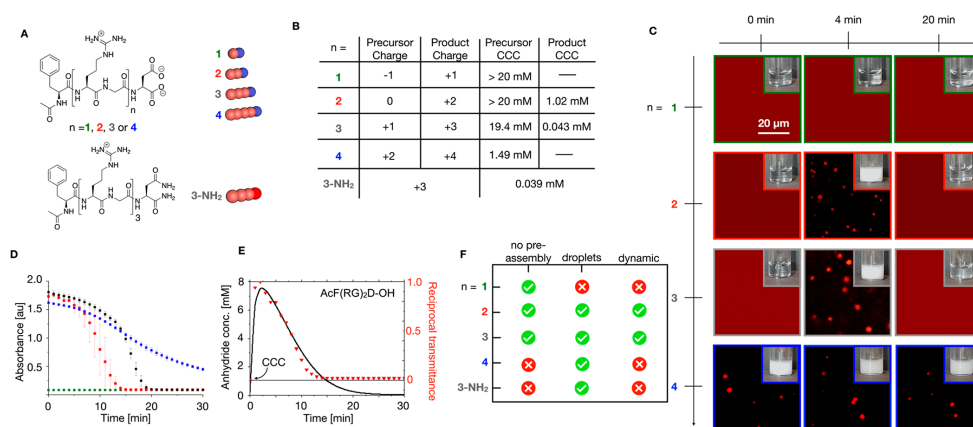
28

Figure 1. Effect of molecular design of the peptide on droplet behavior. (A) Molecular structures of the peptide sequences used in this study. (B–F) Response of the system when 16 mM peptide is fueled with 50 mM EDC in the presence of 25 mM PSS (17 kg/mol) expressed in monomer units and 200 mM MES buffer at pH 5.3: (B) CCC values and changes in charges of the different peptide structures after activation with EDC and conversion into the anhydride. A nonactive model peptide (**3-NH$_2$**) was also tested to compare it to the active peptides. (C) Confocal laser scanning microscopy micrographs acquired at various time-points during the reaction cycle. The insets show photographs of the sample at the same time-points. The scale bar represents 20 μm. (D) Absorbance at 600 nm as a function of time as measured with a plate reader. (E) Overlay of the anhydride concentration of peptide **2** (left axis) and the reciprocal transmittance (right axis) as a function of time. The overlap of the traces demonstrates the high degree of correlation between the chemical reaction cycle and the presence of droplets. The concentration profile is predicted by the kinetic model. The CCC is drawn as a black line at 1.02 mM. The reciprocal transmittance is calculated by $10^{(Absorbance)}$ and then normalized to 1. We plotted the maximum normalized reciprocal transmittance such that the x-axis corresponds to the CCC on the left y-axis. (F) Summary of the different responses of the systems with the different peptides **1–4** and **3-NH$_2$**.

concentration above 0.039 mM (Figure 1B). As such, **3-NH$_2$** is a great model compound for the active state of **3**.

To better understand the dynamic evolution of the droplets, we tested the kinetics of the reaction cycle under conditions described above by analytical HPLC in combination with a previously developed quench method,[23] and a kinetic model (see Supporting Information). For each peptide, the concentrations of EDC, the peptide, and its corresponding product were monitored in response to 50 mM EDC. As expected, the decay of the EDC and the emergence and decay of the product evolved very similarly for peptides **1**, **2**, and **3**. That means, for all peptides, all EDC was consumed in 15 min, whereas the peptide's corresponding product emerged, peaked at around 2 min, and was deactivated after roughly 18 min. The evolution of the reaction cycle could be predicted accurately with our kinetic model. Interestingly, for peptides **1**, **2**, and **3**, the same rate constants were used for each reaction to obtain good fits (Figure S15), which suggests that the chemical reactivity for each peptide is the same and is independent of the presence or absence of droplets, given that **1** never forms droplets, but **2** and **3** do. The evolution of the reaction cycle with peptide **4** was not measured in the presence of PSS, because the turbid solutions were too viscous to be injected in the HPLC.

We correlated the evolution of the turbidity to the evolution of the kinetics of the reaction cycle to better understand how peptide design affects droplet dynamics. We first converted the turbidity to reciprocal transmittance, which, unlike turbidity, scales linearly with increasing total droplet volume (see Supporting Information). We assess the droplets' dynamics by comparing three events in the reaction cycle: (1) the time

points where the anhydride concentration and the reciprocal transmittance reach their maximum, (2) half of their maximum value, and (3) the time where the reciprocal transmittance reaches its original value compared to when the concentration anhydride reaches the concentration required for coacervation. We first measured this critical concentration required for coacervation (CCC, critical coacervation concentration) to be 1.02 mM for the product of **2** and 0.043 mM for the product of **3** (see Supporting Information). Noteworthy, the CCC for the anhydride of peptide **3** is a close match to the CCC of model compound **3-NH$_2$**. The CCC of **3** and **4** without EDC was 1.49 and 19.4 mM, respectively (Figure 1B).

The evolution of the reciprocal transmittance of peptide **2** in response to EDC correlated strongly with the evolution of the kinetics of the reaction cycle; i.e., both maxima were reached after 3 min, the droplets disappeared when the concentration anhydride fell below the CCC after 15 min, and half of the maximums were obtained after 8.5 and 7.5 min, respectively (Figure 1E). The evolution of the turbidity of peptide **3** also correlated with the evolution of the kinetics of the reaction cycles, albeit less strongly. Half of the maximum of turbidity was reached after 11 min, while the peptide anhydride concentration showed a half-life time of 9 min (Figure S16), indicating a minimal delay from the maximum until complete dissolution as soon as the CCC is reached after 20 min. Unsurprisingly, the correlations of peptides **1** and **4** that formed no droplets or permanent droplets, respectively, were poor (Figure S16).

We classify the response of our system to chemical fuel in four categories, i.e., (i) no droplets emerge; the droplets that emerge are (ii) dynamic or (iii) metastable; and droplets are

29

present before the addition of fuel (iv) (Figure 1F). In this classification, dynamic means that droplets follow the behavior of the reaction cycle with a high correlation. In other words, in dynamic droplets, the kinetics of the reaction cycle are regulating the properties of the droplets. This strong correlation is evident for peptides **2** and **3**. For these peptides, droplets form as soon as the CCC for the peptide anhydride is reached. This threshold is exceeded almost instantly after EDC was added, which explains the rapid droplet formation. Their dissolution follows the evolution of the peptide anhydride concentrations very closely, too. The coacervate droplets dissolve as soon as the peptide anhydride concentration falls below the CCC. Before this point is reached, the gradual decrease in turbidity indicates that the droplets also follow the gradual loss in peptide anhydride and therefore the gradual loss of droplet material. In metastable droplets, the decay of the droplets lags the reaction cycle to a certain degree. We can thus conclude that metastable droplets emerge in response to fuel but have a certain degree of stability that does not lead to their immediate decay. Such a delay occurs for peptide **2** with higher-molecular-weight PSS (vide infra). Finally, the droplets based on peptide **4** did not require fuel to form droplets, and the evolution of the turbidity did not change by the addition of fuel (Figure S13).

Role of Polymer Length. Besides the role of the peptide design, the influence of poly(styrenesulfonate) (PSS) chain lengths on the dynamics of the droplets was investigated (Figure 2A). We used turbidimetry at 600 nm for a broad screening of molecular weights ranging from 4.3 kg/mol to 1000 kg/mol. Like the experiments above, we fueled a solution
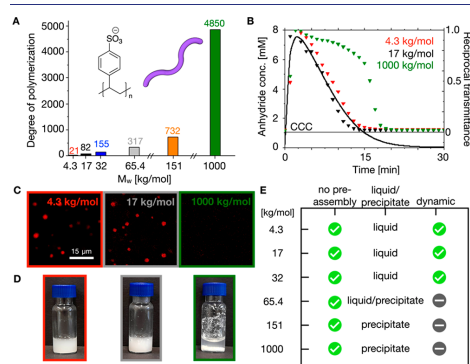

Figure 2. Role of the polymer length on droplet behavior. (A) Different numbers of repeating units (degrees of polymerization) for different poly(styrenesulfonate) polymers used in this study. (B–E) Responses of the system consisting of 25 mM PSS of different chain lengths expressed in monomer units, 16 mM peptide **2**, 50 mM EDC, and 200 mM MES buffer at pH 5.3: (B) Reciprocal transmittance (see Figure 1 and methods for calculation) traces for different poly-(styrenesulfonate) lengths (triangles) from plate reader measurements at 600 nm and the evolution of the peptide anhydride concentration (solid line) from the kinetic model. (C) Confocal fluorescence micrographs of coacervate samples in the solution phase for different PSS lengths 4 min into the cycle. The scale bar is 15 μm. (D) Visual turbidity (4.3 kg/mol and 17 kg/mol) of samples during the cycle and precipitation for 1000 kg/mol PSS. (E) Summary of the response for different poly(styrenesulfonate) lengths.

of 16 mM of peptide **2** with 50 mM EDC in 200 mM MES at pH 5.3. We tested the effect of the molecular weight of PSS on the behavior of droplets. It is important to note that in these tests, we are interested in the role of the length of the polymer, not the amount of polymer chains. Thus, in all experiments, the same concentration of PSS was used when expressed in styrenesulfonate monomer units, i.e., 25 mM PSS. In other words, the weight percentage of polymer in solutions was kept the same between experiments.

We found that for PSS with a molecular weight of 4.3, 17, and 32 kg/mol the turbidity of the solution evolved similarly to the experiments described above, from which we conclude that the droplets were dynamic. In contrast, for 65.4 kg/mol or greater, the turbidity decreased at a later point in the cycle. This trend continued with an increasing molecular weight of PSS; e.g., for 1000 kg/mol PSS, the turbidity started to decrease after 15 min. Compared to 17 kg/mol PSS, the turbidity for 1000 kg/mol PSS was also delayed for lower amounts of EDC. The longer cycle lifetimes can be compensated by adding less EDC (Figure S17). We further studied the behavior by confocal microscopy on the shortest (4.3 kg/mol), our standard (17 kg/mol), and the maximum chain length (1000 kg/mol) of PSS (Figure 2C). To our surprise, almost no coacervate droplets of 1000 kg/mol PSS were present in the solution, and the remaining complex coacervates were extremely small compared to the other samples. Instead, the majority of the condensates were found on the surface of the glass slide. The longer PSS chains tended to form smaller complex coacervates that agglomerated and precipitated quickly before they could grow to larger droplets like PSS strands of 4.3 and 17 kg/mol. Those big droplets also settled and wetted the glass surface but kept their droplet shape (Figure S18). We refer to the sediments in samples with 4.3 or 17 kg/mol PSS as liquid-like, because the droplets were able to fuse and wet the surface. In contrast, the precipitates formed by the 1000 kg/mol PSS based system did not show coalescence and maintained rough, irregular shapes. Moreover, they could be observed by the naked eye as transient precipitates (Figure 2D). Bright-field microscopy further revealed that the liquid-to-precipitate transformation occurred for PSS with chain lengths between 65.4 and 151 kg/mol (Figure S18). We correlated the reciprocal transmission to the evolution of the reaction cycle (Figure 2B, Figure S19 C) and found that the evolution of the reciprocal transmittance for samples from 4.3 kg/mol to 32 kg/mol behaved similarly and could be classified as dynamic droplets. In contrast, for 65.4, 151, and 1000 kg/mol, the reciprocal transmittance regained its original values, but that point was several minutes beyond the point where the CCC was reached. The initial values were regained with a delay of 3, 5, and 7 min, respectively (Figure 2B, Figure S19 C). Moreover, the reciprocal transmittance of these samples peaked much beyond the point where the anhydride concentration peaked. We classify those aggregates as metastable by the apparent delay in dissolution compared to the peptide anhydride evolution (Figure 2E).

We explain the different behavior observed for increasing polymer length by a multivalency effect of the poly-(styrenesulfonate) chains.[24,25] That means that the greater the polymer chain length, the higher the number of activated product molecules per strand, and thus the more cross-links per polymer chain. This increased number of cross-links leads to delayed disassembly kinetics compared to short polymers. In line with this hypothesis, a study by others has shown that an

increase in polymer length results in increased stability of the coacervate phase toward dissolution induced by salt.[26] We find that a similar mechanism operates because our droplets show similarly increased stability toward salt with increasing polymer chain length (Figure S20). Specifically, when we introduced 250 mM NaCl or more to the system, coacervate droplets from 1000 kg/mol PSS were less affected compared to 17 kg/mol PSS. Moreover, these samples could be refueled even when up to 500 mM NaCl was present, which was not the case for shorter polymer strands. A concentration of 1 M NaCl inhibited complex coacervation completely independent of polymer chain length. Fluorescence recovery after photobleaching (FRAP)-based experiments on droplets formed with 17, 65.4, and 1000 kg/mol PSS further confirmed the different phase regime as it showed a 3-fold decrease in diffusion coefficients of the PSS within the polymer-rich phase from 0.015 μm^2 s^{-1} for 17 kg/mol PSS to 0.005 μm^2 s^{-1} for 1000 kg/mol PSS (Figure S21). Taken together, we showed that our droplets formed by peptide **2** can either be dynamic or metastable depending on the polymer length. This insight offers a valid design tool for controlling the response of complex coacervates to our reaction cycle. Different phase behavior of our active coacervate droplets resulting from different PSS lengths combined with different droplet dynamics resulting from the peptide design will serve as a useful model to mimic the rich phase behavior of membraneless organelles. Besides many fully fluid organelles, examples of more gel-like or even solid phases also exist. The phase behavior of such organelles has a direct implication on their functions.[13]

Role of Polymer Structure. With our increased understanding of regulating the dynamics of the complex coacervate phases, we were interested in controlling their morphology. We modified the nature of the anionic polymer from a simple polyanion to a di- or triblock copolymer by addition of a poly(ethylene glycol) (PEG)-block to our PSS that served as a repulsive block, like the headgroup on a surfactant. Thereby, we anticipated that the PEG-blocks alter the morphology of our complex coacervate droplets.[27,28] We used RAFT polymerization to synthesize two block copolymers, PSS$_{77}$-*b*-PEG$_{105}$ and PSS$_{89}$-*b*-PEG$_{227}$-*b*-PSS$_{89}$ (see Supporting Information and Figure 3A). We tested the behavior of these block copolymers in the presence of peptide **2** under otherwise exactly the same conditions as described above (50 mM EDC added to 16 mM **2**, with 25 mM polymer expressed in monomer units). Compared to the homopolymer, we found lower turbidity levels for the block copolymers, while the lifetime of the turbidity remained the same (Figure 3B). The decreased turbidity is an initial indication that the assemblies are smaller compared to the homopolymer (Figure 3C).

Indeed, cryo-TEM micrographs, 4 min after the addition of EDC, revealed the presence of coacervate core micelles for both block copolymers (Figure 3C). Cryo-TEM on the PSS-PEG-based experiment revealed mainly 100- to 200-nm-long and 30-nm-wide worm-like micelles that were densely packed, while the PSS-PEG-PSS assembled into large spherical assemblies with diameters around 100 nm, likely large compound micelles. DLS analysis showed an intensity distribution with a maximum at 164 nm for PSS-PEG-PSS and a major peak with a maximum of 91 nm for the PSS-PEG complex coacervate micelles (Figure S22). Noteworthy, the block copolymer samples could be refueled, resulting in another round of transient turbidity (Figure S23). We
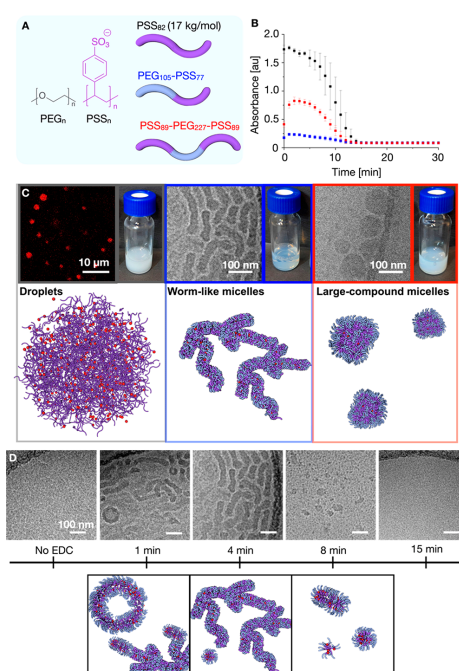

Figure 3. Effect of the polymer nature on the morphology of the phase-separated assembly. (A) Chemical structures of the PSS-PEG block copolymers. (B–D) Analysis of systems with concentrations of 16 mM peptide **2**, 25 mM of homo or block copolymers expressed in styrenesulfonate units and 50 mM EDC in 200 mM MES buffer at pH 5.3: (B) Turbidity traces of PSS homopolymer (17 kg/mol, black), 47.5 kg/mol PSS-PEG-PSS (red), and 21 kg/mol PSS-PEG (blue) from plate reader measurements at 600 nm. (C) Cryo-TEM micrographs of the different coacervate based structures and the visible turbidity of samples 4 min after the addition of EDC. Scale bars are 10 μm (left image) and 100 nm (middle and right image). (D) Different morphologies of PSS$_{77}$–PEG$_{105}$-based micelles at different time-points in the reaction cycle. Scale bars are 100 nm.

hypothesize that the PEG block does not partition in the PSS-based complex coacervate core. Thus, the addition of a PEG block resulted in a repulsive block and hindered the unrestricted growth of the PSS block into large droplets. Instead, block copolymer micelles were observed, i.e., worm-like micelles for PSS-PEG and large-compound micelles for PSS-PEG-PSS.

Excited by the drastic change in morphology by the addition of the PEG block, we tested whether the amount of activated peptide in the system affected the phase-separated system's morphology too. We thus further analyzed the PSS$_{77}$-*b*-PEG$_{105}$ worm-like micelles at different time-points throughout the reaction cycle (Figure 3D). Before the addition of EDC, the cryo-TEM micrograph showed no obvious assemblies. One minute after the fuel was added, a rich mixture of small spherical micelles, long worm-like micelles, and polymersomes was present. After 4 min, only worm-like micelles and spherical assemblies were visible. In the micrograph taken after 8 min,

the decay of the assemblies was clearly evident when only a small fragment of the original micelles remained surrounded by 10 nm globular assemblies. After 15 min, no more obvious assemblies were found.

We explain the morphological transition from polymersomes, to worm-like micelles, to micelles and fragments by a gradual loss of the activated peptide **2**, which is responsible for holding together the PSS-block. The high amount of activated peptide early in the reaction cycle favors the incorporation of more PSS-PEG block copolymers compared to at the later stages. The high density of PEG chains and their repulsion at the micelle corona leads to the elongation of micelles and creates nonspherical shapes like bilayer sheets that form polymersomes and (branched) worm-like micelles, in line with other studies.[29−31] As **2** gradually deactivates, the driving force for the phase separation of the PSS-block decreases, resulting in a gradual loss of block copolymer. The loss of block copolymer results in a decrease in crowding in the corona and less dense packing and thereby a reversion toward micelles that eventually fragment.

Design of Chemically Fueled Coacervate Based Assemblies. Based on the combined findings, we can stipulate pre-emptive design rules for chemically fueled complex coacervate-based assemblies. These rules will hold for designs in which a small molecule transiently increases its number of ionic charges upon chemical activation. Thus, they also apply to the recent designs by Keating[21] and Spruit[32] that use enzymes to activate a precursor by increasing its number of charges. The additional charge increases the affinity for a polymer strand, which can subsequently induce coacervation. When the intention is to form a complex coacervate with a polyanion like our PSS or RNA, the overall charge on the precursor should increase upon chemical activation (+2 in our system). Vice versa, if a polycation like polylysine is to be bound, the overall charge on the precursor should decrease (e.g., by activation via phosphorylation). Whether coacervation will take place depends on the molecular design of the precursor, which, in our case, was gradually altered by the addition of cationic RG-repeats to interact with polyanions. With too little interaction, no coacervation can be expected. On the contrary, if too many groups are added, the precursor itself can also form droplets. Thus, in the molecular design, it is important to find the right balance. In essence, the CCC of the precursor should be higher than the precursor concentration, and, upon activation, that CCC should decrease drastically. Following these design rules, it is reasonable to expect that active droplets can be created using other reaction cycles that change the degree of ionization on their precursor, e.g., the cycle that transiently forms esters at the expense of methylating agents,[33,34] the addition−elimination cycle of dithionite to an aldehyde,[35] and others.[36−38]

On the other hand, the polymer length plays an important role in the design, especially in the dynamics of the emerging droplets. Long polymers result in a loss of the dynamic properties of the droplets due to an increase in the number of cross-links per strand. In other words, if a polymer molecular weight is chosen that is too high, the chemical reactions will become less able to regulate the dynamics of the droplets. Finally, functions can be added to the droplets by adding functional polymers. For example, the droplets are fluorescently labeled when the polymer is fluorescently labeled. Moreover, we show that the morphology of the coacervate can be altered simply by using block copolymers, in which one block has an affinity for the activated peptide, whereas the other does not. In that design, the second block acts as a repelling group like the headgroup on an amphiphile, giving rise to block copolymer amphiphile structures like micelles, worm-like micelles, and polymersomes.

■ CONCLUSION AND OUTLOOK

We performed a systematic study on the influence of peptide and polymer design on the formation of dynamic and transient droplets. We found that droplet formation could be extremely dynamic when the affinity of the peptide for the polymer was chosen correctly and the polymer length was not too high. Under those conditions, the emergence and decay of droplets evolve with a very high correlation to the chemical reaction cycle that regulates the peptide activation and deactivation. Finally, we found that the polymer's nature can alter the morphology of the complex coacervate based assembly. Our findings allow establishing heuristic design rules for chemically fueled complex coacervate-based assemblies. Such dissipative coacervates will help to mimic the highly dynamic character of membraneless organelles in nature and to elucidate their dynamics and transient properties further.[39]

■ ASSOCIATED CONTENT

ⓢ Supporting Information

The Supporting Information is available free of charge at https://pubs.acs.org/doi/10.1021/jacs.1c01148.

> Materials and Methods description and additional data (Synthetic protocols and analysis; Sample preparation; Kinetic model; HPLC Procedures and Quenching; CCC determination; Turbidity Measurements; Correlation details; Confocal Fluorescence Microscopy; FRAP procedures; Bright-field microscopy; Cryo-TEM and DLS) (PDF)

■ AUTHOR INFORMATION

Corresponding Author

Job Boekhoven − *Department of Chemistry and Institute for Advanced Study, Technical University of Munich, 85748 Garching, Germany;* ⓞ orcid.org/0000-0002-9126-2430; Email: job.boekhoven@tum.de

Authors

Fabian Späth − *Department of Chemistry, Technical University of Munich, 85748 Garching, Germany*
Carsten Donau − *Department of Chemistry, Technical University of Munich, 85748 Garching, Germany*
Alexander M. Bergmann − *Department of Chemistry, Technical University of Munich, 85748 Garching, Germany*
Moritz Kränzlein − *WACKER-Chair of Macromolecular Chemistry, Catalysis Research Center, Technical University of Munich, 85748 Garching, Germany*
Christopher V. Synatschke − *Max Planck Institute for Polymer Research, 55128 Mainz, Germany*
Bernhard Rieger − *WACKER-Chair of Macromolecular Chemistry, Catalysis Research Center, Technical University of Munich, 85748 Garching, Germany;* ⓞ orcid.org/0000-0002-0023-884X

Complete contact information is available at:
https://pubs.acs.org/10.1021/jacs.1c01148

Author Contributions

The manuscript was written through contributions of all authors. All authors have given approval to the final version of the manuscript.

Notes

The authors declare no competing financial interest.

■ REFERENCES

(1) Sing, C. E.; Perry, S. L. Recent progress in the science of complex coacervation. *Soft Matter* **2020**, *16* (12), 2885−2914.

(2) Voets, I. K.; de Keizer, A.; Cohen Stuart, M. A. Complex coacervate core micelles. *Adv. Colloid Interface Sci.* **2009**, *147−148*, 300−18.

(3) Sproncken, C. C. M.; Magana, J. R.; Voets, I. K. 100th Anniversary of Macromolecular Science Viewpoint: Attractive Soft Matter: Association Kinetics, Dynamics, and Pathway Complexity in Electrostatically Coassembled Micelles. *ACS Macro Lett.* **2021**, *10*, 167−179.

(4) Zhou, L.; Shi, H.; Li, Z.; He, C. Recent Advances in Complex Coacervation Design from Macromolecular Assemblies and Emerging Applications. *Macromol. Rapid Commun.* **2020**, *41* (21), e2000149.

(5) Schmitt, C.; Turgeon, S. L. Protein/polysaccharide complexes and coacervates in food systems. *Adv. Colloid Interface Sci.* **2011**, *167* (1−2), 63−70.

(6) Blocher, W. C.; Perry, S. L. Complex coacervate-based materials for biomedicine. *Wiley Interdiscip. Rev. Nanomed. Nanobiotechnol.* **2017**, *9* (4), e1442.

(7) Matalanis, A.; Jones, O. G.; McClements, D. J. Structured biopolymer-based delivery systems for encapsulation, protection, and release of lipophilic compounds. *Food Hydrocolloids* **2011**, *25* (8), 1865−1880.

(8) Cabral, H.; Miyata, K.; Osada, K.; Kataoka, K. Block Copolymer Micelles in Nanomedicine Applications. *Chem. Rev.* **2018**, *118* (14), 6844−6892.

(9) De Santis, S.; Diociaiuti, M.; Cametti, C.; Masci, G. Hyaluronic acid and alginate covalent nanogels by template cross-linking in polyion complex micelle nanoreactors. *Carbohydr. Polym.* **2014**, *101*, 96−103.

(10) Kim, H. J.; Yang, B.; Park, T. Y.; Lim, S.; Cha, H. J. Complex coacervates based on recombinant mussel adhesive proteins: their characterization and applications. *Soft Matter* **2017**, *13* (42), 7704−7716.

(11) Dompé, M.; Cedano-Serrano, F. J.; Vahdati, M.; Westerveld, L.; Hourdet, D.; Creton, C.; Gucht, J.; Kodger, T.; Kamperman, M. Underwater Adhesion of Multiresponsive Complex Coacervates. *Adv. Mater. Interfaces* **2020**, *7* (4), 1901785.

(12) Shao, H.; Stewart, R. J. Biomimetic underwater adhesives with environmentally triggered setting mechanisms. *Adv. Mater.* **2010**, *22* (6), 729−33.

(13) Gomes, E.; Shorter, J. The molecular language of membraneless organelles. *J. Biol. Chem.* **2019**, *294* (18), 7115−7127.

(14) Linsenmeier, M.; Kopp, M. R. G.; Grigolato, F.; Emmanoulidis, L.; Liu, D.; Zurcher, D.; Hondele, M.; Weis, K.; Capasso Palmiero, U.; Arosio, P. Dynamics of Synthetic Membraneless Organelles in Microfluidic Droplets. *Angew. Chem., Int. Ed.* **2019**, *58* (41), 14489−14494.

(15) Banani, S. F.; Lee, H. O.; Hyman, A. A.; Rosen, M. K. Biomolecular condensates: organizers of cellular biochemistry. *Nat. Rev. Mol. Cell Biol.* **2017**, *18* (5), 285−298.

(16) Brangwynne, C. P.; Eckmann, C. R.; Courson, D. S.; Rybarska, A.; Hoege, C.; Gharakhani, J.; Julicher, F.; Hyman, A. A. Germline P granules are liquid droplets that localize by controlled dissolution/condensation. *Science* **2009**, *324* (5935), 1729−32.

(17) Rai, A. K.; Chen, J. X.; Selbach, M.; Pelkmans, L. Kinase-controlled phase transition of membraneless organelles in mitosis. *Nature* **2018**, *559* (7713), 211−216.

(18) Mugler, C. F.; Hondele, M.; Heinrich, S.; Sachdev, R.; Vallotton, P.; Koek, A. Y.; Chan, L. Y.; Weis, K. ATPase activity of the DEAD-box protein Dhh1 controls processing body formation. *eLife* **2016**, *5*, e18746.

(19) Weber, C. A.; Zwicker, D.; Julicher, F.; Lee, C. F. Physics of active emulsions. *Rep. Prog. Phys.* **2019**, *82* (6), 064601.

(20) Priftis, D.; Tirrell, M. Phase behaviour and complex coacervation of aqueous polypeptide solutions. *Soft Matter* **2012**, *8* (36), 9396−9405.

(21) Aumiller, W. M., Jr; Keating, C. D. Phosphorylation-mediated RNA/peptide complex coacervation as a model for intracellular liquid organelles. *Nat. Chem.* **2016**, *8* (2), 129−37.

(22) Donau, C.; Späth, F.; Sosson, M.; Kriebisch, B. A. K.; Schnitter, F.; Tena-Solsona, M.; Kang, H. S.; Salibi, E.; Sattler, M.; Mutschler, H.; Boekhoven, J. Active coacervate droplets as a model for membraneless organelles and protocells. *Nat. Commun.* **2020**, *11* (1), 5167.

(23) Schnitter, F.; Boekhoven, J. A Method to Quench Carbodiimide-Fueled Self-Assembly. *ChemSystemsChem.* **2021**, *3* (1), e2000037.

(24) Lu, T.; Spruijt, E. Multiphase Complex Coacervate Droplets. *J. Am. Chem. Soc.* **2020**, *142* (6), 2905−2914.

(25) Priftis, D.; Laugel, N.; Tirrell, M. Thermodynamic characterization of polypeptide complex coacervation. *Langmuir* **2012**, *28* (45), 15947−57.

(26) Chollakup, R.; Beck, J. B.; Dirnberger, K.; Tirrell, M.; Eisenbach, C. D. Polyelectrolyte Molecular Weight and Salt Effects on the Phase Behavior and Coacervation of Aqueous Solutions of Poly(acrylic acid) Sodium Salt and Poly(allylamine) Hydrochloride. *Macromolecules* **2013**, *46* (6), 2376−2390.

(27) Pergushov, D. V.; Muller, A. H.; Schacher, F. H. Micellar interpolyelectrolyte complexes. *Chem. Soc. Rev.* **2012**, *41* (21), 6888−901.

(28) Lemmers, M.; Sprakel, J.; Voets, I. K.; van der Gucht, J.; Cohen Stuart, M. A. Multiresponsive reversible gels based on charge-driven assembly. *Angew. Chem., Int. Ed.* **2010**, *49* (4), 708−11.

(29) Aloi, A.; Guibert, C.; Olijve, L. L. C.; Voets, I. K. Morphological evolution of complex coacervate core micelles revealed by iPAINT microscopy. *Polymer* **2016**, *107*, 450−455.

(30) Takeda, K. M.; Osada, K.; Tockary, T. A.; Dirisala, A.; Chen, Q.; Kataoka, K. Poly(ethylene glycol) Crowding as Critical Factor To Determine pDNA Packaging Scheme into Polyplex Micelles for Enhanced Gene Expression. *Biomacromolecules* **2017**, *18* (1), 36−43.

(31) Osada, K. Development of functional polyplex micelles for systemic gene therapy. *Polym. J.* **2014**, *46* (8), 469−475.

(32) Nakashima, K. K.; Baaij, J. F.; Spruijt, E. Reversible generation of coacervate droplets in an enzymatic network. *Soft Matter* **2018**, *14* (3), 361−367.

(33) Boekhoven, J.; Brizard, A. M.; Kowlgi, K. N.; Koper, G. J.; Eelkema, R.; van Esch, J. H. Dissipative self-assembly of a molecular gelator by using a chemical fuel. *Angew. Chem., Int. Ed.* **2010**, *49* (28), 4825−8.

(34) Boekhoven, J.; Hendriksen, W. E.; Koper, G. J.; Eelkema, R.; van Esch, J. H. Transient assembly of active materials fueled by a chemical reaction. *Science* **2015**, *349* (6252), 1075−9.

(35) Singh, N.; Lainer, B.; Formon, G. J. M.; De Piccoli, S.; Hermans, T. M. Re-programming Hydrogel Properties Using a Fuel-Driven Reaction Cycle. *J. Am. Chem. Soc.* **2020**, *142* (9), 4083−4087.

(36) Grötsch, R. K.; Angi, A.; Mideksa, Y. G.; Wanzke, C.; Tena-Solsona, M.; Feige, M. J.; Rieger, B.; Boekhoven, J. Dissipative Self-Assembly of Photoluminescent Silicon Nanocrystals. *Angew. Chem., Int. Ed.* **2018**, *57* (44), 14608−14612.

(37) Rieß, B.; Grötsch, R. K.; Boekhoven, J. The Design of Dissipative Molecular Assemblies Driven by Chemical Reaction Cycles. *Chem.* **2020**, *6* (3), 552−578.

(38) Wang, G.; Liu, S. Strategies to Construct a Chemical-Fuel-Driven Self-Assembly. *ChemSystemsChem.* **2020**, *2* (4), e1900046.

(39) Yewdall, N. A.; André, A. A. M.; Lu, T.; Spruijt, E. Coacervates as models of membraneless organelles. *Curr. Opin. Colloid Interface Sci.* **2021**, *52*, 101416.

Supporting Information for:

Molecular Design of Chemically Fueled Peptide–Polyelectrolyte Coacervate-Based Assemblies

Authors: Fabian Späth[1], Carsten Donau[1], Alexander M. Bergmann[1], Moritz Kränzlein[2], Christopher V. Synatschke[3], Bernhard Rieger[2], Job Boekhoven[1,4]

Affiliations:

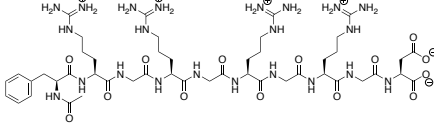[1] Department of Chemistry, Technical University of Munich, Lichtenbergstraße 4, 85748 Garching, Germany.

[2] WACKER-Chair for Macromolecular Chemistry, Catalysis Research Center, Technical University of Munich, Lichtenbergstraße 4, 85748 Garching, Germany.

[3] Max Planck Institute for Polymer Research, Ackermannweg 10, 55128 Mainz, Germany.

[4] Institute for Advanced Study, Technical University of Munich, Lichtenbergstraße 2a, 85748 Garching, Germany.
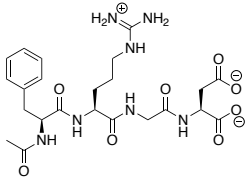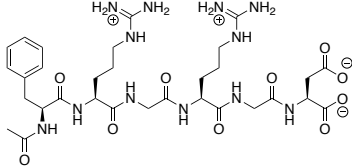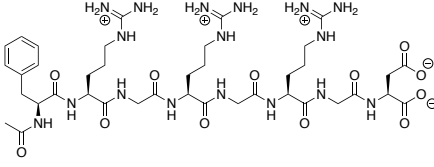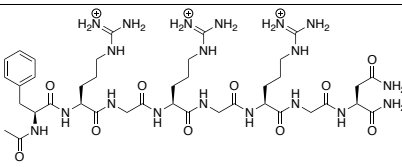
Materials and methods

Materials. All solvents were purchased in analytical grade from Sigma Aldrich and used without further purification. *N,N*-Dimethyl formamide (DMF) was purchased from Sigma-Aldrich in peptide synthesis grade. All amino acids (Fmoc-R(Pbf)-OH, Fmoc-D(OtBu)-OH, Ac-F-OH, Fmoc-G-OH and Fmoc-N(Trt)-OH), *N,N'*-Diisopropylcarbodiimide (DIC), Ethyl cyano(hydroxyimino)acetate (Oxyma, Nova-biochem©), Wang resins, Rink Amide resins (100-200 mesh, 0.4-0.8 mmol/g), 4-(Dimethylamino)-pyridine (DMAP), Trifluoroacetic acid (TFA, 99%), Piperidine (99%), Triisopropylsilane (TIPS), *N,N*-Diisopropylethylamine (DIPEA), 4-Chloro-7-nitrobenzofurazan (NBD-Cl, 98%), 4-Morpholineethanesulfonic acid (MES) hydrate, 1-Ethyl-3-(3-dimethylaminopropyl)carbodiimide (EDC), 4,4'-Azobis(4-cyanovaleric acid (ACPA, ≥98%), 2-(Dodecylthiocarbonothioylthio)-2-methylpropionic acid (98%), Poly(ethylene glycol) bis[2-(dodecylthiocarbonylthioylthio)-2-methylpropionate] (PEG BisDDMAT, M_n = 10.8 kg/mol), Poly(ethylene glycol) methyl ether 2-(dodecylthiocarbonothioylthio)-2-methylpropionate (PEG DDMAT, M_n = 5.0 kg/mol), 4-Styrenesulfonic acid sodium salt hydrate, Benzylamine (99%), Tris(2-carboxyethyl)phosphine hydrochloride, Ethylenediamine (>99%), Sodium borohydride (99%), D_2O (99.9 atom % D), Sulforhodamine B and Latex beads (500 nm, 1.0 μm and 2.0 μm carboxylate modified as aqueous suspensions) were purchased from Sigma-Aldrich and used without further purification. Poly(styrene sulfonate) sodium salt analytical standards (4.3 , 17, 32, 65.4 and 151 kg/mol, Supelco®), 70 kg/mol and 1000 kg/mol Poly(styrene sulfonate) sodium salts were purchased from Sigma-Aldrich and used as received. MilliQ-water was received from a Milli-Q® Direct 8 water purification system. All peptides were synthesized by standard Fluoren-9-ylmethoxycarbonyl (Fmoc) solid-phase peptide synthesis as described below. 1-[3-(Dimethylamino)propyl]-3-ethylurea (EDU) was obtained by refluxing 5 g of EDC in 50 mL of water for 3 days, followed by lyophilization. The full conversion and purity were assessed by analytical HPLC (r.t. of 5.89 min). AcF(RG)₃D-OH (peptide **3**) and AcF(RG)₂D-OH (peptide **2**) were also purchased from CASLO Aps (Denmark) without showing a different complex coacervation behavior in any experiment.

Microwave-assisted, automated solid phase peptide synthesis. The peptides were synthesized in 0.5 mmol scales on a peptide synthesizer Liberty Blue® from CEM. Loading of the aspartic acid on Wang-resin (0.5 mmol, 100-200 mesh, 1.1 mmol/g) was achieved by using the symmetrical amino acid anhydride. Therefore, Fmoc-D(OtBu)-OH (4.94 g, 12 mmol) was reacted for one hour with 0.93 mL *N,N'*-diisopropylcarbodiimide (DIC, 6 mmol) in 29 mL *N,N*-dimethylformamide (DMF, peptide synthesis grade) under continuous agitation. The solution was put in a freezer at -20°C for at least one hour until urea crystals were formed. The solids were removed by filtration. The resulting anhydride solution (0.2 M, 12.5 mL) was reacted with

the pre-swollen Wang resin in the peptide synthesizer at 75°C for 30 minutes together with a solution of 4-(dimethylamino)-pyridine (DMAP) in DMF (20 mM, 2.5 mL). This loading was done twice. Amino acid couplings were performed with the following sequence: Fmoc-deprotection was achieved by reacting 10 mL of a piperidine solution in DMF (20 v/v%) with the resin for 2 minutes at 90°C. The deprotection was repeated once with a washing step with DMF in between. 4 eq. of the corresponding Fmoc-protected amino acid, 4 eq. of DIC in DMF and 4 eq. ethyl (hydroxyimino)cyanoacetate (Oxyma) in DMF were reacted with the resin. For glycine and phenylalanine couplings, the reaction mixture was heated to 90°C for 2 minutes in the microwave. The reaction mixture was heated to 90°C for 4 minutes for arginine couplings. Each amino acid coupling was repeated one time and the resin was washed with DMF in between. Sidechain deprotection and final cleavage from the resin was achieved by reacting the resin with a solution of 2.5% water, 2.5% triisopropylsilane (TIPS) and 95% trifluoroacetic acid (TFA) for one hour under continuous agitation at room temperature. Solvents were removed by rotary evaporation and co-distillation with DCM and cold diethyl ether. The residue was dissolved in water and extracted with diethyl ether before purification by preparative reversed-phase HPLC (Thermo Fisher Dionex Ultimate 3000, Hypersil Gold 250x4.8 mm, linear gradient of ACN from 2% to 98% and water, both with 0.1% TFA, flow rate 20 mL/min). The purity of the peptides was assessed by analytical reversed-phase HPLC and LC-MS (LCQ Fleet Ion Trap Mass Spectrometer, Thermo Scientific, positive mode). Pre-loaded Wang resin (Fmoc-Asp(O^{t}Bu)-Wang resin) could be used for the peptide syntheses as well by omitting the resin loading sequence. AcF(RG)$_3$N-NH$_2$ was synthesized by applying the abovementioned method, but the Wang resin was replaced by Rink Amide resin. The first step in the synthesis was the cleavage of the Fmoc-group of the Rink Amide resin, followed by the standard coupling cycle for Fmoc-Asn(Trt)-OH.

Supporting Table 1. *Peptide characterization.*

AcFRGD-OH.	**mass calc. [g/mol]**	534.55
	mass observed [g/mol]	536.43 $[M_w+2H]^+$
	retention time [min]	7.12
AcF(RG)₂D-OH.	**Mass calc. [g/mol]**	748.80
	mass observed [g/mol]	749.42 $[M_w+H]^+$
	retention time [min]	6.91
AcF(RG)₃D-OH.	**Mass calc. [g/mol]**	963.05
	mass observed [g/mol]	963.30 $[M_w]^+$
	retention time [min]	6.80
AcF(RG)₄D-OH.	**mass calc. [g/mol]**	1177.30
	mass observed [g/mol]	588.76 $[M_w]^{2+}$
	retention time [min]	6.92
AcF(RG)₃N-NH₂.	**mass calc. [g/mol]**	963.09
	mass observed [g/mol]	481.13 $[M_w]^{2+}$
	retention time [min]	6.76

Block copolymer synthesis and analysis.

Polymerizations were carried out under argon atmosphere using Schlenk techniques. 4-styrene sulfonate sodium salt hydrate, the PEG-based CTA and 4,4'-azobis(4-cyanopentanoic acid) (ACPA) were dissolved in MilliQ water. The mixture was heated under vigorous stirring for 30 minutes at 40°C to help the solubilization. Residual air was removed by purging the mixture with argon for 30 minutes. The polymerizations were performed at 75°C for 5 hours and stopped by exposing the mixtures to air and freezing the crude with liquid nitrogen. Dialysis in 12 -14 kDa MWCO dialysis tubes (Spectra/Por® 2, regenerated cellulose) against MilliQ water was performed for 3 days to purify the crude products. The MilliQ water was exchanged twice per day. The dialyzed solutions were lyophilized for at least 3 days to obtain the pure polymers. Table 2 summarizes the applied reaction conditions.

PEG Bis DDMAT (**A**) and PEG DDMAT (**B**) with the following structures were used as Chain Transfer Agents (CTA).

| **A** | **B** |
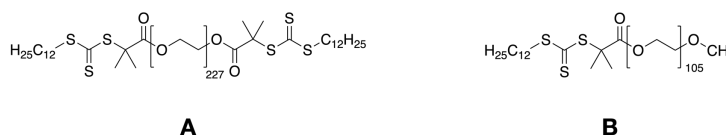
Supporting Table 2. *Applied polymerization conditions.*

polymer	$[CTA]_0$ (mol/L)	$[ACPA]_0$ (mol/L)	$[CTA]_0/[ACPA]_0$	$[NaSS]_0$ (mol/L)	conv. (%)[a]
(**1**) PSS_{77}-*b*-PEG_{105}	0.004 (**B**)	0.001	4	0.42	97[b]
(**2**) PSS_{89}-*b*-PEG_{227}-b-PSS_{89}	0.002 (**A**)	0.001	2	0.43	97[b]

a) determined from ^{1}H-NMR with PEO signals at 3.5-3.6 ppm as the reference. b) after 5 h.

The polymerization conditions were chosen according to literature[1], but the 4-cyanopentatnoic acid dithiobenzoate based PEG macro-CTA was replaced by PEG Bis DDMAT (**A**) and PEG DDMAT (**B**). The resulting polymers were analyzed by aqueous SEC, ^{1}H-NMR-, and IR-spectroscopy (Supporting Table 3, Fig S1-S4).

Supporting Table 3. *Blockcopolymer characterization overview.*

polymer	$M_{n,NMR}$[a] [kg/mol]	$M_{n, SEC}$[b] [kg/mol]	$Đ = M_w/M_n$[c]	DP_{PSS}[a]	yield[d] [%]
(**1**)	20.9	31.0	1.26	77	37
(**2**)	47.5	35.7	1.55	178	67

a) determined by ^{1}H-NMR spectroscopy in D_2O. b) determined by aqueous SEC against PEO Standards. c) determined by SEC-MALS in a 1:1 mixture of H_2O and THF 1:1 with 9 g/L TBAB d) determined gravimetrically after dialysis and lyophilization.

Aqueous SEC analysis (Fig. S1 A) was performed on an Agilent Technolgies 1260 liquid chromatography setup equipped with an isocratic pump, an autosampler and an RI detector. Poly(ethylene glycol) analytical standards in a molecular weight range from 2100 to 970000 g/mol were used to create a calibration curve for aqueous SEC. They were purchased from Polymer Standards Service GmbH. A mixture of 80% 0.07 M NaH_2PO_4 in water and 20% acetonitrile was used at a flow rate of 1 ml/min at 20 °C. A combination of two MCX columns (300 x 8 mm) from Polymer Standards Service GmbH was used.

It was reported that that PEG-PSS copolymers can show strong interactions with SEC columns.[2] We observed tailing for our samples. A better elution was obtained in a SEC-MALS setup using a 1:1-mixture of H_2O and THF with 9 g/L tetra-n-butylammonium bromide (TBAB) and 340 mg/L 3,5-di-*tert*-butyl-4-hydroxytoluene (BHT) as the eluent at 40 °C and a flow rate of 0.6 mL/min (Fig. S1 B). The setup consists of a Shimadzu LC-10ADVP pump, a Shimadzu DGU-3A degasser, a Shimadzu CTO-10A column thermostat and a Wyatt Dawn Heleos II multiangle light scattering unit in combination with a Wyatt Optilab rEX refractive index detector. A combination of two Agilent PL PolargelM columns (7.5 x 300 mm) was used. The data was processed and analyzed with the ASTRA 6 software from Wyatt (Version 6.1.2) with dn/dc = 0.176 mL g^{-1} for PSS-PEG and dn/dc = 0.177 mL g^{-1} for PSS-PEG-PSS.

The PEG based CTAs were analyzed by organic SEC with DMF as the eluent (Fig. S1 C). Thus, 1g/L LiBr was added to DMF. This mixture was used at a flow rate of 1 mL/min at 60 °C. The calibration curve was acquired with poly(ethylene glycol) analytical standards in a molecular weight range from 289 to 970000 g/mol. A combination of 3 GRAM columns (300 x 8 mm) from Polymer Standards Service GmbH was used. The CTA **A** showed an average molecular weight M_n = 10800 g/mol with a dispersity Đ of 1.10, CTA **B** showed an average molecular weight M_n = 4700 g/mol with a dispersity Đ of 1.19. Data Acquisition and Analysis was performed with the Software PSS WinGPC Unichrom from Polymer Standards Service GmbH.

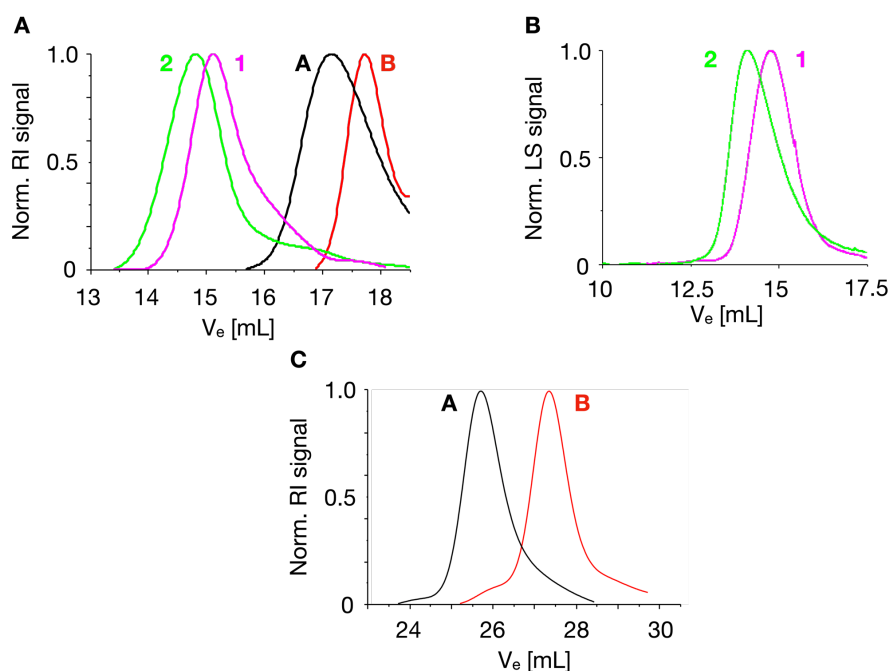Supporting Figure 1 shows the corresponding SEC traces of blockcopolymers 1 and 2 and the CTAs **A** and **B**.

Figure S1. *Chromatograms from aqueous SEC (**A** in phosphate buffer with acetontrile and **B** in a 1:1 mixture of H_2O and THF) and organic SEC (**C**) of the CTAs in DMF with LiBr.*

^{1}H-NMR spectra were recorded with 16 scans at room temperature on Bruker AVHD400 and AVHD500 spectrometers. Chemical shifts are reported in parts per million (ppm) relative to the signal of the deuterated solvent D_2O (δ = 4.7 ppm).

PSS-*b*-PEG-*b*-PSS, PSS-*b*-PEG ^{1}H-NMR (400 MHz, 500 MHz, D_2O) δ (ppm) = 0.8-2.2 (3H, -CH_2-CH-, alkyl backbone, with $C_{12}H_{25}$ tails and methyl groups), 3.5 - 3.6 (4H, -O-$(CH_2)_2$-), 6.0-7.0 (2H, ArH), 7.2-7.7 (2H, ArH). NMR spectra are in good agreement with literature.[1-2]

DP_{PSS} was determined by comparing the integrals of methylene signals for the PEO units with known lengths and the poly(styrene sulfonate) backbone alkyl proton signals.
Figures S2 and S3 show the corresponding ^{1}H-NMR spectra in D_2O for PSS-*b*-PEG and PSS-*b*-PEG-*b*-PSS.
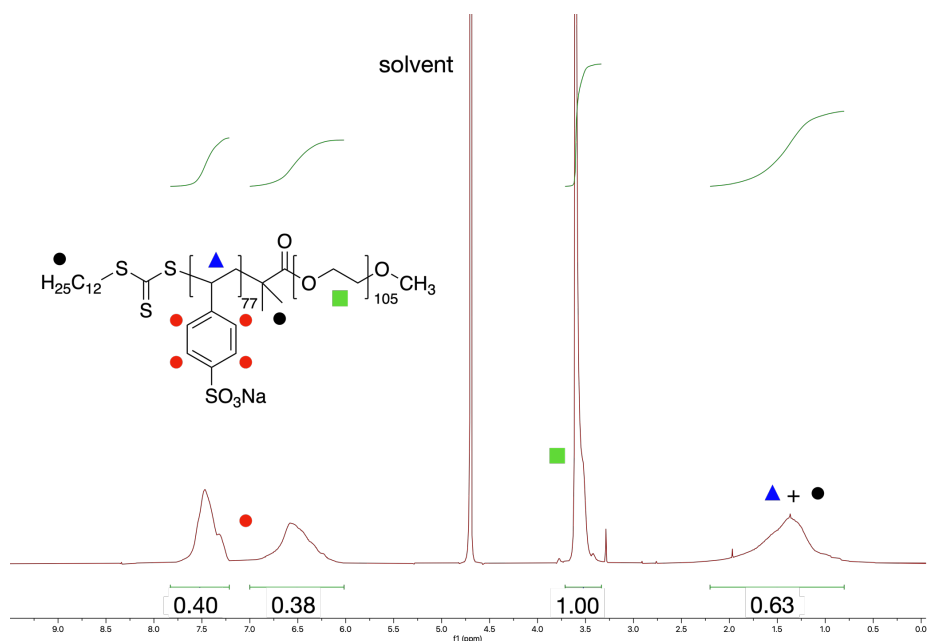
Figure S2. *^{1}H-NMR spectrum of PSS$_{77}$-b-PEG$_{105}$ in D$_2$O.*
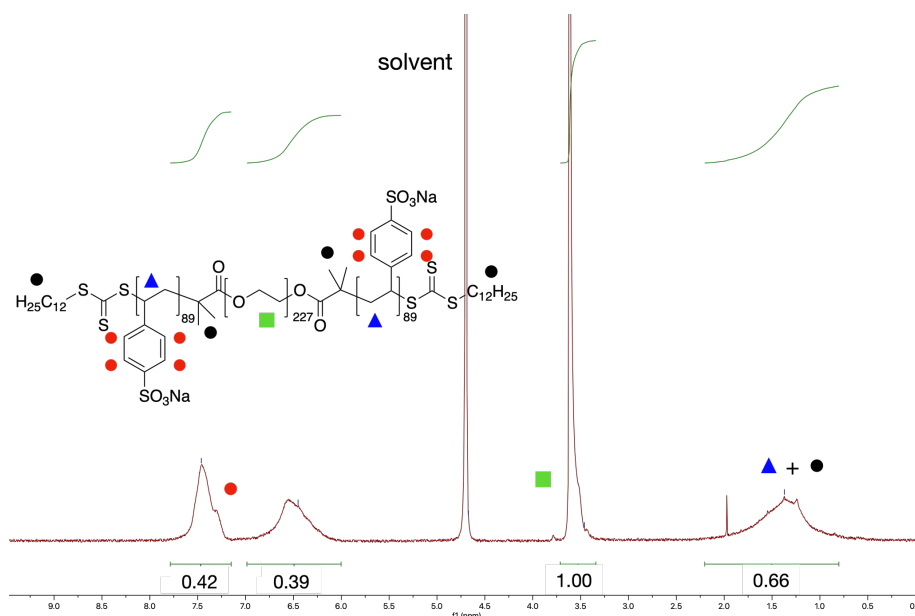
Figure S3. *^{1}H-NMR spectrum of PSS_{89}-b-PEG_{227}-b-PSS_{89} in D_2O.*

FT-IR spectra were recorded on a Bruker Vertex 70 FTIR spectrometer equipped with an ATR unit. One measurement consisted of 16 scans. FT-IR analysis showed the signals of the dominant functional groups of **1** and **2**. The highlighted regions show the presence of the following groups: C-H (ν = 2916 cm^{-1}, blue), SO$_3^-$ (around ν = 1180 cm^{-1} and ν = 1040 cm^{-1}, red), arene (ν = 1130 cm^{-1}, green) and C-O-C from PEG (ν = 1008 cm^{-1}, orange).[1, 3-4]
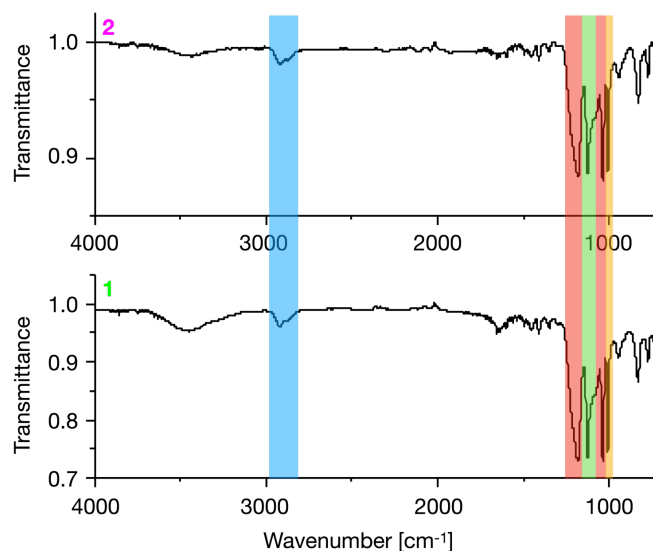
Figure S4. *FT-IR spectra of PSS$_{77}$-PEG$_{105}$ (1) and PSS$_{89}$-b-PEG$_{227}$-b-PSS$_{89}$ (2).*

Methods.

Sample preparation. The standard concentrations for experiments were set to 16 mM of the corresponding peptide AcF(RG)$_n$D-OH, 25 mM poly(styrene sulfonate) expressed in styrene sulfonate monomer units, either from homo- or blockcopolymers, 200 mM MES buffer at pH 5.3 and 50 mM EDC. All experiments were conducted at room temperature (25 °C). Stock solutions were prepared in MilliQ water and the pH adjusted to 5.3 for peptide solutions and the buffer. The concentrations of stock solutions were 2 M for EDC, 76 mM for the peptides, 500 mM for the MES buffer and 780 mM for homo- and block copolymer solutions, expressed in styrene sulfonate monomer units. The buffer concentration was sufficient to keep the pH value of all samples constant at pH 5.3 under all applied conditions and during refueling experiments. The reaction cycle was started by adding the desired volume of EDC stock into samples and mixing them by pipetting. The pH value for the reaction cycle was chosen to get a maximum turbidity response taking the strong pH dependence of the turbidity evolution into account (Fig. S5).
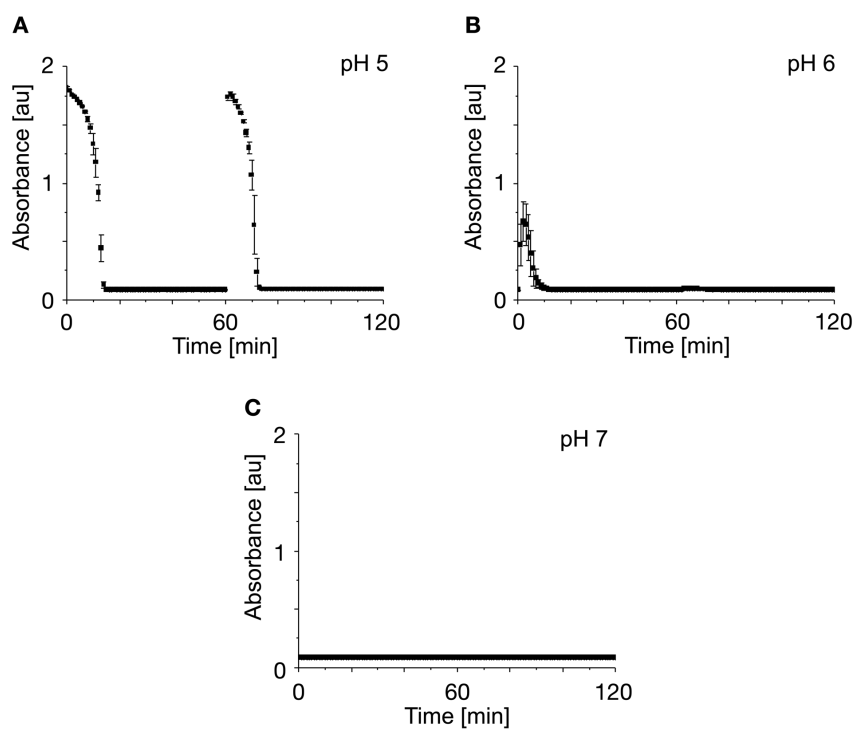
Figure S5. *The effect of different pH values on the reaction cycle (16 mM peptide **2**, 25 mM PSS, 200 mM MES at pH 5 - 7, 50 mM EDC). The samples were refuelled at t = 60 min with 50 mM EDC.*

Increasing amounts of EDC that are added to samples with standard concentrations of the other components (16 mM peptide **2**, 200 mM MES buffer at pH 5.3, 25 mM PSS expressed in monomer units) lead in general to longer turbidity cycle lifetimes, whereas smaller amounts of EDC lead to shorter turbidity cycles compared to 50 mM EDC (Fig. S6).
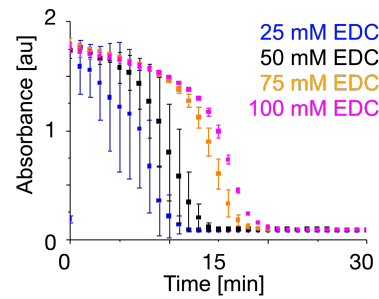
Fig. S6. Different amounts of EDC added to samples under standard conditions (16 mM peptide **2**, 200 mM MES at pH=5.3 and 25 mM PSS (17 kg/mol) expressed in monomer units).

Different peptide/EDC ratios were also tested either by adding different amounts of EDC to a fixed concentration of 16 mM peptide **2** (Fig. S7 A and B) or by adding 50 mM of EDC to different concentrations of peptide **2** (Fig. S7 C and D).
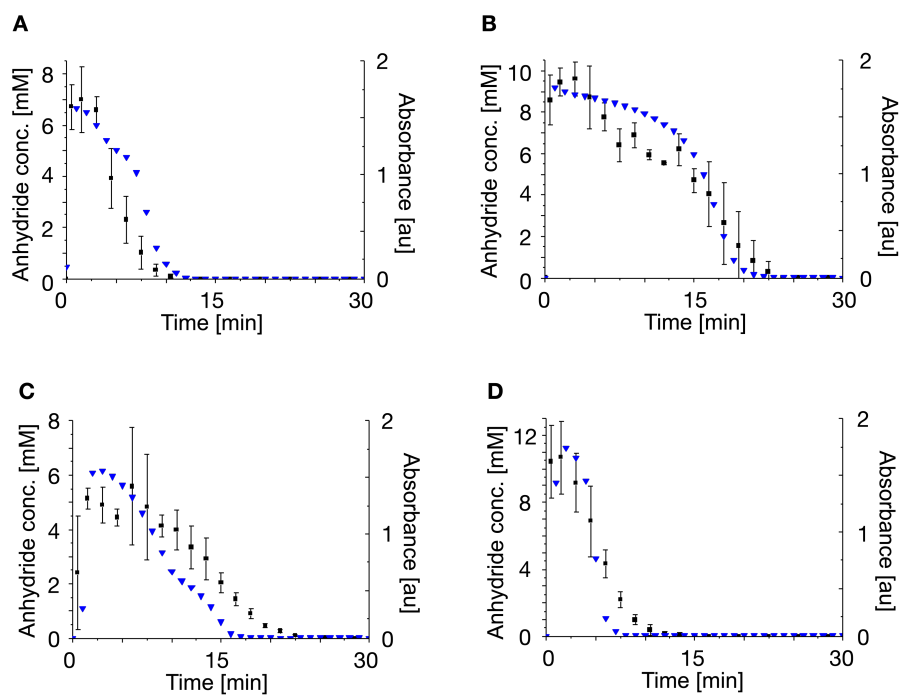
Fig. S7. *Different peptide/EDC ratios and their effect on the kinetics and droplet formation. **A)** 25 mM EDC added to 16 mM peptide **2**, 25 mM PSS expressed in monomer units and 200 mM MES buffer at pH 5.3. **B)** 100 mM EDC added to 16 mM peptide **2**, 25 mM PSS expressed*

in monomer units and 200 mM MES buffer at pH 5.3. **C***) 50 mM EDC were added to a sample containing 8 mM peptide* **2***, 25 mM PSS expressed in monomer units and 200 mM MES buffer at pH 5.3.* **D***) 50 mM EDC added to 32 mM peptide* **2***, 25 mM PSS expressed in monomer units and 200 mM MES buffer at pH 5.3. The blue traces show the turbidity data of the different sample conditions (right y-axis), the black traces (left y-axis) show the corresponding peptide anhydride concentrations that were obtained with the benzylamine quench method. Error bars are from triplicates (N=3).*

The effect of the urea byproduct of the reaction cycle, EDU, was also investigated. Increasing amounts of EDU lead to a decrease in turbidity and shorter cycle times. 250 mM EDU shut down complex coacervation upon EDC addition completely (Fig. S8 B). This amount of EDU equals five consecutive additions of 50 mM EDC and its full conversion into the urea product. EDU alone cannot induce coacervate droplet formation (Fig. S8 A).
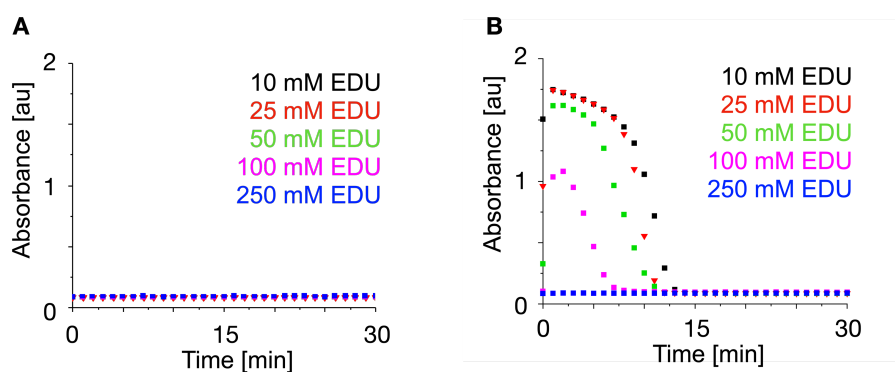
Figure S8. *The effect of different EDU (1-[3-(dimethylamino)propyl]-3-ethylurea) concentrations on samples (16 mM peptide* **2***, 25 mM PSS, 200 mM MES at pH 5.3) without (***A***) and after (***B***) the addition of 50 mM EDC. EDU alone does not induce complex coacervation.*

Kinetic model. A kinetic model in MATLAB was used to fit the peptide anhydride, EDC and precursor concentrations based on HPLC analysis. This model has been described in detail in our previous work.[5-6] The following rate constants were used.

$k_0 = 7.50 \cdot 10^{-5} \text{ s}^{-1}$
$k_1 = 1.80 \cdot 10^{-1} \text{ M}^{-1} \text{ s}^{-1}$
$k_2 = 5.40 \cdot 10^{-1} \text{ s}^{-1}$
$k_3 = 2.16 \cdot 10^{-1} \text{ s}^{-1}$
$k_4 = 0.85 \cdot 10^{-2} \text{ s}^{-1}$

The kinetic model is based on the following reactions.

Reaction 0 (k_0)**:** The direct hydrolysis of the carbodiimide to EDU. The first order rate constant k_0 was obtained by fitting the EDC consumption in 200 mM MES at pH 5.3 in the presence of 25 mM poly(styrene sulfonate) expressed in monomer units by HPLC analysis. The value of k_0 was determined to $7.50 \cdot 10^{-5}$ s^{-1}.
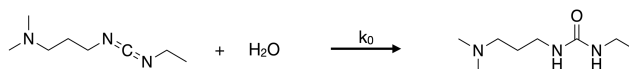

Reaction 1 (k_1)**:** The formation of the O-acylisourea intermediate by the reaction of the C-terminal aspartic acid with the carbodiimide fuel. The rate constant was obtained from fitting the EDC consumption from HPLC experiments. Its value was determined to $1.80 \cdot 10^{-1}$ M^{-1} s^{-1}.
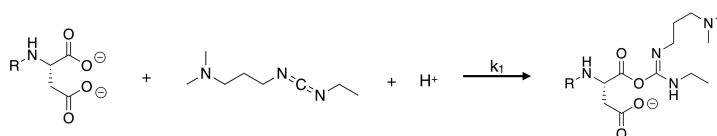

Reaction 2 (k_2)**:** The formation of the acid anhydride. The first-order rate constant k_2 could not be determined experimentally because the O-acylisourea species cannot be observed by HPLC analysis. It was set to be three times the value of k_1.
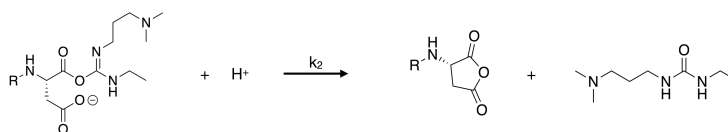
Reaction 3 (k_3)**:** The hydrolysis of the O-acylisourea (an unwanted side reaction). For the same reason as for k_2, the rate constant k_3 was set to a value of $1.2 \cdot k_1$.
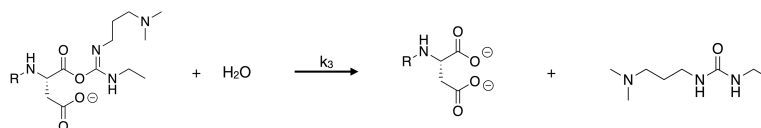
Reaction 4 (k_4)**:** The hydrolysis of the acid anhydride was fitted with the (pseudo)-first order rate constant $k_4 = 0.85 \cdot 10^{-2}$ s^{-1} from HPLC experiments with the benzylamine quench method.
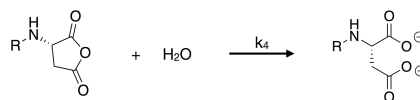
Overlaying the experimental peptide anhydride concentrations and the modelled concentrations shows a good fit (Fig. S15).

- 13 -

The anhydride concentrations of peptide **4** (AcF(RG)$_4$D-OH) could not be measured by analytical HPLC due to the high viscosity of the coacervate phase even after quenching (see Method Analytical HPLC).

Analytical HPLC. Analytical reversed-phase HPLC experiments were performed on a ThermoFisher Dionex Ultimate 3000 liquid chromatography setup (Dionex Ultimate pump, Dionex Ultimate Autosampler, Dionex Ultimate 3000 RS Variable Wavelength Detector). A linear gradient from 2% to 98% ACN and MilliQ water, both with 0.1% TFA, was used for analyte separation on a ThermoScientific Hypersil GOLD column (250 x 4.6 mm, 5 µm particle size). The standard detection wavelengths were set to 220 and 254 nm. The data was collected and analyzed with the Chromeleon 7 Chromatography Data System Software (Version 7.2 SR4).

For quantification of the peptide anhydrides during the reaction cycle, a quenching method with benzylamine was used.[7] Specifically, after the reaction cycle was started by the addition of EDC stock, 20 µL of the corresponding sample were pipetted on 10 µL of a 900 mM benzylamine solution in MilliQ water inside of a 200 µL HPLC vial inlet and mixed by pipetting and vortexing. The turbidity vanished completely or was reduced drastically during the quenching and mixing process. Additionally, the pH of the quenched mixtures increased instantly to 9.6 which also inhibits further hydrolysis of the remaining EDC during the analysis and stops the reaction cycle. Separation was achieved by applying the abovementioned standard method for analytical HPLC experiments. The peptide anhydride concentrations were quantified from the corresponding peptide-benzylamide peaks (Fig. S9).
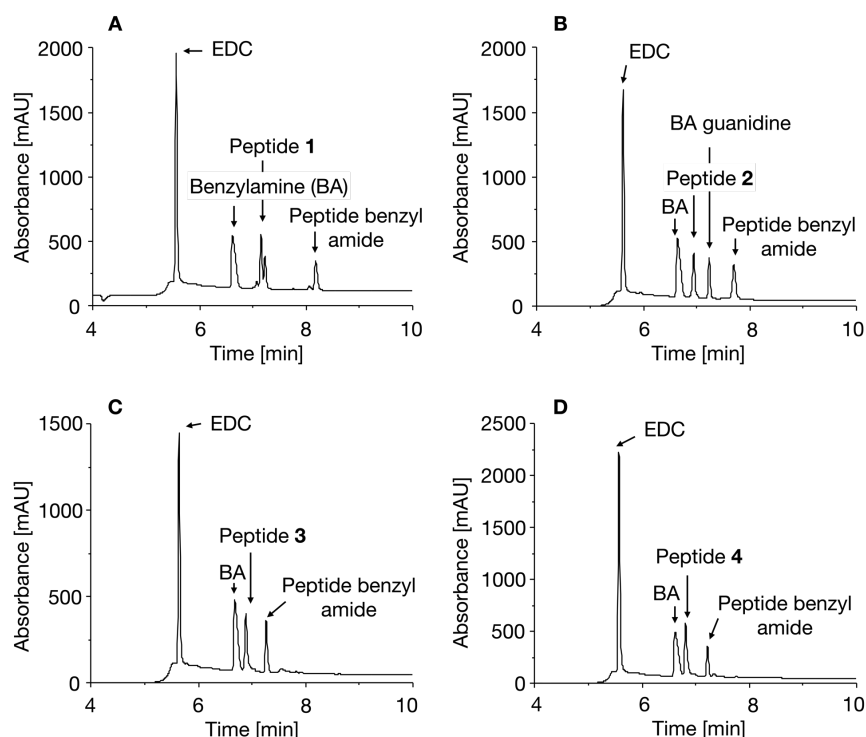
Figure S9. *Exemplary chromatograms of samples with the peptides **1-4** after quenching with benzylamine (see Analytical HPLC Method). The samples contained 16 mM of the corresponding peptide, 25 mM PSS expressed in monomer units and 200 mM MES buffer at pH 5.3 before 50 mM of EDC were added (t = 0). These exemplary chromatograms were measured at the timepoint t = 0.5 min after the addition of EDC and after the quenching with 300 mM benzylamine. **A**) AcF(RG)D-OH (peptide **1**) **B**) AcF(RG)$_2$D-OH (peptide **2**) **C**) AcF(RG)$_3$D-OH (peptide **3**) **D**) AcF(RG)$_4$D-OH (peptide **4**).*

Critical Coacervation Concentration (CCC) Determination. The critical coacervation concentrations for peptide anhydrides were determined by adding various amounts of EDC stock solution to samples with fixed concentrations of all other components (16 mM peptide, 25 mM poly(styrene sulfonate) and 200 mM MES pH 5.3). Visible turbidity indicated the presence of coacervate droplets. A period of up to 1 minute was taken into account to wait for the expected maximum in peptide anhydride concentration after EDC addition. The peptide anhydride concentrations were calculated by the maximum anhydride concentration from the added amount of EDC with our kinetic model. For AcF(RG)$_4$D-OH, AcF(RG)$_3$N-NH$_2$ and AcF(RG)$_3$D-OH, the critical coacervation concentrations without EDC were determined by

- 15 -

increasing the peptide concentration in samples containing 25 mM PSS and 200 mM MES (pH 5.3) gradually.

UV/Vis Spectroscopy/ Turbidity Measurements. UV/Vis measurements were performed on a Multiskan GO Microplate Spectrophotometer from ThermoScientific. The samples were prepared directly in a non-treated tissue culture 96-well plate with a flat bottom from Falcon. 100 μL sample volume were prepared per well. The temperature was set to 25 °C. The absorbance at 600 nm was measured every minute and was taken as a measure for turbidity. Data was acquired and processed with the SkanIt Software (Version 6.0.1) from ThermoScientific.

Absorbance Data Transformation and Correlation to the Anhydride Concentrations.

We transformed the turbidity data from plate-reader experiments in order to compensate for the non-linear regimes. Experiments with suspensions of latex-beads of 0.5, 1.0 and 2.0 μm in diameter showed that the absorbance scaled in a logarithmic manner (Fig. S10 A). We linearized the absorbance by transforming it into $1/T$ with the transmittance $T = I/I_0$ by calculating it from the corresponding absorbance value by $1/T=10^{Absorbance}$ following Beer's Law and subsequent normalization to the maxima. Indeed, the normalized, reciprocal transmittance scales linearly with the total volume of the latex beads in suspension as a concentration measure (Fig. S10 B).
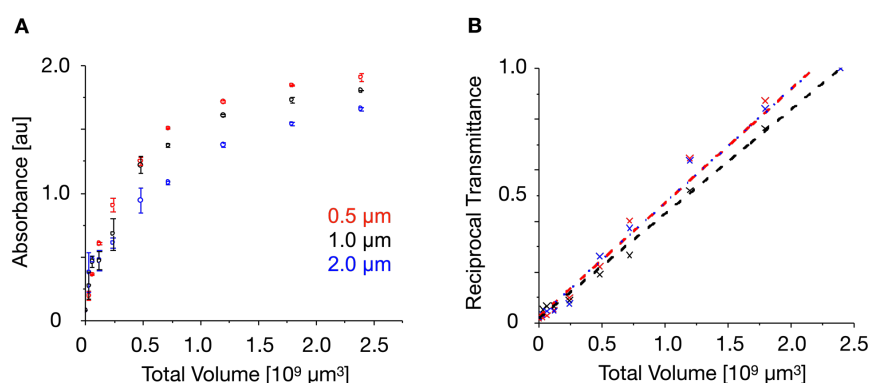

Figure S10. A) *Absorbance traces of latex bead suspensions with beads of different sizes (0.5, 1.0 and 2.0 μm) for different bead concentrations expressed in total volume of latex beads in suspension. Error bars are the standard deviations from triplicates (N=3)* **B**) *The normalized reciprocal transmittance for different latex bead sizes and concentrations with linear fitting.*

- 16 -

The transformation of absorbance data was applied to all turbidity data of the complex coacervate-based assemblies. The normalized, reciprocal transmittance was compared to the evolution of peptide anhydride concentrations from our kinetic model above the corresponding CCC values.

Confocal Fluorescence Microscopy. Confocal fluorescence microscopy was performed on a Leica TCS SP8 confocal microscope using a 63x water immersion objective. Samples were prepared as described above and transferred into micro-well plates (ibidi, µ-Slide Angiogenesis Glass Bottom), but with 0.2 µM Sulforhodamine B as the fluorescent dye. Samples were excited with 552 nm and imaged at 565-635 nm. Measurements were performed at 24 ºC.

Coating Procedure for Fluorescence Recovery After Photobleaching (FRAP) experiments. In order to minimize wetting of the coacervate droplets on the glass surface, a modified coating procedure of Spoelstra and coworkers was applied.[8] Micro-well plates (ibidi, µ-Slide Angiogenesis Glass Bottom) were washed with soap water, MQ water and dried over air pressure. Then, the slide was plasma cleaned for 3 minutes followed by the addition of 50 µL of a freshly prepared 3% poly(vinyl) alcohol (PVA) solution in MQ water to each well. After 15 minutes, the PVA solution was removed, and the wells were thoroughly washed with MQ water and dried with pressurized air. Finally, the wells were placed into an oven at 80 °C for 30 minutes. The obtained coated wells were stored at room temperature and consumed within a week.

Fluorescence Recovery After Photobleaching (FRAP) experiments. FRAP experiments were performed on a Leica TCS SP8 confocal microscope using a 63x water immersion objective. Samples (25 µL total volume) were prepared as described above in PVA-coated micro-well plates (ibidi, µ-Slide Angiogenesis Glass Bottom) with 500 nM (7-Nitrobenzo-2-oxa-1,3-diazol-4-yl)-GRGRGD-OH (NBD-G(RG)$_2$D-OH) as the fluorescently labelled peptide. The FRAP experiments were started 2 minutes after EDC addition to obtain aggregates of sufficient size. Samples were bleached and excited with 488 nm laser and imaged at 498 - 630 nm with an image size of 256x100 pixels. The region of interest (ROI) was set to a radius of 0.8 µm. 5 pre-bleaches (every 0.18 s) were acquired followed by 5 bleaching pulses (every 0.18 seconds as well). After that, fluorescence recovery was tracked every 0.18 – 0.5 seconds with a total of up to 193 images. The raw data was analyzed with ImageJ and normalized by double normalization following literature.8 The

- 17 -

data was fitted to the first-order exponential equation (1) with the spot size and the diffusion coefficient in order to obtain the diffusion coefficient and half-time recovery.[9]

$$F(t) = F_{\infty} \cdot \exp\left[-\frac{2}{1 + \left(\frac{8tD}{a^2}\right)}\right] + C \qquad (1)$$

The constant C was added to account for the y-intercept. Figure S20 shows the corresponding data.

NBD-GRGRGD-OH was synthesized by preparing Fmoc-GRGRGD-OH by the abovementioned standard protocol for microwave-assisted, automated solid phase peptide synthesis. The resin-bound NBD-GRGRGD-OH was then deprotected by reacting the resin with 3 mL of a 20 v/v % solution of piperidine in DMF for 20 minutes at room temperature. The success of this deprotection step was verified with a Kaiser's test. After rinsing the resin three times with DMF and three times with DCM, 200 mg of 4-chloro-7-nitrobenzofurazan (NBD-Cl) and 100 µL of diisopropylethylamine (DIPEA) were added in 8 mL of DMF and reacted with the resin at room temperature for four hours. The crude product was purified by preparative HPLC after global deprotection and cleavage from the resin as described in the automated solid phase peptide synthesis section. The purified product was analyzed by analytical HPLC (r.t. = 7.15 min) and ^{1}H-NMR spectroscopy in DMSO-d_6 (Fig. S11).
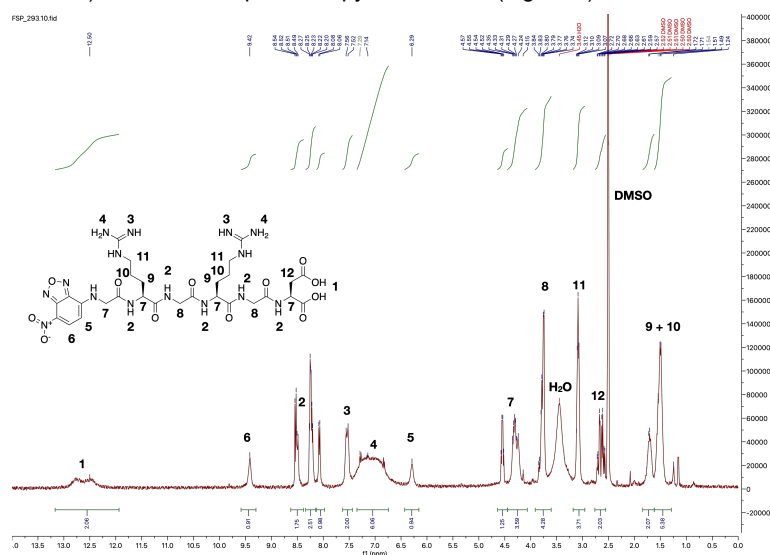

Figure S11. ^{1}H-NMR spectrum of NBD-GRGRGD-OH in DMSO-d_6.

Bright-field Microscopy. Bright-field microscopy was performed on an IM-3LD microscope from OPTIKA. A circular chamber was built with medium viscosity silicone grease on the glass slide. Up to 15 µL of a sample were pipetted into the chamber and it was sealed by pressing a circular cover glass gently on top of it. The 60x objective was used for all experiments.

Cryo-TEM. 100 µL samples were prepared by the standard sample preparation as described above. After the addition of EDC, aliquots of those samples were taken at different timepoints. CryoTEM imaging was performed on a Tecnai Spirit microscope (FEI/Thermo Fisher) operating at 120 kV. Recording of the images was done in a low-dose mode on a CCD camera. Cu-grids (C-flat, 2.0 µm hole size, 2.0 µm hole spacing, 400 mesh) were glow discharged for 90 s at 45 mA and $3 \cdot 10^{-2}$ mbar prior to use. 5 µL of a sample is pipetted on Cu-grids in a FEI/Thermo Fisher Vitrobot at a temperature of 22°C and a relative humidity of 100%. The blotting conditions were set to a waiting time of 30 s, a blot time of 2.5 s and a blot force of - 1. Grids were then plunged into liquid ethane (pre-cooled with liquid nitrogen). The grids were transferred and stored in liquid nitrogen until they were analyzed. They were put into a Gatan cryo-transfer-specimen holder for imaging. The specimen temperature was kept at -170 °C.

Dynamic Light Scattering (DLS). DLS measurements were perfomed on a Zetasizer Nano ZS from Malvern Panalytical. The laser wavelength was 633 nm. Samples were analyzed in disposable polystyrene cuvettes with a final volume of 500 µL. Every data point consists of 6 consecutive runs of 10 seconds each.

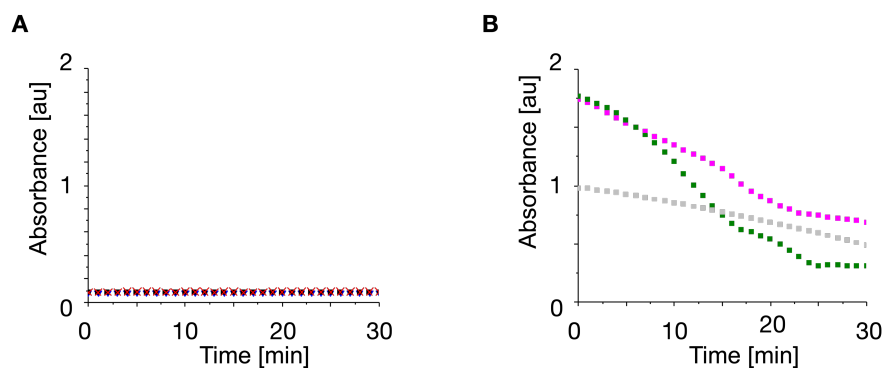**Supporting Figures for the Main Text.**

Figure S12. *(A) Turbidity traces (Absorbance at 600 nm) for 16 mM AcFRGD-OH (peptide **1**), 25 mM of 1000 kg/mol PSS expressed in monomer units with different amounts of EDC (black: 50 mM, blue: 100 mM, red: 200 mM) and 200 mM MES buffer at pH 5.3. AcFRGD-OH also does not form coacervate droplets with all other PSS lengths between 4.3 kg/mol and 151 kg/mol with up to 200 mM of EDC. (**B**) 16 mM of AcF(RG)$_4$D-OH (peptide **4**) with 25 mM PSS of different chain lengths (grey: 1000 kg/mol, green: 32 kg/mol, magenta: 4.3 kg/mol), 200 mM MES buffer at pH 5.3 and 50 mM EDC. The absorbance value of the sample with 1000 kg/mol PSS starts a lower level because the very dense coacervate phase agglomerated instantly and did not lead to uniform turbidity in the sample. The decline of turbidity is caused by sedimentation. Peptide **4** did not form reversible coacervates with any PSS size between 4.3 kg/mol and 1000 kg/mol.*
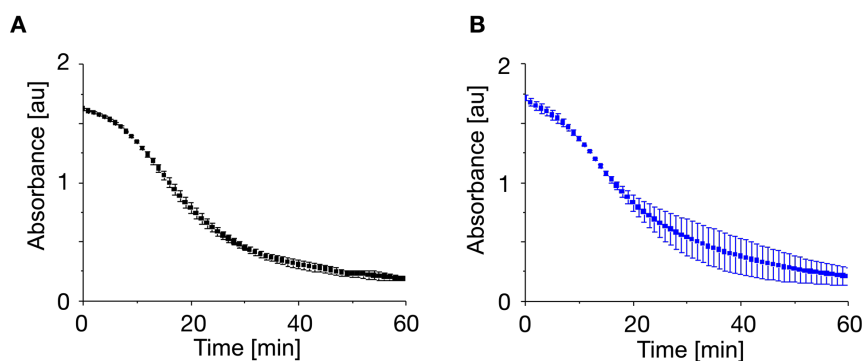

Figure S13. *Turbidity (Absorbance at 600 nm) for 16 mM AcF(RG)$_4$D-OH, 25 mM PSS (17 kg/mol) expressed in monomer units and 200 mM MES buffer at pH 5.3 with (**A**) and without 50 mM EDC (**B**). Error bars stem from triplicates (N=3).*
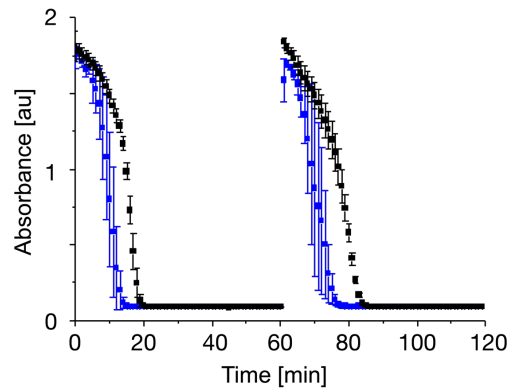
- 20 -

Figure S14. *Turbidity traces (absorbance at 600 nm) of samples with 16 mM AcF(RG)$_2$D-OH (blue curve) and AcF(RG)$_3$D-OH (black curve), 25 mM PSS (17 kg/mol) expressed in monomer units, 50 mM EDC and 200 mM MES buffer at pH 5.3. Error bars are from triplicates (N=3). Refueling was performed with 50 mM EDC at t = 60 min.*
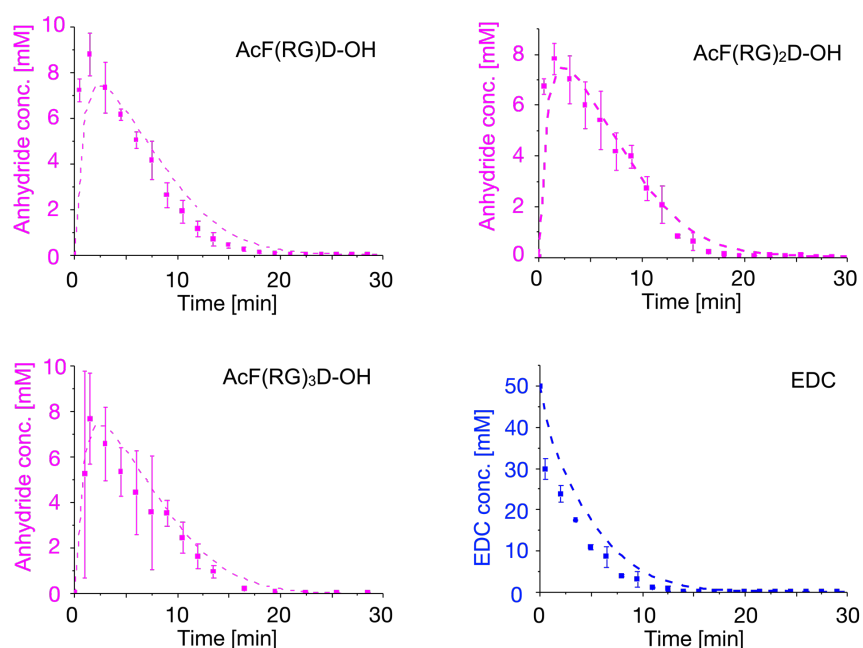
Figure S15. *Overlay of the anhydride concentrations of peptide **1**, **2** and **3** after the addition of 50 mM EDC and the corresponding EDC consumption. The concentrations of the other components were 25 mM PSS (17 kg/mol) expressed in styrene sulfonate units and 200 mM MES buffer at pH 5.3. HPLC analysis was performed after quenching with benzylamine (individual data points, error bars are from triplicates (N=3)) and the traces of peptides anhydrides and the EDC consumption that were calculated from our kinetic model (dashed lines, see Methods for details).*
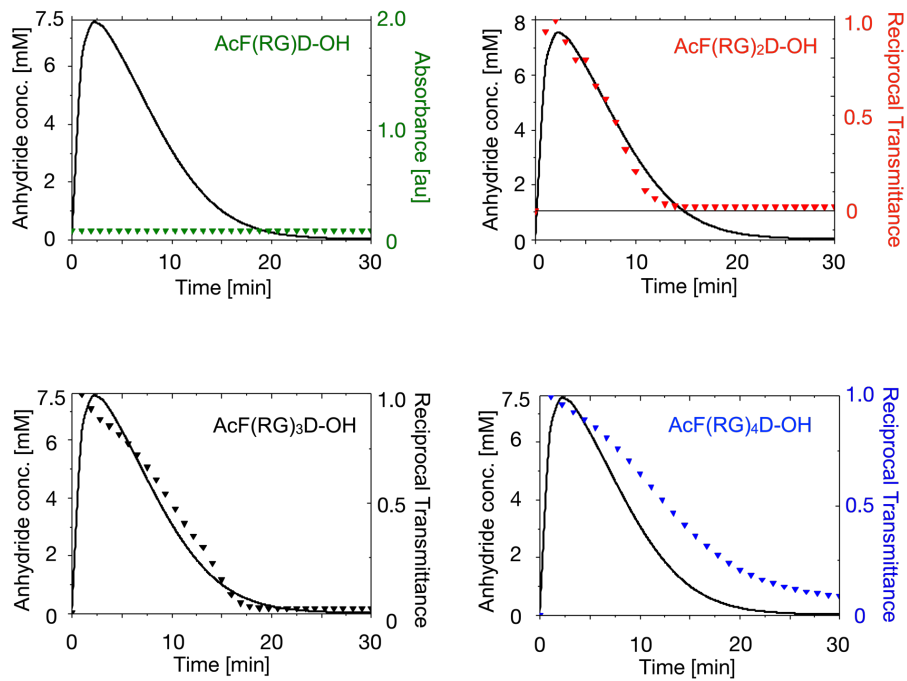
Figure S16. *Overlay of the anhydride concentrations above the CCC during the reaction cycle and the corresponding normalized reciprocal transmittance (see Methods for calculation details) under sample standard conditions (16 mM peptide, 200 mM MES pH 5.3, 25 mM PSS expressed in monomer units and 50 mM EDC) with 17 kg/mol PSS. The reciprocal transmittance traces for the different peptides are depicted as triangles. For AcF(RG)D-OH, the absorbance trace at 600 nm is shown as the measure for turbidity since no turbidity above the blank value was observed.*
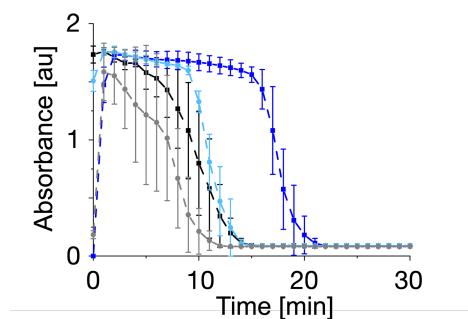
Figure S17. *Turbidity traces for different amounts of EDC that were added to samples with 17 (black and grey trace) and 1000 kg/mol PSS (Dark and light blue traces). The samples contained 16 mM of peptide **2**, 200 mM MES at pH 5.3 and 25 mM of the corresponding PSS strand length, expressed in monomer units. The longer cycle lifetimes of longer PSS strands (blue traces) are also present for lower amounts of EDC but can be compensated by a reduction of the carbodiimide fuel amount. Dark Blue: 50 mM EDC were added to a 1000 kg/mol PSS sample. Light Blue: 25 mM EDC were added to a 1000 kg/mol PSS sample.*
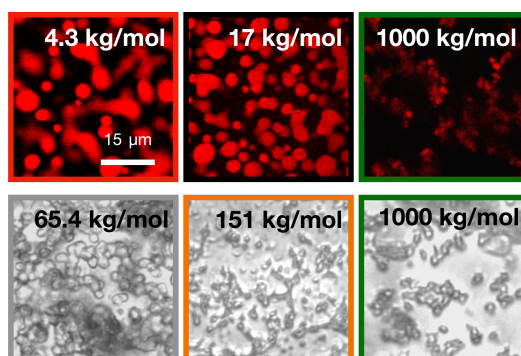
Figure S18. *Sediments of coacervate samples with 4.3, 17 or 1000 kg/mol under a confocal laser microscope with sulforhodamine as the fluorescent dye (the first three micrograph from left to right) with standard concentrations (16 mM AcF(RG)$_2$D-OH, 200 mM MES pH 5.3, 25 mM PSS expressed in monomer units and 50 mM EDC). Bright-field micrographs of coacervate sediments for 65.4, 151 and 1000 kg/mol PSS (bottom row).*
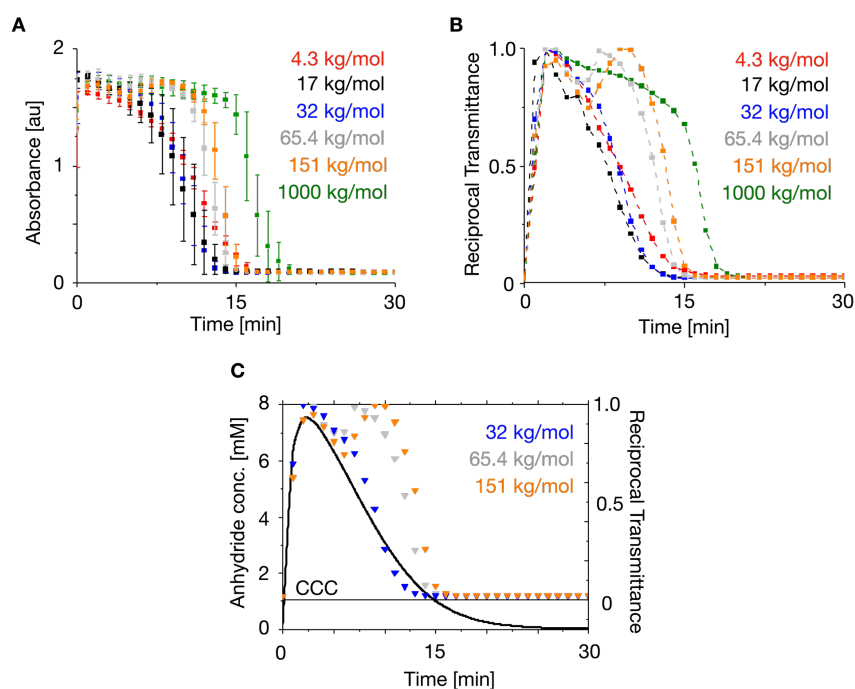
Figure S19. *A) Absorbance evolution for different PSS lengths with peptide* **2** *during the reaction cycle under standard conditions (16 mM AcF(RG)₂D-OH, 200 mM MES pH 5.3, 25 mM PSS expressed in monomer units and 50 mM EDC) B) The corresponding normalized reciprocal transmittance C) Overlay of the reciprocal transmittance for 32, 65.4 and 151 kg/mol PSS with the anhydride concentration evolution of peptide* **2** *above the CCC of 1.02 mM. The reciprocal transmittance traces for different polymer lengths are depicted as triangles.*
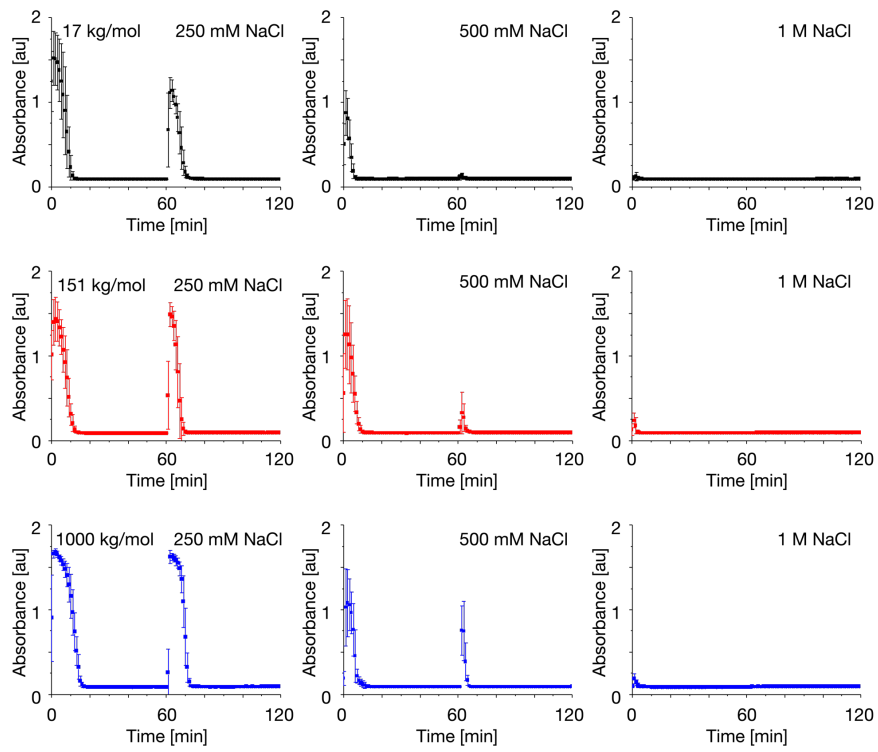
Figure S20. *The influence of different NaCl concentrations on the turbidity evolution of coacervate samples with 17(black), 151(red) and 1000 kg/mol (blue) PSS (25 mM expressed in monomer units). The other concentrations were set to 16 mM AcF(RG)$_2$D-OH, 200 mM MES buffer at pH 5.3 and 50 mM EDC. The samples were refueled with 50 mM EDC at t = 60 min. Errors bars stem from triplicates (N=3).*
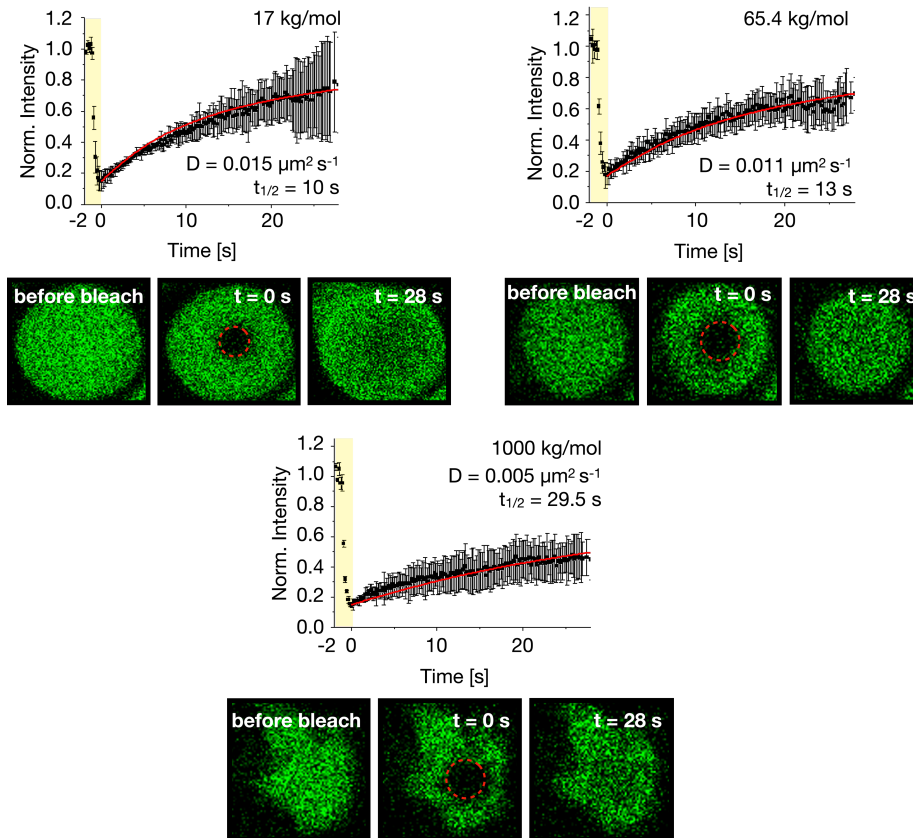
Figure S21. *FRAP experiments for different poly(styrene sulfonate) lengths for standard sample conditions (16 mM AcF(RG)₂D-OH, 200 mM MES pH 5.3, 25 mM PSS expressed in monomer units and 50 mM EDC). 500 nM of NBD-GRGRGD-OH were used as a fluorescently labelled peptide. The highlighted region shows the bleaching phase at the beginning of the FRAP experiments. The ROIs are marked in red circles. The timepoint t = 0 s is the point at which the bleaching was stopped and fluorescence recovery was followed. The fitting functions of the fluorescence recovery are shown in red. Error bars stem from triplicates (N=3).*
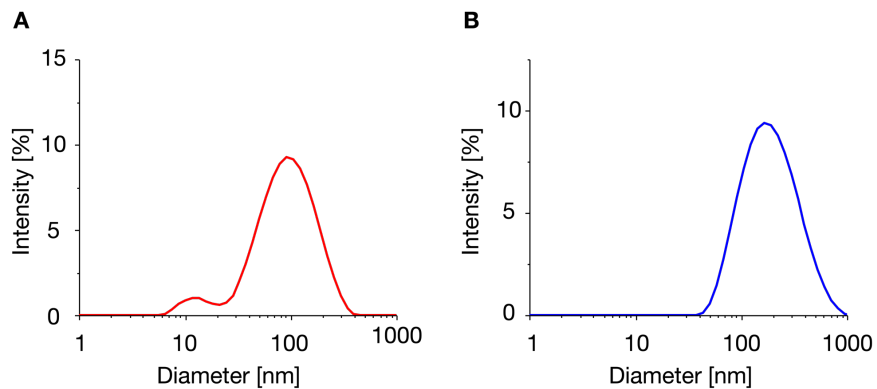
Figure S22. *DLS data of PSS-PEG **A**) and PSS-PEG-PSS **B**) samples 4 minutes into the reaction cycle with standard concentrations (16 mM AcF(RG)$_2$D-OH, 200 mM MES pH 5.3, 25 mM PSS expressed in monomer units and 50 mM EDC).*
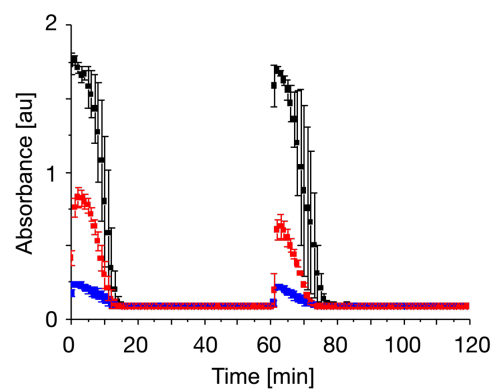

Figure S23. *Refueling of Blockcopolymer and PSS-Homopolymer samples with 50 mM EDC at t = 60 min. Black: PSS Homopolymer 17 kg/mol. Red: PSS-PEG-PSS 47.5 kg/mol. Blue: PSS-PEG 21 kg/mol. All conditions were set to 25 mM PSS expressed in monomer units, 16 mM AcF(RG)$_2$D-OH, 200 mM MES at pH 5.3 and 50 mM EDC for the first increase in turbidity. Error bars stem from triplicates (N=3).*

- 29 -

Supporting References

(1) Peng, Z.; Wang, D.; Liu, X.; Tong, Z., RAFT synthesis of a water-soluble triblock copolymer of poly(styrenesulfonate)-b-poly(ethylene glycol)-b-poly(styrenesulfonate) using a macromolecular chain transfer agent in aqueous solution. *Journal of Polymer Science Part A: Polymer Chemistry* **2007,** *45* (16), 3698-3706.

(2) Ting, J. M.; Wu, H.; Herzog-Arbeitman, A.; Srivastava, S.; Tirrell, M. V., Synthesis and Assembly of Designer Styrenic Diblock Polyelectrolytes. *ACS Macro Letters* **2018,** *7* (6), 726-733.

(3) Shameli, K.; Ahmad, M. B.; Jazayeri, S. D.; Sedaghat, S.; Shabanzadeh, P.; Jahangirian, H.; Mahdavi, M.; Abdollahi, Y., Synthesis and characterization of polyethylene glycol mediated silver nanoparticles by the green method. *Int. J. Mol. Sci.* **2012,** *13* (6), 6639-50.

(4) Yang, J. C.; Jablonsky, M. J.; Mays, J. W., NMR and FT-IR studies of sulfonated styrene-based homopolymers and copolymers. *Polymer* **2002,** *43* (19), 5125-5132.

(5) Donau, C.; Spath, F.; Sosson, M.; Kriebisch, B. A. K.; Schnitter, F.; Tena-Solsona, M.; Kang, H. S.; Salibi, E.; Sattler, M.; Mutschler, H.; Boekhoven, J., Active coacervate droplets as a model for membraneless organelles and protocells. *Nat. Commun.* **2020,** *11* (1), 5167.

(6) Tena-Solsona, M.; Riess, B.; Grotsch, R. K.; Lohrer, F. C.; Wanzke, C.; Kasdorf, B.; Bausch, A. R.; Muller-Buschbaum, P.; Lieleg, O.; Boekhoven, J., Non-equilibrium dissipative supramolecular materials with a tunable lifetime. *Nat. Commun.* **2017,** *8*, 15895.

(7) Schnitter, F.; Boekhoven, J., A Method to Quench Carbodiimide-Fueled Self-Assembly. *ChemSystemsChem* **2021,** *3* (1), e2000037.

(8) Spoelstra, W. K.; van der Sluis, E. O.; Dogterom, M.; Reese, L., Nonspherical Coacervate Shapes in an Enzyme-Driven Active System. *Langmuir* **2020,** *36* (8), 1956-1964.

(9) Kayitmazer, A. B.; Bohidar, H. B.; Mattison, K. W.; Bose, A.; Sarkar, J.; Hashidzume, A.; Russo, P. S.; Jaeger, W.; Dubin, P. L., Mesophase separation and probe dynamics in protein-polyelectrolyte coacervates. *Soft Matter* **2007,** *3* (8), 1064-1076.

- 30 -

5. The Role of Chemically Innocent Polyanions in Active, Chemically Fueled Complex Coacervate Droplets

Abstract

In the previous chapter, special attention was paid to the structure of the cationic peptides to modify active complex coacervates. However, the first results on polymer length influences and the possibility of forming coacervate core micelles with block copolymers have already suggested that the polymer components offer many opportunities to modify chemically fueled complex coacervates further. In this work, polyanions with different electrolyte moieties are introduced and compared, namely poly(styrene sulfonate), poly(vinyl sulfonate) and poly(vinyl phosphonate). Systematic studies showed that strong peptide-polyanion interactions lead to delayed dissolution of active coacervates because they hinder peptides from leaving the coacervate phase. This effect could be reversed by adding salt. A comparison of diblock copolymers further showed that this hindered diffusion only influences micrometer-sized assemblies and that coacervate core micelles are unaffected. In summary, I found that the polymeric components in chemically fueled complex coacervation have a decisive influence without participating in the reaction cycle themselves.

This work has been published:

Systems Chemistry

The Role of Chemically Innocent Polyanions in Active, Chemically Fueled Complex Coacervate Droplets

Fabian Späth, Anton S. Maier, Michele Stasi, Alexander M. Bergmann, Kerstin Halama, Monika Wenisch, Bernhard Rieger, and Job Boekhoven*

Abstract: Complex coacervation describes the liquid-liquid phase separation of oppositely charged polymers. Active coacervates are droplets in which one of the electrolyte's affinity is regulated by chemical reactions. These droplets are particularly interesting because they are tightly regulated by reaction kinetics. For example, they serve as a model for membraneless organelles that are also often regulated by biochemical transformations such as post-translational modifications. They are also a great protocell model or could be used to synthesize life–they spontaneously emerge in response to reagents, compete, and decay when all nutrients have been consumed. However, the role of the unreactive building blocks, e.g., the polymeric compounds, is poorly understood. Here, we show the important role of the chemically innocent, unreactive polyanion of our chemically fueled coacervation droplets. We show that the polyanion drastically influences the resulting droplets′ life cycle without influencing the chemical reaction cycle–either they are very dynamic or have a delayed dissolution. Additionally, we derive a mechanistic understanding of our observations and show how additives and rational polymer design help to create the desired coacervate emulsion life cycles.

Introduction

Liquid-liquid phase separation of oppositely charged species is a process that is omnipresent in biological systems yielding droplets that are present in cells[1] referred to as biomolecular condensates. Their properties and aging phenomena are often regulated by biochemical non-equilibrium reactions,[2] resulting in behavior unparalleled by their in-equilibrium counterparts.[3] Yet, the underlying mechanisms remain poorly understood.[4] Besides, theoretical work showed that droplets formed by materials subject to non-equilibrium chemical reaction cycles—and thereby a constant turnover—can show life-like behavior like self-division, regulated growth, or suppressed Ostwald ripening.[5] Such coacervate droplets have also been recognized as potential protocells that functioned as the first containers to concentrate reagents at the early stages of the emergence of life.[6]

Thus, synthetic models for droplets regulated by chemical reaction cycles can unveil new behavior and elucidate their dynamic properties.[7] Such chemically regulated phase-separated droplets can also help us understand their role as protocells at the origin of life or be a step toward synthetic life. In addition to a growing number of examples of carbodiimide fueled assemblies[8] and motors,[9] we recently introduced a chemically fueled reaction cycle that regulates molecular assembly,[10] DNA-duplex formation,[11] and complex coacervation of a cationic peptide with polyanions.[12] The cycle activates a peptide by converting two negatively charged carboxylates into their corresponding anhydride by a carbodiimide activation reaction (Scheme 1).[12a,b] In this context, we refer to the carbodiimide as a fuel as it is converted in the activation reaction. The activated peptide is short-lived as the anhydride spontaneously deactivates through hydrolysis, yielding the original peptide. The zwitterionic peptide has an overall charge of $+1$. It only weakly interacts with polyanions, whereas the short-lived activated peptide is cationic with an overall charge of $+3$ and can thus bind polyanions to form droplets. Our platform serves as a model system for synthetic protocells that emerge, divide, and decay at the expense of simple chemical fuel.[12a] Besides, new non-equilibrium dynamic behavior in these chemically fueled emulsions, including the formation of spherical shells as a non-equilibrium steady state morphology, can be observed.[12c]

In these chemically fueled coacervates, the polyanion is a passive component. However, its influence on the droplet's behavior is seemingly overlooked and scarcely investigated. Understanding polyanion's role enables the creation of systems that are fully dynamic, metastable, or even in an arrested state without the need to change the kinetics of the reaction network. Such studies would aid protocell studies, for example, by understanding how the lifetime of a droplet varies with the polyanion nature. Besides, such studies help

[*] F. Späth, M. Stasi, A. M. Bergmann, M. Wenisch, J. Boekhoven
Department of Chemistry
School of Natural Sciences, Technical University of Munich
Lichtenbergstrasse 4, 85748 Garching (Germany)
E-mail: job.boekhoven@tum.de

A. S. Maier, K. Halama, B. Rieger
WACKER-Chair of Macromolecular Chemistry
Catalysis Research Center, Technical University of Munich
Lichtenbergstrasse 4, 85748 Garching (Germany)

Research Articles
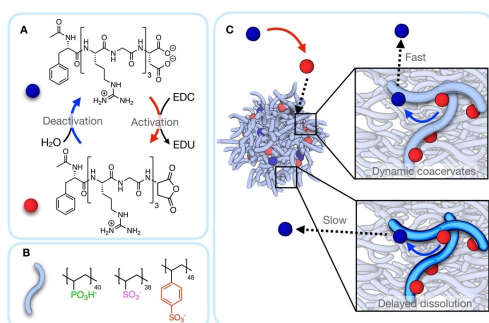
Scheme 1. Polyanions and peptides for chemically fueled complex coacervation. A. The reaction of the carbodiimide EDC with an aspartic acid residue on the C-terminus of a peptide with cationic arginine units reversibly screens two negative charges. This activated peptide—the aspartic anhydride peptide—can complex with polyanions (B) to form complex coacervate droplets (C). The constant turnover of the hydrolytically unstable anhydride in aqueous buffer results in a limited lifetime of the droplets. In this work, the polyanions PSS (red), PVS (magenta), and PVPA (green) are combined with the peptide AcF-(RG)$_3$D–OH and the fuel and the properties of the resulting coacervates are compared. The polyanion choice directly affects the droplet dissolution whenever the precursor-polyanion interactions are too strong.

develop dynamic droplets whose properties like size and ripening dynamics are controlled by reaction kinetics.

In this work, we systematically investigate the role of the polyanionic components in our chemically fueled coacervate droplets and elucidate how they affect the droplet's life cycle. We applied three different polyanions and investigated the role of the peptide-polymer interaction in detail, showing how to tune it systematically to control the outcome of the coacervation reaction cycle.

Results and Discussion

The chemically fueled complex coacervate-based droplets we study here are based on a previously published peptide design AcF(RG)$_3$D–OH in which three arginine-glycine repeat units provide three cationic residues. The C-terminal aspartic acid partly negates these charges resulting in a zwitterionic peptide with an overall charge of +1 (Scheme 1A). The peptide can be chemically activated for coacervation by reacting with the carbodiimide EDC (1-ethyl-3-(3-dimethylaminopropyl) carbodiimide, fuel). Upon activation, the fuel converts the C-terminal aspartic acid into its corresponding anhydride. The activation negates the two anionic carboxylates and thereby increases its overall charge to +3, which increases its interaction strength with polyanions.[12b] A deactivation reaction reverts the activated peptide to the original peptide through anhydride hydrolysis. The half-life of the activated peptide is about 82 seconds. Thus, upon application of fuel to the peptide, a

reaction cycle commences that transiently activates peptides and increases their ability to bind polyanions.

We combine this peptide design with three types of polyanions of comparable size, i.e., poly(styrene sulfonate) (PSS$_{48}$), poly(vinyl sulfonate) (PVS$_{38}$), and poly(vinyl phosphonic acid) (PVPA$_{40}$) (Scheme 1B). PSS and PVS are commercially available, whereas PVPA was synthesized by REM-GTP (Rare Earth Metal-Mediated Group-Transfer Polymerization) of diethyl vinyl phosphonate followed by deprotection of the phosphonate diester (see Supporting Information for details).[13] All of these polyanions, also PVPA, comprise monoacidic units under our working condition of pH 5.3.[14] The minor differences in their chain length are not expected to influence the coacervate droplet properties.[12b]

We combined the peptide with each polyanion, and we monitored the evolution of turbidity in response to the chemical fuel. In this context, turbidity is a measure of the presence of the droplets. The overall lifetime of the population of droplets produced can also be determined with such experiments. We used 23 mM peptide, 15 mM EDC, and 4.1 mM polyanion expressed as the concentration of monomers in 200 mM MES buffered at pH 5.3. Despite the very similar compositions of the experiments, we found the turbidity evolved differently. The lifetimes of the population of droplets were 8 minutes for PVPA, 13 minutes for PVS, and 17 minutes in the case of PSS (Figure 1A). These observations suggest that the polyanion, which should not affect the reaction cycle, plays an important role in the behavior of the droplets.

We determined whether the polyanion influenced the chemical reaction cycle that governs these properties. We
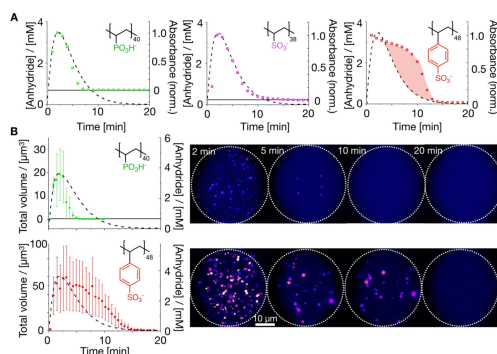
Figure 1. The different polymers affect the droplet lifetimes. A. Overlays of the turbidity traces above the CCC thresholds of different polyanions (PVPA$_{40}$ green, PVS$_{38}$ magenta, PSS$_{48}$ red) with the respective anhydride evolution over time (23 mM AcF(RG)$_3$D–OH, 15 mM EDC, 4.1 mM polyanion expressed in monomer units, 200 mM MES buffer at pH 5.3). B. Microfluidic analysis of the total coacervate volume evolution for PVPA$_{40}$ (green) and PSS$_{48}$ (red) with exemplary images of the droplets over time (PVPA upper row, PSS below). Sulforhodamine B was used as a fluorescent dye at a concentration of 0.2 μM for PSS and 0.6 μM for PVPA samples.

first measured the kinetics of the reaction cycle by HPLC in the presence of the three polyanions. We found that the different polyanions had no significant effect on the kinetics of the reaction cycle (Figure S1). For all polyanions, the EDC was converted in 18 minutes. We used a kinetic model to fit the evolution of the concentration of fuel and activated peptide.[12b] With that kinetic model, we could determine that the activated peptide had a half-life of 82 seconds independent of the polyanion. The finding that the presence of droplets or their composition does not affect the kinetics of the reaction cycle is in line with previously published data.[12a,e] Put differently, the polyanion is seemingly innocent, i.e., it does not affect the chemical reaction cycle which regulates the droplets. Thus, any influence of the polyanion on the behavior of the coacervate droplet can be attributed to its complexation with the peptides.

We first tested if the nature of the polyanion affected the critical coacervation concentration of the activated peptide (CCC). Because the activated peptide is transient, these methods are complicated and subject to hysteresis effects. We, therefore, determined the CCC for the induction of droplets and their dissolution. To do so, we added a batch of fuel and determined by turbidity measurements when droplets were formed and dissolved. We then used the kinetic model to determine the exact concentration of activated peptide at those time points (Figure S2). Droplets were formed when the activated peptide concentration passed 690, 243, or 77 µM for 4.1 mM of PVPA, PVS, and PSS, respectively. Similar values were found for the dissolution threshold concentration for these droplets. These findings suggest that the CCCs differ for various polyanions, but hysteresis, when the system goes through the CCC at dissolution or formation, does not play a large role.

With the kinetic model and the CCC, we could predict the evolution of the reaction cycle and compare it to the evolution of turbidity (Figure 1A). For a fair comparison, we plotted the origin of the turbidity data such that it crosses the CCC of the peptide. When 23 mM peptide was fueled with 15 mM fuel, the turbidity's evolution matched the reaction cycle's evolution almost perfectly for PVPA and PVS. The turbidity and the concentration of activated peptide both peak simultaneously and reach their half-life times, and dissolve when they reach their CCC. In contrast, the evolution of the turbidity of the PSS differs drastically from the reaction cycle. The turbidity peaks slightly early and then decays much slower. Nevertheless, the turbidity is negligible when the concentration peptide falls below the CCC. These observations suggest that PSS droplets dissolve slower than the peptide deactivates, which could be explained by the deactivated peptide not immediately leaving after deactivation. These trends also hold for conditions that yield a significantly higher concentration of activated peptide (16 mM peptide fueled with 50 mM of EDC in the presence of 25 mM polyanion in 200 mM MES at pH 5.3). (Figure S3).

To further understand the relation between droplet behavior and the chemical reaction cycle, we analyzed the individual coacervate's life cycle by confocal microscopy in a microfluidic setup.[12c] In the microfluidic setup, micro-

reactors were prepared by mixing an aqueous stream of polyanion, buffer, and peptide with an aqueous fuel stream. These aqueous flows were mixed and then combined with a perfluorinated oil to yield microreactors with all ingredients for the complex coacervates. The microreactors were trapped in a drop spot chamber, after which imaging was started. Every 17 seconds, the entire microfluidic droplet was imaged by confocal microscopy. With the setup, we could image the nucleation of coacervate-based droplets, their fusion, and, eventually, their dissolution (Figure 1B). We measured the volume of each coacervate-based droplet in each frame in the cycle, from which we calculated the total coacervate volume in the microfluidic droplets. For all polyanions, the total volume rapidly increased after adding the fuel. After a few minutes, it started to decay until all coacervate-based droplets had dissolved. The moment the total volume of droplet material disappeared coincided roughly with when the concentration of activated peptide broke through the CCC.

When we analyzed the evolution of the individual coacervate-based droplets, it became apparent that droplets nucleated within the first minute. From there, their count rapidly decreased because of fusion and dissolution. In the case of PVPA, the dissolution outcompetes fusion after 3 minutes leading to a rapid decrease in the average volume of the droplets. In contrast, the dissolution for PSS is delayed compared to PVPA, and fusion is dominant. Consequently, the average volume of a PSS droplet reaches a maximum later in the cycle and reaches a much higher value. In line with the total volume analysis, the PSS droplets persist longer than PVPA droplets. Thus, from an individual droplet's perspective, the PSS droplets persist longer, have more time to fuse, and reach a much greater final volume (Figure S4).

Our observations have big implications if we consider our compartments the basis for self-sustaining compartments. The appropriate choice of the inert, polymeric droplet scaffold leads to droplets that can better survive starvation periods, i.e., periods without fuel supply. On the other hand, dynamic polymer-peptide combinations like PVPA or PVS are directly susceptible to changes in their building block concentrations. Their properties can be directly correlated to the chemical reaction cycle.

To better understand the mechanism of how the polymers influence the droplet life cycle, we measured the interaction strength of the peptide AcF(RG)$_3$D–OH and the activated peptide. Because the activated peptide is short-lived, it cannot be used in ITC. Instead, we used a model for the activated peptide AcF(RG)$_3$N–NH$_2$, i.e., we mutated the anionic aspartic acid for the charge-neutral asparagine. Like the activated peptide, this model peptide also contains two additional cations compared to the precursor while maintaining all other relevant structural features. The model peptide anhydride also shows similar CCC values to the actual anhydride (Figure 2A).

For PVS and PSS, the K_D values of the peptide were more than an order of magnitude higher than that of the model for the activated peptide. Moreover, significantly different K_D values were obtained for the different peptide-
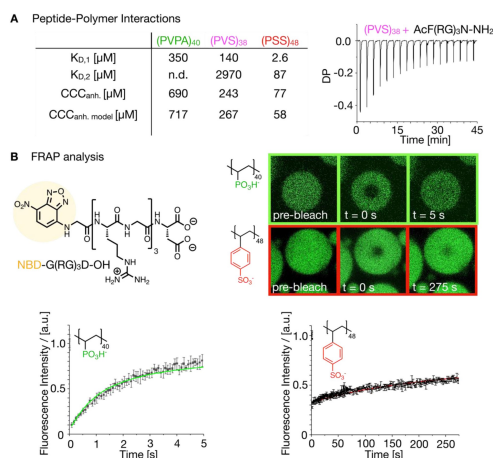
Figure 2. Mechanistic understanding of the polyanion influences. A. K_D values of the different polyanions with the peptide and anhydride model as obtained from ITC analysis. $K_{D,1}$ was obtained with AcF-(RG)$_3$N–NH$_2$, and $K_{D,2}$ with AcF(RG)$_3$D–OH. Right: Example titration obtained from titrating AcF(RG)$_3$N–NH$_2$ to PVS$_{38}$. The CCC values for the peptide anhydride and the anhydride model are in good agreement. B. FRAP experiments with the fluorescently labeled peptide NBD–G–(RG)$_3$D–OH and the polyanions PVPA$_{40}$ (green) and PSS$_{48}$ (red).

polymer pairs, which corroborates the not innocent role of the polyanion (Figure 2A, Figure S5). PSS was interacting by far the strongest with both the model for the activated peptide and the peptide, which we hypothesize is a result of the additional aromatic and cation-π interactions along with a potential contribution of hydrophobic interactions arising from the larger polymer backbone.[15] In contrast, PVPA interacted weakly with the model for the activated peptide and showed no measurable interactions with the peptide. The values for PVS lay between the other two polyanions, which can be attributed to the strong polyelectrolyte character of the sulfonate groups but the missing aromatic interactions that can contribute to the interactions for PSS. For PVS, the interaction with the AcF(RG)$_3$D–OH is already weakened significantly (the K_D value is already 34 times higher than for PSS but still measurable), further hinting at the important role of the precursor for the droplet decay profile. The different K_D values for the polyanion-anhydride model interactions are reflected in the different CCC values for the different polymers.

We used fluorescence recovery after photobleaching (FRAP) experiments to test the precursor's behavior in the droplets. We synthesized a fluorescent analog of the peptide (NBD–G–(RG)$_3$D–OH, Figure 2B). The FRAP experiments on in-equilibrium droplets revealed a 1000 times higher diffusion coefficient for the peptide in PVPA (D$=1$ μm^2/s) than in PSS (D$=0.001$ μm^2/s). This finding further corroborates the strong interaction of PSS with the precursor molecule, while there is no significant interaction with PVPA.

The high affinity of the peptide to PSS and its low diffusion coefficient in droplets of PSS suggest that the precursor building block is hindered from leaving the droplet phase after the activated peptide deactivates. This mechanism would imply that deactivated peptide accumulates in the droplets, which explains why the decay of the turbidity is delayed compared to the kinetics of the reaction cycle. Indeed, partitioning coefficients of in-equilibrium coacervates prepared from PVPA or PSS in combination with AcF(RG)$_3$D–OH and AcF(RG)$_3$N–NH$_2$ show a roughly twice as large partitioning of NBD–G(RG)$_3$D–OH in the droplet phase for PSS coacervates than for PVPA (Figure S6A). For the active systems, after fueling with EDC under the same conditions, there was a 5-fold difference in the partitioning coefficients (397.6±131.5 for PSS and 79.0±26.0 for PVPA) at the expected maximum of anhydride concentration (Figure S6B). Taken together, polyanions with a high affinity for the peptide can prevent the peptide from leaving the droplet after deactivation, which leads to delayed dissolution.

Excited by the mechanistic understanding of how polyanions can influence the lifetime of droplets, we sought a method of controlling it. As the underlying mechanism is related to the binding affinity between the peptide and polyanion, the approach is to tune this interaction strength which is possible by adding salt.[16] Indeed, when we add 250 mM of NaCl, we observe a reduced lifetime and a steeper decay profile of the turbidity compared to the system without NaCl. However, there was still a significant amount of hysteresis when comparing the evolution of peptide anhydride and turbidity. After adding 500 mM NaCl, the turbidity closely follows the evolution of the peptide anhydride concentration. These observations suggest that the critical coacervation concentration increases, leading to a shorter lifetime. Besides, the addition of salt leads to a decrease in the interaction strength between the peptide and the polyanion, which yields less hysteresis between the evolution of the anhydride concentration and turbidity. Indeed, an investigation by ITC showed that with as little as 250 mM NaCl, the K_D values for both the peptide and the model of the activated peptide were drastically higher (Figure 3A, Figure S7). Furthermore, the addition of 500 mM NaCl increased the $K_{D,2}$ value further such that it could not be measured anymore. The ITC data suggests that if $K_{D,2}$ is very high or too large to be measured, we can expect droplets whose evolution follows the anhydride profile nicely. Noteworthy, this relation between $K_{D,2}$ and the droplet dynamics also holds for PVS and PVPA without additional salt (Figure 1A).

These observations show that the addition of NaCl can tune the interaction strength. If the interaction strength of the activated peptide and polyanion decreases ($K_{D,1}$), the droplet's lifetime decreases. If the interaction strength of the peptide and the polyanion is decreased ($K_{D,2}$), the evolution of the turbidity follows the evolution of the kinetics of the reaction cycle.

To further corroborate these findings, we measured the diffusivity of the precursor in response to different amounts of salt by FRAP. To perform FRAP experiments, we
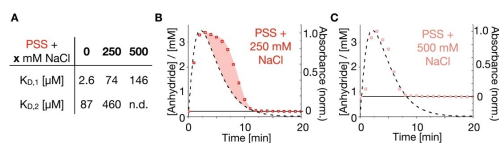
Research Articles

Figure 3. Tuning the droplet dynamics by the addition of salt. A. K_D values of AcF(RG)$_3$N–NH$_2$ ($K_{D,1}$) and AcF(RG)$_3$D–OH ($K_{D,2}$) with PSS with and without NaCl. There was no measurable interaction between the peptide and the polyanion anymore under the applied conditions with 500 mM NaCl. B. Turbidity trace PSS in the presence of 250 mM NaCl (23 mM AcF(RG)$_3$D–OH, 4.1 mM polyanion expressed in monomer units, 200 mM MES buffer at pH 5.3, fueled with 15 mM of EDC) overlayed above the CCC with the respective anhydride evolution from the kinetic model. C. Turbidity trace of PSS coacervates in the presence of 500 mM NaCl under the same conditions, overlayed with the respective anhydride concentration profile above the CCC.

created static droplets with our anhydride model in the presence of 500 mM and 1 M NaCl. The experiments revealed diffusion coefficients of D = 0.003 μm²/s in the presence of 500 mM NaCl and D = 0.0043 μm²/s in the presence of 1 M NaCl, showing a 3- to 4-fold increase in diffusivity for the AcF(RG)$_3$D–OH peptide (Figure S8B) in comparison to PSS coacervates without any additional salt (Figure 2B right). This suggests that adding sodium chloride to the chemically fueled coacervation system reduces the half-life times by reducing the polyanion-inactivated peptide interactions, leading to a steeper decay profile by increasing the peptide's diffusivity. This destabilizing effect of NaCl on the coacervate droplets is also observed under higher fuel and building block concentrations (Figure S8A). Overall, the addition of salt to our coacervate droplets is indeed a valid tool to increase the dynamics of the system by closing the gap between peptide anhydride dissolution and droplet decay and they underline the importance of the precursor-polymer interactions further.

From the above study, we conclude that a high interaction strength between the peptide precursor and the polyanion decreases the peptide's diffusivity and thereby hinders the deactivated peptide from leaving the droplet, leading to a measurable delay in the coacervate dissolution. Following this logic, the smaller the coacervate droplets, the smaller the delay in the dissolution should be.

To test this hypothesis, we synthesized block copolymers of PEG and the respective homopolymers of PVPA and PSS via RAFT polymerization (see Supporting Information).[17] These block copolymers formed assemblies with our peptide after adding EDC, as evidenced by DLS analysis (Figure 4A–D). TEM analysis revealed that both block copolymers formed spherical structures when combined with our peptide anhydride model (Figure 4E). For PEG-b-PVPA, the spherical assemblies were polydisperse with a diameter of up to 400 nm. PEG-b-PSS, on the other hand, assembled into smaller, spherical assemblies than the PEG-b-PVPA structures. These initial observations point towards the formation of large compound micelles for both block copolymers. The size differences between the assemblies are also corroborated by DLS and confocal microscopic analysis
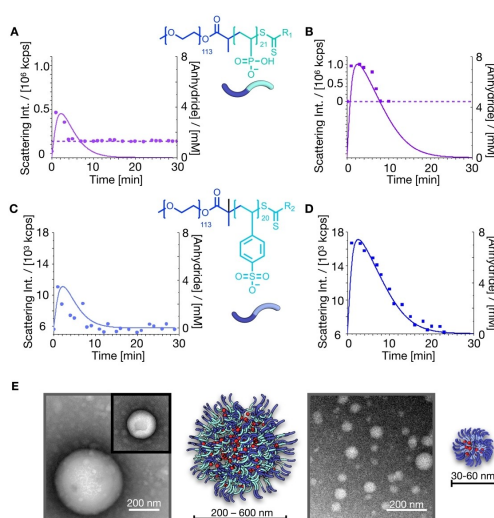

Figure 4. The role of the polyanion in nanosized assemblies/complex coacervate core micelles. A. DLS analysis of PEG-b-PVPA$_{21}$ block copolymers fueled with EDC. 23 mM of AcF(RG)$_3$D–OH were fueled with 15 mM EDC in 200 mM MES buffer at pH 5.3 in the presence of 4.1 mM block copolymer (expressed in monomer units) and the corresponding scattering intensity was followed over time by DLS (left y-axis). The solid lines show the evolution of the anhydride concentration (right y-axis). B. 16 mM AcF(RG)$_3$D–OH was fueled with 50 mM EDC in the presence of 25 mM block copolymer in 200 mM MES pH 5.3. C. and D. Fueling under the same conditions with PEG-b-PSS$_{20}$. E. TEM analysis of static samples (8.54 mM AcF(RG)$_3$D–OH, 7.46 mM AcF(RG)$_3$N–NH$_2$, 25 mM block copolymer, all in 200 mM MES at pH 5.3) after staining with uranyl acetate. Left: PEG-b-PVPA$_{21}$. Right: PEG-b-PSS$_{20}$. R$_1$=—O—C$_2$H$_5$ and R$_2$=—S—C$_{12}$H$_{25}$.

(Table S1 and Figure S9). They could be related to the higher interaction strength between the peptide and the PSS block than the PVPA block. Similar studies suggest that a lower binding strength leads to a looser packing of the core and, thus, larger assemblies.[18]

In the chemically fueled samples, the block copolymer assemblies of PEG-b-PVPA showed similar lifetimes as their dynamic homopolymer coacervates under the same conditions and led to highly turbid samples. Similarly, the PEG-b-PSS assemblies showed no delay in dissolution. This contrasts the dissolution profile of the PSS homopolymer coacervates (Figure S10). ITC analysis for PEG-b-PSS revealed relatively strong binding between the block copolymer and the peptide and peptide anhydride model ($K_{D,1}$ = 80 μM, $K_{D,2}$ = 141 μM, Figure S11).

Based on these binding constants, we would expect a delayed dissolution for PEG-b-PSS. The fact that we did not observe this delay suggests that both the size of the assemblies and the binding constants must be considered when predicting the polyanion's influence on the assembly's dissolution kinetics. We propose that in the nanometer size regime, the hindered peptide diffusion does not play a role

and does not lead to an overall delayed dissolution even with a high binding constant for the peptide and polyanion (Scheme 2).

Conclusion and Outlook

We studied the role of the polyanion in chemically fueled complex coacervates and conclude that they greatly alter the outcome of the resulting droplets despite not affecting the underlying chemical reaction cycle. We find that polyanions that bind strongly to the precursor tend to form droplets that dissolve with delayed kinetics compared to the reaction cycle. This effect can be negated by tuning the binding constants, for example, by adding salt or changing the design of the polyanion. Moreover, we find that these effects operate on the microscopic scale, meaning that smaller assemblies like coacervate core micelles are not affected.

Our findings have implications for chemically fueled protocell models in which a delay in dissolution can be desired. If a protocell could control the nature of its polyanion, for example, by synthesizing or selecting specific polyanions, it is able to regulate its lifetime and become more resilient to fuel starvation. When dynamic behavior, like size control or self-division, is desired, we offer design considerations for the polyanion too.

Supporting Information

The authors have cited additional references within the Supporting Information.[12b,c,13,17,19]

Conflict of Interest

The authors declare no conflict of interest.

Data Availability Statement

The data that support the findings of this study are available from the corresponding author upon reasonable request.

Scheme 2. The different parameters of chemically fueled coacervates that influence their life cycles.

[1] W. M. Aumiller Jr, F. Pir Cakmak, B. W. Davis, C. D. Keating, *Langmuir* **2016**, *32*, 10042–10053.

[2] a) J. Y. Youn, B. J. A. Dyakov, J. Zhang, J. D. R. Knight, R. M. Vernon, J. D. Forman-Kay, A. C. Gingras, *Mol. Cell* **2019**, *76*, 286–294; b) F. Palangi, S. M. Samuel, I. R. Thompson, C. R. Triggle, M. M. Emara, *PLoS One* **2017**, *12*, e0182059.

[3] a) N. A. Yewdall, A. A. M. André, T. Lu, E. Spruijt, *Curr. Opin. Colloid Interface Sci.* **2021**, *52*, 101416; b) E. Gomes, J. Shorter, *J. Biol. Chem.* **2019**, *294*, 7115–7127; c) R. W. Lewis, B. Klemm, M. Macchione, R. Eelkema, *Chem. Sci.* **2022**, *13*, 4533–4544; d) D. Zwicker, *Curr. Opin. Colloid Interface Sci.* **2022**, *61*, 101606.

[4] W. M. Aumiller Jr, C. D. Keating, *Nat. Chem.* **2016**, *8*, 129–137.

[5] a) D. Zwicker, R. Seyboldt, C. A. Weber, A. A. Hyman, F. Jülicher, *Nat. Phys.* **2017**, *13*, 408–413; b) D. Zwicker, A. A. Hyman, F. Jülicher, *Phys. Rev. E* **2015**, *92*, 012317; c) C. Donau, J. Boekhoven, *Trends Chem.* **2023**, *5*, 45–60.

[6] a) I. Gözen, E. S. Koksal, I. Poldsalu, L. Xue, K. Spustova, E. Pedrueza-Villalmanzo, R. Ryskulov, F. Meng, A. Jesorka, *Small* **2022**, *18*, 2106624; b) S. Koga, D. S. Williams, A. W. Perriman, S. Mann, *Nat. Chem.* **2011**, *3*, 720–724.

[7] N. Martin, *ChemBioChem* **2019**, *20*, 2553–2568.

[8] a) L. S. Kariyawasam, C. S. Hartley, *J. Am. Chem. Soc.* **2017**, *139*, 11949–11955; b) M. M. Hossain, I. M. Jayalath, R. Baral, C. S. Hartley, *ChemSystemsChem* **2022**, *4*, e202200016; c) M. M. Hossain, J. L. Atkinson, C. S. Hartley, *Angew. Chem. Int. Ed.* **2020**, *59*, 13807–13813; d) S. Panja, B. Dietrich, D. J. Adams, *ChemSystemsChem* **2019**, *2*, e1900038; e) J. Sun, J. Vogel, L. Chen, A. L. Schleper, T. Bergner, A. J. C. Kuehne, M. von Delius, *Chem. Eur. J.* **2022**, *28*, e202104116; f) S. Bal, K.

Das, S. Ahmed, D. Das, *Angew. Chem. Int. Ed.* **2019**, *58*, 244–247.

[9] a) S. Borsley, D. A. Leigh, B. M. W. Roberts, *J. Am. Chem. Soc.* **2021**, *143*, 4414–4420; b) S. Borsley, E. Kreidt, D. A. Leigh, B. M. W. Roberts, *Nature* **2022**, *604*, 80–85.

[10] a) M. Tena-Solsona, B. Riess, R. K. Grötsch, F. C. Lohrer, C. Wanzke, B. Kasdorf, A. R. Bausch, P. Müller-Buschbaum, O. Lieleg, J. Boekhoven, *Nat. Commun.* **2017**, *8*, 15895; b) X. Chen, M. Stasi, J. Rodon-Fores, P. F. Grossmann, A. M. Bergmann, K. Dai, M. Tena-Solsona, B. Rieger, J. Boekhoven, *J. Am. Chem. Soc.* **2023**, *145*, 6880–6887; c) J. Rodon-Fores, M. A. Würbser, M. Kretschmer, B. Riess, A. M. Bergmann, O. Lieleg, J. Boekhoven, *Chem. Sci.* **2022**, *13*, 11411–11421; d) F. Schnitter, B. Riess, C. Jandl, J. Boekhoven, *Nat. Commun.* **2022**, *13*, 2816; e) B. A. K. Kriebisch, C. M. E. Kriebisch, A. M. Bergmann, C. Wanzke, M. Tena-Solsona, J. Boekhoven, *ChemSystemsChem* **2023**, *5*, e202200035; f) M. A. Würbser, P. S. Schwarz, J. Heckel, A. M. Bergmann, A. Walther, J. Boekhoven, *ChemSystemsChem* **2021**, *3*, e202100015.

[11] M. Stasi, A. Monferrer, L. Babl, S. Wunnava, C. F. Dirscherl, D. Braun, P. Schwille, H. Dietz, J. Boekhoven, *J. Am. Chem. Soc.* **2022**, *144*, 21939–21947.

[12] a) C. Donau, F. Späth, M. Sosson, B. A. K. Kriebisch, F. Schnitter, M. Tena-Solsona, H. S. Kang, E. Salibi, M. Sattler, H. Mutschler, J. Boekhoven, *Nat. Commun.* **2020**, *11*, 5167; b) F. Späth, C. Donau, A. M. Bergmann, M. Kränzlein, C. V. Synatschke, B. Rieger, J. Boekhoven, *J. Am. Chem. Soc.* **2021**, *143*, 4782–4789; c) A. M. Bergmann, C. Donau, F. Späth, K. Jahnke, K. Göpfrich, J. Boekhoven, *Angew. Chem. Int. Ed.* **2022**, *61*, e202203928; d) C. Donau, F. Späth, M. Stasi, A. M. Bergmann, J. Boekhoven, *Angew. Chem. Int. Ed.* **2022**, *61*, e202211905; e) A. M. Bergmann, J. Bauermann, G. Bartolucci, C. Donau, M. Stasi, A.-L. Holtmannspötter, F. Jülicher, C. A. Weber, J. Boekhoven, *bioRxiv preprint* **2023**, https://doi.org/10.1101/2023.01.31.526480.

[13] a) B. S. Soller, S. Salzinger, C. Jandl, A. Pöthig, B. Rieger, *Organometallics* **2015**, *34*, 2703–2706; b) S. Salzinger, U. B. Seemann, A. Plikhta, B. Rieger, *Macromolecules* **2011**, *44*, 5920–5927.

[14] B. Bingöl, W. H. Meyer, M. Wagner, G. Wegner, *Macromol. Rapid Commun.* **2006**, *27*, 1719–1724.

[15] a) L. Li, A. M. Rumyantsev, S. Srivastava, S. Meng, J. J. de Pablo, M. V. Tirrell, *Macromolecules* **2021**, *54*, 105–114; b) K. Sadman, Q. Wang, Y. Chen, B. Keshavarz, Z. Jiang, K. R. Shull, *Macromolecules* **2017**, *50*, 9417–9426; c) J. Huang, J. E. Laaser, *ACS Macro Lett.* **2021**, *10*, 1029–1034; d) G. Krainer, T. J. Welsh, J. A. Joseph, J. R. Espinosa, S. Wittmann, E. de Csillery, A. Sridhar, Z. Toprakcioglu, G. Gudiskyte, M. A. Czekalska, W. E. Arter, J. Guillen-Boixet, T. M. Franzmann, S. Qamar, P. S. George-Hyslop, A. A. Hyman, R. Collepardo-Guevara, S. Alberti, T. P. J. Knowles, *Nat. Commun.* **2021**, *12*, 1085; e) R. A. Kapelner, V. Yeong, A. C. Obermeyer, *Curr. Opin. Colloid Interface Sci.* **2021**, *52*, 101407; f) U. Lang, E. Müller, N. Naujoks, J. Dual, *Adv. Funct. Mater.* **2009**, *19*, 1215–1220.

[16] a) I. Bos, M. Timmerman, J. Sprakel, *Macromolecules* **2021**, *54*, 398–411; b) D. Priftis, N. Laugel, M. Tirrell, *Langmuir* **2012**, *28*, 15947–15957; c) Q. Wang, J. B. Schlenoff, *Macromolecules* **2014**, *47*, 3108–3116; d) M. Lemmers, J. Sprakel, I. K. Voets, J. van der Gucht, M. A. Cohen Stuart, *Angew. Chem. Int. Ed.* **2010**, *49*, 708–711.

[17] a) K. H. Markiewicz, L. Seiler, I. Misztalewska, K. Winkler, S. Harrisson, A. Z. Wilczewska, M. Destarac, J. D. Marty, *Polym. Chem.* **2016**, *7*, 6391–6399; b) J. M. Ting, H. Wu, A. Herzog-Arbeitman, S. Srivastava, M. V. Tirrell, *ACS Macro Lett.* **2018**, *7*, 726–733.

[18] a) H. M. van der Kooij, E. Spruijt, I. K. Voets, R. Fokkink, M. A. Cohen Stuart, J. van der Gucht, *Langmuir* **2012**, *28*, 14180–14191; b) J. M. Horn, R. A. Kapelner, A. C. Obermeyer, *Polymer* **2019**, *11*, 578.

[19] a) S. Salzinger, B. S. Soller, A. Plikhta, U. B. Seemann, E. Herdtweck, B. Rieger, *J. Am. Chem. Soc.* **2013**, *135*, 13030–13040; b) T. M. Pehl, M. Kränzlein, F. Adams, A. Schaffer, B. Rieger, *Catalysts* **2020**, *10*, 448; c) M. Fuentes-Exposito, S. Norsic, T. Février, P.-Y. Dugas, S. Boutti, S. Devisme, A. Bonnet, F. D'Agosto, M. Lansalot, *Polym. Chem.* **2021**, *12*, 5640–5649; d) D. C. Duffy, J. C. McDonald, O. J. Schueller, G. M. Whitesides, *Anal. Chem.* **1998**, *70*, 4974–4984; e) M. Weiss, J. P. Frohnmayer, L. T. Benk, B. Haller, J. W. Janiesch, T. Heitkamp, M. Borsch, R. B. Lira, R. Dimova, R. Lipowsky, E. Bodenschatz, J. C. Baret, T. Vidakovic-Koch, K. Sundmacher, I. Platzman, J. P. Spatz, *Nat. Mater.* **2018**, *17*, 89–96; f) T. W. Hofmann, S. Hanselmann, J. W. Janiesch, A. Rademacher, C. H. Bohm, *Lab Chip* **2012**, *12*, 916–922; g) A. B. Kayitmazer, H. B. Bohidar, K. W. Mattison, A. Bose, J. Sarkar, A. Hashidzume, P. S. Russo, W. Jaeger, P. L. Dubin, *Soft Matter* **2007**, *3*, 1064–1076; h) F. Schnitter, J. Boekhoven, *ChemSystemsChem* **2020**, *3*, e202000037.

Supporting Information

The Role of Chemically Innocent Polyanions in Active, Chemically Fueled Complex Coacervate Droplets

F. Späth, A. S. Maier, M. Stasi, A. M. Bergmann, K. Halama, M. Wenisch, B. Rieger, J. Boekhoven*

Table of Contents

1. Materials and methods

Materials.

All chemicals were purchased from Sigma-Aldrich, Acros Organics, VWR, ABCR or TCI Europe and used without further purification. General solvents were purchased from Sigma Aldrich in analytical or synthesis grade and used without further purification. Deuterated solvents (methanol-d_4, benzene-d_6) were purchased from Sigma-Aldrich or Deutero and dried over activated 3 Å molecular sieve. Dimethylsulfoxide-d_6 was purchased in glass ampoules from Sigma-Aldrich. Sylgard 184 silicon elastomere were all purchased from Sigma-Aldrich. 2 wt% 008-Fluorosurfactant in HFE7500 was purchased from RAN Biotechnologies.

Nuclear magnetic resonance spectroscopy (NMR).

^{1}H- and ^{31}P-NMR-spectra were recorded on a Bruker AV-400HD NMR-spectrometer at 400 MHz (^{1}H) and 162 MHz (^{31}P), respectively. ^{1}H-NMR spectra were also recorded at 500 MHz on a Bruker AV-500HD NMR-spectrometer. All chemical shifts δ are given in parts per million (ppm) and referenced to the residual proton signal of the respective solvent (Methanol-d_4: δ = 3.31 ppm, dimethylsulfoxide-d_6: δ = 2.50 ppm, benzene-d6: δ = 7.16 ppm). The NMR spectra were analyzed using the MestReNova software. Signal multiplicities are abbreviated as following: s - singlet, d - dublet, dd – dublet of dublets, m – multiplet, q - quartet, t – triplet. The prefix b stands for "broad".

2. Microwave-assisted, automated solid phase peptide synthesis and labelling.
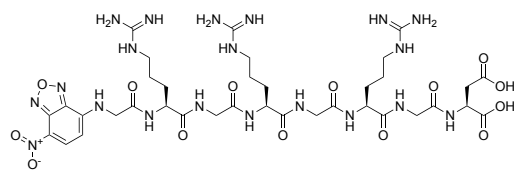
H_2N-G(RG)$_3$D-OH (H_2N-Gly-Arg-Gly-Arg-Gly-Arg-Gly-Asp-OH) was synthesized on 0.25 mmol scale with a Liberty Blue® peptide synthesizer from CEM by standard Fmoc-SPPS. Pre-loaded Wang resign (Fmoc-Asp(OtBu) loaded, 100-200 mesh, 0.67 mmol/g) was used. A double Fmoc-deprotection and double coupling cycle with microwave heating was applied. Therefore, Fmoc-removal was performed twice per amino

acid (2x 5 mL piperidine 20 v/v% solution in DMF, 90°C, 90 s) before each amino acid was coupled twice (2x 5 mL of 0.2 M amino acid in DMF, 2x 2 mL 0.5 M DIC in DMF, 2x 1 mL 1 M Oxyma pure in DMF, 90°C, 120 s each cycle). Arginine couplings were performed for 240 s at 90°C with the same reagent concentrations. Final Fmoc-removal was performed by reacting the peptide three times 120 seconds each on the resin with a 20 v/v% solution of piperidine in DMF at 90 °C.

Labelling of the peptide with the fluorescent dye NBD (7-nitrobenzo-2-oxa-1,3-diazol) was performed by reacting the peptide on the resin with 2 eq. NBD-Cl and 1.2 eq. DIPEA in 4 mL DMF overnight under constant agitation. Cleavage of the labelled peptide from the resin was achieved by reacting it with 10 mL of a 95% TFA, 5% TIPS and 5% H_2O cocktail for 3 hours at room temperature. After removal of the residual solvents by rotary evaporation and co-evaporation with DCM, the crude product was purified by preparative HPLC (see HPLC methods for details).

^{1}H-NMR (DMSO-d_6, 400 MHz): δ 12.61 (s, 2H), 9.41 (s, 1H), 8.52 (d,J=9Hz, 1H), 8.19 (m, 6H), 7.63 (s, 3H), 7.29 (d, J=8.5Hz, 1H), 7.25 – 6.86 (bs, 9H), 6.82 (d, J=8.5Hz, 1H), 4.52 (s, 1H), 4.29 (bs, 5H), 3.75 (s, 6H), 3.08 (m, 6H), 2.66 (m, 1H), 2.61 (m, 1H), 1.69 (bs, 3H), 1.50 (bs, 9H).

LC-MS: calculated 497.22 $[M+2H]^{2+}$, found 497.47 $[M+2H]^{2+}$.

Retention time **analytical HPLC**: 6.85 min (2% to 98% ACN in MQ water, with 0.1% TFA, 15 min gradient).

3.   Polymer synthesis

General experimental information.

All air and moisture sensitive compounds were prepared using standard Schlenk techniques or in a MBraun LabMaster120 glovebox with argon (99.996 vol.-%) from Westfalen as inert gas. All glassware was oven-dried prior to use. Dry solvents were obtained from an MBraun SPS-800 solvent purification system and stored over 3 Å molecular sieve. Diethyl vinylphosphonate (DEVP) was dried over CaH_2 for several days and distilled prior to use. The precursor catalyst $Cp_2YCH_2TMS(thf)$ was prepared according to literature procedures.[1] *Sym*-collidine (2,4,6-trimethylpyridine) was dried over activated alumina and stored over 3 Å molecular sieve prior to use.

Gel-Permeation Chromatography (GPC) of Poly(diethyl vinyl phosphonates).

Average molecular weights and polydispersities of the polymers were determined via size-exclusion chromatography (SEC) with sample concentrations in the range of 3-4 mg mL^{-1}. The measurements of PDEVP were performed by SEC-MALS using a Wyatt Dawn Heleos II MALS light scattering unit and a Wyatt Optilab rEX 536 RI unit with two Agilent PolarGel-M columns at 40 °C. As eluent, a mixture of tetrahydrofuran and water (THF:H2O = 1:1) with 9 g L^{-1} tetra-n-butyl-ammonium bromide and 272 mg L^{-1} 2,6-di-tert-butyl-4-methylphenol added, was applied. For absolute molecular weight determination of PDEVP in triple-detection mode, the refractive index increment dn/dc = 0.0922 mL g^{-1} was used.[2]

Gel-Permeation Chromatography (GPC) of polyethylene glycol – poly(vinylphosphonate) block copolymers in DMF.

Average relative molecular weights and polydispersities of the polymers obtained from RAFT-polymerization and the macroCTA were determined via size-exclusion chromatography (SEC) with a sample concentration between 4 and 6 mg mL^{-1} relative to polystyrene standards. Measurements were performed on an Agilent PL-GPC 50 (Santa Clara, CA, USA) with an integrated RI unit, two light scattering detectors (15° and 90°) and a differential pressure

S 6

viscosimeter with two Agilent PolarGel M columns at 30 °C. As eluent, N,N-dimethylformamide (with 2.096 g L^{-1} lithium bromide) was used.

Aqueous Gel-Permeation Chromatography (GPC) of polyethylene glycol – poly(styrene sulfonate) and polyethylene glycol – poly(vinylphosphonate) block copolymers.

Aqueous SEC analysis was performed on a PSS SECcurity SEC setup with 0.07M Na_2HPO_4 solution as the eluent at a flow rate at 1 mL/min. The SEC setup was equipped with an RI and UV detector (270 nm). Samples were prepared at a concentration of 1 mg/mL, filtered through 0.2 µm PTFE filters and separated on a combination of a MCX1000 and a MCX100000 column at 25 °C. The system was calibrated with PEO standards in a molecular weight range between 238 and 970000 g/mol.

Dialysis.

Purification of polymers via dialysis in water was performed with Spectra/Por 1 dialysis tubing (regenerated cellulose) from Spectrumlabs with a molecular weight cutt-off (MWCO) of 1 kDa or 6-8 kDa, respectively. Prior to use, the membranes were soaked in and rinsed with deionized water multiple times. After dialysis, the polymer samples were lyophilized.

CH-bond activation of *sym*-collidine derivatives with the catalyst precursor $Cp_2YCH_2TMS(thf)$.
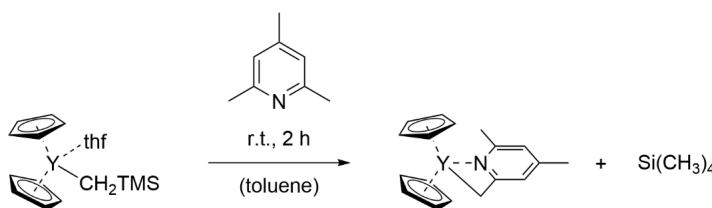
CH-bond activation of *sym*-collidine derivatives with $Cp_2YCH_2TMS(thf)$ was performed according to literature-known procedures.[3] In this context, the calculated amount of the catalyst precursor $Cp_2YCH_2TMS(thf)$ was dissolved in dry toluene and the corresponding amount of initiator (1.10 eq.) added. The reaction was allowed to proceed at room temperature for two hours before an aliquot (0.1 mL of the reaction mixture + 0.4 mL of dry benzene-d_6)

was removed from the reaction mixture to ensure quantitative conversion of the catalyst precursor via ^{1}H-NMR spectroscopy.

Extract of the ^{1}H-NMR spectrum for the CH-bond activation of *sym*-collidine with Cp$_2$YCH$_2$TMS(thf) in C$_6$D$_6$.
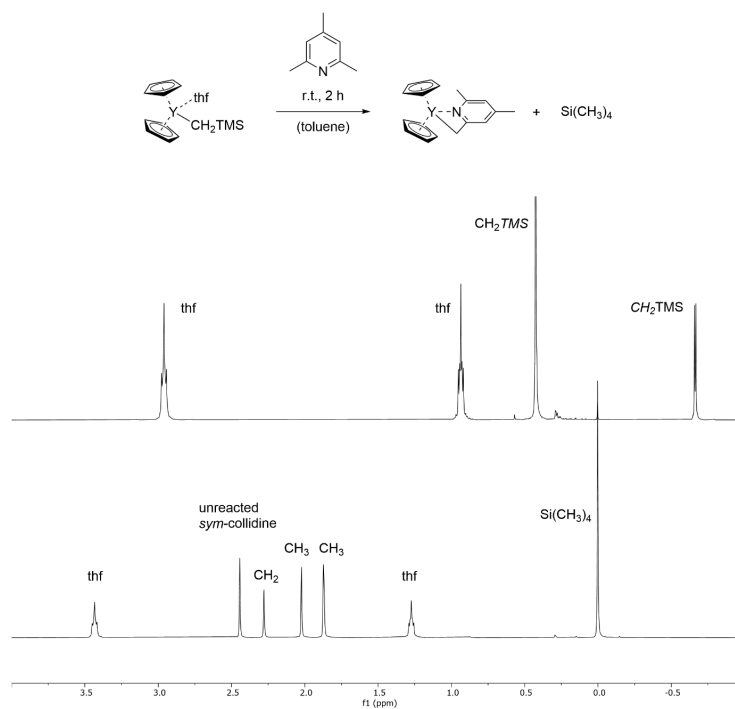
General procedure for the polymerization of diethyl vinylphosphonate (DEVP) with the CH-bond activated species of Cp$_2$YCH$_2$TMS(thf).
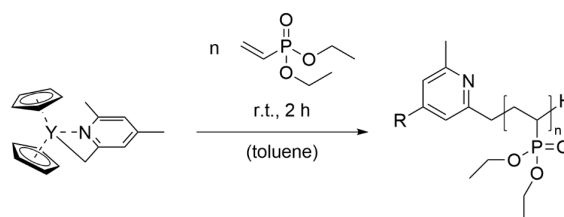
In a screw-cap vial, the calculated amount of catalyst was dissolved in dry toluene and the corresponding amount of initiator (1.10 eq.) added. Subsequently, the reaction mixture was

S 8

stirred at room temperature for two hours. After quantitative *in situ* activation of the initiator with Cp$_2$YCH$_2$TMS(thf) was confirmed via ^{1}H-NMR spectroscopy, the calculated amount of diethyl vinylphosphonate (DEVP) was added in one motion. The polymerization was continued for two hours before an aliquot (0.1 mL of the reaction mixture + 0.4 mL of undried methanol-d$_4$) was withdrawn from the reaction mixture to monitor monomer conversion via ^{31}P-NMR spectroscopy. Following, the reaction was quenched by addition of 0.5 mL of undried methanol and the polymer precipitated from pentane. After centrifugation and decanting of the supernatant, the residual polymer was dissolved in 1,4-dioxane and subjected to freeze-drying, yielding the purified polymer.

Exemplary ^{1}H-NMR spectrum of PDEVP.
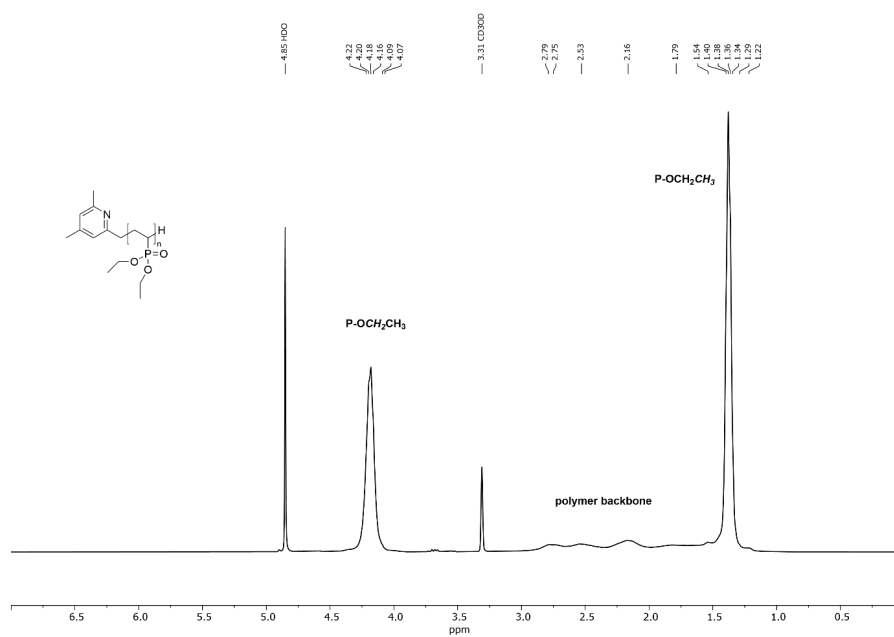
Exemplary ^{31}P-NMR spectrum of PDEVP.
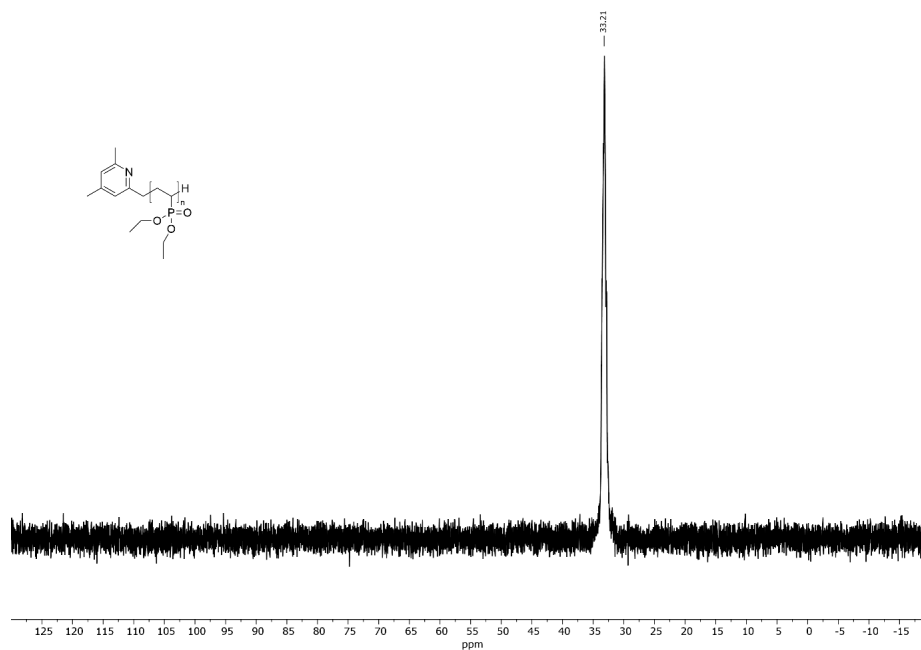
Summary of REM-GTP conditions and results:

Entry	[DEVP]/[Cat.][a] [mol]/[mol]	X[b] [%]	$M_{n,theo}$[c] [kg/mol]	$M_{n,abs}$[d] [kg/mol]	Đ[d]
1	20/1	>99	3.5	3.5	1.29
2	40/1	>99	6.5	8.3	1.05

[a] Desired reactant ratio. [b] Conversion determined via ^{31}P-NMR spectroscopy. [c] Theoretical molecular weight of the polymer determined via $M_{n,theo} = X_{DEVP} \times M_{DEVP} \times$ [DEVP]/[Cat.], assuming full initiator efficiency. [d] Absolute molecular weight $M_{n,abs}$ and polydispersity Đ determined via SEC-MALS in THF:H2O = 1:1 with 9 g L^{-1} *tetra-n*-butyl ammonium bromide and 272 mg L^{-1} 2,6-di-*tert*butyl-4-methylphenol at 40 °C using dn/dc = 0.0922 mL g^{-1} for PDEVP.

S 10

Side-group deprotection of poly(diethyl vinylphosphonate) (PDEVP) to poly(vinylphosphonic acid) (PVPA).
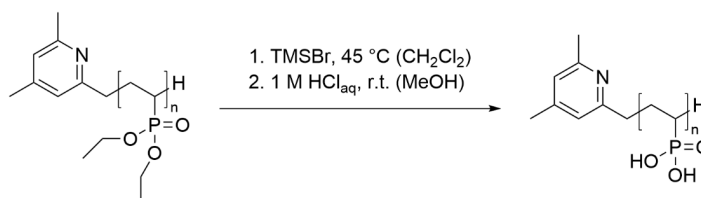
The deprotection of poly(diethyl vinylphosphonate) to poly(vinylphosphonic acid) was performed according to a literature-known procedure.[4] In an oven dried flask, the polymer was dissolved in dry dichloromethane (10.0 mL per 100 mg polymer) and trimethylsilyl bromide (3.30 eq. respective to the ester functionalities) was added. Next, the reaction mixture was refluxed at 50 °C for 24 hours. After cooling to room temperature, the volatiles were removed in vacuo and the residue dissolved in a small amount of methanol, followed by addition of 1 M hydrochloric acid (4.00 eq.). The resulting solution was stirred for another 2 hours at room temperature, before removing the solvent. The crude product was taken up in small amounts of water and subjected to dialysis against deionized water. In the last step, the solution containing the purified polymer was freeze-dried, yielding the pure poly(vinylphosphonic acid)-derivatives.
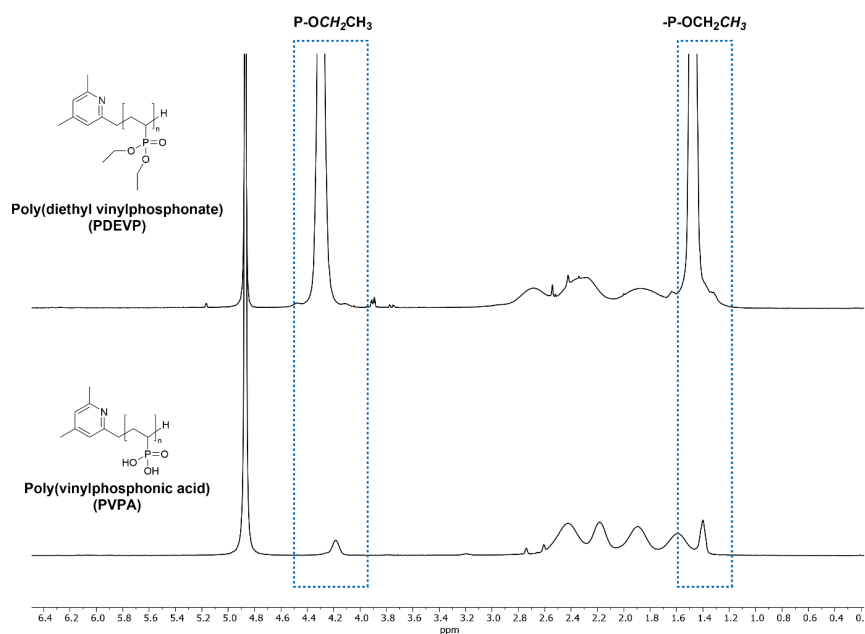
Synthesis of mPEG5k-Br.
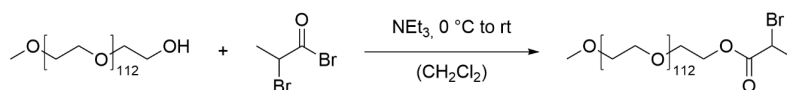
The RAFT-agent precursor mPEG5k-Br was synthesized according to literature-known procedures.[5] In the first step, the polyethylene glycol starting material (5.00 mmol, 1.00 eq.) was placed in an oven-dried Schlenk-flask and dissolved in dry dichloromethane (50 mL) and triethylamine (1.88 mL, 13.5 mmol, 2.70 eq.). Subsequently, the solution was degassed by bubbling argon for ten minutes and cooled to 0 °C. In the next step, 2-bromopropionyl bromide (1.21 mL, 11.5 mmol, 2.30 eq.) was added dropwise. The reaction mixture was allowed to warm to room temperature and stirred for additional 23 h. After filtration the solvent was removed under reduced pressure and the residue dissolved in dichloromethane (200 mL). The organic phase was then washed with saturated NH4Cl-solution (2 × 50 mL), saturated Na2CO3-solution (4 × 50 mL) and deionized water (5 × 100 mL). Finally, the organic phase was dried over MgSO4 and the solvent removed via rotary evaporation. The final product was

S 12

further purified by lyophilization from deionized water, yielding the product as a white powder. (14.7 g, 57%)

^{1}H-NMR (400 MHz, CDCl$_3$): δ = 4.36 (q, ^3J = 6.9 Hz, 1H, -CHBr-), 4.29 - 4.25 (m, 2H, -CH_2OCO), 3.80 - 3.48 (m, 479H, -O-CH_2-CH_2-O-), 3.33 (s, 3H, -OCH_3), 1.78 (d, ^3J = 6.9 Hz, 3H, -CH$_3$).

Synthesis of mPEG$_{5k}$-Xanthate.
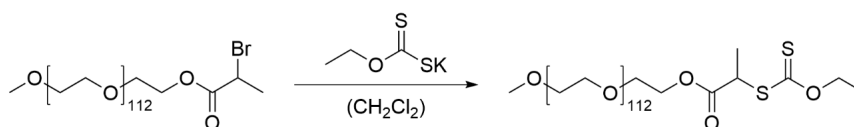
The macromolecular RAFT-agent mPEG$_{5k}$-Xanthate was synthesized from the precursor mPEG$_{5k}$-Br according to literature-known procedures.[5] In the first step, an oven-dried Schlenk-flask was charged with the starting material (1.55 mmol, 1.00 eq.) under argon atmosphere. Subsequently, anhydrous dichloromethane (100 mL) and ethyl potassium xanthate (4.82 mmol, 3.10 eq.) were added and the reaction was allowed to proceed at room temperature for 16 hours. In the next step, the precipitated salt was filtered off and the obtained viscous solution used to precipitate the product from pentane (3 × 50 mL). After centrifugation, the supernatant was discarded and the product dried in vacuo to yield macromolecular RAFT-agent as a white, crystalline solid (5.73 g, 71%).

^{1}H-NMR (500 MHz, CDCl$_3$): δ = 4.62 (q, ^3J = 7.1 Hz, 2H, -CH_2CH$_3$), 4.39 (q, ^3J = 7.4 Hz, 1H, -CH-CH$_3$), 4.30 - 4.27 (m, 2H, -CH_2OCO), 3.63 (s, 479H, PEG), 3.36 (s, 3H, -OCH_3), 1.56 (d, ^3J = 7.4 Hz, 3H, -CH-CH_3), 1.40 (t, ^3J = 7.1 Hz, 3H, -CH$_2$CH_3).

S 13

General procedure for RAFT-polymerization of vinylphosphonic acid with mPEG$_{5k}$-Xanthate.
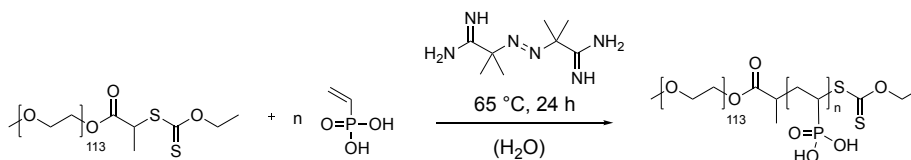
The synthesis of PEG-b-PVPA diblock copolymers was performed according to adapted literature procedures.[5b] In a standard RAFT-polymerization experiment, the chain transfer agent (0.17 mmol, 1.00 eq.) and vinylphosphonic acid (14.2 mmol, 83 eq.) were dissolved in 0.5 mL of MilliQ-water in a Schlenk-flask. The mixture was subsequently degassed by bubbling argon trough it for 30 minutes. In the next step, (2,2′-Azobis(2-methylpropionamidine)dihydrochloride, AIBA) (0.052 mmol, 0.3 eq.) and the flask closed with a relief valve. Polymerization was initiated by placing the Schlenk-flask in a pre-heated oil bath at a temperature of 65 °C. After 24 hours, the reaction was quenched (40% VPA conversion as determined by ^{31}P-NMR) by exposing the reaction mixture to air and freezing in liquid nitrogen. Subsequently, the polymer crude solution was freeze-dried. The crude product was dissolved in deionized water and purified via dialysis. After lyophilization the final products were obtained in the forms of white powders (532 mg, 42%). The block copolymer was analyzed by ^{1}H and ^{31}P-NMR and SEC in aqueous buffer and DMF.

$M_{n,NMR}$ = 7.5 kg/mol, $M_{n,GPC}$ = 8.4 kg/mol, $X_{n,VPA}$ = 21 (from ^{1}H-NMR).

Đ (from SEC-GPC at 30 °C in N,N-dimethylformamide) = 1.21.

Đ (from aqueous SEC analysis in 0.07M Na$_2$HPO$_4$) = 1.23.

Exemplary ¹H-NMR spectrum of mPEG₅ₖ-b-PVPA₂₁:
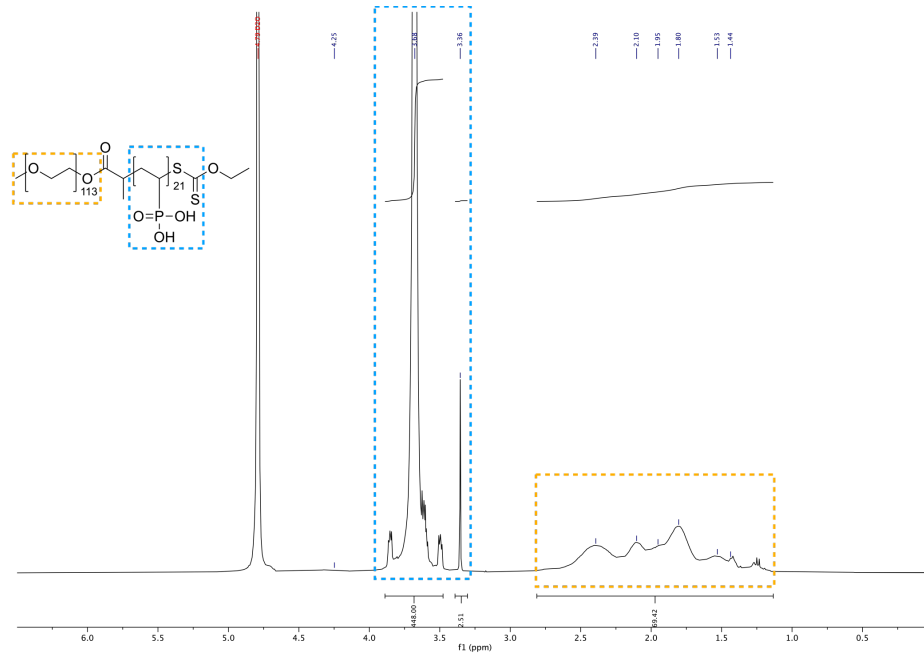
Exemplary ³¹P-NMR spectrum of mPEG₅ₖ-b-PVPA₂₁:
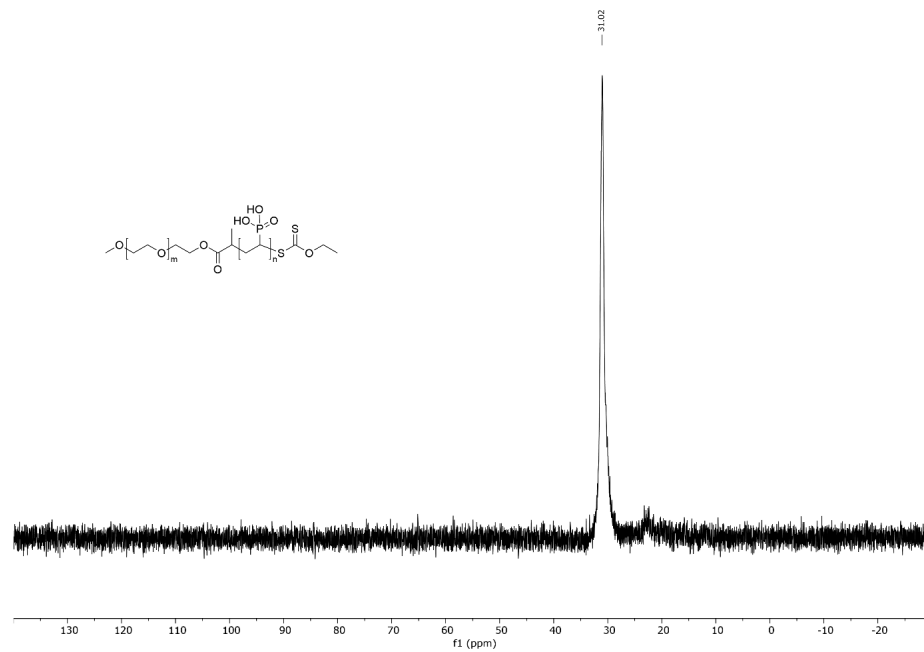
S 15

DOSY spectrum of mPEG$_{5k}$-b-PVPA$_{21}$:
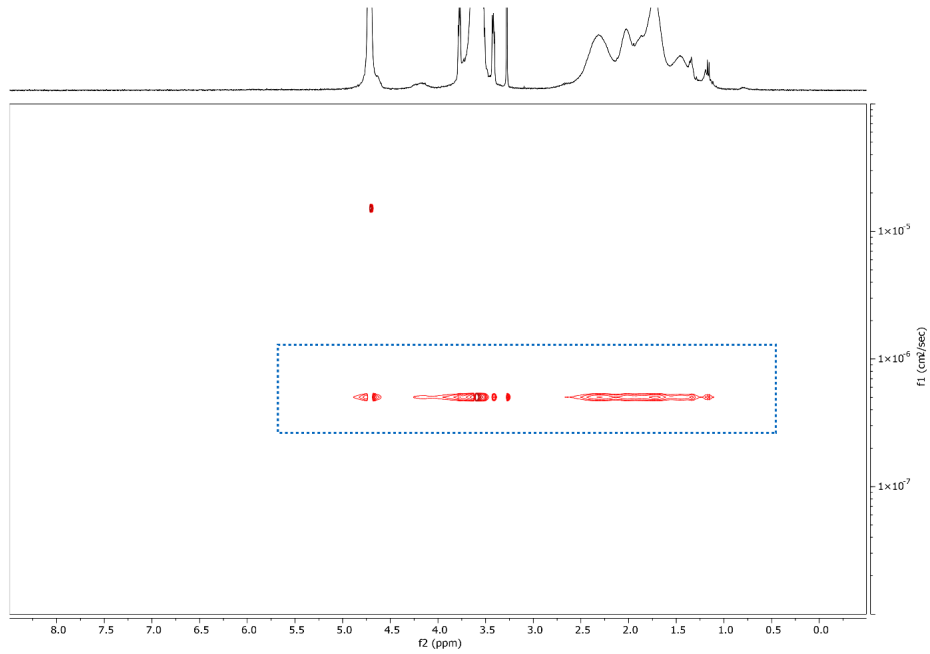
Aqueous SEC Chromatogram (left) and SEC Chromatogram in DMF (right) of PEG$_{5k}$-b-PVPA$_{21}$:

S 16
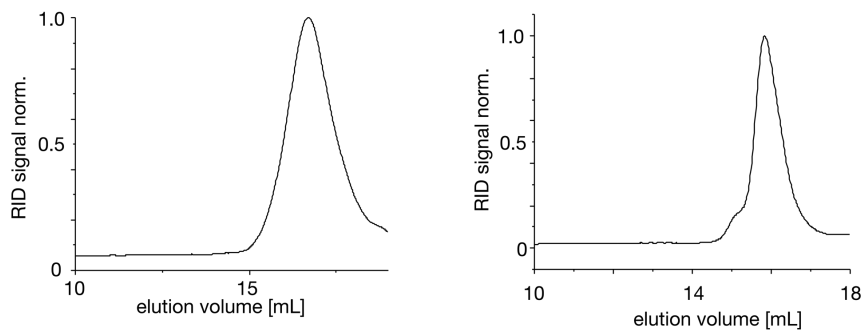
RAFT polymerization of styrene sulfonate with PEG$_{5k}$-macro CTA.
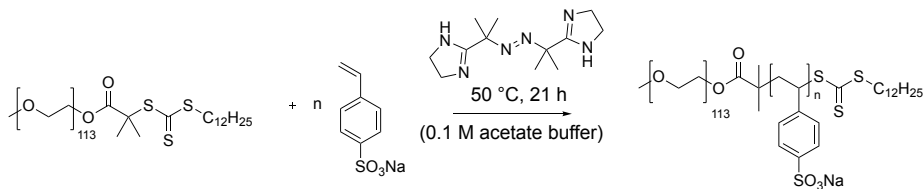
PEG$_{5k}$-b-PSS$_{20}$ was synthesized following a literature known protocol.[6]   50 µmol (1.0 eq.) poly(ethylene glycol) methyl ether 2-(dodecylthiocarbonothioylthio)-2-methylpropionate and 1 mmol (20.0 eq.) of styrene sulfonate hydrate were dissolved in 7 mL of 0.1 M acetate buffer (pH 5.2). The solution was degassed by purging with argon for 30 minutes. 7.4 µmol (0.15 eq.) of 2,2'-Azobis[2-(2-imidazolin-2-yl)propane]dihydrochloride were added and the polymerization was conducted for 21 hours at 50 °C. The reaction was stopped by exposing the mixture to air and cooling it in an ice bath. The crude product was dialyzed against MilliQ-water in 3.5 kDa MWCO Spectra/Por dialysis tubing for 2 days. The purified block copolymer was obtained as a white powder after lyophilization (249 mg, 53%). The polymer was analyzed by ^{1}H-NMR spectroscopy and SEC in aqueous buffer.

$M_{n,NMR}$ = 9.5 kg/mol, $X_{n,PSS}$ = 20 (from ^{1}H-NMR).

Đ (from aqueous SEC analysis in 0.07M Na$_2$HPO$_4$, see Methods) = 1.15.

S 17

Exemplary ^{1}H-NMR spectrum of PEG$_{5k}$-b-PSS$_{20}$:
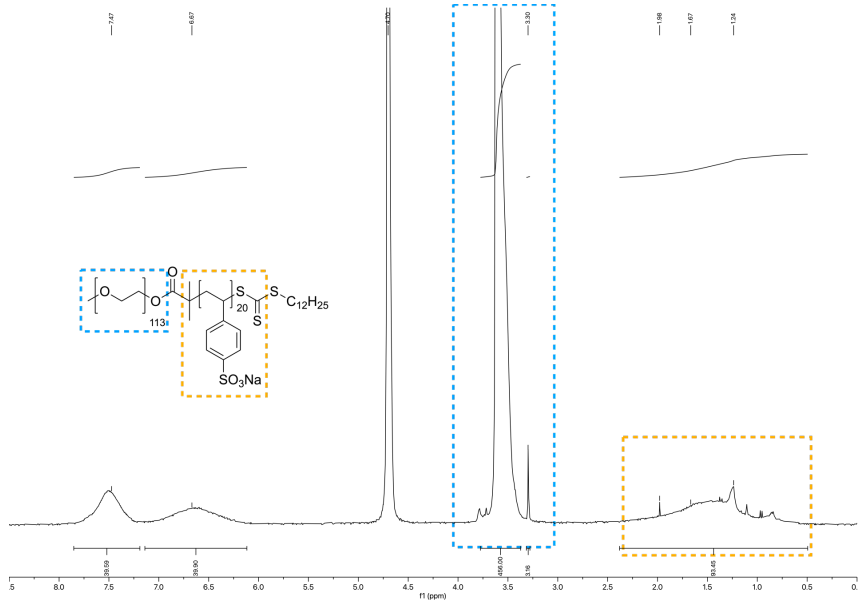
DOSY spectrum of mPEG$_{5k}$-b-PSS$_{20}$:

S 18
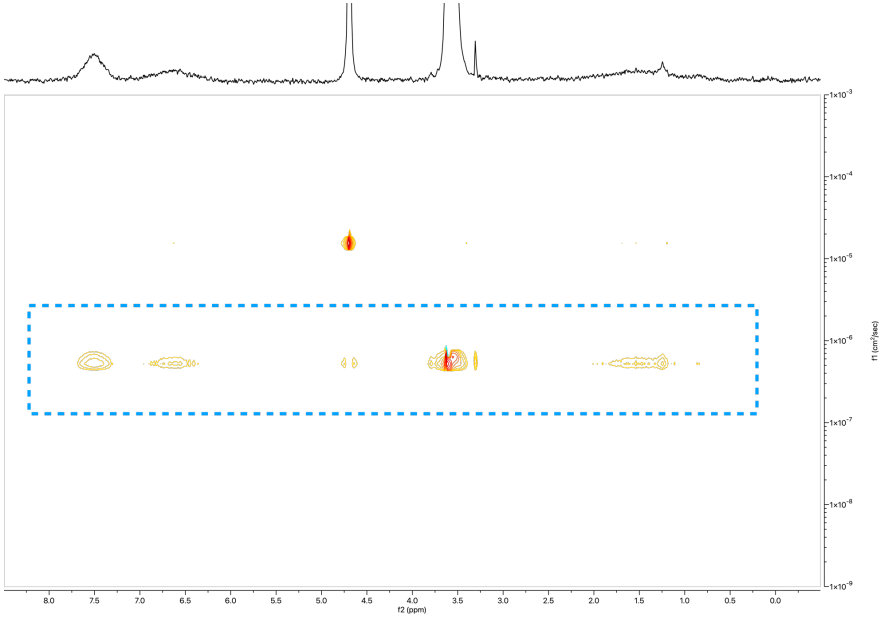
Aqueous SEC Chromatogram of PEG$_{5k}$-b-PSS$_{20}$:
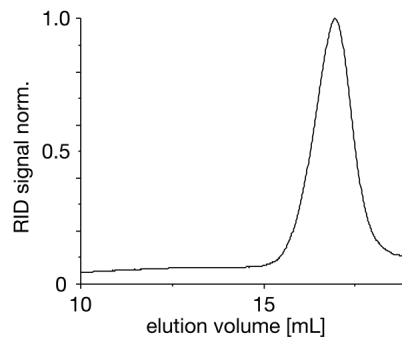
4.   General sample preparations and analytical methods.

UV-Vis measurements on plate reader. UV-Vis measurements in a 96 well plate (tissue culture plates, non-treated) format were performed on a SpectraMax® ABS Plus plate reader from Molecular Devices. The absorbance at 600 nm was used as a measure for turbidity for a sample volume of 100 µL per well. The temperature was set to 25 °C. Absorbance data was normalized to the maximum values after blank subtraction for the comparison of different polyanions under the same sample concentrations.

CCC (critical coacervation concentration) determination. The CCC values for PSS, PVS and PVPA were determined by adding different amounts of AcF(RG)$_3$D-OH peptide and EDC to a solution containing 4.1 mM of the respective polyanion (expressed in monomer units) and 200 mM MES buffer at pH 5.3 (PSS and PVS: 6 mM AcF(RG)$_3$D-OH fueled with 5 mM of EDC; PVPA: 6 mM AcF(RG)$_3$D-OH fueled with 15 mM EDC). The emergence of turbidity and the complete dissolution of the resulting emulsions were monitored on a plate-reader (see UV-Vis measurements on plate reader). The starting and end points of turbidity were taken from the turbidity traces and the corresponding peptide anhydride concentrations were obtained from the kinetic model.

S 19

For the peptide anhydride model AcG(RG)$_3$N-NH$_2$, the CCC values were determined by increasing the peptide concentration gradually in samples containing 4.1 mM of the respective polyanion in 200 mM MES buffer at pH 5.3 until a turbid sample was created.

TEM analysis. Transmission electron microscopy analysis of coacervate core micelle samples were performed on a JEOL JEM 1400 plus instrument at an acceleration voltage of 120 kV. TEM grids were hydrophilized by glow discharge for 30 s before sample preparation. Then, 0.5 µL of the sample (7.46 mM AcF(RG)$_3$N-NH$_2$, 8.54 mM AcF(RG)$_3$D-OH, 25 mM block copolymer expressed in negative charges, 200 mM MES pH 5.3) were placed onto the hydrophilized carbon-coated copper mesh grid and incubated for 30 s. Excess liquid was paper-blotted afterwards. The dried grid was then stained with an aqueous 2 wt% uranyl acetate solution for 30 s and the excess liquid was blotted again with filter paper before imaging.

DLS analysis. DLS analysis was performed on a Litesizer 500 particle size analyzer equipped with a 658 nm 40 mW laser diode. Samples were transferred into a 45 µL low volume quartz cuvette (3x3 mm light path, Hellma Analytics) for size measurements or into an Omega cuvette (Anton Paar) for ζ-potential measurements. The Smoluchowski approximation was used for ζ-potential analysis. Equilibrated coacervates composed of the respective polyanion, polyanion-block copolymers, AcF(RG)$_3$D-OH and AcF(RG)$_3$N-NH$_2$ in 200 mM MES at pH 5.3 were used to mimic the peptide and anhydride concentrations at the anhydride concentration maximum during the reaction cycle as obtained from the kinetic model. Static samples were diluted 10-fold with MQ water right before analysis after an incubation for 10 minutes.

General confocal fluorescence microscopy and microfluidics experiments.[7]

To analyze the coacervate in a microfluidic droplet a lightning SP8 confocal microscope (Leica) with a 63x water immersion objective was used. Coacervates were stained with the fluorophore Sulforhodamine B which was excited at 552 nm and detected from 565-700 nm with a HyD detector. The pinhole was set to 1 Airy unit. To analyze the evolution of coacervates in the entire microfluidic droplet, time series imaging of a single microfluidic droplet was acquired in

S 20

z-stacks with 2 µm between z-planes (20 z-planes in total). All experiments that imaged the entire microfluidic droplet were acquired with a resolution of 600 x 600 pixels at 3.3x zoom and 400x scan speed (bidirectional scan) which results in a time resolution of 17.4 s/stack.

Microfluidic chip production. Microfluidic PDMS (Polydimethylsiloxane, Sylgard 184, Dow Corning)-based devices were designed with QCAD-pro (RibbonSoft GmbH) and fabricated using photo- and soft-lithography[8] as previously described.[9]

Fluorescence recovery after photobleaching (FRAP) experiments.

The diffusivity inside of coacervates was calculated from fluorescence recovery after photobleaching experiments. Measurements were performed in a microscopy well plate chamber (IBIDI, µ-slide Angiogenesis Glass Bottom) that was coated with PVA.[10] Coacervates were stained with NBD-G(RG)$_3$D-OH, the NBD labeled, fluorescent version of the precursor peptide Ac-F(RG)$_3$D-OH, which was excited at 488 nm and detected from 565-635 nm with a PMT detector. FRAP experiments were performed on coacervates that were close to the glass at the bottom of the imaging chamber to ensure having coacervates of sufficient size and to minimize their movement during imaging. Images were acquired at a resolution of 135x135 pixels, 400x scan speed (bidirectional scan) and 15x zoom. A spot size of 1 µm in radius was chosen for bleaching and is kept constant for all experiments. Recovery data were normalized through double normalization with the following equation:

$$F(t) = \frac{(T_0 - B_o)(I_t - B_t)}{(T_t - B_t)(I_0 - B_0)}$$

Here *F(t)* represents the normalized fluorescence intensity which is calculated from the average intensity of 3 ROIs. I_t represents the average intensity of the bleached ROI, T_t represents the average intensity of an unbleached ROI within the bleached coacervate and B_t represents the average intensity of a ROI without any coacervates. The fluorescence recovery *F(t)* is then given by the equation[11]

S 21

$$F(t) = F_{\infty} \exp\left[-\frac{2}{1 + \left(\frac{8tD}{a^2}\right)}\right]$$

with F_{∞} representing the fluorescence at full recovery, a representing the radius of the bleached area and D representing the translational diffusion coefficient of the fluorescent probe.[11]

Analytical HPLC. Analytical RP-HPLC analysis was performed with a ThermoFisher Dionex Ultimate 3000 LC setup (Dionex Ultimate pump, Autosampler, RS Variable Wavelength Detector and column oven set to 25°C). The samples were analyzed in a linear gradient from 2% to 98% ACN in MQ water, both with 0.1% TFA at a flow rate of 1 mL/min. A ThermoScientific Hypersil GOLD column (250 x 4.6 mm, 5 µm particle size) was used. The detection wavelengths were set to 220 and 254 nm and the data was analyzed with the Chromeleon 7 Chromatography Data System Software (Version 7.2 SR4).

Preparative HPLC. Peptide purification was performed by preparative RP-HPLC on an Agilent 1260 Infinity II setup (1260 Infinity II Preparative Binary Pump, 1260 Infinity II Variable Wavelength Detector and 1260 Infinity II Preparative-Scale Fraction Collector). Separation was performed in a linear gradient from 2% to 98% ACN in MQ water, both with 0.1% TFA at a flow rate of 20 mL/min on an Agilent InfinityLab ZORBAX SB-C18 column (250 mm x 21.2 mm, 5 µm particle size). The instrument was operated with the Agilent OpenLab Control software.

ITC measurements. ITC titrations were performed on a MicroCal PEAQ-ITC instrument from Malvern Panalytical. All experiments were performed at 25°C with a control titration of the respective amount of peptide in 200 mM MES buffer (pH 5.3) into the same buffer without any polyanion. All samples were (cell and titration solutions) were prepared with the same concentration of MES buffer (200 mM at pH 5.3) and additional NaCl (none, 250 mM or 500 mM NaCl) to avoid additional dilution effects. The data was analyzed with a non-linear least squares algorithm provided with the PEAQ-ITC analysis software. The component concentrations were chosen in a regime where no coacervation could be observed.

S 22
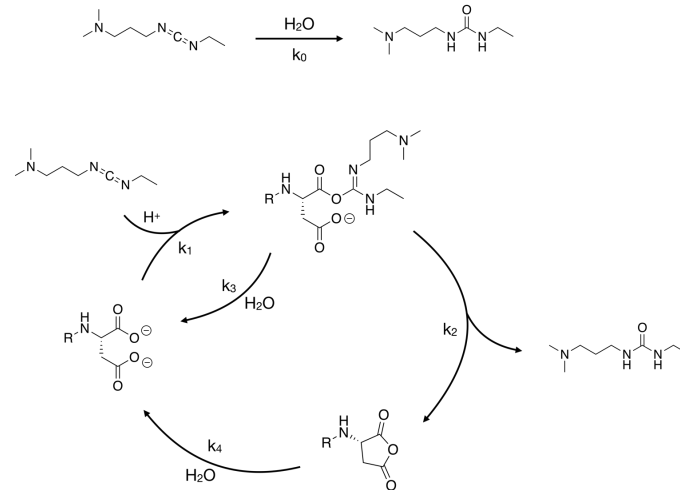
Kinetic modeling.

A kinetic model was written in MATLAB to fit the concentrations of the precursor peptide, the peptide anhydride and EDC based on our chemical reaction cycle (Fig. X).[10] The concentrations of these species was monitored by analytical HPLC with a quenching method applying benzylamine (Fig. 1).[12]
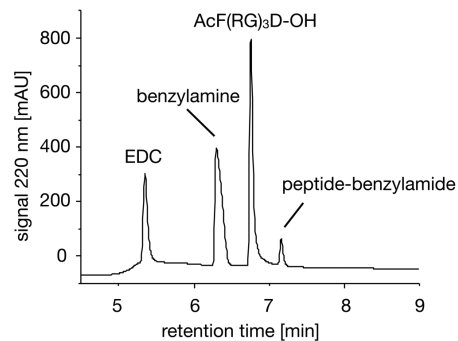
Fig. 1. HPLC-chromatogram of 23 mM of AcF(RG)$_3$D-OH that were fueled with 15 mM of EDC in the presence of 4.1 mM PVS (expressed in monomer units) in 200 mM MES at pH 5.3 after quenching with a 300 mM benzylamine solution at t = 1.5 min. The samples were measured directly after quenching.

The following k-values were obtained:

$k_0 = 7.50 \cdot 10^{-5} \ s^{-1}$

$k_1 = 1.80 \cdot 10^{-1} \ M^{-1} \ s^{-1}$

$k_2 = 5.40 \cdot 10^{-1} \text{ s}^{-1}$

$k_3 = 2.16 \cdot 10^{-1} \text{ s}^{-1}$

$k_4 = 0.85 \cdot 10^{-2} \text{ s}^{-1}$

5.   Supporting Figures and Tables.
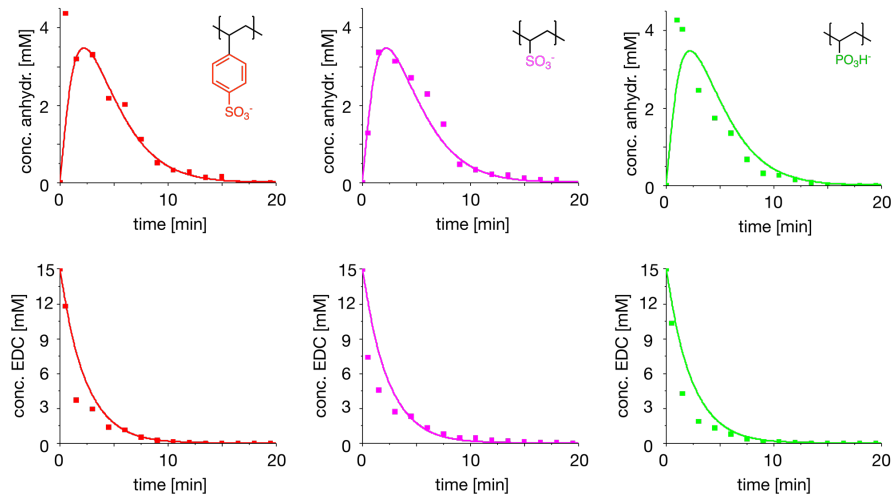
Supporting Figure 1. Analysis of the peptide anhydride concentration (as determined with a quenching method (see Methods for details) and EDC concentration over time. 23 mM of the peptide AcF(RG)$_3$D-OH were fueled with 15 mM of the carbodiimide fuel EDC in the presence of 4.1 mM of the corresponding polyanions (expressed in monomer units). All reactions were performed in 200 mM of MES buffer at a pH of 5.3.
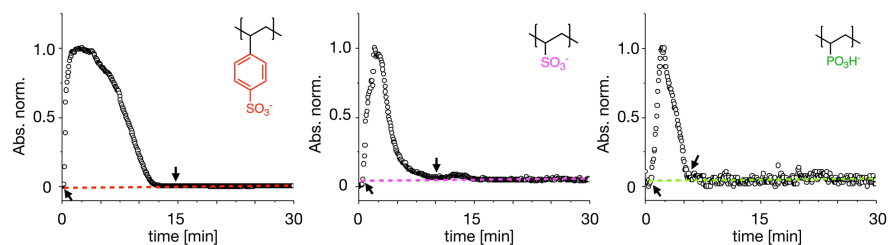
Supporting Figure 2. Determination of the CCC values for 4.1 mM of the different polyanions by turbidity. For PSS and PVS, 6 mM of AcF(RG)$_3$D-OH were fueled with 5 mM of EDC in 200 mM MES pH 5.3. For PVPA, 6 mM of AcF(RG)$_3$D-OH were fueled with 15 mM of EDC.

S 25
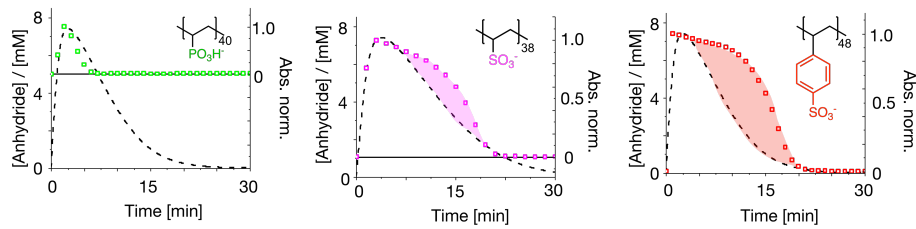
Supporting Figure 3. Turbidity traces of samples after fueling 16 mM of the peptide AcF(RG)$_3$D-OH with 50 mM of EDC in the presence of 25 mM of polyanion (monomer units) all in 200 mM MES buffer at pH 5.3 (N = 3, data was normalized to the maxima).

A

B
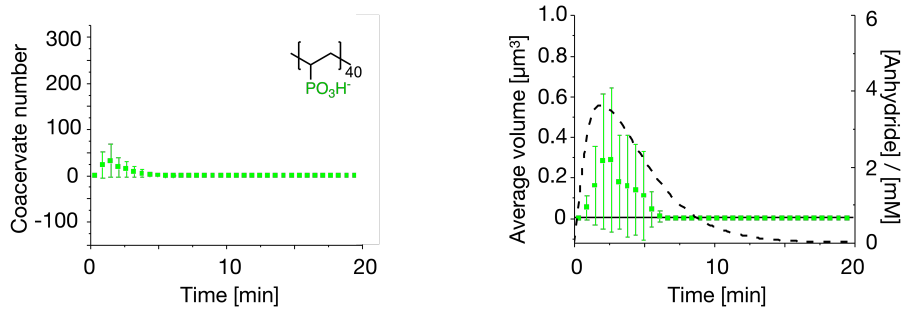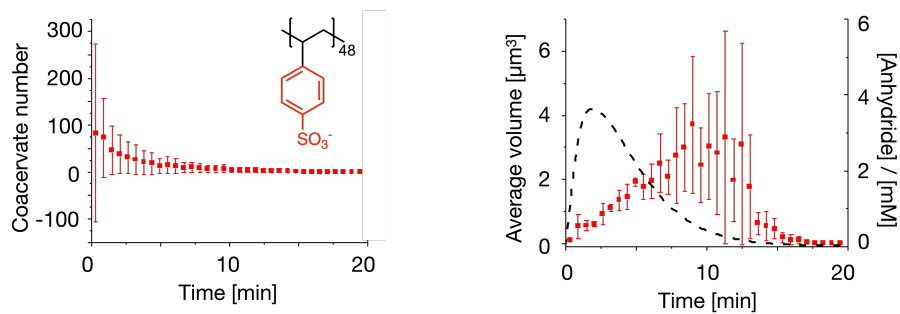
Supporting Figure 4. Analysis of coacervate droplets built from PVPA$_{40}$ (green) and PSS$_{48}$ (red) inside of container droplets created in a microfluidics setup. 23 mM of AcF(RG)$_3$D-OH were fueled with 15 mM of EDC in the presence of 4.1 mM polyanion (monomer units) in 200 mM MES at pH 5.3. Sulforhodamine B was used as the fluorescent dye. The dotted lines are the peptide anhydride concentration profiles obtained from the kinetic model.
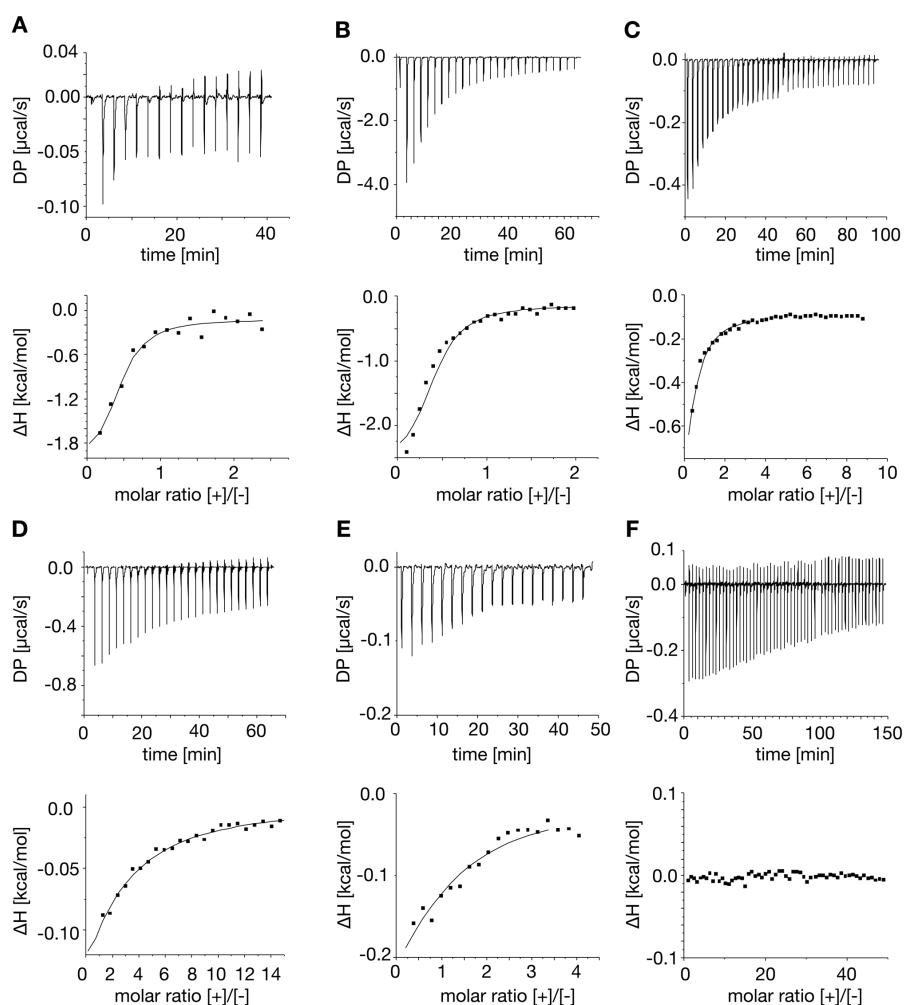
Supporting Figure 5. ITC titrations of the different polyanions with the peptide precursor AcF(RG)₃D-OH and the peptide anhydride model peptide AcF(RG)₃N-NH₂ with the corresponding integrated and modeled data. **A**. 25 µM PSS titrated with 125 µM AcF(RG)₃N-NH₂. **B**. 1 mM PSS titrated with 15 mM AcF(RG)₃D-OH **C**. 250 µM PVS titrated with 1.67 mM AcF(RG)₃N-NH₂. **D**.500 µM PVS titrated with 38 mM AcF(RG)₃D-OH **E**. 250 µM PVPA titrated with 1.67 mM AcF(RG)₃N-NH₂ **F**. 250 µM PVPA titrated with 38 mM AcF(RG)₃D-OH.

S 27
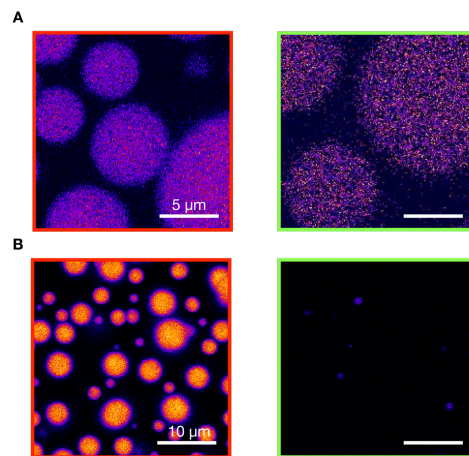
Supporting Figure 6. A. Differences in partitioning of NBD-G(RG)$_3$D-OH in static coacervates built from 7.46 mM AcF(RG)$_3$N-NH$_2$, 8.54 mM AcF(RG)$_3$D-OH and 25 mM of the polyanions (expressed in monomer units), all in 200 mM MES at pH 5.3. Left (red): PSS$_{48}$, partitioning: 14.0 ± 2.6. Right (green): PVPA$_{40}$, partitioning: 7.7 ± 1.3. **B.** Differences in partitioning of NBD-G(RG)$_3$D-OH into coacervates in samples of 16 mM AcF(RG)$_3$D-OH that were fueled with 50 mM of EDC in the presence of 25 mM polyanion (expressed in monomer units) in 200 mM MES at pH 5.3, 2 minutes into the cycle. Left (red): PSS$_{48}$, partitioning: 397.61 ± 131.48 (N = 11). Right (green): PVPA$_{40}$, partitioning: 79.00 ± 26.04 (N = 10).
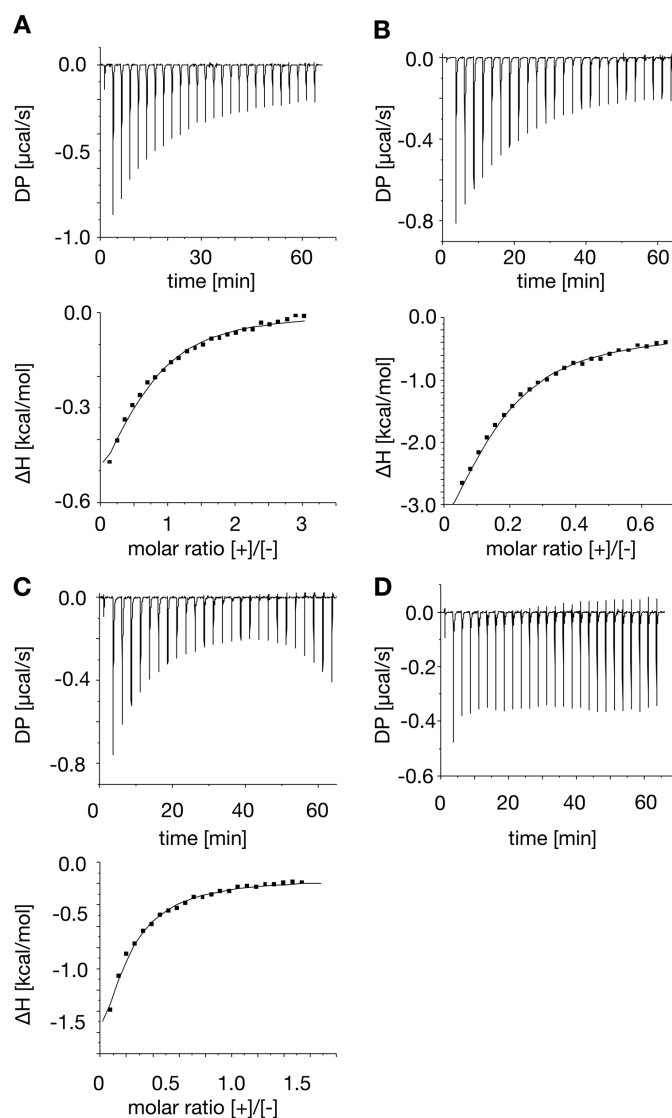
Supporting Figure 7. ITC titrations of PSS with AcF(RG)$_3$D-OH and AcF(RG)$_3$N-NH$_2$ in the presence of NaCl. **A**. 1 mM PSS titrated with 15 mM AcF(RG)$_3$D-OH in the presence of 250 mM NaCl **B.** 600 µM PSS titrated with 0.67 mM AcF(RG)$_3$N-NH$_2$ in the presence of 250 mM NaCl **C**. 600 µM PSS titrated with 1.67 mM AcF(RG)$_3$N-NH$_2$ in the presence of 500 mM NaCl. The data after 45 minutes was not considered for analysis due to the contribution of phase separation. **D**. 1 mM PSS titrated with 10 mM AcF(RG)$_3$D-OH in the presence of 500 mM NaCl. No binding could be observed and only the dilution during the titration was contributing to the signal.

S 29
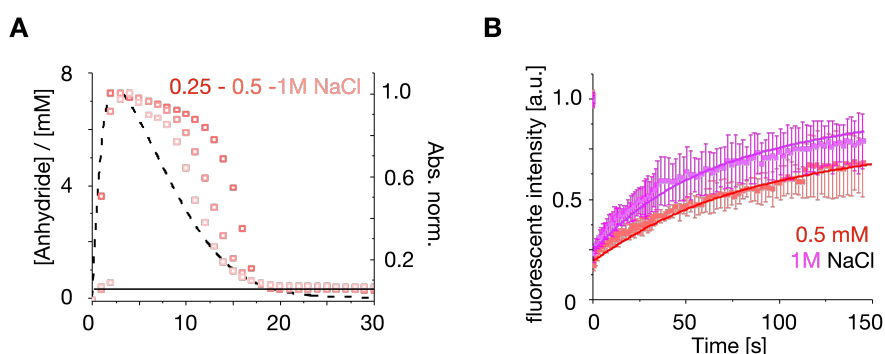
Supporting Figure 8. A. Turbidity traces of coacervates (16 mM of AcF(RG)$_3$D-OH, 50 mM of EDC, 25 mM of PSS (expressed in monomer units), all in 200 mM MES at pH 5.3, N = 3) in the presence of various amounts of salt (250 mM, 500 mM and 1 M NaCl) overlayed with the peptide anhydride concentration profile (dotted line). **B.** FRAP data on static coacervate droplets (7.46 mM AcF(RG)$_3$N-NH$_2$, 8.54 mM AcF(RG)$_3$D-OH, 25 mM PSS, 200 mM MES pH 5.3) with NBD-G(RG)$_3$D-OH as the fluorescently labeled building block in the presence of 500 mM (D = 0.003 µm$^2\cdot$s^{-1}, N = 10) or 1M of NaCl (D = 0.005 µm$^2\cdot$s^{-1}, N = 10).

	(PVPA)$_{20}$	PEG$_{5k}$-b-PVPA$_{21}$	(PSS)$_{21}$	PEG$_{5k}$-b-PSS$_{20}$
d$_{hydr.}$ [µm] [a]	1.9	0.46	5.7	0.054
ζ - potential [mV] [a]	-8.4	-3.0	-4.5	-2.6
d$_{hydr.}$ [µm] [b]	6.0	0.20	6.6	0.058
ζ - potential [mV] [b]	-6.0	-4.9	-2.1	-2.4

Supporting Table 1. DLS analysis of static samples of the homopolymers and the corresponding block copolymers with PEG. To emulate the droplets in chemically fueled samples at the expected maximum of anhydride concentration, [a] 19.34 mM of AcF(RG)$_3$D-OH and 3.66 mM AcF(RG)$_3$N-NH$_2$ were added to 4.1 mM of polyanion and [b] 8.54 mM of AcF(RG)$_3$D-OH and 7.46 mM AcF(RG)$_3$N-NH$_2$ were added to 25 mM of polyanion (monomer units of charged block) in 200 mM MES buffer at pH 5.3.
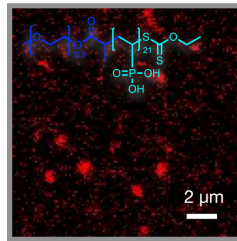
Supporting Figure 9. Confocal microscopy image of the assemblies obtained in samples that contained 25 mM of PEG-b-PVPA and 16 mM of AcF(RG)$_3$D-OH that was fueled by adding 50 mM of EDC in 200 mM MES buffer at pH 5.3. Sulforhodamine B was added as a fluorescent dye.
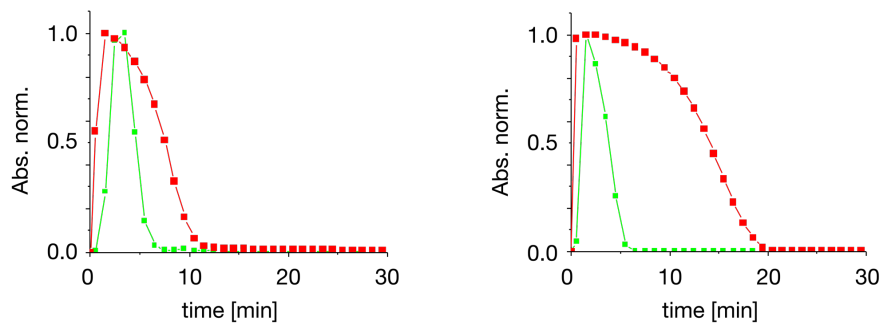
Supporting Figure 10. Left: Turbidity traces of 4.1 mM PVPA$_{20}$ (green) and PSS$_{21}$ (red) after fueling 23 mM of AcF(RG)$_3$D-OH with 15 mM of EDC all in 200 mM of MES buffer at pH 5.3. Right: Turbidity traces of the same polymers after fueling 16 mM of peptide with 50 mM of EDC in the presence of 25 mM of the polyanions in 200 mM MES pH 5.3.

S 31

105
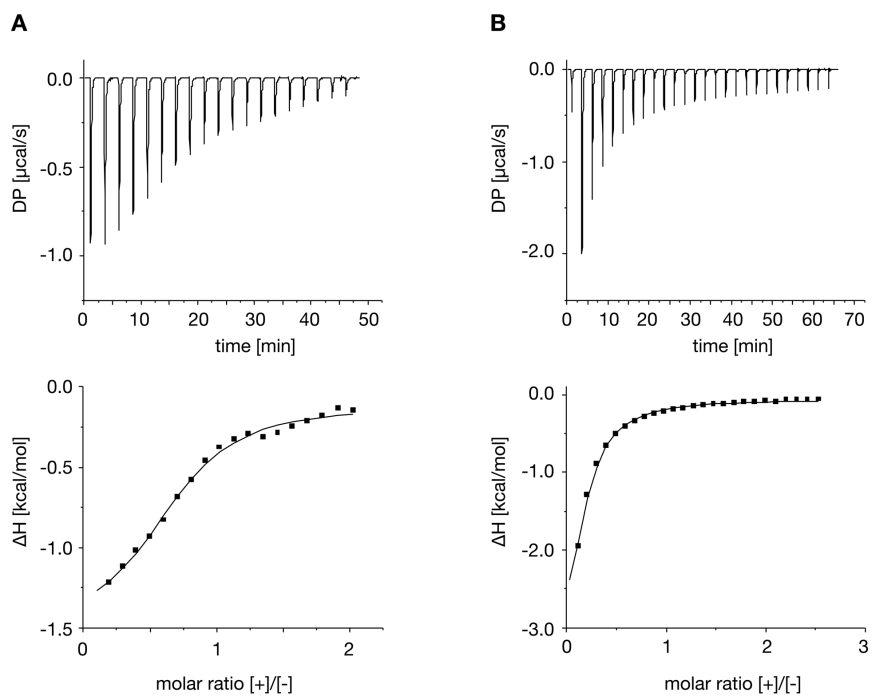
Supporting Figure 11. ITC titration curve (upper row) of PEG-b-PSS with (**A**) AcF(RG)$_3$D-OH and (**B**) AcF(RG)$_3$N-NH$_2$ with the corresponding fitting of the integrated data (lower row). The following conditions were applied: **A.** 800 µM of PEG$_{5k}$-b-PSS$_{20}$ titrated with 10 mM AcF(RG)$_3$D-OH. **B.** 500 µM of PEG$_{5k}$-b-PSS$_{20}$ titrated with 1.67 mM AcF(RG)$_3$N-NH$_2$.

6. References

[1] S. Salzinger, B. S. Soller, A. Plikhta, U. B. Seemann, E. Herdtweck, B. Rieger, *J. Am. Chem. Soc.* **2013**, *135*, 13030-13040.

[2] T. M. Pehl, M. Kränzlein, F. Adams, A. Schaffer, B. Rieger, *Catalysts* **2020**, *10*, 448.

[3] B. S. Soller, S. Salzinger, C. Jandl, A. Pöthig, B. Rieger, *Organometallics* **2015**, *34*, 2703-2706.

[4] S. Salzinger, U. B. Seemann, A. Plikhta, B. Rieger, *Macromolecules* **2011**, *44*, 5920-5927.

[5] a) M. Fuentes-Exposito, S. Norsic, T. Février, P.-Y. Dugas, S. Boutti, S. Devisme, A. Bonnet, F. D'Agosto, M. Lansalot, *Polym. Chem.* **2021**, *12*, 5640-5649; b) K. H. Markiewicz, L. Seiler, I. Misztalewska, K. Winkler, S. Harrisson, A. Z. Wilczewska, M. Destarac, J. D. Marty, *Polym. Chem.* **2016**, *7*, 6391-6399.

[6] J. M. Ting, H. Wu, A. Herzog-Arbeitman, S. Srivastava, M. V. Tirrell, *ACS Macro Lett.* **2018**, *7*, 726-733.

[7] A. M. Bergmann, C. Donau, F. Späth, K. Jahnke, K. Göpfrich, J. Boekhoven, *Angew. Chem. Int. Ed.* **2022**, *61*, e202203928.

[8] D. C. Duffy, J. C. McDonald, O. J. Schueller, G. M. Whitesides, *Anal. Chem.* **1998**, *70*, 4974-4984.

[9] a) M. Weiss, J. P. Frohnmayer, L. T. Benk, B. Haller, J. W. Janiesch, T. Heitkamp, M. Borsch, R. B. Lira, R. Dimova, R. Lipowsky, E. Bodenschatz, J. C. Baret, T. Vidakovic-Koch, K. Sundmacher, I. Platzman, J. P. Spatz, *Nat. Mater.* **2018**, *17*, 89-96; b) T. W. Hofmann, S. Hanselmann, J. W. Janiesch, A. Rademacher, C. H. Bohm, *Lab Chip* **2012**, *12*, 916-922.

[10] F. Späth, C. Donau, A. M. Bergmann, M. Kränzlein, C. V. Synatschke, B. Rieger, J. Boekhoven, *J. Am. Chem. Soc.* **2021**, *143*, 4782-4789.

[11] A. B. Kayitmazer, H. B. Bohidar, K. W. Mattison, A. Bose, J. Sarkar, A. Hashidzume, P. S. Russo, W. Jaeger, P. L. Dubin, *Soft Matter* **2007**, *3*, 1064-1076.

[12] F. Schnitter, J. Boekhoven, *ChemSystemsChem* **2020**, *3*, e2000037.

6. Oligonucleotides as Polyanions in Chemically Fueled Complex Coacervation

Abstract

In Chapter 5, I characterized various polyanions as building blocks in chemically fueled complex coacervates. I described that the affinities to the peptides in these chemically fueled coacervates depend on the functional group of the polyanion. This influence of the passive polymer components controls the macroscopic outcome of the complex coacervation reaction cycle. For example, the weakly binding polyanion PVPA forms droplets with a significantly shorter lifetime than coacervates built from PSS. In this chapter, I investigate a similar relation using oligonucleotides as polyanions. These polymers with phosphodiester backbone share structural similarities with the previously described poly(vinyl phosphonates). However, oligonucleotides offer a bigger structural diversity due to the different nucleobases and sugar moieties in their backbone. Moreover, as oligonucleotides serve as biology's genotype, we envision that these polymers could also be used as a genotype in *de novo* life.

ITC analysis shows that oligonucleotides are weak polyanions with the nucleobases playing a role in the binding. The lower binding affinity can be compensated for by longer chains or higher peptide anhydride concentrations by adjusting the concentrations of the reactive components in the chemical reaction cycle. Still, such an approach can result in metastable coacervates. In addition, double-stranded DNA shows a lower phase separation tendency in the chemical reaction cycle because their hybridization hinders condensation. In conclusion, oligonucleotides are structurally diverse and versatile polyanions for chemically fueled coacervation. The possibility of influencing their behavior in phase separation by hybridization without changing their structure or sequence makes them unique compared to poly(vinyl) or poly(styrene) derived polyanions. Next to their biological relevance, this versatility makes them attractive building blocks for active droplets with life-like properties.

6.1. Introduction

In a biological context, DNA is critical for its information storage capacity and role in cell signaling. Various condensation phenomena and binding pathways to DNA are involved in these processes.[99] Membraneless organelles as biomolecular condensates often contain specific proteins and nucleic acids, *i.e.,* DNA and/or RNA. These reaction hubs are crucial in regulating gene expression by either up-concentrating specific structures or suppressing their activity.[34] DNA's ability to store information and partition inside droplets could help fulfill the requirements for fully autonomous artificial cells that replicate.[100] DNA can be introduced into such non-equilibrium compartments by enzymatic reactions. For example, the group of

Walther introduced an enzymatic reaction network that enables dynamic, multivalency-driven LLPS of sequence-defined nucleic acid polymers. Phase separation by sequence recognition and multivalent binding is triggered by their ATP-driven ligation, competing with their degradation. As soon as the reaction network runs out of ATP, the enzymatic degradation pathway dominates, resulting in a limited lifetime of the coacervate droplets. A suitable tile design even enabled different droplets to exist in parallel or the temporal trapping of objects carrying the fitting complementary ssDNA.[101]

Such droplets rely on the selective and highly specific binding of DNA sequences by base pairing. Nevertheless, DNA molecules are highly charged polymers, making them attractive polyanions for dynamic complex coacervate droplets that form mainly due to electrostatic interactions. RNA molecules were introduced as building blocks in charge-driven, either phosphorylation-controlled, or carbodiimide-driven complex coacervates. In these active droplets, the RNA molecules did not participate in any reaction but served as the polymer scaffold for the active droplets.[65, 69] However, systematic studies on the oligonucleotides' influence on dynamic droplet formation are lacking so far. In this chapter, the properties of oligonucleotides as polyanions in chemically fueled complex coacervation are tested. A detailed understanding of their behavior in response to a chemical reaction cycle is required to exploit their full potential as components in artificial cells and out-of-equilibrium models for membraneless organelles.

6.2. Results and Discussion

We tested various oligonucleotides as polyanions for their ability to produce active droplets with a peptide that is regulated by a fuel-driven chemical reaction cycle. Specifically, a peptide precursor with a C-terminal aspartic acid is activated via the carbodiimide EDC. This reaction leads to the formation of the peptide anhydride and effectively negates two negative charges. The peptide anhydride is hydrolytically unstable and reverts to the dicarboxylate in aqueous media with a half-life of 82 seconds in 200 mM MES buffer at pH 5.3.[102] The two negative charges are reinstated in this deactivation reaction. Due to the three positively charged arginine-glycine repeat units, the peptide AcF(RG)$_3$D-OH can switch its overall charge from +1 to +3 by the peptide anhydride formation and return to +1 via hydrolysis in this reaction cycle. Because of the transient nature of peptide anhydride and its ability to induce complex coacervation with the appropriate polyanion, active coacervate droplets with a limited lifetime can be formed (Fig. 1 **A**). Previous work of our group has shown that different polyanions lead to different outcomes in chemically fueled complex coacervation, such as regimes of metastable droplets or different lifetimes coming from the different binding affinities of the polyanions to the peptide.[72-73, 103]
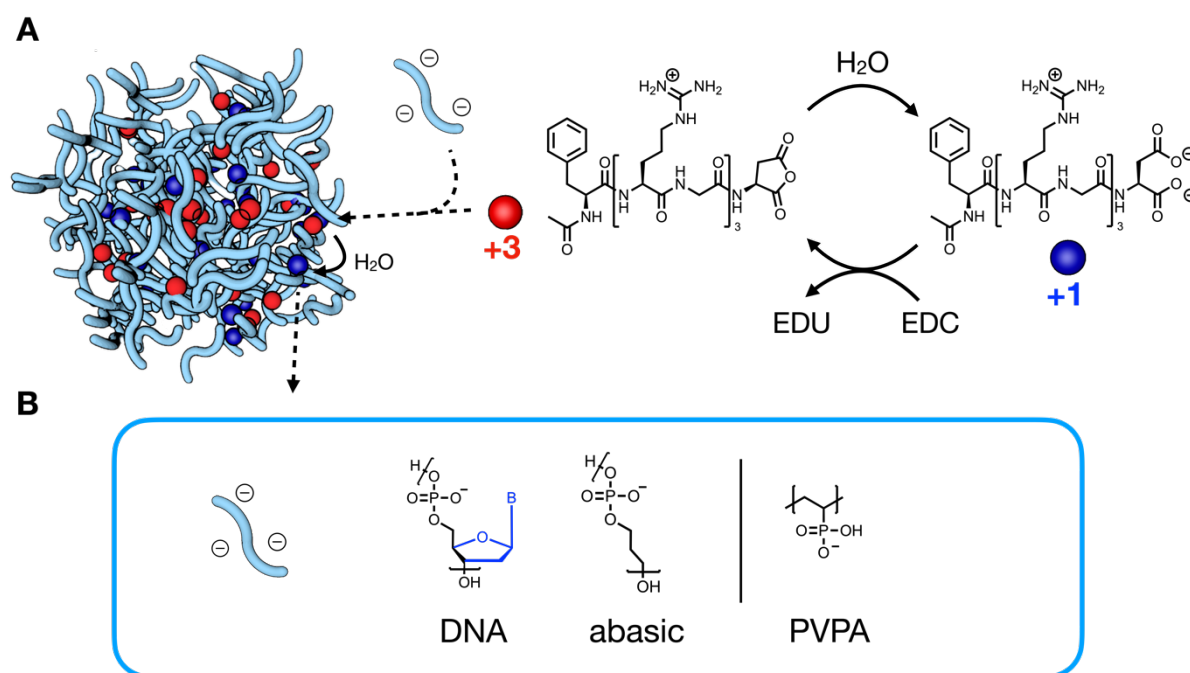
Figure 1. A. The chemical reaction cycle for chemically fueled complex coacervation with a polyanion. The peptide AcF(RG)$_3$D-OH is reversibly transformed into the peptide anhydride, leading to a charge switch from +3 to +1. Since it only phase-separates in its +3 state with a suitable polyanion, active droplets with a limited lifetime are obtained **B**. The general structures of oligonucleotides and abasic strands that are compared to poly(vinyl phosphonates) (PVPA**)** as polyanions in chemically fueled complex coacervation. Inspired and adapted from reference [103], Copyright © 2023, The Authors. CC BY 4.0 DEED, https://creativecommons.org/licenses/by/4.0/.

In this work, we focused on the role of the polyanion in these active coacervate-based droplets with a focus on oligonucleotides. We thus synthesized a library of oligonucleotides with different chain lengths ranging from 20- to 80-mers by solid-phase synthesis. As we were interested in the role of the nucleobases, we synthesized random oligonucleotides, oligomers of thymidine, and also abasic oligomers. In these abasic oligonucleotides, we used a three-carbon spacer to keep a similar carbon count between phosphodiester bonds compared to native DNA and to omit the deoxyribofuranose units in the DNA backbone. We also made variations of abasic and basic DNA sequences. We compared these oligonucleotides to PVPA (Fig. 1**B**) due to the structural similarities between the phosphonic acid and phosphodiester units and previous work showed that PVPA is a suitable polyanion for active droplets.[103] We thus hypothesized that the DNA-based polyanions should behave very similarly in their binding to the peptide.

We used ITC experiments on short model strands with controlled sequences to determine the dissociation constants (K_D-values) with a stable variant of the peptide anhydride. We applied AcF(RG)$_3$N-NH$_2$ (Fig. 2**A**) as a stable model for the anhydride of AcF(RG)$_3$D-OH. AcF(RG)$_3$N-NH$_2$ has a non-charged asparagine amino acid instead of the charged aspartic acid in AcF(RG)$_3$D-OH. Like the anhydride of AcF(RG)$_3$D-OH, it is thus also +3 in overall charge and it has proven useful as a model for the anhydride.[102-103] From now on, AcF(RG)$_3$N-NH$_2$ will be referred to as anhydride model.

The anhydride model was titrated to a 20-mer oligonucleotide with the sequence 5'-ATT TGG TCA GTA TCG AAT GG-3'. The titration revealed a K_D-value of 456 µM for this random sequence with the anhydride model, a value higher than the 350 µM that was obtained for PVPA before (Fig. 2 **B**).[103] For a T-only 20-mer, a value of 404 µM was obtained. To our surprise, the titrations revealed no significant binding of the anhydride model to the abasic 20-mers (Supporting Figure 1 **A** and **B**). Overall, we conclude that phosphodiester-based polymers are weaker polyanions than PVPA. The differences between the abasic oligomer and the oligonucleotides with nucleobases showed that the charged phosphodiester backbone is not the main contributor to the peptide-DNA interactions and that additional interactions with the nucleobases are seemingly important. For example, hydrogen bonding, hydrophobic interactions, and π-π interactions with the nucleobases were identified to play a significant role in the binding of peptides to DNA.[104-106] Taking previous results into consideration, oligonucleotides turned out to be weaker polyanions than all other polyelectrolytes that we introduced before for chemically fueled complex coacervation.[103]
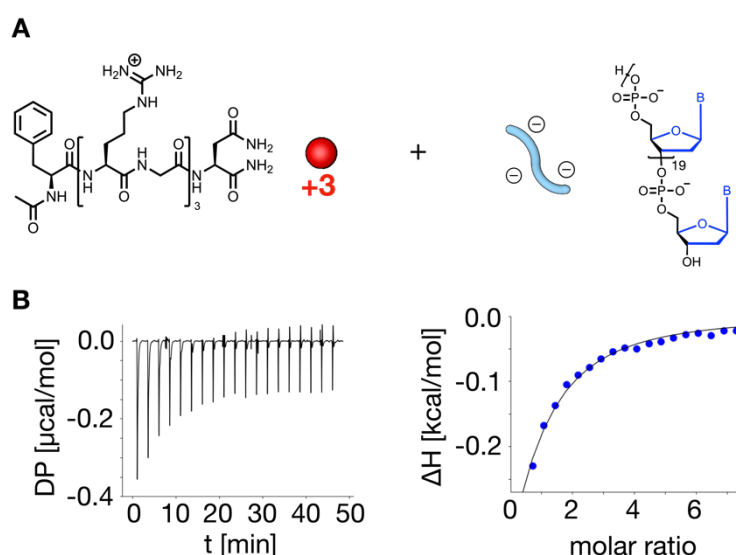
Figure 2. A. ITC analysis of oligonucleotide model strands with the anhydride model. The model strands were 5'-ATT TGG TCA GTA TCG AAT GG-3', a T-only 20-mer and an abasic 20-mer. The last deoxythymidine unit was added to the abasic strands for analytical purposes. **B.** The exemplary titration curve that was obtained when a 3 mM stock of AcF(RG)$_3$N-NH$_2$ was

titrated to 250 µM 5'-ATT TGG TCA GTA TCG AAT GG-3' (expressed in monomer units) in 200 mM MES buffer at pH 5.3 and 25°C.

With an understanding of the binding capability of the anhydride model to oligonucleotides, we tested their ability to form complex coacervates upon fueling with EDC as the carbodiimide fuel. We applied oligomers with discrete lengths from 20 to 80mers of different sequences. The library contained a 20-mer and 45-mer sequence with random bases, a 20-mer sequence that was abasic, and 20-, 40-, 45- and 80-mers of T-only sequences (Table 1). Long single-stranded DNA (587-831 bp) and long double-stranded DNA (<2000 bp) were also tested. To 4.1 mM of every oligonucleotide (expressed in monomer units or charges) and 23 mM of AcF(RG)$_3$D-OH, 15 mM of EDC was added in 200 mM MES buffer at pH 5.3. Under these fueling conditions, a maximum peptide anhydride concentration of 3.6 mM is reached, sufficient to make droplets using PVPA as the polyanion (see Supporting Figure 2). Unlike this sample, none of the DNA samples showed signs of coacervation as they all remained clear. To be able make droplets with DNA, we decreased the amount of peptide and increased the amount of fuel. Specifically, we added 16 mM of AcF(RG)$_3$D-OH and 50 mM of EDC and observed emerging turbidity only for the DNA samples containing the T-only 80-mer, (dT)$_{80}$, and long single- or double-stranded DNA (Table 1). Under these fueling conditions, a maximum peptide anhydride concentration of 7.46 mM is obtained, a value more than twice as high as 3.6 mM for 23 mM of AcF(RG)$_3$D-OH fueled with 15 mM EDC.[102-103]

Entry	Sequence (5'→3')	Coacervation with AcF(RG)$_3$D-OH upon fueling?
[1]	(C3)$_{19}$T	-
[2]	T$_{20}$	-
[3]	ATT TGG TCA GTA TCG AAT GG	-
[4]	(C3-T)$_{20}$	-
[5]	T$_{40}$	-
[6]	T$_{45}$	-
[7]	CTT CGG TGT AAA GAT TCA TCT CAG TCC ATT CGA TAC TGA CCA AAT	-
[8]	T$_{80}$	Yes
[9]	ssDNA (587-831 bp)	Yes
[10]	dsDNA (<2000 bp)	Yes
[11]	PVPA$_{40}$	Yes

Table 1. Different oligonucleotide sequences were tested for their coacervation ability with AcF(RG)$_3$D-OH upon fueling with EDC. The applied conditions were 16 mM AcF(RG)$_3$D-OH,

4.1 mM negative charges (calculated from the monomer unit concentration) from the oligonucleotide, and 50 mM EDC in 200 mM MES at pH 5.3. The emergence of turbidity was assessed via UV-Vis spectroscopy by the absorbance at 600 nm.

With these working conditions, namely 16 mM AcF(RG)$_3$D-OH, 4.1 mM negative charges and 50 mM EDC in 200 mM MES buffer at pH 5.3, we compared the evolution of turbidity in (dT)$_{80}$ samples to PVPA$_{40}$ samples on a UV-Vis plate reader. In direct comparison (Fig. 3 **A** and **B**), turbidity peaked one minute after fuel addition for both samples, but (dT)$_{80}$ coacervates showed only half the droplet lifetime (7 minutes) compared to PVPA$_{40}$ coacervates (15 minutes). We ruled out any influence of the oligonucleotides on the reaction cycle by measuring the peptide anhydride concentration over time by HPLC. Indeed, the peptide anhydride concentration nicely followed the predicted concentration evolution from a kinetic model (see Supporting Figure 3).[102] Since the reaction cycle was unaffected by the oligonucleotides, we explain the different outcomes of chemically fueled coacervation between (dT)$_{80}$ and PVPA with a significant difference in their critical coacervation concentration (CCC). By comparing the lifetime of the resulting coacervates to the evolution of the peptide anhydride in the kinetic model, a CCC value of 5.69 mM peptide anhydride was obtained for (dT)$_{80}$ and a CCC value of 1.01 mM for PVPA$_{40}$. Put differently, a higher peptide anhydride concentration is necessary to maintain a cohesive coacervate phase with oligonucleotides due to their weak interactions. The fact that oligonucleotides require higher peptide anhydride concentrations in chemically fueled complex coacervation than other polyanions follows from their low binding affinity to the anhydride model as determined by ITC. However, this low binding affinity can be compensated by the multivalency of binding to longer strands, e.g. 80-mers, to enable phase separation. For comparison, PVPA strands as short as 20mers readily formed complex coacervates, even under low peptide concentration and fueling conditions (23 mM AcF(RG)$_3$D-OH fueled with 15 mM EDC, see Supporting Figure 4).[103]
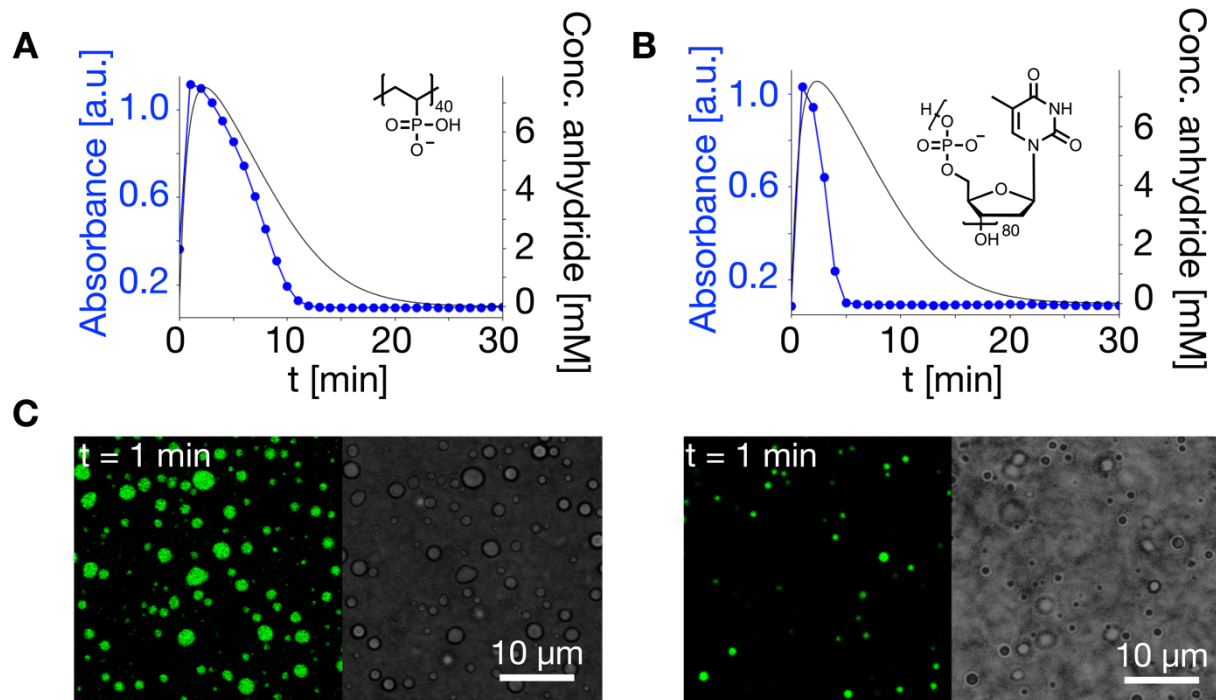
Figure 3. A. Evolution of turbidity (blue trace) during the ongoing reaction cycle of 4.1 mM PVPA$_{40}$. 16 mM AcF(RG)$_3$D-OH were fueled with 50 mM EDC in 200 mM MES buffer pH 5.3. Turbidity was monitored via the absorbance at 600 nm. **B.** Evolution of turbidity (blue trace) during the ongoing reaction of 4.1 mM (dT)$_{80}$ under the same conditions. The turbidity data is overlayed with the evolution of the peptide anhydride concentration (black traces) as obtained from a kinetic model. **C.** Confocal laser micrographs of samples of PVPA$_{40}$ and (dT)$_{80}$. NBD-G(RG)$_3$N-NH$_2$ was used as a fluorescent tracer.

The samples were also imaged via laser confocal microscopy to correlate the emerging turbidity to the appearance of the coacervate droplets (Fig. 3**C**). We added fluorescently labeled anhydride model, NBD-G(RG)$_3$N-NH$_2$, for the imaging (see Methods). One minute after EDC was added to the sample, PVPA$_{40}$ coacervates were present multiple micrometers in size (Fig. 3**C** left). They appeared as liquid droplets that fused readily. In contrast, coacervates from (dT)$_{80}$ were significantly smaller, formed in a lower number, but still fused (Fig. 3**C** right). For both polyanions, the presence of droplets followed the evolution of turbidity from UV-Vis plate reader experiments tightly and no residues remained after all EDC was consumed. We also connect the lower total amount of coacervate phase (smaller number of droplets with smaller size) to the weak peptide-oligonucleotide binding. Compared to PVPA$_{40}$, the peptide anhydride cannot recruit as much oligonucleotide as droplet material, limiting droplet emergence and growth.

DNA's hybridization state is another factor that controls its complex coacervation behavior for in-equilibrium complexes. In general, double-stranded DNA is a stiffer polymer with a higher

charge density and higher hydrophilicity. These factors disfavor the coacervation of double-stranded compared to single-stranded DNA.[107-108] Such effects on chemically active coacervates have not been investigated yet, but we hypothesized that the hybridization state could give another level of control over chemically active coacervation. Thus, we compared the long ssDNA (587-831 bp) to long dsDNA (<2000 bp). The samples showed different responses in chemically fueled coacervation with AcF(RG)$_3$D-OH (Fig. 4). When 4.1 mM of long ssDNA was combined with 16 mM AcF(RG)$_3$D-OH and fueled with 50 mM EDC, turbidity emerged quickly. The evolution of turbidity closely followed the concentration profile of the peptide anhydride (Fig. 4**A** blue trace). We rationalize the longer coacervate lifetime compared to (dT)$_{80}$ (Fig. 3**B**) with the multivalent binding of the longer strands.
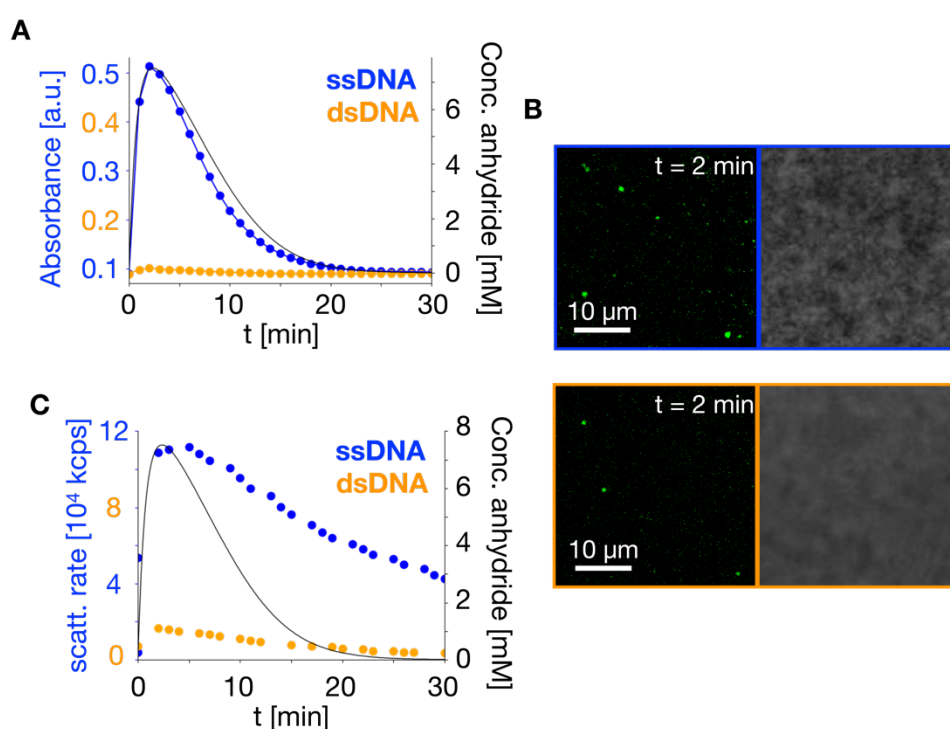
Figure 4. A. Evolution of turbidity of single-stranded (blue) and double-stranded DNA (orange) due to complex coacervation with AcF(RG)$_3$D-OH upon fueling with the carbodiimide fuel EDC. 16 mM of peptide were fueled with 50 mM of EDC in the presence of 4.1 mM DNA (expressed in negative charges/monomer units) in 200 mM MES buffer at pH 5.3 and 25°C. Turbidity was monitored by UV-Vis spectroscopy on a plate-reader via the absorbance value at 600 nm. **B.** Laser-confocal micrographs of chemically fueled complex coacervates formed with ssDNA (blue) and dsDNA (orange) under the abovementioned conditions. NBD-G(RG)$_3$N-NH$_2$ was used as the fluorescent dye at a concentration of 200 μM and compared to bright field images. **C.** Evolution of the scattering rate of ssDNA (blue) and dsDNA (orange) when 16 mM AcF(RG)$_3$D-OH were fueled with 50 mM EDC in the presence of 4.1 mM of oligonucleotide

(expressed in monomer units) in 200 mM MES at pH 5.3. The traces are shown together with the peptide anhydride concentration profile obtained from a kinetic model.

We could only measure low turbidity levels for long dsDNA after fueling in the presence of the peptide, indicating that its phase separation is hindered in its hybridized form (Fig. 4**A** orange trace). This trend is in line with studies that demonstrate that the higher rigidity of double-stranded oligonucleotides impedes condensation due to a higher energy penalty for bending the hybridized strands.[99, 107, 109-110] This effect was also reported for combinations of oligonucleotides with small cationic molecules like the oligoamine spermine.[111] Laser-confocal microscopy revealed that for both samples, only small coacervate droplets were formed, but in a smaller number for the sample with dsDNA compared to ssDNA (Fig. 4**B**). Besides, we observed some solid-like aggregates in this sample, as expected for complexes of double-stranded DNA.[107-108]

Finally, we monitored the response to the reaction cycle via DLS to capture the evolution of the small aggregates that might not have been visible under the microscope or were not captured properly via turbidimetry at 600 nm. Maximum scattering rates 5 times lower for dsDNA than ssDNA were measured (Fig. 4**C**), further proving that the dsDNA coacervate formation was indeed hindered. Aside from that, both scattering rates' evolutions lagged behind the peptide anhydride's concentration profile, particularly in the decay phase. We conclude from this that long DNA strands can still lead to metastable active droplets, even if they only show very weak interactions with the peptide. This is in line with the behavior that we have already observed for polyU of comparable length (2200 bp) or long poly(styrene sulfonate) in chemically fueled complex coacervation having a similar delaying effect in combination with AcF(RG)$_3$D-OH.[69, 103]

6.3.   Conclusion and Outlook

In this work, different oligonucleotides were introduced and tested as polyanions in chemically fueled complex coacervates. Oligonucleotides are helpful to create models for membraneless organelles or artificial cells, but systematic studies on their influences in non-equilibrium coacervates were lacking. This chapter assessed their complex coacervation ability in a carbodiimide-driven reaction cycle. Our study shows that oligonucleotides only weakly interact with the peptide anhydride, resulting in shorter lifetimes of the coacervate droplets compared to PSS, PVS, or PVPA under the given reaction conditions. The low binding affinity towards the peptide anhydride needs to be compensated by longer chains and higher peptide anhydride concentrations. Due to the influence of the nucleobases on the binding affinity to the peptides, it may even be necessary to optimize the conditions of the reaction cycle for specific oligonucleotide sequences in the future. In addition, the hybridization state of oligonucleotides

can be used to further control their complex coacervation behavior. Single-stranded oligomers have a higher tendency to phase-separate than double-stranded ones. This finding will be relevant for coacervate designs with functional oligonucleotides that often require specific secondary structures to be active, *e.g.* tRNA or ribozymes. In summary, we can state that oligonucleotides are versatile polyanions with complex behavior in chemically fueled complex coacervation.

6.4. Supporting Information

The following part presents additional figures and data for Chapter 6.
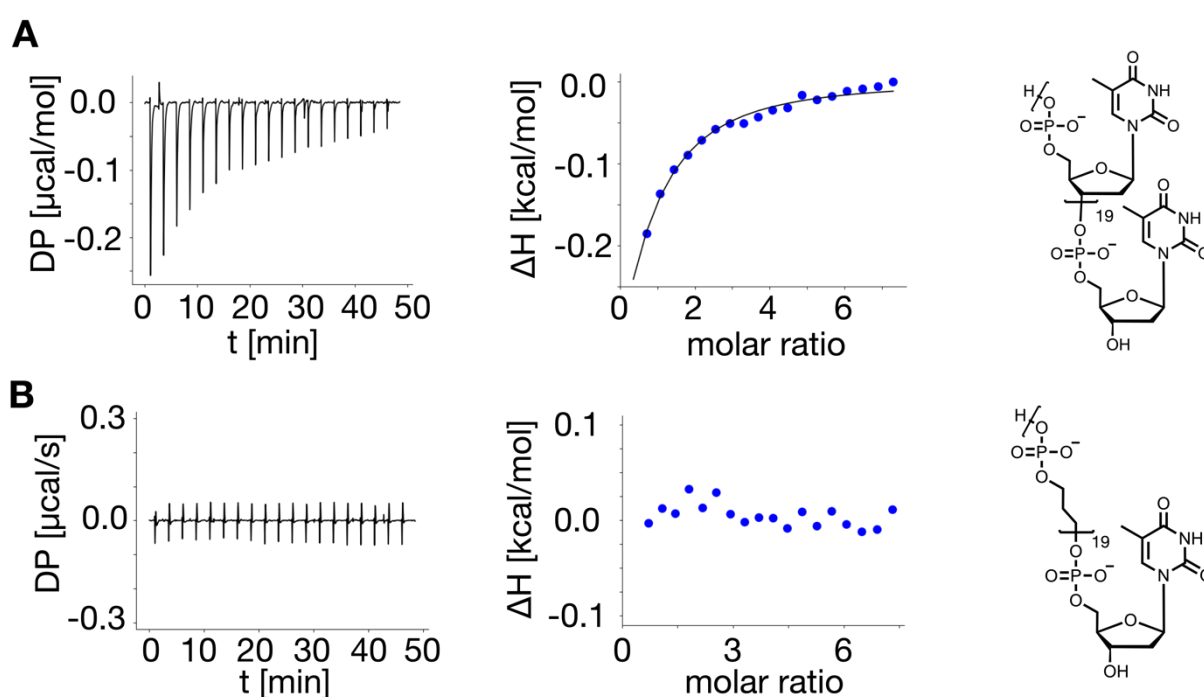
Supporting Figure 1. ITC titration of AcF(RG)$_3$N-NH$_2$ to a T-only 20-mer (**A**) or abasic 20-mer (**B**). 3 mM of AcF(RG)$_3$N-NH$_2$ were titrated to 250 µM of the oligomers (expressed in monomer units or charges) in 200 mM MES buffer at pH 5.3 and 25°C.
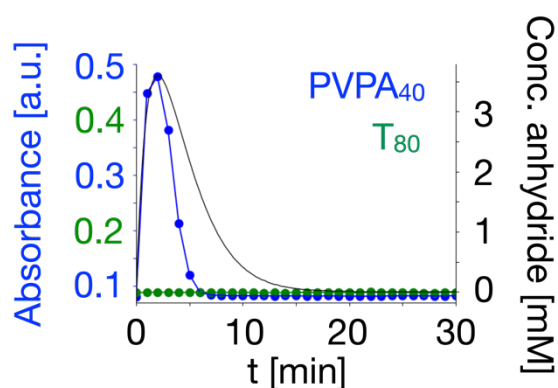
Supporting Figure 2. The evolution of turbidity (blue: $PVPA_{40}$, green: $(dT)_{80}$) of coacervate samples that were obtained from fueling 16 mM $AcF(RG)_3D$-OH with 50 mM EDC in the presence of 4.1 mM polyanion in 200 mM MES buffer at pH 5.3 and 25°C. The data is overlayed with the peptide anhydride evolution that is obtained from a kinetic model.
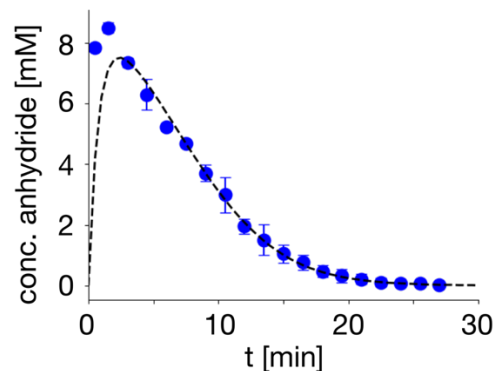
Supporting Figure 3. Overlay of the anhydride concentration obtained from HPLC analysis with benzylamine quench (blue, number of individual runs N = 2). The dashed line is the evolution of peptide anhydride concentration from the kinetic model.
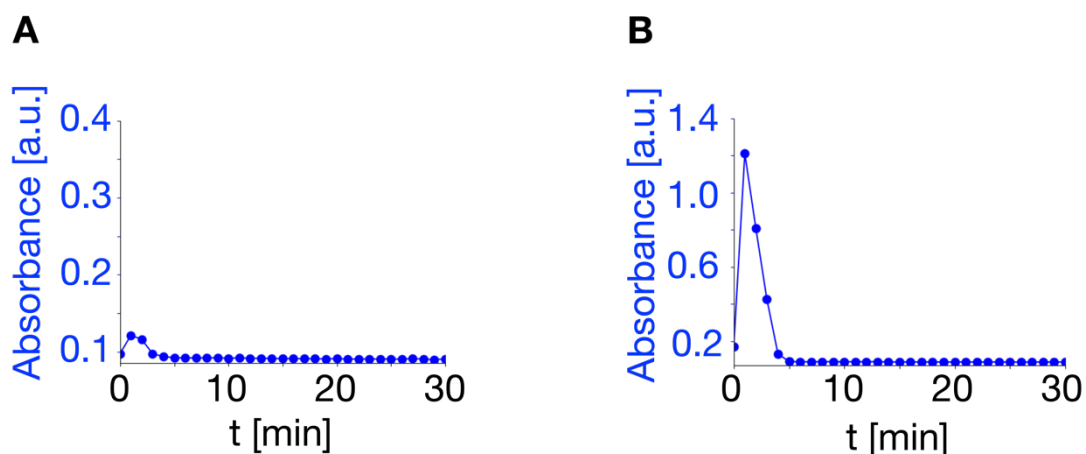
Supporting Figure 4. Evolution of turbidity for $PVPA_{20}$ samples. **A.** 23 mM of $AcF(RG)_3D$-OH fueled with 15 mM EDC in the presence of 4.1 mM $PVPA_{20}$ in 200 mM MES at pH 5.3. **B.** 16 mM of $AcF(RG)_3D$-OH was fueled with 50 mM of EDC in the presence of 4.1 mM $PVPA_{20}$ in 200 mM MES at pH 5.3.

7. Fuel-Driven Dynamic Combinatorial Peptide Libraries

Abstract

So far, I investigated the influence of the molecular structures of cationic peptides and polyanions on the life cycle of carbodiimide fueled complex coacervates. This approach aimed to understand how to optimize the characteristics of the chemically fueled droplets without changing the anhydride-forming reaction cycle. Now, I was able to modify the reaction cycle by adding an additional reaction pathway, namely ester bond formation. For this purpose, peptides with tyrosine side chains were prepared to react with their own aspartic anhydride or intermolecularly after EDC was added as a fuel. Through suitable peptide design including aromatic and cationic amino acids, simple coacervation could be achieved next to complex coacervation with polyanions. Due to the higher stability of the ester bonds, the corresponding assemblies showed longer lifetimes in aqueous solution than the previously described chemically fueled coacervates. The in-situ generated mixtures of intra- and intermolecular reaction products are ideal mimics for the complex compositions of membraneless organelles.

This work is currently under review.

Title: Fuel-Driven Dynamic Combinatorial Peptide Libraries

Authors: Fabian Späth, Michele Stasi, Héctor Soria-Carrera, Judit Sastre, Brigitte A. K. Kriebisch, Job Boekhoven

The following section states the individual contributions of each author. F. Späth and J. Boekhoven designed the experiments. F. Späth carried out the experiments. F. Späth and M. Stasi performed syntheses. H. Soria-Carrera wrote the kinetic model and performed the fitting of kinetic data. J. Sastre performed confocal laser scanning microscopy. Brigitte A. K. Kriebisch helped with cryo-TEM analysis. F. Späth and J. Boekhoven wrote the manuscript. All authors have given approval to the final version of the manuscript.

RESEARCH ARTICLE

Fuel-Driven Dynamic Combinatorial Peptide Libraries

Fabian Späth, Michele Stasi, Héctor Soria-Carrera, Judit Sastre, Brigitte A. K. Kriebisch,[a] and Job Boekhoven*[a]

[a]   F. Späth, M. Stasi, H. Soria-Carrera, J. Sastre, B. A. K. Kriebisch, J. Boekhoven
       School of Natural Sciences, Department of Bioscience, Technical University of Munich
       Lichtenbergstrasse 4, 85748 Garching (Germany)
       E-mail: job.boekhoven@tum.de

Abstract: Dynamic combinatorial chemistry (DCC) creates libraries of molecules that are constantly interchanging in a dynamic combinatorial library. When a library member self-assembles, it can displace the equilibria, leading to emergent phenomena like its selection or even its replication. However, such dynamic combinatorial libraries typically operate in or close to equilibrium. This work introduces a new dynamic combinatorial chemistry fueled by a catalytic reaction cycle that forms transient, out-of-equilibrium peptide-based macrocycles. The products in this library exist out of equilibrium at the expense of fuel and are thus regulated by kinetics and thermodynamics. By creating a chemically fueled dynamic combinatorial library with the vast structural space of amino acids, we explored the liquid-liquid phase separation behavior of the library members. The new versatile chemistry enables simple and complex coacervation and creates structures with significantly longer lifetimes than other chemically fueled examples.

Introduction

Molecules in dynamic combinatorial libraries react with one another reversibly to form a network of library members.[1] Such dynamic combinatorial chemistries generate a mixture of compounds that interconvert into one another. Processes like self-assembly,[2] folding,[3] or hybridization can displace the equilibria, leading to emergent phenomena like replication.[4] For example, library members who assemble are thermodynamically favored and can thus be selected. Various dynamic covalent bonds have been explored to create dynamic combinatorial libraries, including metathesis,[5] hydrazone formation,[6] disulfide exchange,[7] peptide bond formation, [8] or transamination[9]. Such dynamic combinatorial libraries serve as a great model for the cellular reaction networks, which are also dynamic combinatorial libraries. For example, building blocks like nucleotides or amino acids form a vast library of oligonucleotides and proteins. Complex replication and translation machinery based on enzymes tightly regulate the product distribution in such networks in energy-consuming processes. When such reaction networks exist out of equilibrium, the abundance of library members is no longer solely controlled by thermodynamics but also by kinetics.

As a model for biology's complex, out-of-equilibrium reaction networks, dynamic combinatorial libraries out of equilibrium have been designed.[10] For example, in dissipative dynamic libraries, catalytic reaction cycles that convert reagents with high chemical potential (fuels) into products with low chemical potential (wastes) generate dynamic libraries that can only be at the expense of chemical potential. Specifically, fuel conversion into waste is required to form a dynamic covalent bond between library members of the combinatorial library. A backward reaction pathway breaks the bonds between the library members. The combination of fuel-driven bond formation and spontaneous bond cleavage means these dynamic covalent bonds are present, and library members can only exist when fuel is supplied. After the conversion of the fuel, the library will collapse towards equilibrium. For example, Otto described recently self-assembling self-replicators based on disulfide exchange that require an oxidizing agent as fuel to form but are reacted back by reducing agents of the environment. The ability of a product to assemble catalyzed the formation of its building blocks, thereby shifting the concentrations away from the equilibrium conditions.[11] Our group introduced transient anhydride linkages between isophthalic acid building blocks. In this system, the self-assembly[12]   and hybridization of oligomers[13] also influenced the reaction kinetics by increasing the activation and decreasing the hydrolysis rates of certain library members.

The scope of chemically fueled dynamic combinatorial libraries remains limited. Peptide-based building blocks can help to broaden the scope of such systems by the large variety of structures and straightforward preparation.[14] Thus, in this work, we combine the power of chemically fueled dynamic combinatorial libraries with the vast library space of amino acids. We demonstrate how molecular design affects the outcome of the library and resulting self-assembled structures.

Results and Discussion

Molecular design affects the library products.

For a dynamic combinatorial library, we require building blocks with functional groups such that they dimerize through a dynamic covalent bond. Moreover, the product dimer should again be a library member, such that it can form a trimer. Thus, a building block needs to be bi-functional—it should contain both the donating and receiving components for the dynamic covalent bond (Scheme 1A). Finally, to create a dynamic combinatorial library under kinetic control, the building blocks should be coupled to a reaction cycle to be in the thermodynamically favored state. In contrast, the library's products exist only higher in the free

energy landscape. Put differently, the dynamic covalent bond should be transient by forming upon reacting with a high-energy fuel and spontaneously decaying to the building block state.

We chose a chemically fueled, dynamic covalent bond between the ester of a peptide's C-terminus and a tyrosine's phenol. In aqueous media, an ester will not form spontaneously but requires an activating agent (fuel-driven activation). Moreover, it will hydrolyze spontaneously (deactivation). Specifically, we work with the peptide motif Ac-X-Y-XX-D-OH, in which Y stands for tyrosine and carries the phenol side group, D means aspartic acid, and X being either glycines, arginines, alanines, phenylalanine or tryptophan to direct the self-assembly of the peptides (Scheme 1B). In previous work, we have demonstrated that C-terminal aspartic acid easily converts into its corresponding anhydride by reaction with carbodiimides like EDC. One carboxylate is first activated by EDC and the O-acylurea is converted by an intramolecular attack of the second carboxylate group. The anhydride is hydrolytically unstable, so it has a limited lifetime in aqueous media.[15] Depending on the structure of the starting material, transient vesicles,[16] fibres,[17] or complex coacervates[18] were accessible with this chemical reaction cycle. By applying dicarboxylates that were derived from succinic acid with long alkyl or alkenyl tails, dynamic emulsions could be formed that could even be applied as drug delivery platforms.[19] We hypothesized that a tyrosine's phenol as a nucleophile would react with such anhydrides to form an intermolecular phenol ester. The resulting ester contains a C-terminal aspartic acid and a free tyrosine and can thus continue the process. Put differently, a monomer can react with fuel to be dimerized, after which it can further react to make trimers and further oligomers. Besides, all peptides can also form intramolecular esters corresponding to the cyclic monomer, dimer, and oligomers. Finally, because of the hydrolytically labile nature of phenol esters,[20] all library members are transient and will decay to their monomer state unless constantly supplied with fuel.
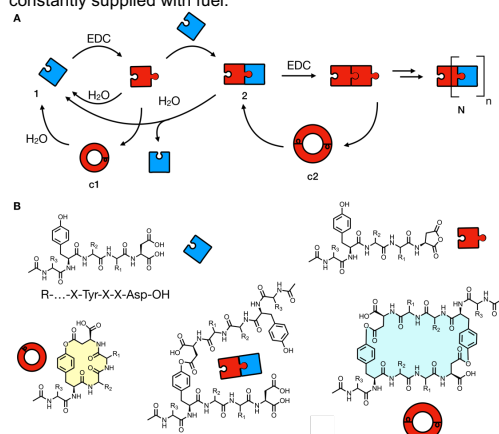
Scheme 1. A. Schematic representation of a dynamic combinatorial library built from a bifunctional precursor. The depicted cycle also includes cyclization pathways, forming an intramolecular cyclic monomer and an intermolecular cyclic dimer. **B**. Schematic representation of the peptide core structure Ac-X-Y-X-X-D-OH fueled with the carbodiimide fuel EDC. Selected products are shown.

We tested the simplest library member possible, Ac-YGGD-OH, in which G stands for glycine, the smallest natural amino acid

(Fig. 1). We used 3 mM of peptide in 200 mM MES at pH 5.3. We applied 10 mM of the chemical fuel and, after 45 minutes, analyzed the outcome of the chemical reaction cycle using HPLC (Figure 1B). Excitingly, we observed around 15 new peaks in the chromatogram, demonstrating that the dynamic combinatorial library produces an abundance of new species. By mass spectrometry, we identified the molecular weights corresponding to the cyclic monomer, linear dimer, cyclic dimer, and linear trimer (see SI for details). Noteworthy, potential isomers with the same molecular weight exist in this dynamic combinatorial library. For example, a linear trimer has the same molecular weight as a branched dimer, while a cyclic trimer has the same molecular weight as a cyclic dimer with a branch. This combinatorial explosion explains the high number of product peaks in a chromatogram. Nevertheless, these new species were dynamically evolving until, after roughly 15 hours, the last peak had completely decayed. The decay of all peaks implies that all the new library members formed in response to fuel were transient.

To control the formation of the library members, we substituted the flexible glycine for a non-nucleophilic, cationic amino acid. We hypothesized that this amino acid can form a salt bridge with the C-terminal aspartic acid, facilitating peptide cyclization. Indeed, when comparing the chromatograms of Ac-YGGD-OH and Ac-YRGD-OH 45 minutes after adding EDC, two main products were favored in the case of Ac-YRGD-OH, namely the cyclic monomer and a smaller fraction of linear dimer. To substantiate the idea of pre-organization, we also analyzed the evolution of products from Ac-YRGD-OH in the presence of 1.9 M guanidinium chloride, which is known to disrupt salt bridges.[21] In the experiment, the yield of cyclic monomer and dimer products decreased by 42%.
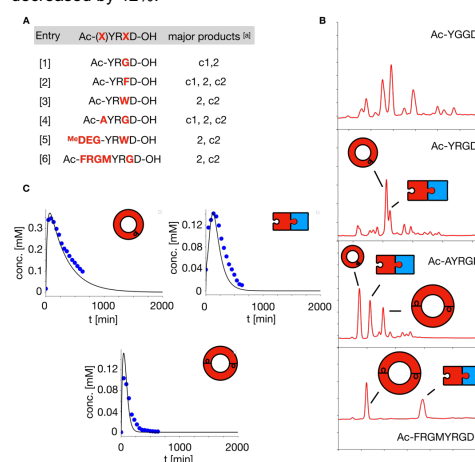
Figure 1. The peptide library and their main products after fueling with EDC. A. The main products were determined as the transient products with the highest intensity in the chromatograms and those that could be identified unambiguously. The cyclodimer product was differentiated from the cyclic monomer by isolating the product and hydrolyzing it after readjusting the pH to 5.3. The evolution of the transient products during the hydrolysis was monitored by HPLC. **B.** Comparison of the different chromatograms of the dynamic combinatorial libraries with different peptides 45 minutes after adding EDC. **C.** The kinetic profiles when 3 mM Ac-AYRGD-OH was fueled with 10 mM of EDC. The markers represent HPLC data, and the solid line is the kinetic model data.

To further control the outcome of the combinatorial library, we introduced bulky amino acids besides the arginine. Specifically,

2

we substituted the remaining glycine for phenylalanine or tryptophan (Ac-YRFD-OH or Ac-YRWD-OH). Moreover, we also made a peptide with an acetyl-protected alanine at the N-terminus (Ac-AYRGD-OH). In line with the literature,[22] we hypothesized that the increased bulkiness diminishes cyclic monomer formation, favoring dimerization and cyclic dimer formation. After the fuel was applied, we observed that the ratio of cyclic monomer to linear dimer and cyclic dimer had decreased. Consequently, there were now only three main products in the chromatograms – cyclic monomer, dimer, and cyclic dimer. Moreover, in the case of Ac-YRWD-OH, hardly any cyclic monomer was formed. Comparing the total amount of products to the starting material showed that the arginine-containing peptides, compared to Ac-YGGD-OH, form up to 50% more ester products, further showing the preorganization effect. When we further modified the N-termini with peptides, we found that the general trend still held, *i.e.*, the main products were dimer and cyclic dimer. These modifications allowed us, in later stages of the work, to control the self-assembly of the products of this combinatorial library. In conclusion, we observed that the outcome of the dynamic combinatorial library is very sensitive to the peptide structure Ac-XYRXD-OH.

With the peptide Ac-AYRGD-OH, we followed the kinetics of the reaction cycle in more detail by HPLC (Fig. 1C). After adding 10 mM of EDC as fuel to 3 mM of peptide, we found that the EDC was consumed within 2 hours. The consumption of EDC produced three major new peaks that we attributed to the cyclic monomer, regular dimer, and cyclodimer. Each of these peaks, as well as the smaller peaks, were transient and had completely disappeared after 6 hours. We did not find a peak for the corresponding O-acylisourea or the aspartic acid anhydrides, most likely because they are converted quickly into esters. With these kinetic profiles, we developed a kinetic model that predicts the evolution of the reaction cycle by fitting the HPLC data using a set of differential equations for each reaction. The reactions we consider are the peptide anhydride formation, and the peptide anhydride can react further inter- or intramolecularly with tyrosine to form a cyclic monomer or linear dimer. The linear dimer can also form its respective anhydride, which can again react intramolecularly to the cyclic dimer. We did not consider reactions further to the linear trimer as it was only observed in neglectable amounts or not at all. Hydrolysis can revert these reactions (see Supporting Information for details).

The kinetic model showed that most EDC - between 60 and 80% - was used to produce anhydride. A small fraction of these anhydrides reacted further with inter- or intramolecular tyrosine to produce the products of the dynamic combinatorial library while the rest hydrolyzed to the peptide. Specifically, with 1 mM of peptide, only 6% of the anhydride is converted into linear esters, while 34% is converted through intramolecular ring closure. Increasing the peptide concentration to 3 mM increased the fraction of anhydride used to make linear esters to 19%, while cyclization was unaffected at 29%. The half-life of each of these esters is 3.5 hours for the cyclomonomer, 1.3 hours for the linear dimer, and 40 minutes for the cyclodimer, as calculated from the corresponding k-values of the ester hydrolysis.

Overall, our proposed peptide family with the general structure Ac-X-Y-X-X-D-OH generates a new chemically fueled dynamic combinatorial library. The peptide's substitution pattern structure drastically affects the composition of the dynamic, transient library.

Chemically Fueled Phase Separation by Simple Coacervation.

Next, we tested whether certain library members could assemble or phase separate. Short peptide sequences with multiple aromatic residues have been shown to phase separate into simple coacervate-based droplets, *i.e.,* droplets with a high water content formed by a self-interacting building block.[23] Even cationic sequences as short as dipeptides with aromatic residues could assemble into such droplets.[24] Since cation-π interactions are one of the main driving forces for such phase-separations of peptides,[25] we hypothesized that the ester products derived from Ac-YWRD-OH could also phase-separate upon fueling the peptide with the right amount of EDC.

After fueling the peptide Ac-YRWD-OH with EDC (3 mM of EDC added to 10 mM of peptide or 10 mM of EDC added to 20 mM of peptide), the sample rapidly turned turbid, indicative of the formation of assemblies sufficiently large to scatter light (Fig. 2A). Noteworthy, the peptide Ac-YRFD-OH did not show any sign of self-assembly under the same fueling conditions likely due to weaker cation-π interactions between arginine and phenylalanine compared to tryptophan.[26] The turbidity evolution was tracked by UV-Vis spectroscopy with a plate reader at a wavelength of 600 nm (Fig. 2A). The turbidity emerged and decayed after 10 hours when 10 mM peptide was fueled with 20 mM of EDC. Laser scanning confocal microscopy revealed the increased turbidity resulting from small amorphous assemblies (Fig. 2B).
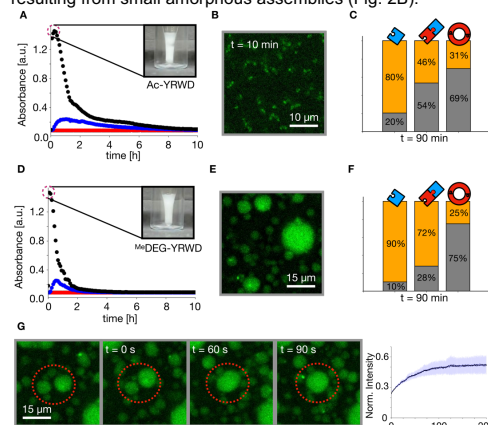
Figure 2. Chemically fueled assembly of the X-YRWD-OH family. A. Evolution of turbidity of Ac-YRWD-OH assemblies at different concentrations and different amounts of EDC (black: 10 mM peptide and 20 mM EDC, blue: 3 mM peptide and 10 mM EDC, red: 1 mM peptide and 10 mM EDC). **B**. Confocal micrographs 10 mM Ac-YWRD-OH fueled with 20 mM EDC in 200 mM MES buffer at pH 5.3. NBD-G(RG)2N-NH2 was used as a fluorescent dye. **C**. Distribution of total concentrations of the peptide monomer, linear dimer, and cyclodimer species (grey: in droplets, orange: in the supernatant) as determined by HPLC (see Supporting Information and Methods for details). **D**. Turbidity evolution of 2-[2-(2-methoxyethoxy)ethoxy]acetyl-YRWD-OH under different conditions (black: 10 mM peptide and 20 mM EDC, blue: 3 mM peptide and 10 mM EDC, red: 1 mM peptide and 10 mM EDC). **E**. Confocal microscopy image of a sample of 10 mM peptide fueled with 20 mM of EDC in 200 mM MES buffer at pH 5.3. NBD-G(RG)2N-NH2 was used as a fluorescent dye. **F**. Distribution of the total concentration of peptide monomer, linear dimer, and cyclodimer species (grey: in droplets, orange: in the supernatant) as determined by HPLC. **G**. Left: Confocal micrographs of liquid droplets from 10 mM peptide fueled with 20 mM EDC, 10 minutes after EDC addition. Right: Fluorescence recovery from FRAP analysis.

3

RESEARCH ARTICLE

We tested the composition of the assemblies by spinning down the samples 90 minutes after fuel addition. We then analyzed the supernatant by HPLC and used these concentrations as a reference for all components that did not assemble. We also analyzed the composition of samples that had not been spun down, but instead, we dissolved all the assemblies by diluting the solution with 4M guanidinium chloride solution and rigorous mixing. We found that the assemblies were a co-assembly of peptide precursor, linear dimer, and cyclodimer product. To put that into the context of the dynamic combinatorial library members, 54% of the total linear dimer was in the assembly, whereas the rest remained in the solution. In contrast, 69% of the total cyclodimer concentration is taken up in the assemblies, indicating that the cyclodimer has a higher tendency to self-assemble (Fig. 2C).

As we aimed for liquid assemblies through phase separation, we modified the YRWD-OH peptide sequence to create liquid assemblies. We added a 2-[2-(2-methoxyethoxy)ethoxy]acetic acid tail to the N-terminus of the peptide structure to increase its overall solubility without influencing the reactive core. This peptide also showed a fast increase in turbidity upon fueling with EDC (Fig. 2D). Confocal microscopy revealed micron-sized spherical assemblies that rapidly fused, from which we concluded they were liquid. Spinning down the droplets and analyzing the supernatant revealed that most cyclic dimer partitions into these droplets (75%). The liquid nature of the simple coacervate droplets was further investigated by FRAP analysis, which revealed a fast recovery of fluorescence intensity after bleaching (Fig. 2G). The corresponding diffusion coefficient was determined to be $D = 0.063$ μm^2.s^{-1}.

Chemically Fueled Phase Separation by Complex Coacervation.

Complex coacervation describes the phase separation of at least two charged components, usually involving a polyionic species. We reasoned that combining our in-situ generated cationic building blocks with polyanions enables us to create droplets through complex coacervation. Given the chemically fueled nature of our chemically fueled dynamic combinatorial library, complex coacervation of the library members should lead to active droplets, *i.e.,* those requiring fuel to be sustained. We first tested the peptide structure Ac-FRGMYRGD-OH in combination with the polyanion PSS because it forms large amounts of linear dimer and cyclodimer products in response to EDC (Fig. 1B). Besides, the peptide is zwitterionic (+2, -2) and overall charge neutral. In contrast, the linear dimer has an overall charge of +1, and the cyclodimer has an overall charge of +2. In other words, we expect minimal interaction between the peptide and polyanions. In contrast, the products of the reaction cycle are expected to interact strongly with the polyanion to form complex coacervate-based droplets. This chemically fueled charge switching has been previously explored in active droplets but not in the context of a dynamic combinatorial library.[18, 27] To further enhance the interaction with polyanions, we added methionine (M), known for its ability to interact with π-systems, thereby driving phase separation.[28]

Indeed, when we combined 10 mM of the peptide with 20 mM of EDC in 200 mM MES buffer at pH 5.3 in the presence of 1 mM of the polyanion PSS, turbidity quickly emerged. The turbidity peaked at around 1 hour after fuel addition and slowly declined over 24 hours when the absorbance value reached its initial value again (Fig 3A). We tested the coacervate composition by spinning down the droplets and analyzing the supernatant. After 90 minutes, the EDC was fully consumed, and we found that 31% of the total cyclodimer was taken up into the droplets together with 15 % of the linear dimer. After 450 minutes, no more peptide precursor is present in the coacervate droplets, and 20% of the linear dimer and 38% of the total cyclodimer concentration in the mixture are concentrated in the coacervate droplets. These results show nicely that the cyclodimer is the most potent coacervating agent among library members. Similar mixtures without PSS did not show any evidence of assemblies, from which we conclude that the assemblies are a complex coacervate between peptide and PSS.
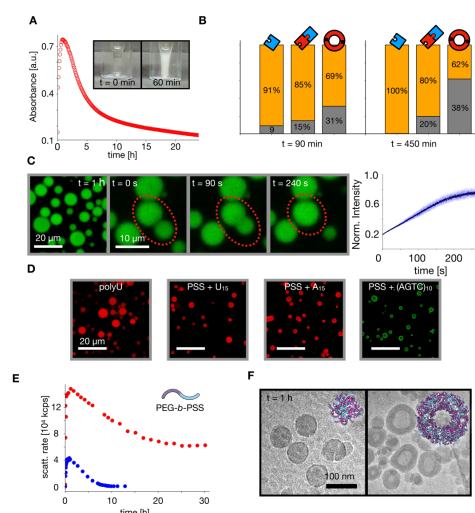
Figure 3. Complex coacervation of Ac-FRGMYRGD-OH with the polyanion poly(styrene sulfonate) – PSS. A. Evolution of turbidity of a sample consisting of 10 mM of peptide that were fueled with 20 mM of EDC in the presence of 1 mM of PSS (expressed in monomer concentration). **B**. The different concentrations of the peptide precursor, linear dimer and cyclodimer of the peptide in the coacervate phase (grey) and in the supernatant (orange) at different time points into the cycle. **C**. Confocal microscopy images of the coacervate droplets with NBD-G(RG)$_2$N-NH$_2$ as the fluorescent dye. 10 mM of peptide were fueled with 20 mM EDC in the presence of 1 mM PSS all in 200 mM MES buffer at pH 5.3. The coacervate droplets fuse and show fluorescence recovery in FRAP analysis. **D**. Confocal laser micrographs of oligonucleotide and mixed PSS-oligonucleotide coacervates (10 mM of Ac-FRGMYRGD-OH with 20 mM of EDC in the presence of 1 mM polyanion expressed in monomer units). Left: 1 mM of polyU as the polyanion with 200 nM of Cy5-U$_{15}$. Other samples: 1 mM PSS with 200 nM of Cy5-U$_{15}$, Cy5-A$_{15}$ or Cy3-(AGTC)$_{10}$ (from left to right). All images were taken one hour after the EDC was added. **E**. DLS analysis of coacervate core micelles from the peptide with EDC in the presence of 1 mM of the block copolymer PEG$_{5K}$-b-PSS$_{77}$. Red trace: 10 mM of peptide fueled with 20 mM of EDC. Blue trace: 3 mM of the peptide fueled with 10 mM of EDC in 200 mM MES at pH 5.3. **F**. Cryo-TEM images of coacervate core micelles one hour after adding 20 mM EDC to 10 mM of peptide and 1 mM of the block copolymer (expressed in charge concentrations).

We further studied the assemblies by confocal microscopy and found micron-sized droplets that rapidly fused, from which we concluded they were liquid (Fig. 3 C). Furthermore, FRAP

4

RESEARCH ARTICLE

experiments revealed fast fluorescence recovery with a diffusion coefficient (D) of 0.0145 μm^2/s. To test whether the PSS-based coacervates were able to take up functional oligonucleotides, we combined them with the RNA-oligonucleotides Cy5-U_{15} or Cy5-A_{15}, or the DNA-oligomer Cy3-$(AGTC)_{10}$. In all cases, the oligonucleotides were taken up into the coacervates but were more concentrated on the periphery of the droplets, suggesting a demixing tendency of the two polyanions. Aside from that, the coacervates were significantly smaller compared to those made from pure PSS.

To test the peptide's versatility in making coacervates, we tested it with other anionic (block co-) polymers. First, we analyzed it in combination with 1 mM polyU as polyanion. The sample transiently turned turbid with EDC, similar to using PSS as polyanion (Supporting Figure 1). These polyU-based coacervates appeared as spherical droplets slightly smaller than the corresponding PSS-based coacervates (Fig. 3D). Next, we combined the peptide with block copolymers made from PEG and PSS to further tune their properties, *i.e.*, change their size. To test its ability to form complex coacervate core micelles (C3Ms), we applied 20 mM EDC to 10 mM of peptide in the presence of 1 mM of PEG$_{5K}$-b-PSS$_{77}$ and monitored the assembly process by DLS (Fig. 3E). This analysis showed a quick increase in scattering rate after EDC was added, indicating the immediate complexation of block copolymer by the dynamic combinatorial library members. The maximum scattering rate was reached after 1 hour, coinciding with the maximum turbidity for the complex coacervation of PSS homopolymer. CryoTEM further corroborated the formation of block copolymer assemblies upon fueling (Fig. 3F). Specifically, the micrographs show large compound micelles of 80 to 100 nm diameter that coexist with polymersomes with a diameter around 150 nm. These sizes matched well with the z-average size obtained from DLS (Supporting Figure 2). The lifetime of the assemblies could be increased by adding more peptides and EDC.

Conclusion

We found a new, versatile, dynamic covalent bond that exists only out of equilibrium at the expense of chemical energy. The tyrosine ester-based dynamic covalent bond creates a dynamic combinatorial library by expanding a chemical reaction cycle based on EDC and aspartic acid-derived peptides with an esterification pathway. We found the new bond gives rise to a dynamic mixture of cyclic and linear tyrosine esters that form intra- and intermolecularly. The kinetics of the chemical reactions are quantitatively understood, allowing us to tune the product distribution through molecular design. Moreover, we showed that, through molecular design, the library could be linked to simple or complex coacervation. We envision the resulting coacervates or coacervate core micelles with lifetimes of multiple hours could be attractive for future applications, e.g., for controlled release systems for DNA or RNA. They are also valuable models for membraneless organelles, which are also coacervate-based droplets regulated through chemical reaction cycles. Finally, we envisage these droplets as a powerful protocell model or a compartment in life's de novo synthesis.

Supporting Information

The authors have cited additional references within the Supporting Information.[27a, 29]

[1]   J. M. Lehn, A. V. Eliseev, *Science* **2001**, *291*, 2331-2332.
[2]   a) B. Liu, M. A. Beatty, C. G. Pappas, K. Liu, J. Ottele, S. Otto, *Angew. Chem. Int. Ed. Engl.* **2021**, *60*, 13569-13573; b) Y. Cao, J. Yang, D. Eichin, F. Zhao, D. Qi, L. Kahari, C. Jia, M. Peurla, J. M. Rosenholm, Z. Zhao, S. Jalkanen, J. Li, *Angew. Chem. Int. Ed. Engl.* **2021**, *60*, 3062-3070; c) C. B. Minkenberg, F. Li, P. van Rijn, L. Florusse, J. Boekhoven, M. C. Stuart, G. J. Koper, R. Eelkema, J. H. van Esch, *Angew. Chem. Int. Ed. Engl.* **2011**, *50*, 3421-3424.
[3]   a) B. Liu, C. G. Pappas, E. Zangrando, N. Demitri, P. J. Chmielewski, S. Otto, *J .Am. Chem. Soc.* **2019**, *141*, 1685-1689; b) C. G. Pappas, B. Liu, I. Maric, J. Ottele, A. Kiani, M. L. van der Klok, P. R. Onck, S. Otto, *J. Am. Chem. Soc.* **2021**, *143*, 7388-7393.
[4]   a) J. M. Carnall, C. A. Waudby, A. M. Belenguer, M. C. Stuart, J. J. Peyralans, S. Otto, *Science* **2010**, *327*, 1502-1506; b) J. Li, P. Nowak, S. Otto, *J. Am. Chem. Soc.* **2013**, *135*, 9222-9239.
[5]   a) J. A. Berrocal, M. M. Nieuwenhuizen, L. Mandolini, E. W. Meijer, S. Di Stefano, *Org. Biomol. Chem.* **2014**, *12*, 6167-6174; b) A. Kravchenko, B. J. J. Timmer, A. K. Inge, M. Biedermann, O. Ramström, *ChemCatChem* **2021**, *13*, 4841-4847; c) I. Colomer, A. Borissov, S. P. Fletcher, *Nat. Commun.* **2020**, *11*, 176.
[6]   a) S. Kulchat, M. N. Chaur, J. M. Lehn, *Chemistry* **2017**, *23*, 11108-11118; b) J. Boekhoven, J. M. Poolman, C. Maity, F. Li, L. van der Mee, C. B. Minkenberg, E. Mendes, J. H. van Esch, R. Eelkema, *Nat Chem* **2013**, *5*, 433-437.
[7]   a) B. M. Matysiak, P. Nowak, I. Cvrtila, C. G. Pappas, B. Liu, D. Komaromy, S. Otto, *J. Am. Chem. Soc.* **2017**, *139*, 6744-6751; b) S. Otto, S. Kubik, *J. Am. Chem. Soc.* **2003**, *125*, 7804-7805.
[8]   C. G. Pappas, R. Shafi, I. R. Sasselli, H. Siccardi, T. Wang, V. Narang, R. Abzalimov, N. Wijerathne, R. V. Ulijn, *Nat Nanotechnol* **2016**, *11*, 960-967.
[9]   a) F. Schaufelberger, L. Hu, O. Ramstrom, *Chemistry* **2015**, *21*, 9776-9783; b) M. Ciaccia, R. Pilati, R. Cacciapaglia, L. Mandolini, S. Di Stefano, *Org. Biomol. Chem.* **2014**, *12*, 3282-3287.
[10]   D. Del Giudice, E. Spatola, M. Valentini, G. Ercolani, S. Di Stefano, *ChemSystemsChem* **2022**, *4*.

5

[11]   S. Yang, G. Schaeffer, E. Mattia, O. Markovitch, K. Liu, A. S. Hussain, J. Ottele, A. Sood, S. Otto, *Angew. Chem. Int. Ed. Engl.* **2021**, *60*, 11344-11349.

[12]   C. M. E. Kriebisch, A. M. Bergmann, J. Boekhoven, *J. Am. Chem. Soc.* **2021**, *143*, 7719-7725.

[13]   C. Kriebisch, L. Burger, O. Zozulia, M. Stasi, A. Floroni, D. Braun, U. Gerland, J. Boekhoven, **2023**, Research Square preprint https://doi.org/10.21203/rs.21203.rs-2710976/v2710971.

[14]   M. Tena‑Solsona, J. Boekhoven, *Israel Journal of Chemistry* **2019**, *59*, 898-905.

[15]   M. Tena-Solsona, B. Riess, R. K. Grötsch, F. C. Lohrer, C. Wanzke, B. Kasdorf, A. R. Bausch, P. Müller-Buschbaum, O. Lieleg, J. Boekhoven, *Nat. Commun.* **2017**, *8*, 15895.

[16]   C. Wanzke, A. Jussupow, F. Kohler, H. Dietz, V. R. I. Kaila, J. Boekhoven, *ChemSystemsChem* **2019**, *2*.

[17]   B. A. K. Kriebisch, A. Jussupow, A. M. Bergmann, F. Kohler, H. Dietz, V. R. I. Kaila, J. Boekhoven, *J. Am. Chem. Soc.* **2020**, *142*, 20837-20844.

[18]   C. Donau, F. Späth, M. Sosson, B. A. K. Kriebisch, F. Schnitter, M. Tena-Solsona, H. S. Kang, E. Salibi, M. Sattler, H. Mutschler, J. Boekhoven, *Nat. Commun.* **2020**, *11*, 5167.

[19]   L. Tebcharani, C. Wanzke, T. M. Lutz, J. Rodon-Fores, O. Lieleg, J. Boekhoven, *J. Control. Release* **2021**, *339*, 498-505.

[20]   D. Gimenez, A. Phelan, C. D. Murphy, S. L. Cobb, *Org. Lett.* **2021**, *23*, 4672-4676.

[21]   H. Meuzelaar, M. R. Panman, S. Woutersen, *Angew. Chem. Int. Ed. Engl.* **2015**, *54*, 15255-15259.

[22]   a) C. J. White, A. K. Yudin, *Nat. Chem.* **2011**, *3*, 509-524; b) J. M. Humphrey, A. R. Chamberlin, *Chem. Rev.* **1997**, *97*, 2243-2266.

[23]   M. Abbas, W. P. Lipinski, K. K. Nakashima, W. T. S. Huck, E. Spruijt, *Nat. Chem.* **2021**, *13*, 1046-1054.

[24]   S. Cao, T. Ivanov, J. Heuer, C. T. J. Ferguson, K. Landfester, L. Caire da Silva, *Nat .Commun.* **2024**, *15*, 39.

[25]   S. Kim, H. Y. Yoo, J. Huang, Y. Lee, S. Park, Y. Park, S. Jin, Y. M. Jung, H. Zeng, D. S. Hwang, Y. Jho, *ACS Nano* **2017**, *11*, 6764-6772.

[26]   a) A. Baruch Leshem, S. Sloan-Dennison, T. Massarano, S. Ben-David, D. Graham, K. Faulds, H. E. Gottlieb, J. H. Chill, A. Lampel, *Nat. Commun.* **2023**, *14*, 421; b) A. Ghorai, B. Achari, P. Chattopadhyay, *Tetrahedron* **2016**, *72*, 3379-3387.

[27]   a) F. Späth, C. Donau, A. M. Bergmann, M. Kränzlein, C. V. Synatschke, B. Rieger, J. Boekhoven, *J. Am. Chem. Soc.* **2021**, *143*, 4782-4789; b) C. Donau, F. Späth, M. Stasi, A. M. Bergmann, J. Boekhoven, *Angew. Chem. Int. Ed. Engl.* **2022**, *61*, e202211905; c) A. M. Bergmann, J. Bauermann, G. Bartolucci, C. Donau, M. Stasi, A. L. Holtmannspötter, F. Julicher, C. A. Weber, J. Boekhoven, *Nat. Commun.* **2023**, *14*, 6552.

[28]   N. Kolchina, V. Khavinson, N. Linkova, A. Yakimov, D. Baitin, A. Afanasyeva, M. Petukhov, *Nucleic Acids Res.* **2019**, *47*, 10553-10563.

[29]   a) J. Schindelin, I. Arganda-Carreras, E. Frise, V. Kaynig, M. Longair, T. Pietzsch, S. Preibisch, C. Rueden, S. Saalfeld, B. Schmid, J. Y. Tinevez, D. J. White, V. Hartenstein, K. Eliceiri, P. Tomancak, A. Cardona, *Nat. Methods* **2012**, *9*, 676-682; b) X. Chen, H. Soria-Carrera, O. Zozulia, J. Boekhoven, *Chem. Sci.* **2023**, *14*, 12653-12660.

6

RESEARCH ARTICLE

Entry for the Table of Contents
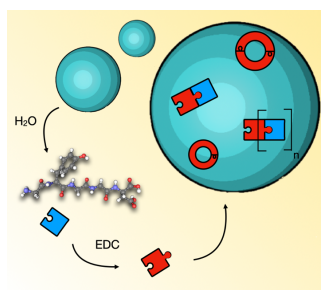
A new chemically fueled dynamic covalent bond is introduced and coupled to combinatorial library formation. We describe design rules to tune the library and control the phase separation of certain library members into droplets.

Institute and/or researcher Twitter usernames: @BoekhovenLab

Supporting Information for

Fuel-Driven Dynamic Combinatorial Peptide Libraries

Fabian Späth, Michele Stasi, Héctor Soria-Carrera, Judit Sastre, Brigitte Kriebisch, Job Boekhoven[*][a]

[a]   F. Späth, M. Stasi, H. Soria-Carrera, J. Sastre, B. A. K. Kriebisch, J. Boekhoven
School of Natural Sciences, Department of Bioscience, Technical University of Munich
Lichtenbergstrasse 4, 85748 Garching (Germany)
E-mail: job.boekhoven@tum.de

1

Table of Contents

Materials and methods.

Solvents were purchased in analytical grade and used as received without further purification. DMF was used in peptide synthesis grade. MilliQ® water was obtained from a Milli- Q® Direct 8 water purification system. All peptide synthesis reagents (standard Fmoc-protected amino acids suitable for orthogonal protecting group protocols in solid-phase synthesis, resins and solid supports, bases, auxiliary agents and deprotection reagents) were purchased from Merck/Sigma-Aldrich and used as received. Cy3-labeled U_{15} and A_{15} were purchased from biomers.net GmbH. Cy5-labeled $(AGTC)_{10}$ was purchased from Sigma-Aldrich/Merck.

NMR spectroscopy.

^{1}H-NMR spectra were recorded on a Bruker AV-400HD NMR spectrometer at 400 MHz or on an AV-300HD NMR spectrometer at 300 MHz. All chemical shifts δ are given in parts per million (ppm) relative to the residual proton signal of the solvent. The spectra were analyzed in the MestreNova software (Version 14.1.1).

Solid phase peptide synthesis by Fmoc-chemistry.

The different peptides were synthesized by standard Fmoc-chemistry with heating either with the assistance of a microwave or in an oil-bath setup. Both methods can be used interchangeably, giving equally high purities and yields after purification.

Microwave-assisted automated solid phase synthesis.

Based on an already published procedure, automated solid phase peptide synthesis with microwave assistance was performed on a 0.25 mmol scale on a Liberty Blue® synthesizer from CEM. NBD-G(RG)$_2$N-NH$_2$ was synthesized and purified according to published protocols.[1]

Manual solid-phase synthesis with controlled heating.

The peptides were synthesized on a 0.25 mmol scale with pre-loaded Wang resin (Fmoc-Asp(OtBu)-Wang resin (100-200 mesh), 0.69 mmol/g loading) by standard

3

Fmoc-chemistry. A glass reaction vessel equipped with a frit and a connection to a nitrogen and vacuum line was used. The resin was initially swollen in DMF for 20 minutes under continuous agitation by a stream of nitrogen. The syntheses were performed at 68 °C.

Before each coupling step, Fmoc-deprotection was performed with 10 to 30 mL of a 5 w/v% piperazine solution in DMF. The mixture was agitated continuously for 1 to 5 minutes with a nitrogen stream. After draining of all remaining liquid, extensive washing of the resin with DMF was performed. The coupling solutions for each amino acid were prepared freshly (3 eq. of amino acid, 2.8 eq. of HCTU and 6 eq. of DIPEA) and mixed thoroughly by vortexing. The solution was then added to the resin and mixed with the resin for 6 minutes by bubbling with the nitrogen stream. The deprotection, washing and coupling sequence was performed until all amino acids were coupled. N-terminal acetylation was performed with 6 eq. of acetic anhydride and 6 eq. of DIPEA in DMF that were added to the resin and the mixture was agitated at room temperature for 10 minutes by bubbling. After all synthesis steps, the resin was washed with multiple additions of DMF and DCM.

The peptide was removed from the resin by adding the cleavage cocktail (95% TFA, 2.5% TIPS and 2.5% H_2O) to the resin in a peptide synthesis vessel and mixing everything continuously on a shaker for one to three hours. The solution was then collected in a round bottom flask and the solvents were removed by rotary evaporation (co-distillation with DCM).

Peptide purification.

The crude peptide products were purified by preparative RP-HPLC. An Agilent 1260 Infinity II setup (1260 Infinity II Preparative Binary Pump, 1260 Infinity II Variable Wavelength Detector and 1260 Infinity II Preparative-Scale Fraction Collector) was used. The separation was performed on an Agilent InfinityLab ZORBAX SB-C18 column (250 mm x 21.2 mm, 5 μm particle size) in a linear gradient from 2% to 98% ACN in MQ water, both with 0.1% TFA at a flow rate of 20 mL/min. The peptides were analyzed after purification by LC-MS and ^{1}H-NMR.

4

Peptide structure	m/z observed (calculated)	r.t. HPLC [min]
	[M-H]⁻ = 451.41 (451.15)	8.54 [a]
	[M+H]⁺ = 552.42 (552.24)	9.01 [a]
	[M+H]⁺ = 642.55 (642.29)	13.30 [a]
	[M+H]⁺ = 681.2 (681.73)	13.57 [a]
	[M+H]⁺ = 623.52 (623.28)	8.93 [a]
	[M+H]⁺ = 683.43 (683.28)	10.75 [a]
	[M+H]⁺ = 799.49 (799.36)	15.29 [a]
	[M+2H]²⁺ = 522.61 (522.24) [M+H]⁺ = 1043.39 (1043.47)	23.10 [b]

(a) in a gradient of 98% to 2% MilliQ-water with ACN, both with 0.1% TFA, over 40 minutes (b) in a gradient of 98% to 60% MilliQ-water with ACN, both with 0.1% TFA, over 40 minutes.

5

6

UV-Vis plate reader experiments.

UV-Vis absorbance measurements at 600 nm wavelength were performed on a SpectraMax® ABS Plus plate reader from Molecular Devices. Samples were prepared in 96 or 384 Well plates with 100 µL or 20 µL sample volume. The evolution of turbidity was monitored after the addition of the carbodiimide fuel EDC and mixing everything by pipetting thoroughly.

Blockcopolymer synthesis.

The PEG_{5k}-b-PSS_{77} block copolymer was synthesized and analyzed according to a published procedure via RAFT polymerization from the corresponding PEG chain transfer agent.[1]

Sample preparation.

The samples were prepared in standard 100, 30, or 20 µL volumes. Concentrated stocks (25 mM for peptides, 500 mM for MES buffer at pH 5.3, and 1M for EDC) were combined in appropriate ratios, and their final volume was adjusted with MilliQ®-water. EDC, as the fuel, was always added in the last step to start the reaction cycle. The solutions were mixed by vigorous pipetting.

HPLC and LC-MS analysis.

Analytical HPLC analysis was performed on a ThermoFisher Ultimate 3000 LC setup (Dionex Ultimate pump, Autosampler, RS Variable Wavelength Detector, and column oven set to 25°C). The analytes were separated in a linear gradient of solvents (2% to 98% ACN in MQ water, both with 0.1% TFA at a flow rate of 1 mL/min) on a ThermoScientific Hypersil GOLD column (250 x 4.6 mm, 5 µm particle size). Wavelengths of 220, 254, 269 and 280 nm were used to detect the analytes. For LC-MS analysis, a ThermoFisher HPLC system was used in combination with an LCQ Fleet Ion Trap Mass Spectrometer (Thermo Scientific).

Semipreparative HPLC.

Peptides were purified by semipreparative RP-HPLC on a 1260 Infinity ll setup from Agilent. The system is built from a 1260 Infinity ll Preparative Binary Pump, a 1260 Infinity ll Variable Wavelength Detector, and a 1260 Infinity ll Preparative-Scale

10

Fraction Collector. Linear Gradients from 2% to 98% ACN in MilliQ-water (both with 0.1% TFA) were applied at a flow rate of 20 mL/min. An Agilent Infinity Lab ZORBAX SB-C18 column (250 mm x 21.2 mm, 5 µm particle size) was used. The system was operated and controlled with the Agilent OpenLab Control software.

Determination of coacervate and supernatant contents.

The supernatant concentration of simple coacervates was determined by preparing the samples (10 mM peptide fueled with 20 mM EDC in 200 mM MES at pH 5.3), starting the coacervation process, spinning the coacervate phase down at the desired time point (90 or 450 min) for 5 minutes and removing some of the supernatant and subjecting it to HPLC analysis. The total peptide concentrations in samples were determined by quenching samples by adding 4M guanidinium chloride solution in a 1:1 volumetric ratio after the desired timepoint when coacervation was started. HPLC was used to analyze the clear solution, and the dilution factor was compensated for in the concentration calculations.

The supernatant concentrations of complex coacervates that formed after fueling samples containing 10 mM of AcFRGMYRGD-OH and 1 mM PSS with 20 mM EDC was determined by spinning these samples down for 5 minutes and injecting a sample of the supernatant into the HPLC setup. The control samples for the total linear dimer and cyclodimer concentrations were without PSS and got injected directly into the HPLC.

DLS analysis.

DLS analysis was performed on a Litesizer 500 particle size analyzer from Anton Paar. The instrument is equipped with a 658 nm 40 mW laser diode. The samples were loaded into the instrument with a 45 µL quartz cuvette (3x3 mm light path, Hellma Analytics).

CryoTEM analysis.

Cu-grids (C-flat^{Tm} 2/1 on 400 copper mesh) were glow-discharged for 90 seconds at 45 mA and 3×10^{-2} mbar. 5 µL of sample were transferred onto the grids and frozen by plunging with a Vitrobot Mark IV (FEI/ThermoScientific) with the following settings: 100% humidity, 22 °C temperature, 30 seconds wait time, -1 blot force, 2.5 seconds

11

blot time. The prepared grids were stored in liquid nitrogen until they were imaged on a Tecnai Spirit microscope (FEI/ThermoScientific). For imaging, the grids were placed into a Gatan cryo-transfer specimen holder. The images were acquired with serialEM on a TVIPS-416 CCD camera (TVIPS).

Laser confocal fluorescence microscopy and FRAP analysis.

Laser confocal microscopy was performed on a Leica TCS SP8 confocal microscope with a 63x water immersion objective (1.2 NA). 30 µL samples were prepared in micro-well plates (ibidi, µ-Slide Angiogenesis Glass Bottom) that were passivated with PVA before use. NBD-G(RG)$_2$N-NH$_2$ was excited at 488 nm and imaged in the range of 500 to 650 nm, Cy3-labelled oligonucleotides were excited at 488 nm and imaged from 550 to 650 nm, Cy5-labelled oligonucleotides were excited at 638 nm and imaged from 670 to 750 nm. All dye-labeled probes were used in a final concentration of 200 nM in the samples.

FRAP experiments were conducted using the same confocal microscope with a PMT detector. The samples were prepared as described above. For a FRAP experiment, 10 pre-bleaching frames were acquired, followed by 10 bleaching frames. Imaging times varied depending on the region of interest and sample but was typically between 200-400 ms/frame. The fluorescence intensity as a function of time for the bleached area, reference, and background was obtained using FIJI [2], and the recovery of the bleached region was normalized against the background and the reference region. Data was fitted to a single exponential to obtain the half-time of recovery. The diffusion coefficient is related to T$_{1/2}$ by:

$$D = 0.88 \frac{r^2}{4T_{1/2} \log(2)}$$

Where r is the radius of the bleached spot.

Kinetic modeling.

a) Workflow

We used the following set of ODEs to describe the systems using a steady-state approximation that removed any explicit dependence on the concentration of O-acylurea which forms after precursor activation and in the linear dimer (E2). For the sake of simplicity, we neglected the formation of N-Acylurea. Data was fitted using an

12

in-house developed Python workflow based on previous work.[3] In the script, we use the following nomenclature for the species. Precursor (Ac), EDC (F), Waste (W), Anhydride (An), Cyclomonomer (E1), Linear Dimer (E2), Cyclodimer (E2) and Linear dimer anhydride (An2).

We solve the ODE system and fit it to the experimental data, minimizing an error function defined as the distance between the predicted value and the experimental (error function in the code). Depending on the quality of the data, we also used the Root-mean-square deviation (RMSEerror in the code). It is important to note that fitting using RMSEerror requires longer times. We used least squares (*least-squares* in lmfit package) as a method to minimize such error functions. Compared to previous work,[3] we did not use bootstrapping for fitting due to the elevated complexity of the kinetics. Examples of how to fit was carried out are in the GitHub repository. https://github.com/hsoria/Cyclic-peptide-kinetics

b)   Differential Equations

r0: F $\longrightarrow$ W; k0·F

r1: Ac + F $\longrightarrow$ O; k1·Ac·F

r2: O $\longrightarrow$ An + W; k2·O

r3: O $\longrightarrow$ Ac + W; k3·O

r4: An $\longrightarrow$ Ac; k4·An

r5: An $\longrightarrow$ E1; k5*An;

r6: An + Ac $\longrightarrow$ E2; k6·An·Ac;

r7: E2 + F $\longrightarrow$ O2; k7·E2·F;

r8: O2 $\longrightarrow$ An2 + W; k8·O2;

r9: O2 $\longrightarrow$ E2 + W; k9·O2

r10: An2 $\longrightarrow$ E3; k10·An2

r11: E1 $\longrightarrow$ Ac; k11·E1;

r12: E2 $\longrightarrow$ Ac + Ac; k12·E2;

r13: E3 $\longrightarrow$ E2; k13·E3;

Using the steady-state approximation:

13

$O = ((k1*Ac*F) / (k2+k3))$

$O2 = ((k7*E2*F) / (k8+k9))$

For peptides that do not form E1, we set dE1dt = 0.

```python
def ode_model(z, t, k0, k1, k2, k3, k4, k5, k6, k7, k8, k9, k10, k11, k12, k13):

    """
    takes a vector of the initial concentrations that are previously defined.
    YOu have to provide also initial guesses for the kinetic constants.
    You must define as much constants as your system requires. Note that the reactions are expressed as differential
    equations

    F: Fuel
    Ac: Precursor
    An: Anhydride
    W: Waste
    E1: Cyclomonomer/phenolester
    E2: Linear dimer (non activated)
    E3: cyclodimer (non activated)

    O: O-acylurea of monomer species
    O2: O-acylure of dimer species

    An2: Linear dimer anhydride

    Time is considered to be in **minutes**. Concentrations are in **mM**

    """

    #O = ((k1*Ac*F) / (k2+k3))
    #O2 = ((k7*E2*F) / (k8+k9))

    F, W, Ac, An, E1, E2, E3, An2 = z


    dFdt = - k0*F - k1*Ac*F - k7*E2*F
    dWdt = + k0*F + k2*((k1*Ac*F) / (k2+k3)) + k3*((k1*Ac*F) / (k2+k3)) + k8*((k7*E2*F) / (k8+k9)) + k9*((k7*E2*F) / (k8+k9))

    dAcdt = - k1*Ac*F + k3*((k1*Ac*F) / (k2+k3)) + k4*An - k6*An*Ac + k11*E1 + 2*k12*E2
    dAndt = + k2*((k1*Ac*F) / (k2+k3)) - k4*An - k5*An - k6*An*Ac

    dE1dt = + k5*An - k11*E1
    dE2dt = + k6*An*Ac - k7*E2*F + k9*((k7*E2*F) / (k8+k9)) - k12*E2 + k13*E3
    dE3dt = + k10*An2 - k13*E3

    dAn2dt = + k8*((k7*E2*F) / (k8+k9)) - k10*An2

    return [dFdt, dWdt, dAcdt, dAndt, dE1dt, dE2dt, dE3dt, dAn2dt]
```

The following k-values were used for modeling:

Ac-AYRGD-OH			
	20 mM EDC-10 mM Precursor	10 mM EDC-3 mM Precursor	10 mM EDC-1 mM Precursor
k0	0,0045	0,0045	0,0045
k1	0,011394275	0,012246902	0,042501689
k2	0,124292019	0,029667483	0,033754151
k3	0,314015406	0,476763871	0,466188301
k4	0,257612216	0,000234596	0,439634328
k5	0,094101163	0,362770056	0,381931384
k6	0,025408056	0,167835646	0,090061135
k7	0,114867076	0,015753696	0,057492105
k8	0,031523695	0,096209204	0,027431391
k9	0,096333305	0,000101742	0,076804023
k10	0,966126872	0,005486047	0,761743649
k11	0,003258903	0,002149034	0,001971443
k12	0,008450088	0,015151364	0,00564592
k13	0,029792241	0,01778299	0,042925665

14

PEG-YRWD-OH		
	10 mM EDC-1 mM Precursor	20 mM EDC-10 mM Precursor
k0	0,0045	0,0045
k1	0,008649345	0,016673588
k2	0,582221669	0,025649727
k3	0,111667549	0,139674585
k4	0,421416517	0,116989879
k5	0,01429864	0,000100078
k6	0,040182646	0,361977464
k7	0,226925576	0,028771889
k8	0,012717867	0,10105032
k9	0,491858077	0,082633705
k10	0,857611699	0,974364651
k11	0,9950005	0,006807753
k12	0,006771725	0,019395434
k13	0,009777597	0,032629584

Ac-FRGMYRGD-OH		
	10 mM EDC-1 mM Precursor	20 mM EDC-10 mM Precursor
k0	0,0045	0,0045
k1	0,007346959	0,008316725
k2	0,046840369	0,000610479
k3	0,287644441	0,000574912
k4	0,015889587	0,142081282
k5	0,000100162	0,011245793
k6	0,292018026	0,01886744
k7	0,032773966	0,787123586
k8	0,025463649	0,53944565
k9	0,278464029	0,892787856
k10	0,753253563	0,002388376
k11	0,085542508	0,139381091
k12	0,007548677	0,017452261
k13	0,007077044	0,011179116

c) Percentage Calculations in Ac-AYRGD-OH

We use the set of kinetic constants values from the first condition, i.e., 10 mM EDC and 3 mM Precursor. Then, we integrated the differential equation for the compound of interest and calculated percentages as the total amount of each species

15

produced/consumed over time for the current condition. Finally, the values were normalized from 0 to 100 (Plotting_and_%_AYRGD.ipynb).
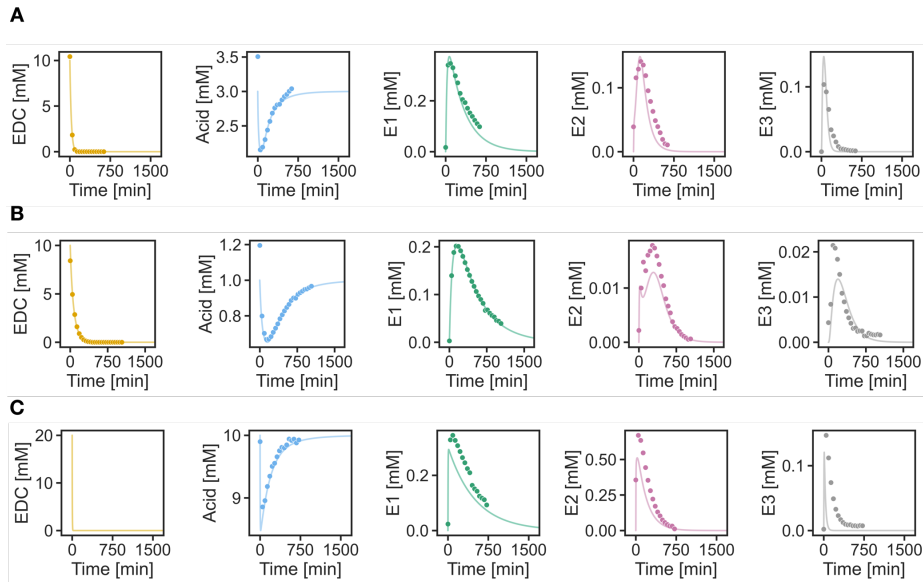
Figure 1. Results of the fitting using Ac-AYRGD-OH at different conditions: **A)** 10 mM EDC and 3 mM Precursor. **B)** 10 mM EDC and 1 mM Precursor. **C)** 20 mM EDC and 10 mM Precursor.
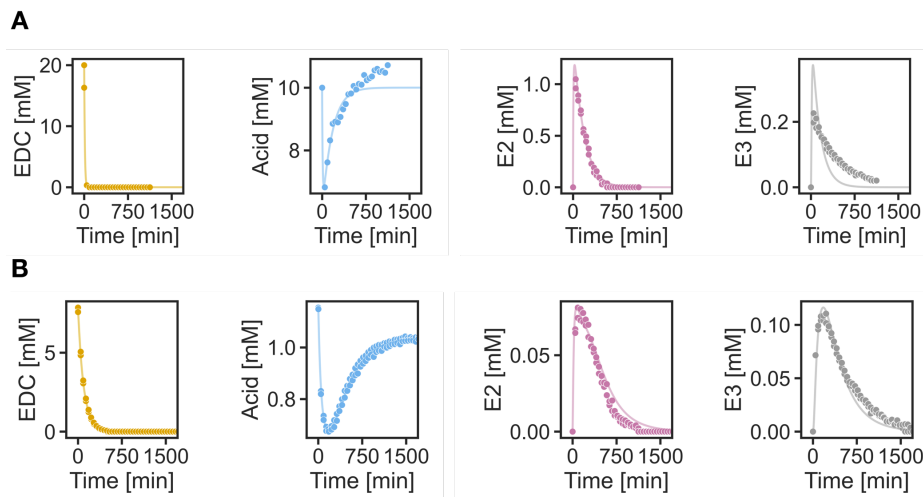
Figure 2. Results of the fitting using 2-[2-(2-methoxy-ethoxy)ethoxy]acetyl-YRWD-OH at different conditions: **A)** 20 mM EDC and 10 mM Precursor. **B)** 10 mM EDC and 1 mM Precursor.
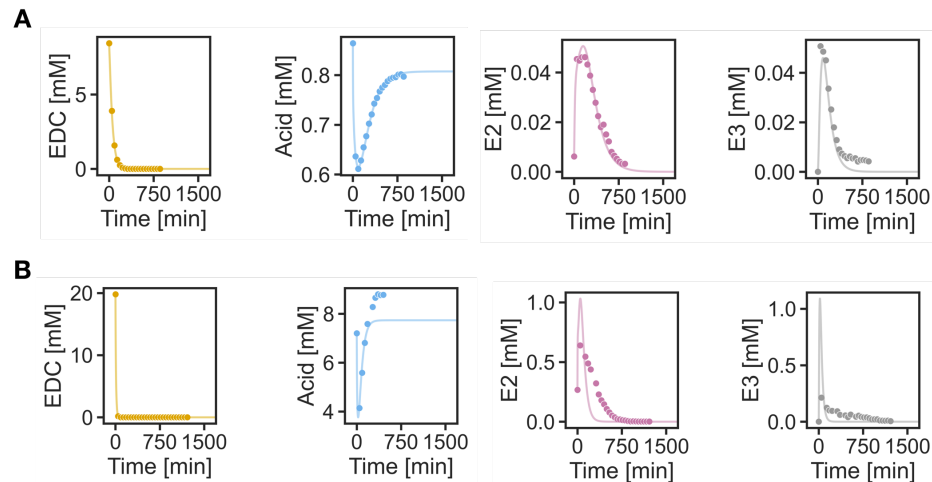
Figure 3. Results of the fitting using Ac-FRGMYRGD-OH at different conditions: **A)** 10 mM EDC and 1 mM Precursor. **B)** 20 mM EDC and 10 mM Precursor.

d) Note: Fittings are not as robust as in other examples of carbodiimide reaction cycles we have described before. We observed differences in the optimal fitted values of the same parameters in different experiments, e.g., changing concentrations, which may indicate the presence of unknown and unmodeled reactions or complexes that affect our model.

Differentiation of peptide macrocycles by MS and hydrolysis.

LC-MS analysis gave the following [m/z] values for the corresponding ester products.

peptide	cyclomonomer [m/z]	linear dimer [m/z]	cyclodimer [m/z]
Ac-YGGD-OH	433.25 [M-H]$^-$	442.57 [M-2H]$^{2-}$ 885.35 [M-H]$^-$	433.78 [M-2H]$^{2-}$ 867.28 [M-H]$^-$
Ac-YRGD-OH	534.40 [M+H]$^+$	543.58 [M+2H]$^{2+}$ 1085.36 [M+H]$^+$	---
Ac-YRFD-OH	624.74 [M+H]$^+$	633.79 [M+2H]$^{2+}$	624.88 [M+2H]$^{2+}$
Ac-YRWD-OH	---	672.64 [M+2H]$^{2+}$	663.85 [M+2H]$^{2+}$
Ac-AYRGD-OH	605.38 [M+H]$^+$	614.79 [M+2H]$^{2+}$	605.81 [M+2H]$^{2+}$ 1209.50 [M+H]$^+$
Ac-MYRGD-OH	674.98 [M+2H]$^{2+}$	674.98 [M+2H]$^{2+}$	665.94 [M+2H]$^{2+}$ 1329.45 [M+H]$^+$
2-[2-(2-methoxy-ethoxy)ethoxy]acetyl-YRWD-OH	---	791.16 [M+2H]$^{2+}$ 1579.31 [M+H]$^+$	781.39 [M+2H]$^{2+}$
Ac-FRGMYRGD-OH	---	518.20 [M+4H]$^{4+}$ 690.30 [M+3H]$^{3+}$ 1034.71 [M+2H]$^{2+}$	513.64 [M+4H]$^{4+}$ 684.10 [M+3H]$^{3+}$ 1025.28 [M+2H]$^{2+}$

By LC-MS analysis, both the cyclized monomers and the dimer macrocycles of the peptides can lead to very similar m/z values. To distinguish them further, the expected dimer macrocycles were collected from HPLC and diluted 1:1 with 500 mM MES at a pH of 5.3 (250 mM final MES concentration). The hydrolysis of the cyclic peptide dimers was then tracked for multiple hours by HPLC. The proposed cyclic dimer peptides were hydrolyzing by the proposed pathway A (Scheme 1). They formed the open dimer form and hydrolyzed further to build up the peptide monomer.

In addition, these hydrolysis experiments helped to rule out the formation of the ester product in pathway B, which would have formed via the activation of the internal, remaining carboxylate group of a linear dimer in solution. A cyclic dimer hydrolysis

18

pathway like B was observed for none of the peptides, proving the head-to-tail cyclization pattern for the dimer macrocycles.

A

B
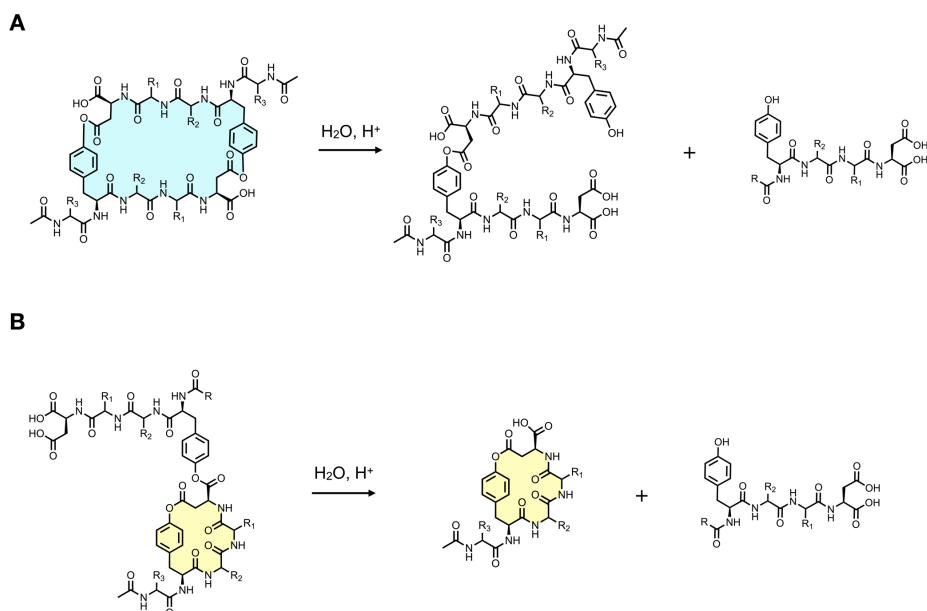
Scheme 1. Differentiation of the double-ester products. The hydrolysis pathway **A** was observed for all expected cyclodimer product (head-to-tail cyclization product). The products did not show a hydrolysis pathway **B** that would correspond to a head-to-side chain cyclization product.

19

Supporting Figures for the Main Text.
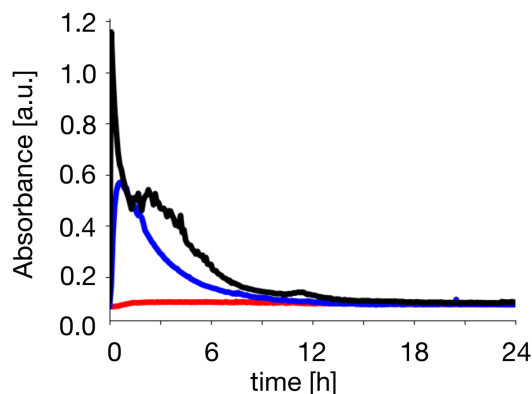
Supporting Figure 1. Turbidity traces of complex coacervate samples from Ac-FRGMYRGD-OH that were fueled with EDC under different conditions in the presence of 1 mM polyU (expressed in monomer units) in 200 mM MES buffer at pH 5.3. Black trace: 10 mM of peptide were fueled with 20 mM of EDC. Blue trace: 3 mM of peptide were fueled with 10 mM of EDC. Red trace: 1 mM of peptide were fueled with 10 mM of EDC. Irregularities in the turbidity traces come from the droplets settling on the bottom of the wells over time. For all solutions, turbidity vanished completely, and no residues were present after 24 hours.
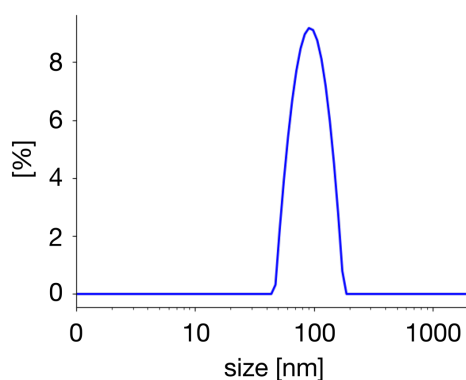
Supporting Figure 2. Intensity-weighted size distribution of 10 mM of Ac-FRGMYRGD-OH that were fueled with 20 mM of EDC in the presence of 1 mM PEG$_{5k}$-b-PSS$_{77}$ in 200 mM MES buffer at pH 5.3. This size distribution was obtained one hour after the EDC was added, corresponding to the expected maximum of turbidity/scattering rate.

20

References

[1]   F. Späth, C. Donau, A. M. Bergmann, M. Kränzlein, C. V. Synatschke, B. Rieger, J. Boekhoven, *J. Am. Chem. Soc.* **2021**, *143*, 4782-4789.

[2]   J. Schindelin, I. Arganda-Carreras, E. Frise, V. Kaynig, M. Longair, T. Pietzsch, S. Preibisch, C. Rueden, S. Saalfeld, B. Schmid, J. Y. Tinevez, D. J. White, V. Hartenstein, K. Eliceiri, P. Tomancak, A. Cardona, *Nat. Methods* **2012**, *9*, 676-682.

[3]   X. Chen, H. Soria-Carrera, O. Zozulia, J. Boekhoven, *Chem. Sci.* **2023**, *14*, 12653-12660.

8. Conclusion and Outlook

This thesis aimed to explore modifications of chemically fueled coacervates to create coacervate-based materials with life-like properties. As described in Chapter 1.2.2, these dynamic properties and behaviors are the consequences of droplet material fluxes. To influence these fluxes, it is necessary to understand the building blocks' influences on the outcome of a chemical reaction cycle forming coacervates and how to design them, regardless of whether the building blocks take part in the carbodiimide-driven reaction cycle or not.

The first variant of the reaction cycle for chemically fueled complex coacervation was based on the peptide family AcF(RG)$_n$D-OH. As described in Chapter 4, the charge of the peptide precursor determines whether active, *i.e.,* chemically responsive complex coacervates, could be formed by adding the carbodiimide fuel. Dynamic complex coacervates were only obtained for peptide designs with no or little positive net charge in its deactivated state. These results show that the charge-switching mechanism requires fine-tuning of the precursor charge in order to achieve maximum effect and control in such a chemically fueled complex coacervation platform. Ideally, the design starts from precursors with no net charge and increases their charge sufficiently upon activation to result in a maximum effect of the charge-switching while keeping the resulting assemblies as dynamic as possible. The polymer component also influences the dynamics of chemically fueled coacervates via its multivalent binding to the peptides. Block copolymers were introduced as polyanions, leading to chemically fueled complex coacervate core micelles. These dynamic nanostructures even transitioned between different morphologies in the ongoing reaction cycle. Overall, I could show that the polymeric building blocks as chemically passive components influence the outcome of the reaction cycle by affecting the material fluxes. The shortest possible polyanions should be used to achieve maximum dynamics for the formation of chemically active coacervates. At the structural level, block copolymers can provide a further degree of dynamicity in active polyelectrolyte complexes.

Based on these findings, I then investigated different electrolyte groups for the polyanions in Chapter 5. The charged groups control the binding affinities towards the peptide AcF(RG)$_3$D-OH and its anhydride without influencing the reaction cycle. Changing the passive polymer scaffold allowed control over the droplet evolution and their lifetimes. Strong interactions, *e.g.,* of PSS with the peptide precursor and the peptide anhydride, lead to droplets with a slow decay — less strongly interacting polymers, *e.g.,* PVPA and PVS, form coacervates that follow the anhydride evolution dynamically. I could show that hindered peptide diffusion for strongly interacting peptide-polymer pairs only affects the coacervate dynamics on micrometer scales and not for nanometer-sized complexes. Weak polyelectrolyte groups hinder the peptide

material fluxes the least and consequently also do not hinder the response of the chemically fueled complex coacervates to the evolution of the building block concentrations. Polyanions such as PVPA would therefore be ideal candidates for active droplets with life-like properties, as they do not weaken the impact of the anhydride hydrolysis on the material flows in these externally maintained droplets.

Chapter 6 emphasized oligonucleotides as biologically relevant and structurally diverse polyanions. I showed that they are weak polyelectrolytes and proved the nucleobases' influence on DNA-peptide interactions. Therefore, higher chain lengths are required for the chemically fueled phase separation with AcF(RG)$_3$D-OH. The hybridization state offered another possibility to control the outcome of the active coacervation platform. Double-stranded DNA formed smaller aggregates in lower numbers due to its higher persistence length in comparison to single-stranded DNA. Any structure formation that hinders the condensation of the polyanions must be avoided to obtain dynamic droplets, even for weak polyanions like DNA. These results indicate that secondary structures are another feature of polyanions that needs to be controlled for chemically fueled complex coacervates. In addition to the polymer length and the type of the electrolyte group, it represents another influence that goes beyond the reaction cycle.

An extension of the reaction cycle in Chapter 7 overcame the limitation of carbodiimide-driven coacervation to complex coacervates alone. Introducing tyrosine side chains into aspartic acid-terminated peptides enabled an additional reaction pathway that forms ester bonds. These ester groups form by inter- or intramolecular opening of the peptide anhydrides and they have longer lifetimes than the anhydrides. This extended chemical reaction network creates fuel-driven dynamic combinatorial peptide libraries. Next to complex coacervation with polyanions, chemically fueled simple coacervation was achieved by incorporating arginine units, aromatic amino acids, and different N-termini. The associated phase separation selects for certain library members due to their different phase separation propensities. The lifetimes of the resulting assemblies, which lasted several hours, were significantly longer than those of peptide anhydride-based condensates. Overall, introducing this new reversible chemical bond made it possible to control the lifetime of the active droplets directly, apart from the charge state of the precursors or different fuel concentrations. The complexity of combinatorial library mixtures makes them ideal mimics of structurally complex membraneless organelles.

I could show that the molecular structures of building blocks play a detrimental role in chemically fueled coacervation. I introduced various new molecular designs and significantly expanded the toolbox for chemically fueled complex coacervates. For future studies, many building block combinations should be tested under continuous fueling conditions. The

microfluidic techniques that our group introduced can be useful in achieving steady-states of the species' concentrations.[72, 75] Due to the sustained material fluxes in these steady states, life-like behavior could emerge. The dynamic combinations of peptides and polyanions, *e.g.,* AcF(RG)$_3$D-OH and PVPA, might be particularly interesting because strong peptide building block fluxes can be expected due to weak peptide-polyanion interactions. The ester-forming peptide AcFRGMYRGD-OH could serve as another extreme example in such experiments due to the slow deactivation reaction driving the destabilizing material flux.

The polyanion chain length's influence on the complex coacervates' properties could be exploited in droplets where the chains are extended *in situ*. It was shown that ribozymes, for example, retain or even increase their activity in complex coacervates.[112-113] Thus, hybrid platforms could be realized where oligonucleotides are extended *in situ* by ribozyme catalysis in chemically fueled coacervates. This would create the possibility to investigate how the effects of changing building block concentrations and growing polyanion chains influence each other similar to genotype-phenotype coupling.[113]

The coacervate droplets based on cationic tyrosine esters could serve as a delivery platform, releasing its building blocks over hours due to hydrolysis. The long coacervate lifetimes might be useful for a sustained release of functional cargo, e.g. DNA or RNA, in therapeutic applications.

9. Methods

The experimental methods for Chapters 4,5 and 7 are given directly after the individual sections. The following section contains additional information for Chapter 6.

Materials

All β-cyanoethyl phosphoramidites (dA, dT, dC, dmf-dG, C3 Spacer), CPG solid supports, synthesis reagents (Activator, Diluent, Anhydrous Wash, Cap Mix A and B, Oxidizer and Deblock) for oligonucleotide synthesis and Glen-Pak™ DNA purification cartridges were purchased from GlenResearch/Eurogentec. Single stranded deoxyribonucleic acid (587-831 bp, 10 mg/mL) was purchased from Sigma-Aldrich/Merck. Double-stranded deoxyribonucleic acid ($\leq$ 2000 bp, 10 mg/mL) was purchased from Invitrogen™/Thermo Fisher. All other solvents and reagents were purchased from Sigma-Aldrich/Merck or VWR and used without further purification.

Sample Preparation

The samples in their final concentrations were obtained by mixing the appropriate volumes of stock solutions. The peptide stock solution had a concentration of 100 mM, the oligonucleotide stocks a concentration of 41 mM expressed in monomer units or negative charges, and the MES buffer was used in a concentration of 500 mM at pH 5.3. The final sample volume was adjusted by adding MilliQ© water. Stocks of EDC were prepared at either 1 M or 2 M concentrations in MilliQ© water. They were always prepared freshly to avoid long periods of hydrolysis. The stock solution of single-stranded DNA was boiled for 10 minutes and cooled on ice for at least 5 minutes prior to use to prevent reannealing.

Oligonucleotide Synthesis

Oligonucleotide synthesis was performed on an Applied Biosystems Model 392 DNA/RNA automated synthesizer or a PerSeptive Expedite 8909 Nucleic Acid Synthesis System. Syntheses were performed on a 1.0 μmole scale by applying standard coupling cycles for DMT protected β-cyanoethyl phosphoramidites. The first base (starting from the 3` end) was already loaded onto the CPG support. The crude oligos were cleaved from the solid support by reacting the loaded CPG support with 1 mL of a 30% ammonium hydroxide solution overnight. The crude product was then purified with Glen-Pak™ DNA purification cartridges following the manufacturer protocols for DMT-on procedures. The purified oligos were lyophilized and analyzed via mass spectrometry (Supporting Table 1) and HPLC or polyacrylamide gel

electrophoresis. All oligomers were obtained in high purity after their purification with Glen-Pak[TM] cartridges (Supporting Figure 1).

Entry	Sequence (5'→3')	Mass found [a), b)]	Mass calculated (monoisotopic)
[1]	$(C3)_{19}T$	1432.11 [a)]	1431.68 (2-)
[2]	T_{20}	6016.9 [b)]	6021.03 (1-)
[3]	ATT TGG TCA GTA TCG AAT GG	6166.2 [b)]	6167.92 (1-)
[4]	$(C3-T)_{20}$	2194.75 [a)]	2194.8 (4-)
[5]	T_{40}	2420.08 [a)]	2420.20 (5-)
[6]	T_{45}	13626.83 [b)]	13628.05 (1+)
[7]	CTT CGG TGT AAA GAT TCA TCT CAG TCC ATT CGA TAC TGA CCA AAT	13757.8 [b)]	13755.03 (1+)
[9]	T_{80}	1212.701 [a)]	1212.692 (20-)

Supporting Table 1. The table shows the results of MS analysis of the given oligonucleotide sequences. The results were obtained from LC-MS [a)] or MALDI-TOF [b)] analysis.

A

B
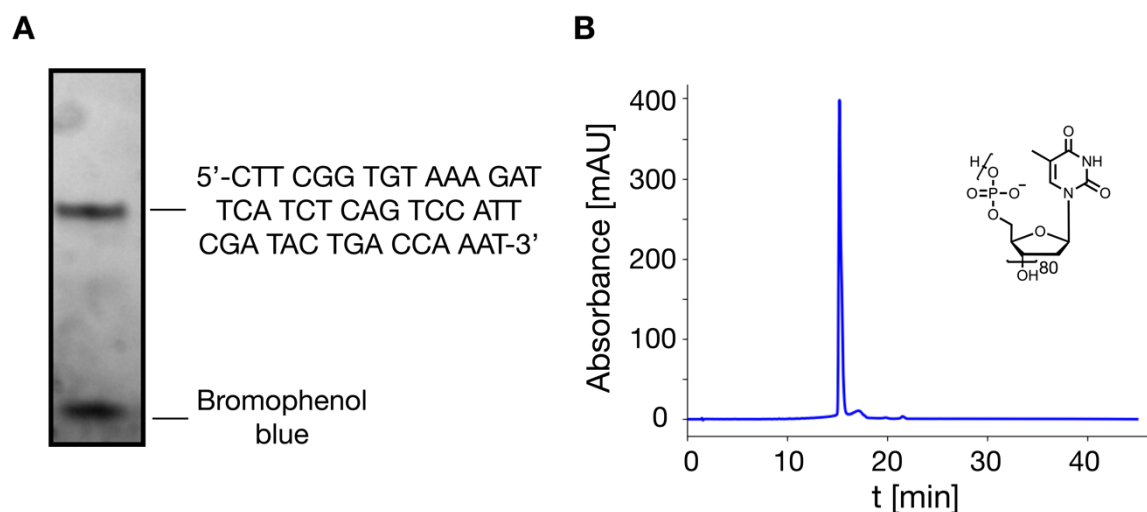
Supporting Figure 1. A. Exemplary analysis of oligonucleotide purity by gel electrophoresis after synthesis and purification. **B.** Exemplary HPLC chromatogram of $(dT)_{80}$ after purification.

Polyacrylamide Gel Electrophoresis

15% or 10%-PAGE gels were prepared freshly from urea, 40% Acrylamide and Bisacrylamide solutions (19:1), 10% APS solution, and TEMED with 5X TBE buffer and MilliQ© water. The mixtures were cast between two glass plates that were separated with a 0.75 mm spacer in a

cassette holder. After a minimum polymerization time of one hour, urea residues were removed with MilliQ© water before using the gels. Bromophenol blue (0.25% Bromophenol blue solution with 40 w/v % sucrose) was used as a tracking dye to monitor the separation. After separation on a Mini-PROTEAN III from BioRad, the gels were soaked in Stains-All solution (1:1 Formamide/water mixture) for 10 minutes and then visualized on an ImageQuant RT ECL instrument from GE Healthcare Life Science.

HPLC chromatography

Oligonucleotides were analyzed by analytical HPLC on a DNA PacRP column (Thermofisher Vanquish, DNA PacRP, 4 µm, 2.1x100mm) in a linear gradient of HAA 25 mM and ACN:HAA 25 mM 50:50 at 60°C (HAA = hexylammonium acetate, pH = 8.5) over 35 minutes (3 minutes pre-equilibration 50%:50%, then 50%:50% to 0%:100% solvent mixtures).

Peptide anhydride concentrations were quantified during the ongoing reaction cycle in the presence of $(dT)_{80}$. A quenching method with benzylamine was applied and the mixtures were separated on a ThermoScientific Hypersil GOLD column (250 x 4.6 mm, 5 µm particle size) with a ThermoFisher Dionex Ultimate 300 liquid chromatography setup (Dionex Ultimate pump, Dionex Ultimate Autosampler, Dionex Ultimate 3000 RS Variable Wavelength Detector). To quench the hydrolytically unstable peptide anhydride, 20 µL aliquots of the reaction mixture were mixed into 10 µL of an aqueous benzylamine solution (900 mM) at different time points after the start of the reaction cycle with EDC. A linear gradient from 2% to 98% ACN and MilliQ© water (both with 0.1% TFA) was applied over 12 minutes to achieve separation of all components at 25°C. The data was analyzed with the Chromeleon 7 Chromatography Data System Software (Version 7.2 SR4). The peptide anhydride was quantified via the peptide-benzylamide. The experiment was performed in duplicates. The anhydride concentration follows the kinetic model nicely in the presence of $(dT)_{80}$ proving that the DNA does not participate in any unwanted side reaction. A previously published kinetic model was applied.[102]

Laser Confocal Microscopy

Samples were analyzed via laser confocal microscopy on a Leica TCS SP8 confocal microscope with a 63x water immersion objective (1.2 NA). Samples were prepared in micro-well plates (ibidi, µ-Slide Angiogenesis Glass Bottom) that were passivated with PVA before use. NBD-G(RG)3N-NH2 was used as the fluorescent dye in a concentration of 200 nM and it was excited at 488 nm and imaged in the range of 500 nm to 650 nm.

MALDI MS Analysis

Matrix-assisted Laser Desorption Ionization (MALDI) mass spectrometry was performed on a Voyager Elite system from Applied Biosystems equipped with a TOF (time of flight) mass analyzer. A minimum amount of 1 nmol of the oligonucleotide was dissolved in 3 μL of MilliQ© water and 3 μL of a matrix solution before spotting the sample on a target. The matrix solution was prepared by mixing a 25 mg/mL solution of ammonium citrate in MilliQ© water with a 25 mg/mL 2,4,6-Trihydroxyacetophenone (THAP) solution in a 1:1 acetonitrile- MilliQ© water mixture.

LC-MS Analysis

HPLC-MS analysis was performed on bioinert instrumentation from Agilent Technologies (Quaternary pump and solvent degasser, temperature-controlled sample holder at 16°C, UV absorption diode array detector (DAD)). The separation was performed on an AdvanceBio Oligonucleotide column (4.6 x 150 mm, 2.7 μm) at 30°C. The outflow was injected into the ESI-QTOF. The mass spectra were recorded in negative mode with a drying gas flow of 8 L/min at 300 °C and an acquisition time of 200 ms per spectrum (5 spectra per second, fragmentor voltage 175 V, capillary voltage 4 kV, nozzle voltage 2 kV). The data was processed with the Agilent MassHunter Analysis Navigator Software B.08.00.

Turbidity Measurements via UV-Vis spectroscopy

The evolution of turbidity upon fueling samples with EDC was followed on a UV-Vis plate reader (SpectraMax® ABS Plus, Molecular Devices). The absorbance at 600 nm was tracked at 25°C in 100 μL sample volumes in 96 well plates.

ITC analysis

Titrations were performed at 25°C on a MicroCal PEAQ-ITC instrument from Malvern Panalytical. 2 μL aliquots of a 3 mM $AcF(RG)_3N-NH_2$ solution were titrated into 250 μM of oligonucleotide (expressed in monomer units). All solutions were prepared in 200 mM MES buffer at pH 5.3. Control titrations of only the peptide into the buffer were performed and subtracted from the oligonucleotide samples. Data analysis was performed with the PEAQ-ITC analysis software.

DLS analysis

DLS experiments were performed on a Litesizer 500 particle size analyzer from Anton Paar. The instrument was equipped with a 658 nm 40 mW laser diode. The samples were measured in a 45 µL low volume quartz cuvette with a 3x3 mm light path (Hellma Analytics).

10. Further Publications

The following list shows publications that I have contributed to but have not been reprinted above.

[1]   Donau, C.; <u>Späth, F.</u>; Sosson, M.; Kriebisch, B. A. K.; Schnitter, F.; Tena-Solsona, M.; Kang, H. S.; Salibi, E.; Sattler, M.; Mutschler, H.; Boekhoven, J., Active coacervate droplets as a model for membraneless organelles and protocells. *Nat. Commun.* **2020,** *11* (1), 5167.

[2]   Donau, C.; <u>Späth, F.</u>; Stasi, M.; Bergmann, A. M.; Boekhoven, J., Phase Transitions in Chemically Fueled, Multiphase Complex Coacervate Droplets. *Angew. Chem. Int. Ed. Engl.* **2022,** *61* (46), e202211905.

[3]   Bergmann, A. M.; Donau, C.; <u>Späth, F.</u>; Jahnke, K.; Göpfrich, K.; Boekhoven, J., Evolution and Single-Droplet Analysis of Fuel-Driven Compartments by Droplet-Based Microfluidics. *Angew. Chem. Int. Ed. Engl.* **2022,** *61* (32), e202203928.

11. Acknowledgements

I want to thank Job Boekhoven for making it possible to pursue my doctorate in his research group. He has supported my work since my Master's degree in the form of a research internship and a Master's thesis. Many thanks for the constant support and the different projects I was able to work on. I could learn a lot both professionally and personally during my time in your group.

I would also like to thank Julianne Gibbs for hosting me during my research stay abroad at the University of Alberta in Canada. During this time, I gained experience in the exciting world of oligonucleotides and learned many new skills in oligonucleotide synthesis and analysis. Many thanks also to Nahida and Anantha for the support during this time and the scientific exchange during the annual ATUMS meetings.

I also want to thank my collaborators from the WACKER-Chair. Thank you for your help and your knowledge. Thanks to you, I could continue pursuing my passion for polymers.

Thank you to all the former and current group members of the Boekhoven Lab. Working with you taught me a lot and I always experienced a positive working atmosphere. We were able to discuss both scientific and non-scientific topics and always had a lot of fun. I want to especially thank the others from my office especially: Laura, Judit, Michele, Héctor, Xiaoyao, and Jennifer (with Savannah). Thank you for putting up with my nonsense and for making me laugh so often. Laura, thank you for showing me the true meaning of "girlboss".

I also want to thank my family and friends. Thank you for always being there for me, always supporting me and motivating me. Without you, I would have never been able to take this path. Thank you for everything Matthias, particularly your patience.

12.   References

1.   Sing, C. E.; Perry, S. L., Recent progress in the science of complex coacervation. *Soft Matter* **2020,** *16* (12), 2885-2914.
2.   Sing, C. E., Development of the modern theory of polymeric complex coacervation. *Adv. Colloid Interface Sci.* **2017,** *239*, 2-16.
3.   Wang, Q.; Schlenoff, J. B., The Polyelectrolyte Complex/Coacervate Continuum. *Macromolecules* **2014,** *47* (9), 3108-3116.
4.   Kayitmazer, A. B., Thermodynamics of complex coacervation. *Adv. Colloid Interface Sci.* **2017,** *239*, 169-177.
5.   Bucur, C. B.; Sui, Z.; Schlenoff, J. B., Ideal mixing in polyelectrolyte complexes and multilayers: entropy driven assembly. *J. Am. Chem. Soc.* **2006,** *128* (42), 13690-1.
6.   Priftis, D.; Laugel, N.; Tirrell, M., Thermodynamic characterization of polypeptide complex coacervation. *Langmuir* **2012,** *28* (45), 15947-57.
7.   Chen, S.; Wang, Z. G., Driving force and pathway in polyelectrolyte complex coacervation. *PNAS* **2022,** *119* (36), e2209975119.
8.   Singh, A. N.; Yethiraj, A., Liquid-Liquid Phase Separation As the Second Step of Complex Coacervation. *J. Phys. Chem. B* **2021,** *125* (12), 3023-3031.
9.   Timilsena, Y. P.; Akanbi, T. O.; Khalid, N.; Adhikari, B.; Barrow, C. J., Complex coacervation: Principles, mechanisms and applications in microencapsulation. *Int. J. Biol. Macromol.* **2019,** *121*, 1276-1286.
10.   Neitzel, A. E.; Fang, Y. N.; Yu, B.; Rumyantsev, A. M.; de Pablo, J. J.; Tirrell, M. V., Polyelectrolyte Complex Coacervation across a Broad Range of Charge Densities. *Macromolecules* **2021,** *54* (14), 6878-6890.
11.   Yu, B.; Rumyantsev, A. M.; Jackson, N. E.; Liang, H.; Ting, J. M.; Meng, S.; Tirrell, M. V.; de Pablo, J. J., Complex coacervation of statistical polyelectrolytes: role of monomer sequences and formation of inhomogeneous coacervates. *Molecular Systems Design & Engineering* **2021,** *6* (10), 790-804.
12.   Magana, J. R.; Sproncken, C. C. M.; Voets, I. K., On Complex Coacervate Core Micelles: Structure-Function Perspectives. *Polymers* **2020,** *12* (9).
13.   Voets, I. K.; de Keizer, A.; Cohen Stuart, M. A., Complex coacervate core micelles. *Adv. Colloid Interface Sci.* **2009,** *147-148*, 300-18.
14.   van der Kooij, H. M.; Spruijt, E.; Voets, I. K.; Fokkink, R.; Cohen Stuart, M. A.; van der Gucht, J., On the stability and morphology of complex coacervate core micelles: from spherical to wormlike micelles. *Langmuir* **2012,** *28* (40), 14180-91.
15.   Rumyantsev, A. M.; Zhulina, E. B.; Borisov, O. V., Scaling Theory of Complex Coacervate Core Micelles. *ACS Macro Lett.* **2018,** *7* (7), 811-816.
16.   Shin, Y.; Brangwynne, C. P., Liquid phase condensation in cell physiology and disease. *Science* **2017,** *357* (6357).
17.   Gupta, A.; Bohidar, H. B., Kinetics of phase separation in systems exhibiting simple coacervation. *Phys. Rev. E Stat. Nonlin. Soft Matter Phys.* **2005,** *72* (1 Pt 1), 011507.
18.   Mohanty, B.; Bohidar, H. B., Systematic of alcohol-induced simple coacervation in aqueous gelatin solutions. *Biomacromolecules* **2003,** *4* (4), 1080-6.
19.   Wang, J.; Choi, J. M.; Holehouse, A. S.; Lee, H. O.; Zhang, X.; Jahnel, M.; Maharana, S.; Lemaitre, R.; Pozniakovsky, A.; Drechsel, D.; Poser, I.; Pappu, R. V.; Alberti, S.; Hyman, A. A., A Molecular Grammar Governing the Driving Forces for Phase Separation of Prion-like RNA Binding Proteins. *Cell* **2018,** *174* (3), 688-699 e16.
20.   Nott, T. J.; Petsalaki, E.; Farber, P.; Jervis, D.; Fussner, E.; Plochowietz, A.; Craggs, T. D.; Bazett-Jones, D. P.; Pawson, T.; Forman-Kay, J. D.; Baldwin, A. J., Phase transition of a disordered nuage protein generates environmentally responsive membraneless organelles. *Mol. Cell* **2015,** *57* (5), 936-947.
21.   Zydziak, N.; Iqbal, M. H.; Chaumont, A.; Combes, A.; Wasielewski, E.; Legros, M.; Jierry, L.; Lavalle, P.; Boulmedais, F.; Chan-Seng, D., Unexpected aqueous UCST behavior of a cationic comb polymer with pentaarginine side chains. *Eur. Polym. J.* **2020,** *125*.

22. Oh, S.-H.; Lee, J.; Lee, M.; Kim, S.; Lee, W. B.; Lee, D. W.; Choi, S.-H., Simple Coacervation of Guanidinium-Containing Polymers Induced by Monovalent Salt. *Macromolecules* **2023,** *56* (11), 3989-3999.

23. Moulik, S. P.; Rakshit, A. K.; Pan, A.; Naskar, B., An Overview of Coacervates: The Special Disperse State of Amphiphilic and Polymeric Materials in Solution. *Colloids and Interfaces* **2022,** *6* (3).

24. Ban, E.; Kim, A., Coacervates: Recent developments as nanostructure delivery platforms for therapeutic biomolecules. *Int. J. Pharm.* **2022,** *624*, 122058.

25. Blocher, W. C.; Perry, S. L., Complex coacervate-based materials for biomedicine. *Wiley Interdiscip. Rev. Nanomed. Nanobiotechnol.* **2017,** *9* (4).

26. Margossian, K. O.; Brown, M. U.; Emrick, T.; Muthukumar, M., Coacervation in polyzwitterion-polyelectrolyte systems and their potential applications for gastrointestinal drug delivery platforms. *Nat. Commun.* **2022,** *13* (1), 2250.

27. Forenzo, C.; Larsen, J., Complex Coacervates as a Promising Vehicle for mRNA Delivery: A Comprehensive Review of Recent Advances and Challenges. *Mol. Pharm.* **2023,** *20* (9), 4387-4403.

28. Nguyen, N. T.; Jennings, J.; Milani, A. H.; Martino, C. D. S.; Nguyen, L. T. B.; Wu, S.; Mokhtar, M. Z.; Saunders, J. M.; Gautrot, J. E.; Armes, S. P.; Saunders, B. R., Highly Stretchable Conductive Covalent Coacervate Gels for Electronic Skin. *Biomacromolecules* **2022,** *23* (3), 1423-1432.

29. Pace, G. T.; Le, M. L.; Clément, R. J.; Segalman, R. A., A Coacervate-Based Mixed-Conducting Binder for High-Power, High-Energy Batteries. *ACS Energy Letters* **2023,** *8* (6), 2781-2788.

30. Hyman, A. A.; Weber, C. A.; Julicher, F., Liquid-liquid phase separation in biology. *Annu. Rev. Cell Dev. Biol.* **2014,** *30*, 39-58.

31. Lin, Z.; Beneyton, T.; Baret, J. C.; Martin, N., Coacervate Droplets for Synthetic Cells. *Small Methods* **2023,** *7* (12), e2300496.

32. Banani, S. F.; Lee, H. O.; Hyman, A. A.; Rosen, M. K., Biomolecular condensates: organizers of cellular biochemistry. *Nat. Rev. Mol. Cell Biol.* **2017,** *18* (5), 285-298.

33. Lyon, A. S.; Peeples, W. B.; Rosen, M. K., A framework for understanding the functions of biomolecular condensates across scales. *Nat. Rev. Mol. Cell Biol.* **2021,** *22* (3), 215-235.

34. Hirose, T.; Ninomiya, K.; Nakagawa, S.; Yamazaki, T., A guide to membraneless organelles and their various roles in gene regulation. *Nat. Rev. Mol. Cell Biol.* **2023,** *24* (4), 288-304.

35. Brangwynne, Clifford P.; Tompa, P.; Pappu, Rohit V., Polymer physics of intracellular phase transitions. *Nature Physics* **2015,** *11* (11), 899-904.

36. Alberti, S.; Hyman, A. A., Biomolecular condensates at the nexus of cellular stress, protein aggregation disease and ageing. *Nat. Rev. Mol. Cell Biol.* **2021,** *22* (3), 196-213.

37. Linsenmeier, M.; Hondele, M.; Grigolato, F.; Secchi, E.; Weis, K.; Arosio, P., Dynamic arrest and aging of biomolecular condensates are modulated by low-complexity domains, RNA and biochemical activity. *Nat. Commun.* **2022,** *13* (1), 3030.

38. Hondele, M.; Heinrich, S.; De Los Rios, P.; Weis, K., Membraneless organelles: phasing out of equilibrium. *Emerg. Top. Life Sci.* **2020,** *4* (3), 331-342.

39. Ray, S.; Singh, N.; Kumar, R.; Patel, K.; Pandey, S.; Datta, D.; Mahato, J.; Panigrahi, R.; Navalkar, A.; Mehra, S.; Gadhe, L.; Chatterjee, D.; Sawner, A. S.; Maiti, S.; Bhatia, S.; Gerez, J. A.; Chowdhury, A.; Kumar, A.; Padinhateeri, R.; Riek, R.; Krishnamoorthy, G.; Maji, S. K., alpha-Synuclein aggregation nucleates through liquid-liquid phase separation. *Nat. Chem.* **2020,** *12* (8), 705-716.

40. Wang, B.; Zhang, L.; Dai, T.; Qin, Z.; Lu, H.; Zhang, L.; Zhou, F., Liquid-liquid phase separation in human health and diseases. *Signal Transduct. Target. Ther.* **2021,** *6* (1), 290.

41. Hondele, M.; Sachdev, R.; Heinrich, S.; Wang, J.; Vallotton, P.; Fontoura, B. M. A.; Weis, K., DEAD-box ATPases are global regulators of phase-separated organelles. *Nature* **2019,** *573* (7772), 144-148.

42. Protter, D. S. W.; Parker, R., Principles and Properties of Stress Granules. *Trends Cell Biol.* **2016,** *26* (9), 668-679.

43. Sivananthan, S.; Gosse, J. T.; Huard, S.; Baetz, K., Pab1 acetylation at K131 decreases stress granule formation in Saccharomyces cerevisiae. *J. Biol. Chem.* **2023,** *299* (2), 102834.

44. Fulton, M. D.; Brown, T.; Zheng, Y. G., The Biological Axis of Protein Arginine Methylation and Asymmetric Dimethylarginine. *Int. J. Mol. Sci.* **2019,** *20* (13).

45. Wang, J. T.; Smith, J.; Chen, B. C.; Schmidt, H.; Rasoloson, D.; Paix, A.; Lambrus, B. G.; Calidas, D.; Betzig, E.; Seydoux, G., Regulation of RNA granule dynamics by phosphorylation of serine-rich, intrinsically disordered proteins in C. elegans. *Elife* **2014,** *3*, e04591.

46. Zwicker, D.; Seyboldt, R.; Weber, C. A.; Hyman, A. A.; Jülicher, F., Growth and division of active droplets provides a model for protocells. *Nature Physics* **2016,** *13* (4), 408-413.

47. Zwicker, D.; Hyman, A. A.; Julicher, F., Suppression of Ostwald ripening in active emulsions. *Phys. Rev. E Stat. Nonlin. Soft Matter Phys.* **2015,** *92* (1), 012317.

48. Kirschbaum, J.; Zwicker, D., Controlling biomolecular condensates via chemical reactions. *J. R. Soc. Interface* **2021,** *18* (179), 20210255.

49. Donau, C.; Boekhoven, J., The chemistry of chemically fueled droplets. *Trends in Chemistry* **2023,** *5* (1), 45-60.

50. Weber, C. A.; Zwicker, D.; Julicher, F.; Lee, C. F., Physics of active emulsions. *Rep. Prog. Phys.* **2019,** *82* (6), 064601.

51. Zwicker, D., The intertwined physics of active chemical reactions and phase separation. *Current Opinion in Colloid & Interface Science* **2022,** *61*.

52. Seyboldt, R.; Jülicher, F., Role of hydrodynamic flows in chemically driven droplet division. *New Journal of Physics* **2018,** *20* (10).

53. Weißenfels, M.; Gemen, J.; Klajn, R., Dissipative Self-Assembly: Fueling with Chemicals versus Light. *Chem* **2021,** *7* (1), 23-37.

54. Tena-Solsona, M.; Riess, B.; Grotsch, R. K.; Lohrer, F. C.; Wanzke, C.; Kasdorf, B.; Bausch, A. R.; Muller-Buschbaum, P.; Lieleg, O.; Boekhoven, J., Non-equilibrium dissipative supramolecular materials with a tunable lifetime. *Nat. Commun.* **2017,** *8*, 15895.

55. Hess, H.; Ross, J. L., Non-equilibrium assembly of microtubules: from molecules to autonomous chemical robots. *Chem. Soc. Rev.* **2017,** *46* (18), 5570-5587.

56. Schwarz, P. S.; Tena-Solsona, M.; Dai, K.; Boekhoven, J., Carbodiimide-fueled catalytic reaction cycles to regulate supramolecular processes. *Chem. Commun.* **2022,** *58* (9), 1284-1297.

57. Rieß, B.; Grötsch, R. K.; Boekhoven, J., The Design of Dissipative Molecular Assemblies Driven by Chemical Reaction Cycles. *Chem* **2020,** *6* (3), 552-578.

58. Chen, X.; Würbser, M. A.; Boekhoven, J., Chemically Fueled Supramolecular Materials. *Acc. Mater. Res.* **2023,** *4* (5), 416-426.

59. van Rossum, S. A. P.; Tena-Solsona, M.; van Esch, J. H.; Eelkema, R.; Boekhoven, J., Dissipative out-of-equilibrium assembly of man-made supramolecular materials. *Chem. Soc. Rev.* **2017,** *46* (18), 5519-5535.

60. Wang, Q.; Qi, Z.; Chen, M.; Qu, D. H., Out-of-equilibrium supramolecular self-assembling systems driven by chemical fuel. *Aggregate* **2021,** *2* (5).

61. Boekhoven, J.; Brizard, A. M.; Kowlgi, K. N.; Koper, G. J.; Eelkema, R.; van Esch, J. H., Dissipative self-assembly of a molecular gelator by using a chemical fuel. *Angew. Chem. Int. Ed. Engl.* **2010,** *49* (28), 4825-8.

62. Boekhoven, J.; Hendriksen, W. E.; Koper, G. J.; Eelkema, R.; van Esch, J. H., Transient assembly of active materials fueled by a chemical reaction. *Science* **2015,** *349* (6252), 1075-9.

63. Slootbeek, A. D.; van Haren, M. H. I.; Smokers, I. B. A.; Spruijt, E., Growth, replication and division enable evolution of coacervate protocells. *Chem. Commun.* **2022,** *58* (80), 11183-11200.

64. Nakashima, K. K.; Vibhute, M. A.; Spruijt, E., Biomolecular Chemistry in Liquid Phase Separated Compartments. *Front. Mol. Biosci.* **2019,** *6,* 21.

65. Aumiller, W. M., Jr.; Keating, C. D., Phosphorylation-mediated RNA/peptide complex coacervation as a model for intracellular liquid organelles. *Nat. Chem.* **2016,** *8* (2), 129-37.

66. Wang, J.; Abbas, M.; Wang, J.; Spruijt, E., Selective amide bond formation in redox-active coacervate protocells. *Nat. Commun.* **2023,** *14* (1), 8492.

67. Abbas, M.; Lipinski, W. P.; Nakashima, K. K.; Huck, W. T. S.; Spruijt, E., A short peptide synthon for liquid-liquid phase separation. *Nat. Chem.* **2021,** *13* (11), 1046-1054.

68. Nakashima, K. K.; Baaij, J. F.; Spruijt, E., Reversible generation of coacervate droplets in an enzymatic network. *Soft Matter* **2018,** *14* (3), 361-367.

69. Donau, C.; Späth, F.; Sosson, M.; Kriebisch, B. A. K.; Schnitter, F.; Tena-Solsona, M.; Kang, H. S.; Salibi, E.; Sattler, M.; Mutschler, H.; Boekhoven, J., Active coacervate droplets as a model for membraneless organelles and protocells. *Nat. Commun.* **2020,** *11* (1), 5167.

70. Riess, B.; Wanzke, C.; Tena-Solsona, M.; Grotsch, R. K.; Maity, C.; Boekhoven, J., Dissipative assemblies that inhibit their deactivation. *Soft Matter* **2018,** *14* (23), 4852-4859.

71. Wanzke, C.; Tena-Solsona, M.; Rieß, B.; Tebcharani, L.; Boekhoven, J., Active droplets in a hydrogel release drugs with a constant and tunable rate. *Materials Horizons* **2020,** *7* (5), 1397-1403.

72. Bergmann, A. M.; Donau, C.; Späth, F.; Jahnke, K.; Göpfrich, K.; Boekhoven, J., Evolution and Single-Droplet Analysis of Fuel-Driven Compartments by Droplet-Based Microfluidics. *Angew. Chem. Int. Ed. Engl.* **2022,** *61* (32), e202203928.

73. Donau, C.; Späth, F.; Stasi, M.; Bergmann, A. M.; Boekhoven, J., Phase Transitions in Chemically Fueled, Multiphase Complex Coacervate Droplets. *Angew. Chem. Int. Ed. Engl.* **2022,** *61* (46), e202211905.

74. Lu, T.; Spruijt, E., Multiphase Complex Coacervate Droplets. *J. Am. Chem. Soc.* **2020,** *142* (6), 2905-2914.

75. Bergmann, A. M.; Bauermann, J.; Bartolucci, G.; Donau, C.; Stasi, M.; Holtmannspotter, A. L.; Julicher, F.; Weber, C. A.; Boekhoven, J., Liquid spherical shells are a non-equilibrium steady state of active droplets. *Nat. Commun.* **2023,** *14* (1), 6552.

76. Xu, C.; Hu, S.; Chen, X., Artificial cells: from basic science to applications. *Mater. Today* **2016,** *19* (9), 516-532.

77. Cook, A. B.; Novosedlik, S.; van Hest, J. C. M., Complex Coacervate Materials as Artificial Cells. *Acc. Mater. Res.* **2023,** *4* (3), 287-298.

78. van Stevendaal, M.; Vasiukas, L.; Yewdall, N. A.; Mason, A. F.; van Hest, J. C. M., Engineering of Biocompatible Coacervate-Based Synthetic Cells. *ACS Appl. Mater. Interfaces* **2021,** *13* (7), 7879-7889.

79. Gao, N.; Mann, S., Membranized Coacervate Microdroplets: from Versatile Protocell Models to Cytomimetic Materials. *Acc. Chem. Res.* **2023,** *56* (3), 297-307.

80. Mason, A. F.; Buddingh, B. C.; Williams, D. S.; van Hest, J. C. M., Hierarchical Self-Assembly of a Copolymer-Stabilized Coacervate Protocell. *J. Am. Chem. Soc.* **2017,** *139* (48), 17309-17312.

81. Pir Cakmak, F.; Marianelli, A. M.; Keating, C. D., Phospholipid Membrane Formation Templated by Coacervate Droplets. *Langmuir* **2021,** *37* (34), 10366-10375.

82. Dora Tang, T. Y.; Rohaida Che Hak, C.; Thompson, A. J.; Kuimova, M. K.; Williams, D. S.; Perriman, A. W.; Mann, S., Fatty acid membrane assembly on coacervate microdroplets as a step towards a hybrid protocell model. *Nat. Chem.* **2014,** *6* (6), 527-33.

83. Altenburg, W. J.; Yewdall, N. A.; Vervoort, D. F. M.; van Stevendaal, M.; Mason, A. F.; van Hest, J. C. M., Programmed spatial organization of biomacromolecules into discrete, coacervate-based protocells. *Nat. Commun.* **2020,** *11* (1), 6282.

84. Abbas, M.; Lipinski, W. P.; Wang, J.; Spruijt, E., Peptide-based coacervates as biomimetic protocells. *Chem. Soc. Rev.* **2021,** *50* (6), 3690-3705.

85.   Capasso Palmiero, U.; Paganini, C.; Kopp, M. R. G.; Linsenmeier, M.; Kuffner, A. M.; Arosio, P., Programmable Zwitterionic Droplets as Biomolecular Sorters and Model of Membraneless Organelles. *Adv. Mater.* **2022,** *34* (4), e2104837.

86.   Iglesias-Artola, J. M.; Drobot, B.; Kar, M.; Fritsch, A. W.; Mutschler, H.; Dora Tang, T. Y.; Kreysing, M., Charge-density reduction promotes ribozyme activity in RNA-peptide coacervates via RNA fluidization and magnesium partitioning. *Nat. Chem.* **2022,** *14* (4), 407-416.

87.   Chang, L. W.; Lytle, T. K.; Radhakrishna, M.; Madinya, J. J.; Velez, J.; Sing, C. E.; Perry, S. L., Sequence and entropy-based control of complex coacervates. *Nat. Commun.* **2017,** *8* (1), 1273.

88.   Choi, S.; Meyer, M. O.; Bevilacqua, P. C.; Keating, C. D., Phase-specific RNA accumulation and duplex thermodynamics in multiphase coacervate models for membraneless organelles. *Nat. Chem.* **2022,** *14* (10), 1110-1117.

89.   Ghosh, B.; Bose, R.; Tang, T. Y. D., Can coacervation unify disparate hypotheses in the origin of cellular life? *Current Opinion in Colloid & Interface Science* **2021,** *52*.

90.   Poudyal, R. R.; Guth-Metzler, R. M.; Veenis, A. J.; Frankel, E. A.; Keating, C. D.; Bevilacqua, P. C., Template-directed RNA polymerization and enhanced ribozyme catalysis inside membraneless compartments formed by coacervates. *Nat. Commun.* **2019,** *10* (1), 490.

91.   Mann, S., Systems of creation: the emergence of life from nonliving matter. *Acc. Chem. Res.* **2012,** *45* (12), 2131-41.

92.   Nakashima, K. K.; van Haren, M. H. I.; Andre, A. A. M.; Robu, I.; Spruijt, E., Active coacervate droplets are protocells that grow and resist Ostwald ripening. *Nat. Commun.* **2021,** *12* (1), 3819.

93.   Martin, N., Dynamic Synthetic Cells Based on Liquid-Liquid Phase Separation. *Chembiochem* **2019,** *20* (20), 2553-2568.

94.   Robertson, A.; Sinclair, A. J.; Philp, D., Minimal self-replicating systems. *Chem. Soc. Rev.* **2000,** *29* (2), 141-152.

95.   Clixby, G.; Twyman, L., Self-replicating systems. *Org. Biomol. Chem.* **2016,** *14* (18), 4170-84.

96.   Buddingh, B. C.; van Hest, J. C. M., Artificial Cells: Synthetic Compartments with Life-like Functionality and Adaptivity. *Acc. Chem. Res.* **2017,** *50* (4), 769-777.

97.   Adamala, K.; Szostak, J. W., Competition between model protocells driven by an encapsulated catalyst. *Nat. Chem.* **2013,** *5* (6), 495-501.

98.   Tawfik, D. S.; Griffiths, A. D., Man-made cell-like compartments for molecular evolution. *Nat. Biotechnol.* **1998,** *16* (7), 652-6.

99.   Teif, V. B.; Bohinc, K., Condensed DNA: condensing the concepts. *Prog. Biophys. Mol. Biol.* **2011,** *105* (3), 208-22.

100. Takinoue, M., DNA droplets for intelligent and dynamical artificial cells: from the viewpoint of computation and non-equilibrium systems. *Interface Focus* **2023,** *13* (5), 20230021.

101. Deng, J.; Walther, A., Programmable and Chemically Fueled DNA Coacervates by Transient Liquid-Liquid Phase Separation. *Chem* **2020,** *6* (12), 3329-3343.

102. Späth, F.; Donau, C.; Bergmann, A. M.; Kränzlein, M.; Synatschke, C. V.; Rieger, B.; Boekhoven, J., Molecular Design of Chemically Fueled Peptide-Polyelectrolyte Coacervate-Based Assemblies. *J. Am. Chem. Soc.* **2021,** *143* (12), 4782-4789.

103. Späth, F.; Maier, A. S.; Stasi, M.; Bergmann, A. M.; Halama, K.; Wenisch, M.; Rieger, B.; Boekhoven, J., The Role of Chemically Innocent Polyanions in Active, Chemically Fueled Complex Coacervate Droplets. *Angew. Chem. Int. Ed. Engl.* **2023,** *62* (41), e202309318.

104. Kolchina, N.; Khavinson, V.; Linkova, N.; Yakimov, A.; Baitin, D.; Afanasyeva, A.; Petukhov, M., Systematic search for structural motifs of peptide binding to double-stranded DNA. *Nucleic Acids Res.* **2019,** *47* (20), 10553-10563.

105. Wilson, K. A.; Kellie, J. L.; Wetmore, S. D., DNA-protein pi-interactions in nature: abundance, structure, composition and strength of contacts between aromatic amino acids and DNA nucleobases or deoxyribose sugar. *Nucleic Acids Res.* **2014,** *42* (10), 6726-41.

106. Chen, C.; Esadze, A.; Zandarashvili, L.; Nguyen, D.; Montgomery Pettitt, B.; Iwahara, J., Dynamic Equilibria of Short-Range Electrostatic Interactions at Molecular Interfaces of Protein-DNA Complexes. *J. Phys. Chem. Lett.* **2015,** *6* (14), 2733-7.

107. Vieregg, J. R.; Lueckheide, M.; Marciel, A. B.; Leon, L.; Bologna, A. J.; Rivera, J. R.; Tirrell, M. V., Oligonucleotide-Peptide Complexes: Phase Control by Hybridization. *J. Am. Chem. Soc.* **2018,** *140* (5), 1632-1638.

108. Fraccia, T. P.; Jia, T. Z., Liquid Crystal Coacervates Composed of Short Double-Stranded DNA and Cationic Peptides. *ACS Nano* **2020,** *14* (11), 15071-15082.

109. Hayashi, K.; Chaya, H.; Fukushima, S.; Watanabe, S.; Takemoto, H.; Osada, K.; Nishiyama, N.; Miyata, K.; Kataoka, K., Influence of RNA Strand Rigidity on Polyion Complex Formation with Block Catiomers. *Macromol. Rapid Commun.* **2016,** *37* (6), 486-93.

110. Liu, J.; Zhorabek, F.; Chau, Y., Nucleic Acids Modulate Liquidity and Dynamics of Artificial Membraneless Organelles. *ACS Macro Lett.* **2022,** *11* (4), 562-567.

111. Aumiller, W. M., Jr.; Pir Cakmak, F.; Davis, B. W.; Keating, C. D., RNA-Based Coacervates as a Model for Membraneless Organelles: Formation, Properties, and Interfacial Liposome Assembly. *Langmuir* **2016,** *32* (39), 10042-10053.

112. Poudyal, R. R.; Keating, C. D.; Bevilacqua, P. C., Polyanion-Assisted Ribozyme Catalysis Inside Complex Coacervates. *ACS Chem. Biol.* **2019,** *14* (6), 1243-1248.

113. Le Vay, K. K.; Salibi, E.; Ghosh, B.; Tang, T. Y. D.; Mutschler, H., Ribozyme activity modulates the physical properties of RNA-peptide coacervates. *Elife* **2023,** *12*.